Graduate School ETD Form 9
(Revised 12/07)

PURDUE UNIVERSITY
GRADUATE SCHOOL
Thesis/Dissertation Acceptance

This is to certify that the thesis/dissertation prepared

By Merrell A. Johnson

Entitled
Near-Field Investigations
of the Anisotropic Properties of Supported Lipid Bilayers

For the degree of Doctor of Philosophy

Is approved by the final examining committee:

Ricardo Decca
Chair

Horia Petrache

Andrew J Rader

Stephen Wassall

Ken Ritchie

To the best of my knowledge and as understood by the student in the *Research Integrity and Copyright Disclaimer (Graduate School Form 20)*, this thesis/dissertation adheres to the provisions of Purdue University's "Policy on Integrity in Research" and the use of copyrighted material.

Approved by Major Professor(s): Ricardo Decca

Approved by: Ricardo Decca 6/22/2011
Head of the Graduate Program Date

Graduate School Form 20
(Revised 9/10)

PURDUE UNIVERSITY
GRADUATE SCHOOL

Research Integrity and Copyright Disclaimer

Title of Thesis/Dissertation:

Near-Field Investigations
of the Anisotropic Properties of Supported Lipid Bilayers

For the degree of Doctor of Philosophy

I certify that in the preparation of this thesis, I have observed the provisions of *Purdue University Executive Memorandum No. C-22,* September 6, 1991, *Policy on Integrity in Research.**

Further, I certify that this work is free of plagiarism and all materials appearing in this thesis/dissertation have been properly quoted and attributed.

I certify that all copyrighted material incorporated into this thesis/dissertation is in compliance with the United States' copyright law and that I have received written permission from the copyright owners for my use of their work, which is beyond the scope of the law. I agree to indemnify and save harmless Purdue University from any and all claims that may be asserted or that may arise from any copyright violation.

Merrell A. Johnson
Printed Name and Signature of Candidate

06/21/2011
Date (month/day/year)

*Located at http://www.purdue.edu/policies/pages/teach_res_outreach/c_22.html

NEAR-FIELD INVESTIGATIONS OF THE ANISOTROPIC PROPERTIES OF SUPPORTED LIPID BILAYERS

A Dissertation

Submitted to the Faculty

of

Purdue University

by

Merrell A. Johnson

In Partial Fulfillment of the

Requirements for the Degree

of

Doctor of Philosophy

August 2011

Purdue University

Indianapolis, Indiana

[To my wife, parents and brother for being supportive over the many years.]

TABLE OF CONTENTS

Page

LIST OF TABLES

LIST OF FIGURES

Figure Page

Figure Page

Figure Page

Figure Page

Figure Page

NOMENCLATURE

AFM	Atomic Force Microscopy
C_p	Heat Capacitance at constant pressure
C_p^{exc}	Excess Heat Capacity at constant pressure
c_p	Stray of Parasitic Capacitance
DLPC	1,2-dilauroyl-sn-glycero-3-phosphocholine
DMPC	1,2-dimyristoyl-sn-glycero-3-phosphocholine
DOPC	1,2-dioleoyl-sn-glycero-3-phosphocholine
DPPC	1,2-dipalmitoyl-sn-glycero-3-phosphocholine
DSC	Differential Scanning Calorimetry
F	Helmholtz free energy
G	Gibbs free energy
L_α	Lamellar liquid crystalline or Liquid disorder
L_β	Lamellar gel or Solid ordered
$L_{\beta'}$	Lamellar gel with acyl chains at some orientation different from 0° with respect to the membranes normal.
LP	Linear Polarizer
MD	Molecular Dynamics
MFT	Mean Field Theory
NMR	Nuclear Magnetic Resonance
NSOM	Near-Field Scanning Optical Microscopy
P	Pressure
$P_{\beta'}$	Ripple phase

PC	phosphocholine
PEM	Photo Elastic Modulator
PM	Polarization Modulation
POPC	1-palmitoyl-2-oleoyl-sn-glycero-3-phosphocholine
QWP	Quarter Wave Plate
RLC	Resistor Inductor Capacitor
SEM	Scanning Electron Microscopy
SF	Shear Force
T	Temperature
TEC	Thermo-Electric Cooler
T_m	Main Phase Transition Temperature
T_x	Phase transition temperature

ABSTRACT

Johnson, Merrell A. Ph.D., Purdue University, August 2011. Near-Field Investigations of the Anisotropic Properties of Supported Lipid Bilayers. Major Professor: Ricardo S. Decca.

The details of Polarization Modulation Near-Field Scanning Optical Microscopy (PM-NSOM) are presented. How to properly calibrate and align the system is also introduced. A measurement of Muscovite crystal is used to display the capabilities of the setup. Measurements of supported $L_{\beta'}$ 1,2-dipalmitoyl-sn-glycero-3-phosphocholine (DPPC) lipid bilayers are presented, emphasizing how it was tooled in exploiting the anisotropic nature of the acyl chains. A discussion of how the effective retardance ($\Delta S = \frac{2\pi(n_e - n_o)t}{\lambda}$) and the direction of the projection of the acyl chains (θ) are measured simultaneously is given, (where t is the thickness of the bilayer and λ is the wavelength of light used). It is shown from ΔS the birefringence ($n_e - n_o$) of the bilayer is determined, by assuming the acyl chain tilt with respect to the membrane's normal to be $\phi \approx 32°$. Time varying experiments show lateral diffusions of $\sim 2 \times 10^{-12}$ $\frac{cm^2}{s}$. Temperature controlled PM-NSOM is shown to be a viable way to determine the main phase transition temperature (T_m) for going from the gel $L_{\beta'}$ to liquid disorder L_α state of supported DPPC bilayers. A change of $\Delta S \sim$ (3.8 $\pm$0.3 mrad) at the main phase transition temperature T_m ($\approx 41°$C) is observed. This agrees well with previous values of ($n_e - n_o$) and translates to an assumed $\langle\phi\rangle \sim 32°$ when T $< T_m$ and 0° when T $> T_m$. Evidence of supper heating and supper cooling will be presented, along with a discussion of the fluctuations that occur around T_m. Finally it is shown how physical parameters such as the polarizability are extracted from the data. Values of the transverse (α_t) and longitudinal (α_l) polarizabilites of

the acyl chains are shown to be, $\alpha_t = 44.2$Å^3 and $\alpha_l = 94.4$ Å^3, which correspond well with the theoretical values of a single palmitic acid (C_{16}) $\alpha_t = 25.14$ Å^3 and $\alpha_l = 45.8$ Å^3.

1. INTRODUCTION

In biological systems, cells are a part of the fundamental building blocks of life. Mammalian cells are made of a complex aggregate of materials, but most could not exist without lipids. Lipids can account for up to 70% [1] of the cellular membrane, which isolate the cell from its environment. In the process of understanding cellular function, it is vastly important to determine how lipids within the cell affect the system. Due to the complexity of cellular membranes, it becomes difficult to isolate the specific functions associated with each component. To simplify the system, many scientists use model membranes to solve various questions pertaining to lipids and their properties.

Lipid membranes, like most materials, can assume different states of matter, further detailed in Section 2.2. Transitions between these states are thought to play an important role in cellular function [2]. Lipid components within membranes of different phases are suggested to contribute in domain stabilization, cell adhesion and mobility [3]. Cellular membranes are composed of a variety of lipids, proteins, etc., which all contribute to the overall function of the cell. By using model membranes we can attempt to understand the fundamental properties of various lipid components of a cell. The investigation of the collective nature of molecular interactions in lipid bilayer systems can be examined, to determine how they uniquely impact the free energy of that system. Membrane curvature, acyl chain length, lipid composition, and head group interactions are a few variables that can contribute to the free energy, and translate to determine the state of the lipid membrane. By studying phase

transitions as well as other thermodynamically influenced properties, we may gain further insight on how these interactions contribute to the system.

In general, lipid molecules are anisotropic due to their asymmetric acyl chains. The long extension of hydrocarbons can be thought of a cylindrical or rod like charge distribution, which would imply that its polarizability (α_{ij}) or response to an applied electric field, is asymmetric. This idea will be further detailed in Section 4.1, but as an introduction, this anisotropy can be exploited by studying how the electric field interacts with the membrane. As an electromagnetic wave passes through the lipid membrane in a direction parallel to the normal, the index of refraction along perpendicular directions to the propagating wave are going to be related to the projections of the acyl chains. Materials that posses such property are called birefriengent ($n_e - n_o$). This study will demonstrate how information containing this difference may be extracted through a measurement of their effective retardance ($S = \frac{2\pi t(n_e - n_o)}{\lambda}$), a parameter that is a function of acyl chain tilt (ϕ), thickness of the membrane (t) and differences in indices of refractions along the radial and length directions of the lipid molecules.

In a birefringent material, polarized light experiences different indices of refraction along the vertical and horizontal axis, in the plane of the object. The effective phase shift between the two components of the wave is called the retardance S. Anisotropic ordered crystals such as calcite and quartz display such qualities, which are easily measurable. As aforementioned, lipid bilayers are anisotropic in nature, but also exhibit an ordered packing configuration, which allows for the exploitation of these birefringent properties similar to crystals structures. As an example, while in the gel state ($L_{\beta'}$), the lipid molecules are oriented at a $\phi \neq 0$, this results in the polarizablilty in the plane parallel ($\parallel$) to the surfaces normal to differ along each $\perp$ axis. The effective S lipid bilayer causes, is dependent on the molecular orientation (ϕ)

of the acyl chains, relative to the surface normal. This arises from the directional difference from the hydrocarbon rich acyl chains, as seen in figure 1. When the lipid molecules are oriented along the direction of the normal and light passes through in that direction, the $n_e - n_o$ is zero. While if the lipid molecules have a $\phi \neq 0$ then the projection of the acyl chains give a non-zero value $n_e - n_o$ that results in an effective S. Knowing that membrane phase transitions depend on molecular orientation, we can study these transitions by measuring S and the direction of acyl chain projections in the plane of the membrane θ. This information is useful in determining the change in phase of the lipid system. Hence, in our work, we will show that phase transitions of planar lipid bilayers can be well studied by measuring S and θ.

Phase transitions in lipid bilayers have been theoretically described using methods ranging from Mean Field Theory (MFT) approximations [4–6] to Molecular Dynamics (MD) simulations [7]. These techniques usually section the free energy into lipid head group interactions, and van der Waals attraction between nearest parallel acyl chains. MFT uses the average positions of the acyl chains and predicts first order phase transitions in lipids systems [5]. Membrane phase transitions have been shown to be a function of acyl chain length, non-membrane molecular interactions and head group exchanges. Experimentally these traits have been well characterized with techniques ranging from H^2-NMR [8] to calorimetric studies [9]. These experimental methods fail to study planar membranes, measuring large areas of material ($\sim \mu m^2$). Additional phase transition focused studies on planar membranes utilized Atomic Force Microscopy (AFM), which target changes in height of the membrane as the material starts to phase separate, displaying regions of the membrane in different phases [10]. The limitations this method possess is that it is restricted to highlighting the changes in height across the membrane and does not determine how the acyl chains behave within the membrane as the phase transition temperature (T_m) is approached. We

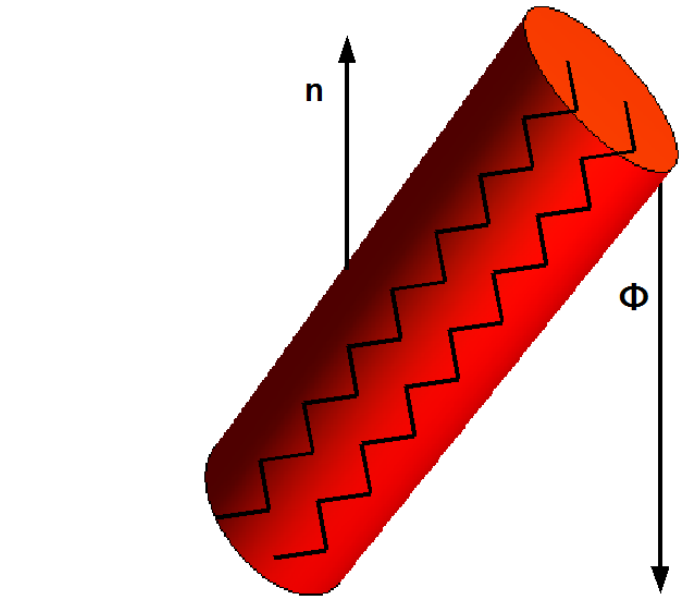

(a)

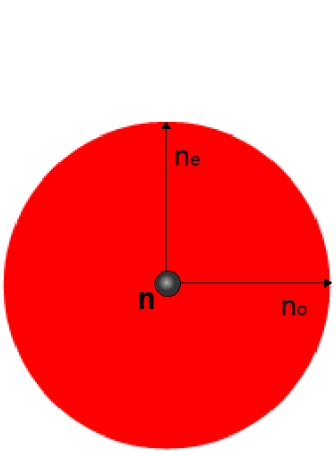

(b)

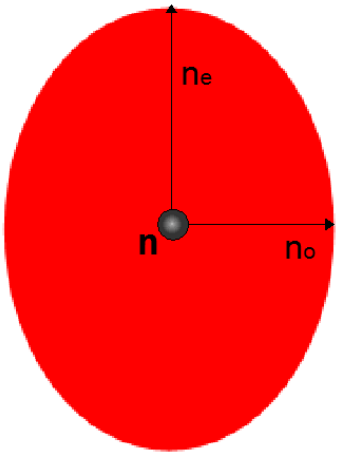

(c)

Figure 1.1. a) Cylindrical representation of the acyl chains positioned at an angle ϕ. This shows the asymmetric nature along the length versus the diameter of the cylinder. b) Projection of the cylinder when $\phi = 0$, where $n_e = n_o$, which would result in no effective S. c) Projection of the cylinder when $\phi \neq 0$, where $n_e \neq n_o$, which would result in an effective S.

Table 1.1
List of experimental techniques and their lateral resolution capabilities.

Experimental Technique	lateral resolution
NMR	> 1 μm [11]
DSC	~ 500 μm
X-Ray	~ 500 μm
AFM	$> 20 - 10$ nm [12]
NSOM	$100 - 50$ nm [13]

will show how a measurement of the effective ϕ change across a planar membrane sample can be preformed as we transition through states in lipids, with a lateral resolution ~ 100 nm. Table 1.1 highlights how NSOM's lateral resolution compares to other widely used techniques.

Using the effective retardance of lipid systems is not a new practice in studying model membranes in biophysics. Birefringence measurements on 1,2-dipalmitoyl-sn-glycero-3-phosphocholine (DPPC) bilayers in the gel state have been used to determine molecular orientation [14–16]. By assuming the molecular tilt, $\phi \sim 32^\circ$ [17], to be constant across the structure and knowing the perpendicular component of the refractive index $n_\perp$, the optical orientation θ and parallel refractive index $n_\parallel$ were determined. With the use of a Near-Field Scanning Optical Microscope (NSOM), Lee et al. [14] were able to explore these structural effects, having a lateral resolution on the order of $\sim$ 100nm. In addressing the limitations of this experiment, we introduce the equation

$$\begin{pmatrix} \cos(\theta) & \sin(\theta) \\ -\sin(\theta) & \cos(\theta) \end{pmatrix} \begin{pmatrix} e^{i\frac{S}{2}} & 0 \\ 0 & e^{-i\frac{S}{2}} \end{pmatrix} \begin{pmatrix} \cos(\theta) & -\sin(\theta) \\ \sin(\theta) & \cos(\theta) \end{pmatrix}, \tag{1.1}$$

to serve as a mathematical representation of a sample with a retardance S, oriented relative to the system's axis at an angle θ. In the experiment performed by Lee et.

al. [14], the sample was placed between two cross polarizers. Because the direction of polarization was know the components may be represented using Jones' matrices. Each component can be represented by a 2×2 matrix that rotates the electric field vector $\left(\frac{\mathbf{E_x}}{\mathbf{E_y}}\right)$. The Jones' matrix representation may be presented as,

$$\begin{pmatrix} e^{i\frac{S}{2}} & 0 \\ 0 & e^{-i\frac{S}{2}} \end{pmatrix} \begin{pmatrix} \cos(\theta) & -\sin(\theta) \\ \sin(\theta) & \cos(\theta) \end{pmatrix} \begin{pmatrix} 1 & 0 \\ 0 & 0 \end{pmatrix} \begin{pmatrix} 0 & 0 \\ 0 & 1 \end{pmatrix} \begin{pmatrix} \cos(\theta) & \sin(\theta) \\ -\sin(\theta) & \cos(\theta) \end{pmatrix} \tag{1.2}$$

An electric field passing through the system would yield,

$$\begin{pmatrix} \mathbf{E}_x \\ \mathbf{E}_y \end{pmatrix} \propto \begin{pmatrix} 0 \\ -i\ \sin(2\theta)\sin\left(\frac{S}{2}\right) \end{pmatrix} \tag{1.3}$$

The intensity ($\mathbf{EE}^*$) for this particular configuration is,

$$\mathbf{EE}^* \propto \sin^2\left(\frac{S}{2}\right)\sin^2(2\theta). \tag{1.4}$$

Because the intensity is a function of both S and θ, it was assumed by Lee et. al. [14] that S was constant across the sample and variations of θ were determined across the sample.

By using a Polarization Modulating (PM) technique presented in Chapter 5, we will demonstrate how S and θ can be extracted simultaneously from the experiment, obtaining all information independently. Also in the same chapter crucial system alignment procedures will be presented that were used to obtain highly sensitive measurements of S and θ. By combining the PM technique with a NSOM, topo-

graphical and optical information with a lateral resolution on the order ∼100 nm can be gathered. Because of the lateral and retardance resolution, additional information germane to the localized structural effects on lipid phase transitions will be shown. In addition, unlike calorimetry or Nuclear Magnetic Resonance (NMR) techniques, the advantage of studying a single planar membrane eliminates any curvature contributions to the free energy which could affect T_m.

2. THE BIOCHEMISTRY OF LIPIDS

Information presented will address the variation of lipids used in the experiments. Their chemical structures and unique properties will be discussed. Aspects specific to the lipids collective behavior and how they are experimentally characterized will be shared.

2.1 Lipid Structure

Lipids contain three basic components, either a glycerol or sphingosyl backbone, a head group and fatty acids. Their glycerol backbone is a hydrocarbon chain that is three carbons long with hydroxides attached to every carbon, as shown in figure 2.1. (The hydroxides are numbered 1 through 3, as depicted in figure 2.1(b).)

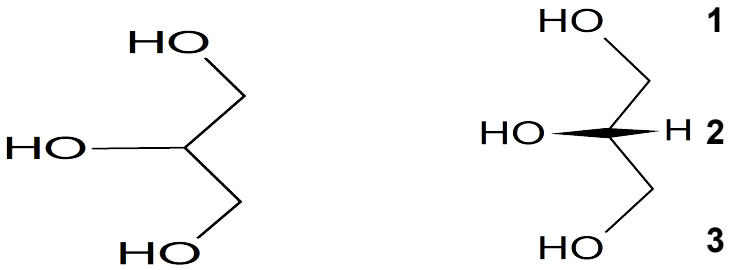

(a) (b)

Figure 2.1. a) Representation of a glycerol backbone with hydroxyl groups on the end of each arm. b) Glycerol backbone with the bonds numbered 1 through 3 with the IUPAC-IUB convention.

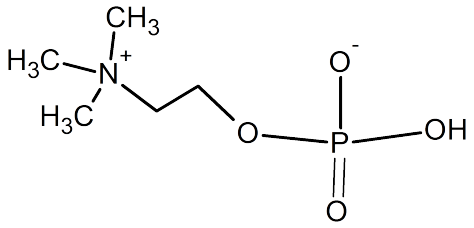

Figure 2.2. Chemical representation of a phosphocholine (PC) head group.

The sphingosine backbones are the essential components of sphingolipids. These lipids contain a long-chain amino alcohol, where a fatty acid is adjoined to the nitrogen (amide) segment. Without a headgroup, the sphigosine in conjunction with a fatty acid is commonly known as ceramide. With a sugar or oligosaccharide for a headgroup [18], various forms of sphingolipids can be found in the tissues of brain, kidney, lungs and spleen. Nevertheless they are not very abundant in microorganisms [19]. A ceramide with a phosphocholine(PC) or phosphoethanolamine (PE) headgroup, is known as sphingomyelin. In mammalian cells sphingomyelin lipids are primarily found in the plasma membrane, contributing to signal response in cells [1].

The glyceride head groups of the lipid can be divided into two sections, sugar or phosphorus (phosphorus headgroups were primarily utilized in this study). The phosphorus head groups are polar and can be charged or neutral (having no net charge). The particular head group of focus for this study was phosphocholine (PC). PC contains a phosphorous surrounded by four oxygen linked by hydrocarbons to a nitrogen. This results in a net positive charge on the nitrogen and a negative charge on the oxygen. This charge bonds singly to the phosphorous, as shown in figure 2.2. The overall charge distribution results in the polar properties of the head group, and is the reason behind their hydrophilic nature.

The hydrocarbon tails are naturally hydrophobic and can be either saturated or unsaturated. Saturated fatty acids have single carbon bonds, while unsaturated fatty

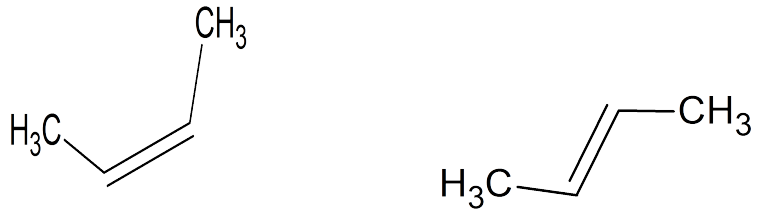

(a) (b)

Figure 2.3. Chemical structure of unsaturated bond configurations. a) The *cis* configuration, where both connecting hydrocarbons on the same side. b) The *trans* configuration, both connecting hydrocarbons on opposite sides.

acids have one (monounsaturated) or more (polyunsaturated) double bonds along the fatty acid or acyl chain. These double bonds can take the form of *trans* or *cis* [18], configurations. The *cis* configuration consists of the acyl chain carbons on each end of the double bond to be on the same side (see figure 2.3(a)). For the *trans* arrangement the carbons are on opposite sides of the double bond (see figure 2.3(b)).

Unsaturated bonds are more rigid than saturated bonds, due to the higher rotational energy barrier of ≈ 250 kJ/mol versus 10 kJ/mol in single bonds [19]. The lipid structure can be determined from the IUPAC-IUB [18] convention. From the written name sn-glycero indicates that the lipid has a stereo specifically numbered glycerol backbone. In figure 2.1(b) the hydroxides on the glycerol backbone were numbered 1 through 3. This convention is used when the model is drawn in a Fisher projection with the second hydroxyl group to the left [20]. This projection assists with determining the location of each attachment on the backbone. 1,2-dipalmitoyl indicates that two palmitic acid molecules are connected to the first and second sites on the glycerol backbone. Sometimes for convention 16:0 is used to indicate the length of the hydrocarbon tail (16) and the number of unsaturated carbon bonds (0). The

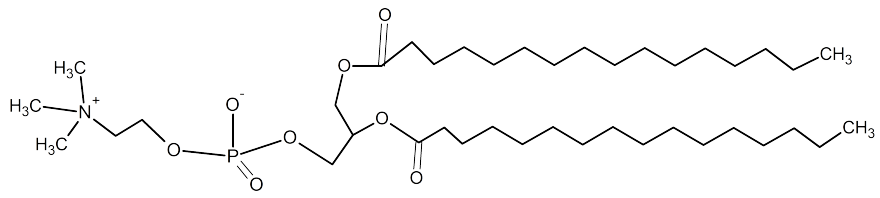

Figure 2.4. Chemical representation of 1,2-dipalmitoyl-sn-glycero-3-phosphocholine (DPPC). The lipid has a PC headgroup with two saturated acyl chains, 16 carbons long, connected to a glycerol backbone.

phosphocholine headgroup is then attached to the third position on the backbone. From this information a model of the characterized lipid molecule can be constructed (see figure 2.4).

Using the IUPAC-IUB convention we introduce the additional lipids 12:0 PC (DLPC) 1,2-dilauroyl-sn-glycero-3-phosphocholine and PC 14:0 (DMPC) 1,2-dimyristoyl-sn-glycero-3-phosphocholine, both with glycerol backbones, phosphocholine headgroups, and saturated fatty acids, 12 and 14 hydrocarbons in length (see figures 2.5(a) and 2.5(b)). An example of a mono-unsaturated lipid is PC 18:1(9*cis*) (DOPC) 1,2-dioleoyl-sn-glycero-3-phosphocholine, where it has the same backbone and headgroup as the two previous examples, but has two mono-unsaturated fatty acids eighteen carbons long with an unsaturation, in the *cis* confirmation, at the ninth hydrocarbon in the chain, seen in figure 2.5(c). Finally a non-symmetric lipid, PC 16:0/18:1(9*cis*)(POPC) 1-palmitoyl-2-oleoyl-sn-glycero-3-phosphocholine. This lipid differs from the previous lipids presented by having one saturated fatty acid 16 hydrocarbons long on the first position of the glycerol backbone, and a mono-unsaturated fatty acid eighteen carbons in length on the second (see figure 2.5(d)).

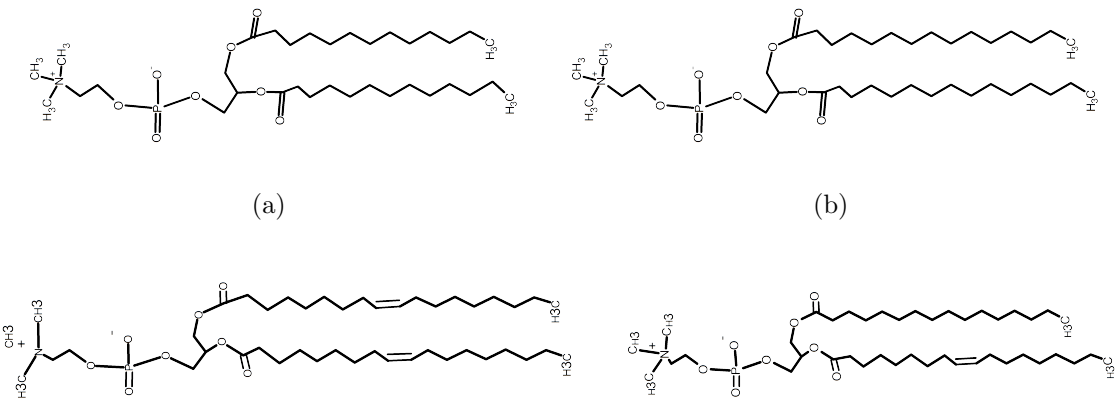

(a) (b)

(c) (d)

Figure 2.5. a) DLPC has two symmetric saturated acyl chains 12 hydrocarbons long. b) DMPC has two symmetric saturated acyl chains 14 hydrocarbons long. c) DOPC has two symmetric mono unsaturated acyl chains 18 hydrocarbons long, with a *cis* bond on the 9^{th} bond. d) POPC has a saturated acyl chains 16 hydrocarbons in length on the first position of the glycerol backbone and one mono unsaturated acyl chains 18 hydrocarbons long, with a *cis* bond on the 9^{th} bond on the second.

2.2 Lipid Phases

Lipids in nature, due to their hydrophobic acyl chains and polar headgroups, form vesicles in water. It is more energetically favorable for the lipid molecules to group together and form an enclosure where the headgroups are on the outside surrounded by water with the hydrocarbon tails tucked within the enclosure. The dynamics of the structure is dependent on the internal and external interactions of the lipid membrane. These dynamic properties have very distinct characteristics that are grouped into phases.

Lipid membranes, under various thermodynamic situations can exist in different states. Depending on the type of lipid and its environment they can form structures ranging from lamellar (L) to a hexagonal (H), with characteristic short range organizational properties. The α characteristic, is highly disordered with an average chain orientation parallel to the membrane normal [21]. It also has the unique attribute, where the bilayer thickness decrease as the temperature increases.

An additional characterization is β and β'. The fatty acids are free to rotate about each hydrocarbon bond, but have limited bending flexibility along its length. β describes the phase when the acyl chains orient parallel to the membrane normal, while β' represents the acyl chains positioned at an angle. Lastly δ, has a helical coil chain and the rotational and bending freedoms of the acyl chains are both limited.

Lipid membranes are classified into different distinct phases dependent on their structure and characterization. As an example,L_α means that we have a lamellar disordered phase, where as the $P_{\beta'}$ phase is referred to as the ripple phase. So we know from just the name that L_α is a stack of lipids with freely moving acyl chains that are parallel to the normal of the molecule, seen in figure 2.6(a). We also have a membrane in the $L_{\beta'}$ state, which would imply that it is lamellar, with its acyl chains oriented at an angle $\neq 0$, seen in figure 2.6(b). This information will be used

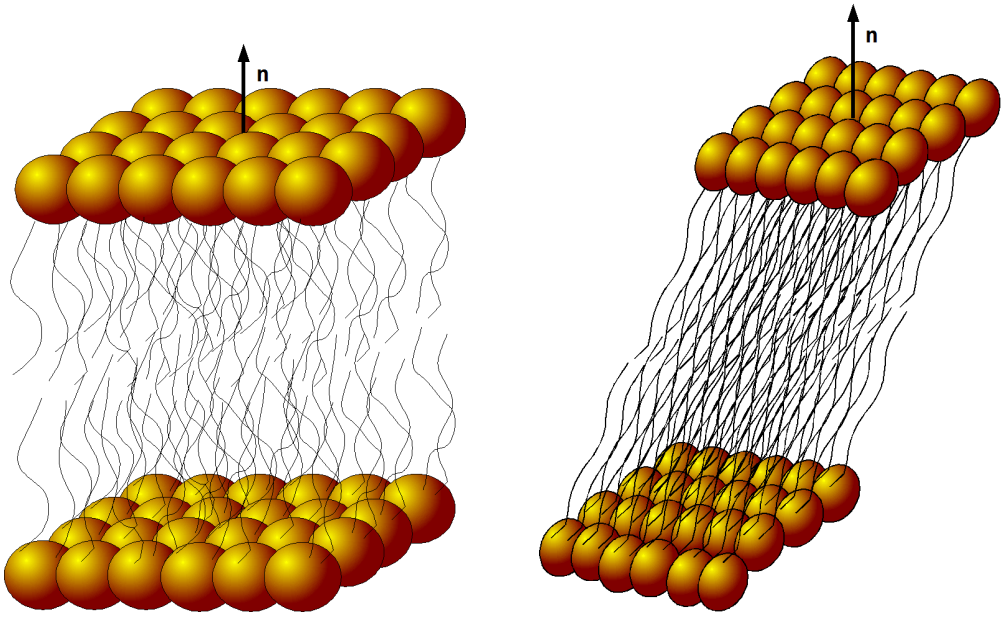

(a) (b)

Figure 2.6. Pictorial representation of two lamellar lipid phases. a) The L_α phase, where the acyl chains are disordered and parallel to the membrane normal b) The $L_{\beta'}$ phase, the fatty acids are more rigid and at an angle with respect to the normal ($\mathbf{n}$).

in later chapters to classify properties such as L_α and $L_{\beta'}$, so that we may distinctly determine changes of state of our system.

3. PHASE TRANSITIONS

The types of phase transitions that exist and their properties will be discussed within this chapter. First order phase transitions using Landau's Mean Field Theory (MFT) will be illustrated. Finally, the thermodynamic behaviour of lipid phase transitions will be presented.

The phase of a system has particular attributes that distinguishes it from other homogeneous elements of the same system. A phase transition may be defined when a system attributes change due to an external influence of a characterizing thermodynamic property (e.g. pressure, temperature, magnetic field) [22]. For an example, when water freezes the temperature decreases, resulting in the molecules transitioning from a liquid phase a solid. When water is in the liquid phase it has more degrees of freedom with no long range correlations between molecules. During the solid phase the translational motion of the molecules become ≈ 0 and forms a crystal structure [23]. The temperature at which this change of state happens is referred to as the phase transition temperature (T_x). At $T_x = 0°\text{C}$, the system releases energy, its latent heat of fusion. That thermal energy is used to reorient the molecules. As a result, there is a discontinuity in the density and the material solidifies. Phase transitions can provide valuable information about the interactions and properties within a system.

When a phase transition occurs the Gibbs (G) or Helmholtz (F) free energies of the two phases are equal. As an example the Gibbs free energy of phase one ($G(1)$) and phase two ($G(2)$) coexist as $G(1) = G(2)$ when a phase transition transpires. Under the conditions that only one thermodynamic variable is changed, this is labeled as

the phase transition point. Extending this to another thermodynamic variable such as pressure (P), this point can be extended to a coexistence curve, seen in figure 3.1. We characterize this point to be a first order phase transition when the first derivative of G or F is discontinuous at the transition point [22]. Figure 3.2 shows a graph of G as a function of temperature (concave for both phases, which implies a positive heat capacitance). The two free energy curves cross the other at the transition point, where as a function of the temperature the slope changes abruptly. The differential of G is

$$dG = -SdT + VdP, \tag{3.1}$$

from which $(\frac{\partial G}{\partial T})_p = -S$ implies a discontinuity in entropy, which is shown in figure 3.2(b). This discontinuity results in excess enthalpy at the transition needed to change phases, which we often refer too as latent heat. Under the conditions of constant P using equation 3.1 we obtain the following properties

$$\left(\frac{\partial G}{\partial T}\right)_P = -S \qquad \text{and} \qquad \left(\frac{\partial G}{\partial P}\right)_T = V, \tag{3.2}$$

where S and V are the entropy and volume.

Second order phase transitions occur when there is a discontinuity at the second derivative, shown in figure 3.3. Using the differential for the enthalpy (H),

$$dH = TdS + VdP \quad \text{and} \quad \left(\frac{\partial H}{\partial T}\right)_P = T\left(\frac{\partial S}{\partial T}\right)_P = C_p$$

$$-\left(\frac{\partial^2 G}{\partial T^2}\right)_P = \left(\frac{\partial S}{\partial T}\right)_P = \frac{C_p}{T} \quad \text{and} \quad -\left(\frac{\partial^2 G}{\partial P^2}\right)_T = -\left(\frac{\partial V}{\partial P}\right)_P = \beta_T V \tag{3.3}$$

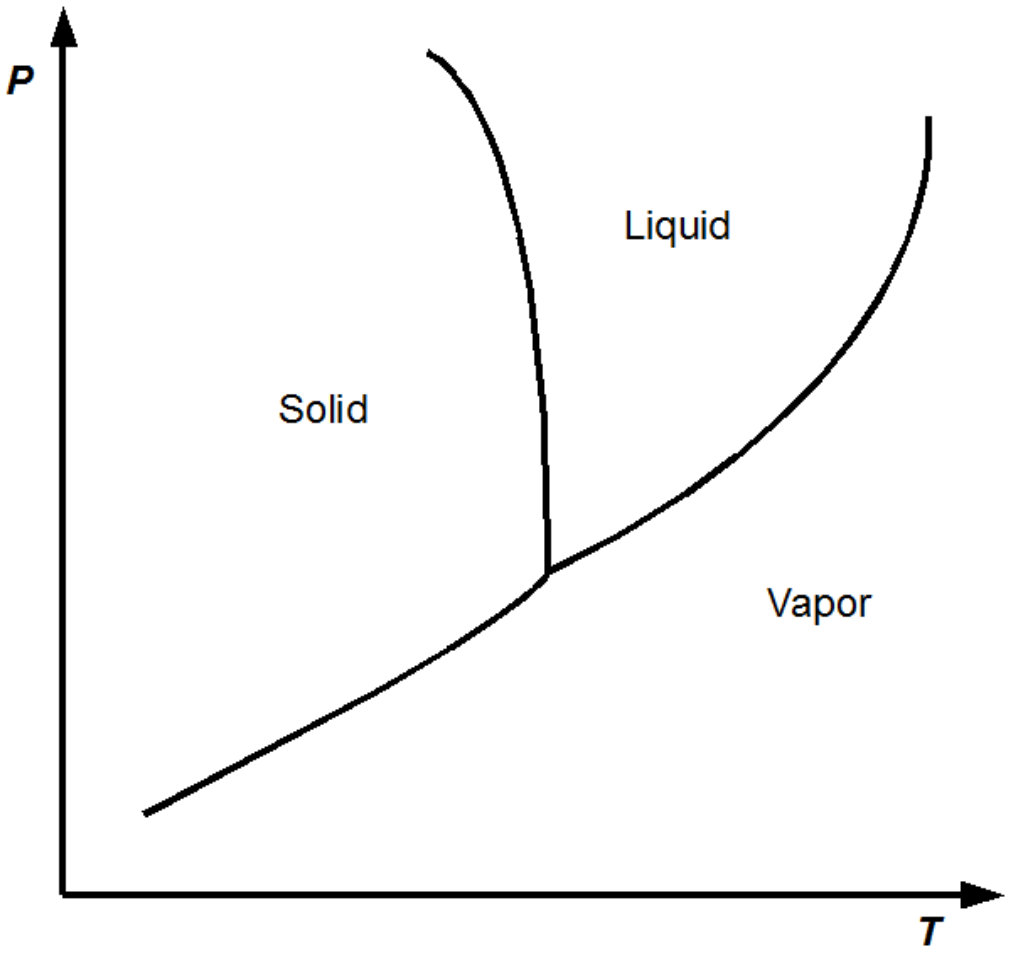

Figure 3.1. P versus T phase diagram showing coexisting curves for liquid, solid and vapour states.

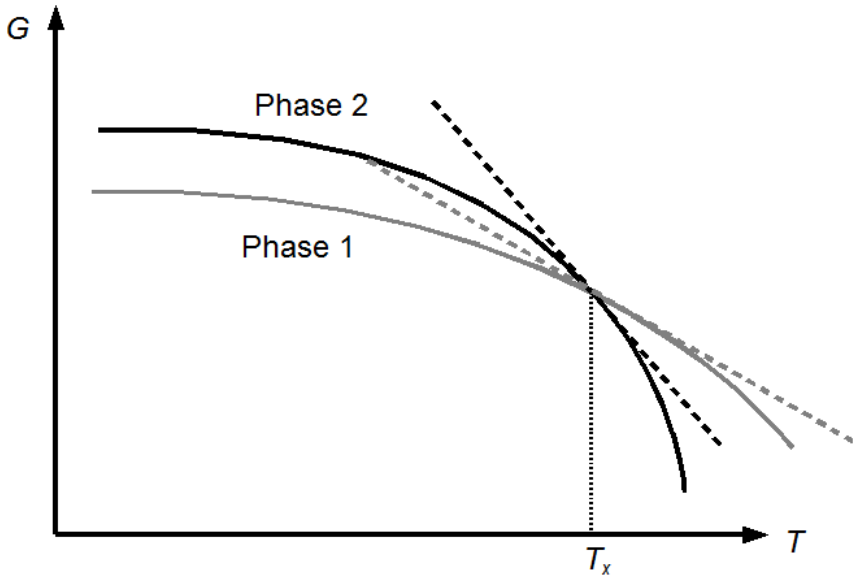

(a)

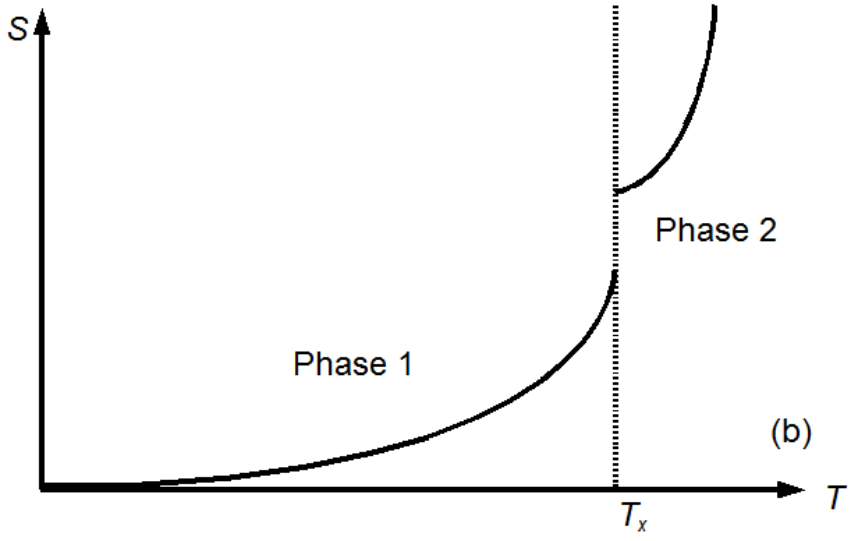

(b)

Figure 3.2. Representation of the Gibbs free energy of a system that exhibits a first order phase transition. a) A graph of the Gibbs free energy as a function of temperature of two different phases, where the transition temperature (T_x) is the intersecting point of the two lines. b) The entropy as a function of temperature, showing a discontinuity in $S = -\left(\frac{\partial G}{\partial T}\right)_P$.

In equation 3.3, C_p and β_T are the heat capacitance at constant pressure and the compressibility of the material at constant T, respectively. A discontinuity in C_p can be seen as we approach T_m, as depicted in figure 3.3(b).

3.1 Landau Mean Field Theory

Lev Landau suggested that phases can be expressed in terms of an order parameter (Γ), where above the transition temperature T_x $\Gamma = 0$ and for $T < T_x$ $\Gamma \neq 0$. From this, the Gibbs free energy can be put in terms of Γ, in addition to pressure (P) and temperature (T) [22]. Around T_x, the free energy can be expanded in terms of the order parameter.

$$G(P, T, \Gamma) = G_o(P, T, \Gamma) + \alpha\Gamma + A\Gamma^2 + C\Gamma^3 + B\Gamma^4 + \dots \tag{3.4}$$

We know that in order to minimize G in terms of Γ, we have the conditions,

$$\frac{\partial G}{\partial \Gamma} = 0 \qquad \text{and} \qquad \frac{\partial^2 G}{\partial \Gamma^2} > 0.$$

Using this result, under the condition of $\Gamma = 0$ for $T > T_x$, we obtain, $\alpha = 0$ and A > 0 for $T > T_x$. Also, for T $< T_x$ we have a non zero value for Γ where A is negative. We can then conveniently have A take the form,

$$A = a\,(T - T_x) \tag{3.5}$$

where $a > 0$.

Using this, we can then show that under constant pressure equation 3.4 takes the form

$$G(T, \Gamma) = G_o(T, \Gamma) + A\Gamma^2 + C\Gamma^3 + B\Gamma^4, \tag{3.6}$$

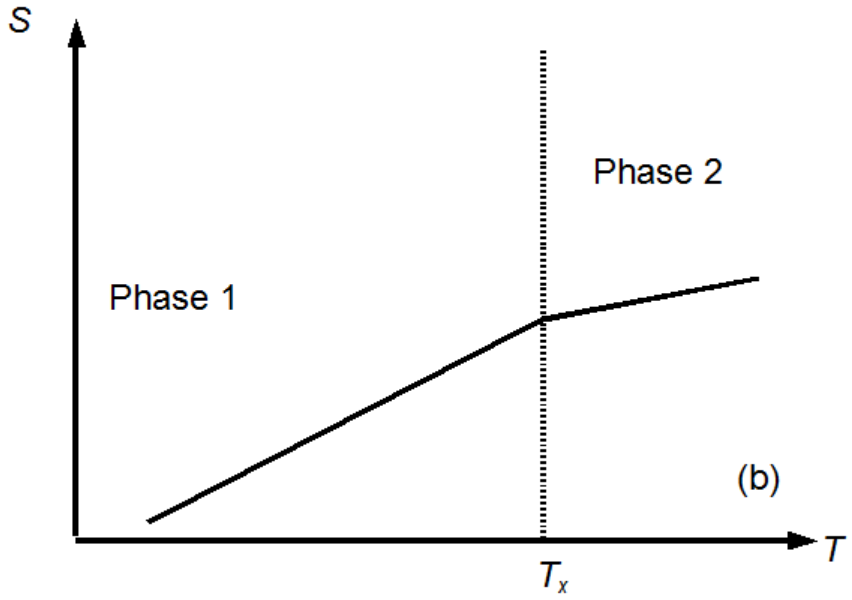

(a)

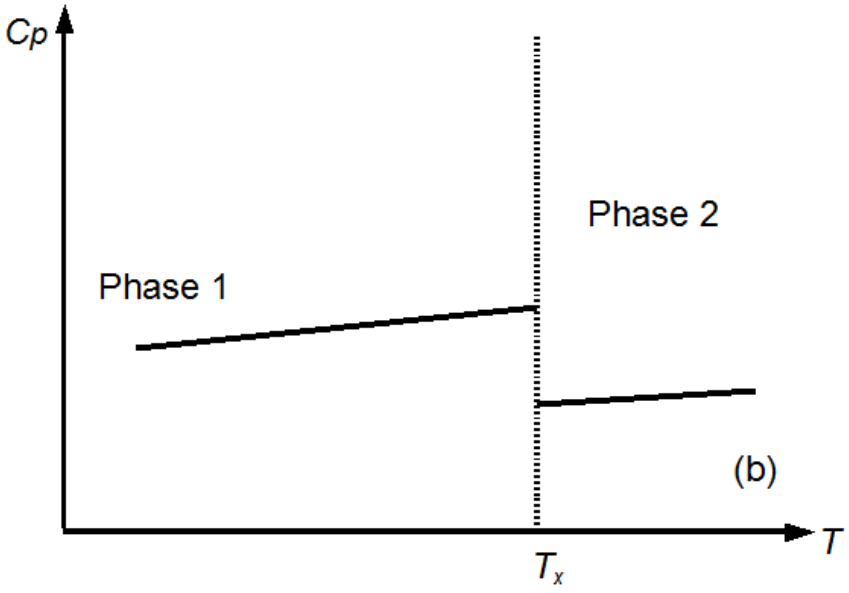

(b)

Figure 3.3. Representation of the Gibbs free energy of a system that undergoes a second order phase transition. a) A graph of the the entropy as a function of temperature. b) The heat capacitance at constant pressure $C_p = -T\left(\frac{\partial^2 G}{\partial T^2}\right)_p$ as a function of temperature, showing a discontinuity in C_p at T_x.

since $\frac{\partial G}{\partial \Gamma} = 0$,

$$2A\Gamma + 3C\Gamma^2 + 4B\Gamma^3 = 0, \tag{3.7}$$

implies that

$$\begin{aligned} \Gamma_1 &= 0, \\ \text{and} & \\ \Gamma_2 &= \frac{-3C \pm \sqrt{(3C)^2 + 32AB}}{8B} \\ &= \frac{-3C}{8B} \pm \sqrt{\left(\frac{3C}{8B}\right)^2 + \frac{a\,(T - T_x)}{2B}}. \end{aligned} \tag{3.8}$$

This insinuates that a temperature exists such that, $G\,(T^*, \Gamma_1) = G\,(T^*, \Gamma_2)$, yielding G as a function of Γ being discontinuous over T^*. This suggests that we have a first order phase transition. Landau's theory qualitatively describes first order phase transitions, but cannot be used to accurately predict quantitative results [23].

3.2 Phase Transitions of Lipids

Thermodynamic phases of lipids bilayers, being associated with the acyl chain orientation (ϕ), can be characterized in terms of an order parameter (Ω), where $\Omega = \frac{1}{2}\langle 3\cos^2(\phi) - 1\rangle$ [6]. Ω describes how well the molecule is aligned with the axis perpendicular to the membrane's surface. The different phases for the acyl chains generate different rotational and translational degrees of freedom. A bilayer of 1,2-dimyristoyl-sn-glycero-3-phosphocholine (DMPC) undergoes two phase transitions. At $14.2°C$ it transforms from the gel state ($L_{\beta'}$) into the ripple phase ($P_{\beta'}$). The main phase transition occurs at $23.9°C$, where it shifts from the $P_{\beta'}$ to the liquid disorder L_α phase [24]. As the transition temperature is reached, the acyl chain order

changes, which translates to a discontinuity in Ω, and a latent heat to conduct the transition. This is a unique characteristic of first order phase transitions, which we commonly refer too as the main phase transition T_m in membrane systems.

3.2.1 Differential Scanning Calorimetry

To study lipids a wide array of instrumentations are used. Such techniques include deuterium magnetic resonance (H^2-NMR), where the magnetic moments are plotted versus temperature [8]. Differential scanning calorimetry (DSC) is a technique that measures heat flow. All are used to characterize the phase behaviour of lipid systems. DSC was used in determining T_m of DPPC. The knowledge of T_m will be used in our our temperature controlled experiments that will be later presented.

In differential scanning calorimetry (DSC), a reference sample and the sample of interest are heated. The reference sample is usually a buffer solution of equivalent mass and does not posses a phase transition in the temperature range of interest. The instrument measures the temperature of both samples while raising or lowering the temperature of each by adding heat. The amount of heat injected into each sample is monitored while the device attempts to maintain a constant temperature difference of zero between the two [9]. If there is a particular amount of additional heat that is needed to raise or maintain the temperature, it is recorded. This additional heat is referred to as the latent heat or excess enthalpy H (figure 3.4(a)). It is common practice to classify quantities in terms of heat capacity (C). C is defined as the the amount of heat (Q) required to increase the temperature some ΔT.

$$C = \frac{Q}{\Delta \mathrm{T}} \tag{3.9}$$

Now remembering the expression for H in equation 3.3

$$\begin{aligned} H &= TdS + VdP \\ &= Q + VdP, \end{aligned} \tag{3.10}$$

where at constant pressure, H can be related to the heat capacitance by,

$$C_P = \left(\frac{\partial H}{\partial T}\right)_P. \tag{3.11}$$

The information on the enthalpy can be displayed in terms of excess heat capacitance (C_p^{exc}), as seen in figure 3.4(b).

Taken from DSC measurements, figure 3.4(c) depicts two peaks of the main phase transitions of DMPC (14:0) ($T_m \approx 24^\circ$ C) and DPPC (16:0) ($T_m \approx 41.5^\circ$ C). The area under the curve of each graph represents the latent, which from numerous experiments is found to be ~ 6.5 kcal mol^{-1} and 8.7 kcal mol^{-1} respectively [9]. For each curve on the graph in figure 3.4(c), the lipid membrane transitions from a $P_{\beta'}$ state to a L_α state. This presents a strong evidence that as acyl chain length increases, so does the interaction between them, therefore causing a shift upward in T_m. While these measurements of many lipid membranes have numerous benefits, a significant limitation is that it does not measure localized regions of a single planar lipid bilayer.

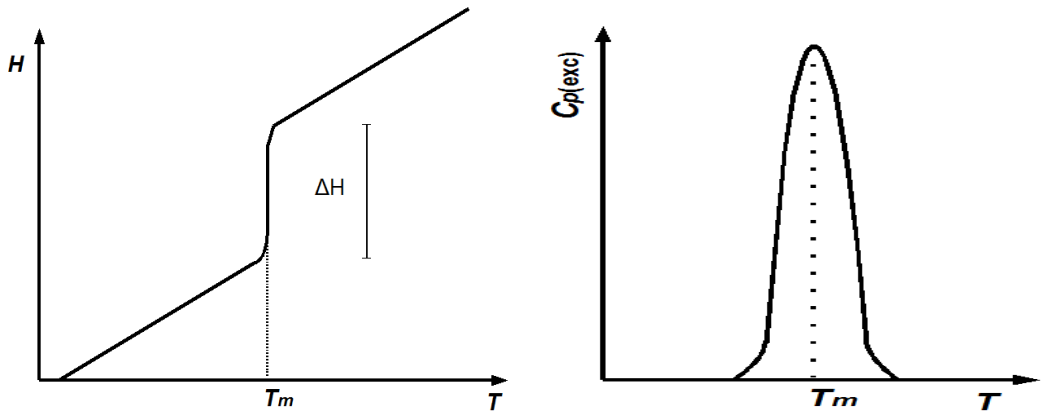

(a) (b)

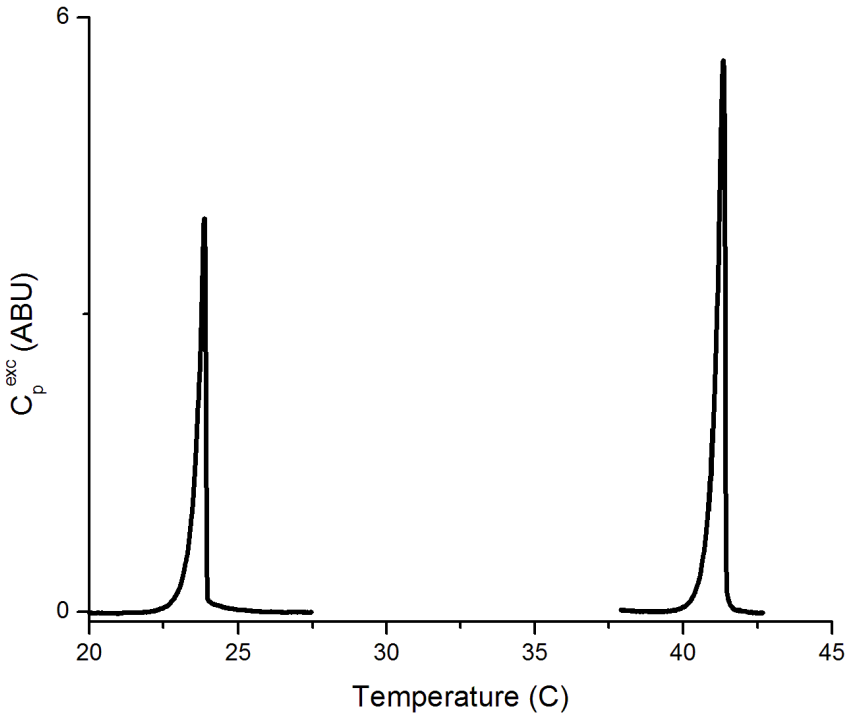

(c)

Figure 3.4. a) Graph of H versus T showing a change in enthalpy associated with a phase transition at T_m. b) A graph of the excess Heat Capacity C_p^{exc} as a function of T, showing a spike at T_m. c) DSC data for DMPC (14:0) and DPPC (16:0) showing excess heat capacitance spikes at 24° C and 41.5° C respectively.

4. ELECTRIC FIELDS AND MATTER

A review of what happens as materials interact with an external electric field and how that interaction pertains to lipid molecular structures will be discussed, along with lipid molecule anisotropic properties. Finally an explanation of how electromagnetic waves propagate through anisotropic materials and what physical parameters can be obtained from studying these interactions will be presented.

4.1 Anisotropic Materials

All materials in nature have a characteristic charge distribution. In dielectric media the charges are fixed, and when they interact with an external electric field ($\mathbf{E}_{ext}$). A net dipole moment $\mathbf{p}$ is the result, which then itself creates an electric field that modifies the external field [25]. For materials with a linear response, the local reaction to an external field at a particular site can be represented as [26]

$$\mathbf{p}_j = \alpha_{ij}\mathbf{E}_i{}^{local}, \tag{4.1}$$

where we sum over all direction for i and j. The vector $\mathbf{p}_j$ is proportional to the electric field by the polarizability tensor (α_{ij}).

We can represent equation 4.1 in terms of the dipole moment per unit volume (V) $\frac{\mathbf{p}}{V} = \mathbf{P}$, referred to as the polarization [27, 28]. The total macroscopic electric field in terms of the average induced internal electric field ($\langle\mathbf{E}\rangle$) and $\mathbf{E}_i{}^{local}$

$$\mathbf{E}_i = \langle\mathbf{E}\rangle + \mathbf{E}_i{}^{local}, \tag{4.2}$$

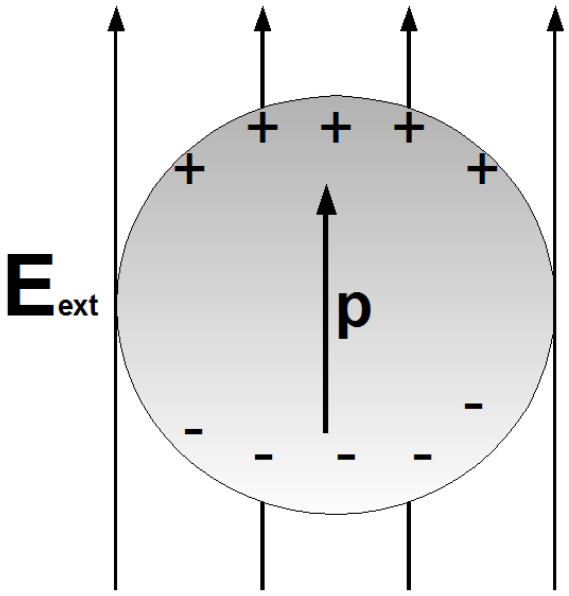

Figure 4.1. Pictorial representation of a spherical dielectric in an external electric field $\mathbf{E}_{ext}$. There is an induced dipole that creates an opposing electric field that weakens the external field.

where

$$\mathbf{E}_i{}^{local} = \mathbf{E}_{ext} + \langle \mathbf{E} \rangle. \tag{4.3}$$

Solving for $\mathbf{E}_i{}^{local}$ in terms of $\mathbf{E}_{ext}$ and the resulting $\mathbf{P}$, the following is obtained,

$$\mathbf{E}_i{}^{local} = \mathbf{E}_i + \frac{L_i \mathbf{P}_i}{\epsilon_o}. \tag{4.4}$$

Where ϵ_o is the permittivity of free space and L_i is called a shape factor, which adjusts the internal field contribution of $\mathbf{P}$.

Due to an external electric field, the charges within the material experience a force and try to align with the field, inducing a net dipole moment, an example can be seen in figure 4.1. The average induced internal electric field in terms of the radius of the sphere R and dipole moment can be written as [27],

$$\langle \mathbf{E} \rangle = \frac{-1}{4\pi\epsilon_o} \frac{\mathbf{p}}{R^3} \tag{4.5}$$

In terms of $\mathbf{P}$,

$$\langle E \rangle = \frac{-\mathbf{P}}{3\epsilon_o} \tag{4.6}$$

For a sphere L_i is equal to $\frac{1}{3}$, where $L_x = L_y = L_z$. For a cylinder of length l and diameter d we obtain the shape factors [29]

$$L_z = \left(1 - \frac{L_x}{2\pi}\right) \quad \text{and} \quad L_x = L_y = \frac{2\pi l}{\sqrt{(l^2 + d^2)}}. \tag{4.7}$$

For an ellipsoid [30, 31]

$$L_i = \frac{a_x a_y a_z}{2} \int_0^\infty \frac{1}{(s + {a_i}^2)\sqrt{(s + {a_x}^2)(s + {a_y}^2)(s + {a_z}^2)}}\, ds. \tag{4.8}$$

Where a_x, a_y and a_z are the axis of the ellipse. All factors can now be expressed in terms of measurable quantities such as the permittivity ϵ and the index of refraction n. Using equations 4.1, 4.4, and the following,

$$\frac{\mathbf{P}}{\epsilon_o} = \left(\frac{\epsilon_i}{\epsilon_o} - 1\right) \langle \mathbf{E} \rangle \tag{4.9}$$

We can follow the procedure in appendix B, and obtain an expression for $\epsilon_i = {n_i}^2$,

$$\epsilon_i = {n_i}^2 = \frac{\alpha_i \epsilon_o}{(V - \alpha_i L_i)} + \epsilon_o, \tag{4.10}$$

where the V is volume.

4.1.1 Anisotropic Nature of Lipids

Phospholipids have long fatty acids, which gives rise to their anisotropic charge distributions. These acyl chains can be represented as a dielectric cylinder with a length l and diameter d [15, 29], seen in figure 4.2. As expected the polarizability α of the fatty acids are higher along their length versus the width. By modelling the system in this manner, knowledge of anisotropic materials can be utilized to extract physical information about lipid molecules.

Knowing the shape factor L_i, we will show how the α_i of the dielectric cylinder can be expressed in terms of material dependent properties. To describe the orientation of the fatty acid, an average position from what is known as the orientation parameter Ω is assigned (a measure of how the molecule orients relative to membrane's normal ($\mathbf{n}$) [32]).

$$\Omega = \frac{1}{2}\left(3\left\langle \cos^2(\phi) \right\rangle - 1\right) \tag{4.11}$$

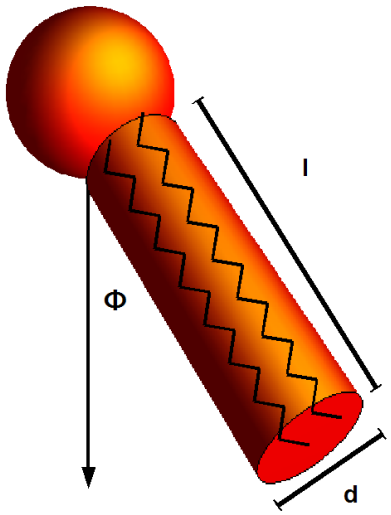

Figure 4.2. Display of acly chains treated as a cylindrical charge distribution of length l and diameter d. The orientation of the lipid molecule is described by ϕ, which is measured relative to the membranes' normal.

We now represent the parameters of the cylinder in terms of average quantities, where $L_i \Rightarrow {L_i}^{avg}$. Relating the projection of the cylinder's components to L_i, l now becomes $l\cos(\phi)$ and d becomes $2\sqrt{\frac{A}{\pi}}$, where A is the average area of the lipid molecule. To represent α_i in terms of average quantities [15],

$$ {\alpha_z}^{avg} = \alpha_{\text{avg}} + \frac{2}{3}\left(\alpha_l - \alpha_t\right) S \tag{4.12} $$

$$ {\alpha_x}^{avg} = \alpha_{\text{avg}} - \frac{1}{3}\left(\alpha_l - \alpha_t\right) S \tag{4.13} $$

From equation 4.10 we obtain an expression for the average index of refraction ${n_i}^{avg}$ in terms of ${\alpha_i}^{avg}$

$$ \left({n_i}^{\text{avg}}\right)^2 = \epsilon_o \left(\frac{{\alpha_i}^{\text{avg}}}{\epsilon_o \left(V - {\alpha_i}^{\text{avg}} {L_i}^{\text{avg}}\right)} + 1 \right) \tag{4.14} $$

This refraction can be utilized to determine the polarizabilities of the acyl chains by knowing the index of refraction along the $\perp$ and $\parallel$ directions of the molecule.

4.2 Isotropic vs Anisotropic Materials

From Gauss′s Law it is known that the divergence of the polarization $\mathbf{P}$ is equivalent to the bounded charge density ρ_b. As a result, there is an accumulation of bound charges on the surface proportional to P [26], mathematically depicted as,

$$ \mathbf{D} = \epsilon_o \mathbf{E} + \mathbf{P}, \qquad \text{where} \qquad \mathbf{D} = \epsilon \mathbf{E} \tag{4.15} $$

Accordingly, the polarization $\mathbf{P}$ serves as the vector difference between the displacement field $\mathbf{D}$ and the total electric field multiplied by the permittivity of free

space $\epsilon_o \mathbf{E}$. Since the permittivity (ϵ_{ij}) is a tensor, $\mathbf{D}$ can be considered as a scaling of $\mathbf{E}$. So when $\mathbf{E}^{external}$ polarizes a medium that is isotropic, $\epsilon_{ij} = \epsilon\delta_{ij}$.

$$\begin{pmatrix} \epsilon & 0 & 0 \\ 0 & \epsilon & 0 \\ 0 & 0 & \epsilon \end{pmatrix} = \epsilon \begin{pmatrix} 1 & 0 & 0 \\ 0 & 1 & 0 \\ 0 & 0 & 1 \end{pmatrix} \tag{4.16}$$

Then $\mathbf{E}$ is scaled by a factor ϵ, where $\mathbf{P}$ is in the same direction of the electric field and displacement field. A visual representation can be seen in figure 4.3(a). When the material is anisotropic, then ϵ is also anisotropic. In this case $\mathbf{D}$ is now a scaled rotation of $\mathbf{E}$.

$$\mathbf{D} = \begin{pmatrix} \epsilon_{\text{xx}} & \epsilon_{\text{xy}} & \epsilon_{\text{xz}} \\ \epsilon_{\text{yx}} & \epsilon_{\text{yy}} & \epsilon_{\text{yz}} \\ \epsilon_{\text{zx}} & \epsilon_{\text{zy}} & \epsilon_{\text{zz}} \end{pmatrix} \begin{pmatrix} \mathbf{E}_x \\ \mathbf{E}_y \\ \mathbf{E}_z \end{pmatrix} \tag{4.17}$$

Within this scenario $\mathbf{P}$ is not necessarily in the same direction of either the electric displacement or field, as seen in figure 4.3(b).

4.3 Electric-Field Propagation through Dielectric Materials

The electrical energy density μ_E, can be defined by,

$$\mu_E \propto \mathbf{E} \cdot \mathbf{D} \tag{4.18}$$

and can be represented in ellipsoidal form as,

$$\mu_E \propto \frac{\mathbf{D}_x{}^2}{\epsilon_x} + \frac{\mathbf{D}_y{}^2}{\epsilon_y} + \frac{\mathbf{D}_z{}^2}{\epsilon_z} \tag{4.19}$$

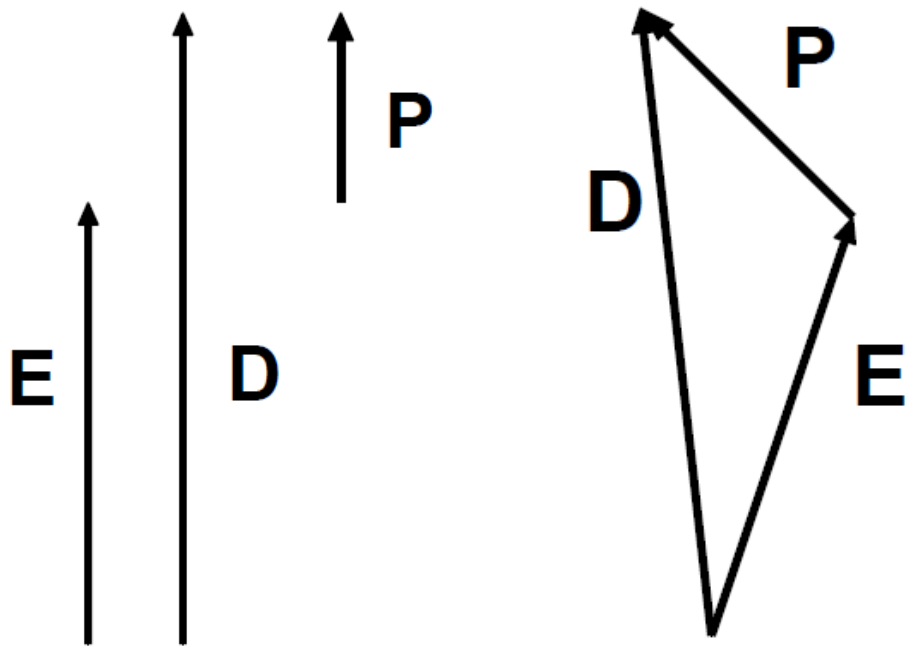

(a) (b)

Figure 4.3. Vector representation of **P**, **D** and **E** total for different scenarios. a) The isotropic case where **P** is in the direction of **E** and **D**. b) The anisotropic situation where **P**, **E** and **D** are in different directions.

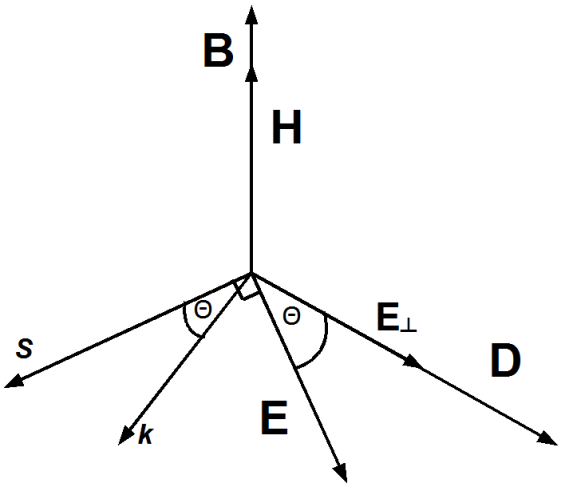

Figure 4.4. Vector representation of how in an anisotropic material **D** may not be parallel to **E** but is always perpendicular to **k**. The energy propagation **S** is perpendicular to **E** and the two vectors are rotated by Θ relative to **k**. All **D**, **E**, **k** and **S** are perpendicular to **H** and **B**, as is the case with an electromagnetic wave propagating through an non-magnetic transparent material.

When $\epsilon_x = \epsilon_y = \epsilon_z$, an ellipse no longer exist, yielding a circular isotropic case. Taken from appendix C, **D** is,

$$\mathbf{D} \cdot \mathbf{k} = 0, \qquad \text{and} \qquad \mathbf{D} = \frac{n^2}{\mu c^2}\mathbf{E}_{\perp_k} \tag{4.20}$$

where **k** is the direction of the electromagnetic wave propagation and n is the index of refraction.

A particular group of materials that display anisotropic behavior are uniaxial and biaxial crystals. These crystals either have one or two axis of their permittivity that differ. The optical properties can be conveniently represented in terms of the index of refraction instead of the permittivity, where $n^2 = \epsilon$, resulting in an indicatrix of n (see figure 4.5).

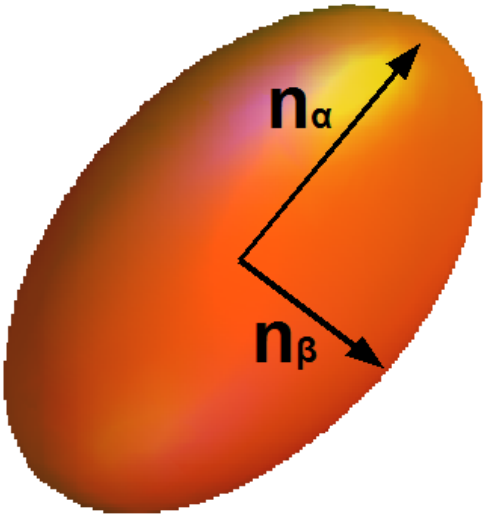

Figure 4.5. Graphical representation of an indicatrix with axes n_α and n_β. Anisotropic materials posses the property of $n_\alpha \neq n_\beta$.

For a uniaxial crystal one of the three axis of the indicatrix is different. We will show that depending on the orientation of the material a corresponding phase shift of the polarization of the propagating electric field will occur.

$$\begin{pmatrix} \mathbf{E}_x{}' \\ \mathbf{E}_y{}' \end{pmatrix} = \begin{pmatrix} e^{iS} & 0 \\ 0 & 1 \end{pmatrix} \cdot \begin{pmatrix} \mathbf{E}_x \\ \mathbf{E}_y \end{pmatrix},$$

where

$$\mathbf{E}_x = E_\circ e^{i\omega t} \quad \text{and} \quad \mathbf{E}_x{}' = E_\circ e^{i(\omega t+S)}. \tag{4.21}$$

Figure 4.6(b), depicts polarized light as it passes through a uniaxial crystal with its axis oriented at ϕ with respect to the surfaces' normal. The different electric field components travelling through this crystal, experience different indices of refraction, which leads to a phase shift between the two vector components, as displayed in equation 4.21. Within the material, the displacement field components ($\mathbf{D}_x$ and $\mathbf{D}_y$) travel along the path where the plane wave is parallel to the tangent of the indicatrix. $\mathbf{D}_x$ passes through the crystal perpendicular to the normal of the crystal surface as the ordinary ray. This happens because the plane wave is parallel to the tangent of the indicatrix in the x direction. For the situation of $\mathbf{D}_y$ the wave passes through the point where the tangent line of the indicatrix and plane wave are exactly parallel. This light propagation is referred to as the extraordinary ray. Because $\mathbf{D}$ propagates perpendicular to $\mathbf{k}$ through the material, we can introduce an expression of the plane wave's velocity v_S in terms of the v_k using appendix C

$$\frac{v_k}{\cos(\Theta)} = v_S, \tag{4.22}$$

where Θ is the angle between the extraordinary wave and the normal to the surface. By using $v = nc$, we obtain

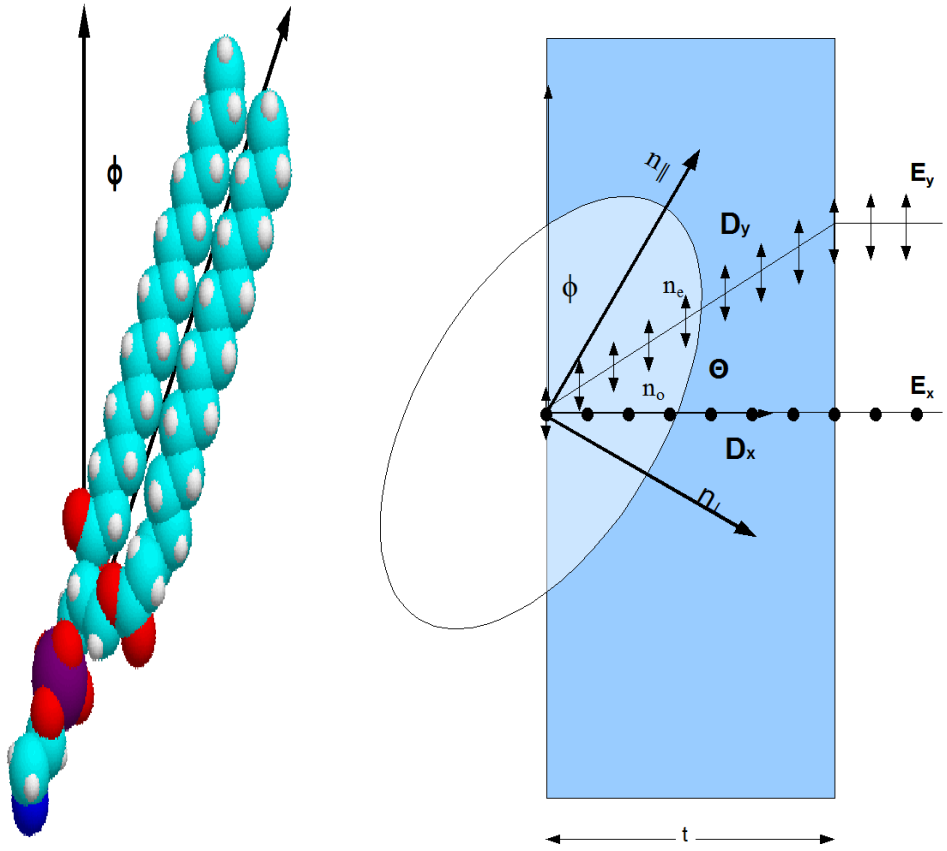

(a) (b)

Figure 4.6. a) Three dimensional model of a DPPC molecule oriented at ϕ, similar to the $L_{\beta'}$ state. b) Figure of a uniaxial indicatrix showing an electromagnetic wave separating into ordinary and extraordinary rays, as it propagates through the material. The picture displays how **D** propagates through the material and shows a phase lag in **E** as it emerges.

$$\frac{n_k}{\cos(\Theta)} = n_S, \tag{4.23}$$

where n_k is the index of refraction along the path that $\mathbf{D}_y$ takes. To determine n_k, the distance from the center of the indiactrix to the point $\mathbf{D}_y$ intercepts the point it aligns with the tangent must be calculated.

Using equation A.4 from appendix A, the following expression for n_k, referred to as the effective index of refraction (n_{eff}) [33, 34] was obtained,

$$n_{\text{eff}} = \frac{n_\perp n_\parallel}{\sqrt{{n_\parallel}^2 \cos^2(\phi) + {n_\perp}^2 \sin^2(\phi)}}. \tag{4.24}$$

When the light emerges from the material, the phase of $\mathbf{E}_y$ lags the phase of $\mathbf{E}_x$, as depicted in figure 4.6(b). The phase difference S is,

$$S = \frac{2\pi}{\lambda}(n_e - n_o)\, t \tag{4.25}$$

Here n_e and n_o are the extraordinary and ordinary indices of refraction, (where $(n_e - n_o)$ is reffered to as the birefringence), λ is the wavelength of light and t is the thickness of the material. The ordinary ray passes through the material normally, while the extraordinary travels in the direction of n_{eff}. For a uniaxial crystal, in equation 4.25 $n_o t$ becomes $n_\perp t$, and $n_e t$ becomes $\frac{n_{eff} t}{\cos(\Theta)}$. Equation 4.25 is now,

$$S = \frac{2\pi}{\lambda}\left(n_\perp - \frac{1}{\sin\left(\arctan\left(\frac{{n_\parallel}^2}{{n_\perp}^2}\cot(\phi)\right) + \phi\right)} \frac{n_\perp n_\parallel}{\sqrt{{n_\parallel}^2 \cos^2(\phi) + {n_\perp}^2 \sin^2(\phi)}}\right). \tag{4.26}$$

To calculate the phase shift for a biaxial crystal the same process is repeated, calculating n_{eff} for both components of the electric field.

With this repetition the phase shift of a given material, with a know indicatrix, can be calculated. The same formalism for lipid molecules, where the effective retar-

dance (S), is a function of the acyl chain tilt (ϕ) is utilized in this study. How the molecules' ϕ relates to the uniaxial indicatrix can be seen in figure 4.6(a). Through this method physical parameters from planar lipid bilayers will be extracted, by experimentally measuring the retardance (S) and determine the unknown components of the indicatrix.

5. EXPERIMENTAL SET-UP AND PROCEDURES

An introduction to near-field scanning optical microscopy will be presented along with a polarization modulation technique and calibration procedures. The total experimental setup along with modifications are introduced to allow for temperature control. A brief synopsis of atomic force microscopy together with a description of how sample characterization is executed will be outlined.

5.1 Near-Field Scanning Optical Microscopy

Near-Field Scanning Optical Microscopy (NSOM) is an imaging technique that allows for optical as well as topographical information to be obtained simultaneously to create an image. NSOM is a scanning probe technique that uses a small aperture ($\sim$ 100 nm), made from an altered optical fiber, to obtain optical information beyond the diffraction limit, i.e. with a lateral resolution better than $\sim \frac{\lambda}{2}$, where λ is the wavelength of the light under consideration. An example of a NSOM probe can be seen in figure 5.1. As a direct consequence of using an aperture smaller than λ, the resulting field is evanescent and decays quickly, requiring the probe to sample distance to be small ($\sim$ 10 nm). To control the distance we use a shear-force mechanism, where topographical information from the sample is also collected [13, 35].

A NSOM microscope consists of a light source, probe, shear force mechanism and a detector, as shown in figure 5.2. The light source is usually a laser, which is then coupled into an optical fiber. The fiber is spliced to a NSOM probe. The probes themselves derive from optical fibers, that are either heated and pulled or chemically etched to create a tapered end, with a diameter of $\sim$ 50-100 nm [36]. Because the

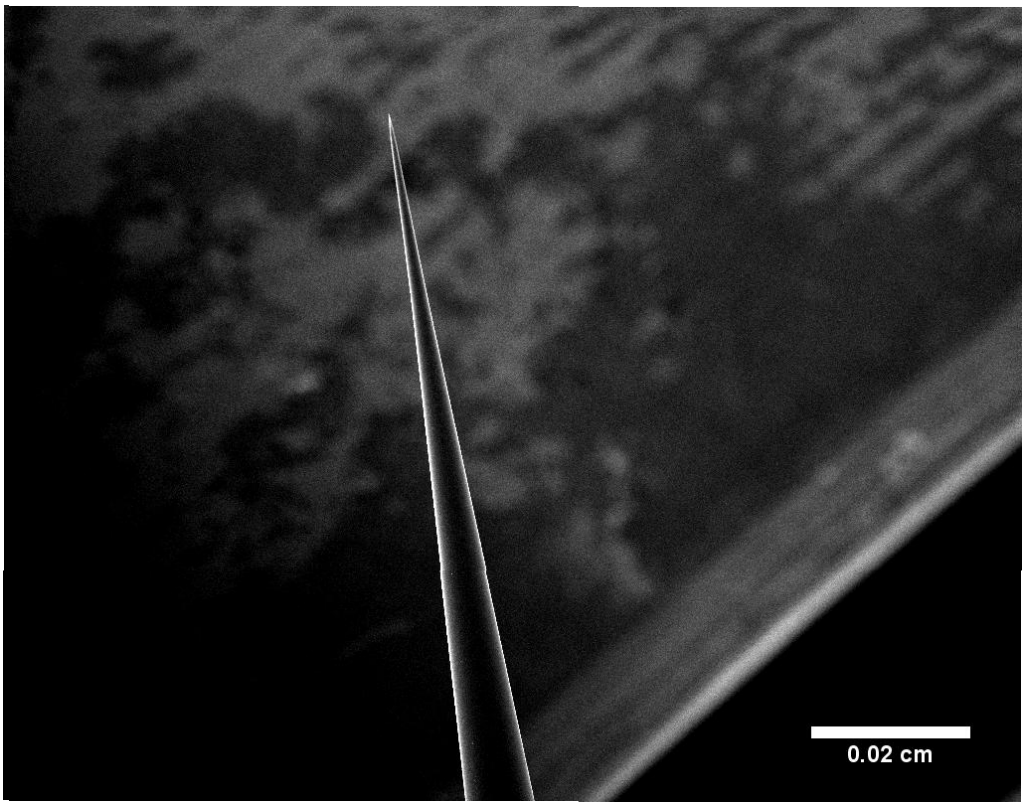

Figure 5.1. Scanning Electron Microscopy (SEM) image of a NSOM probe.

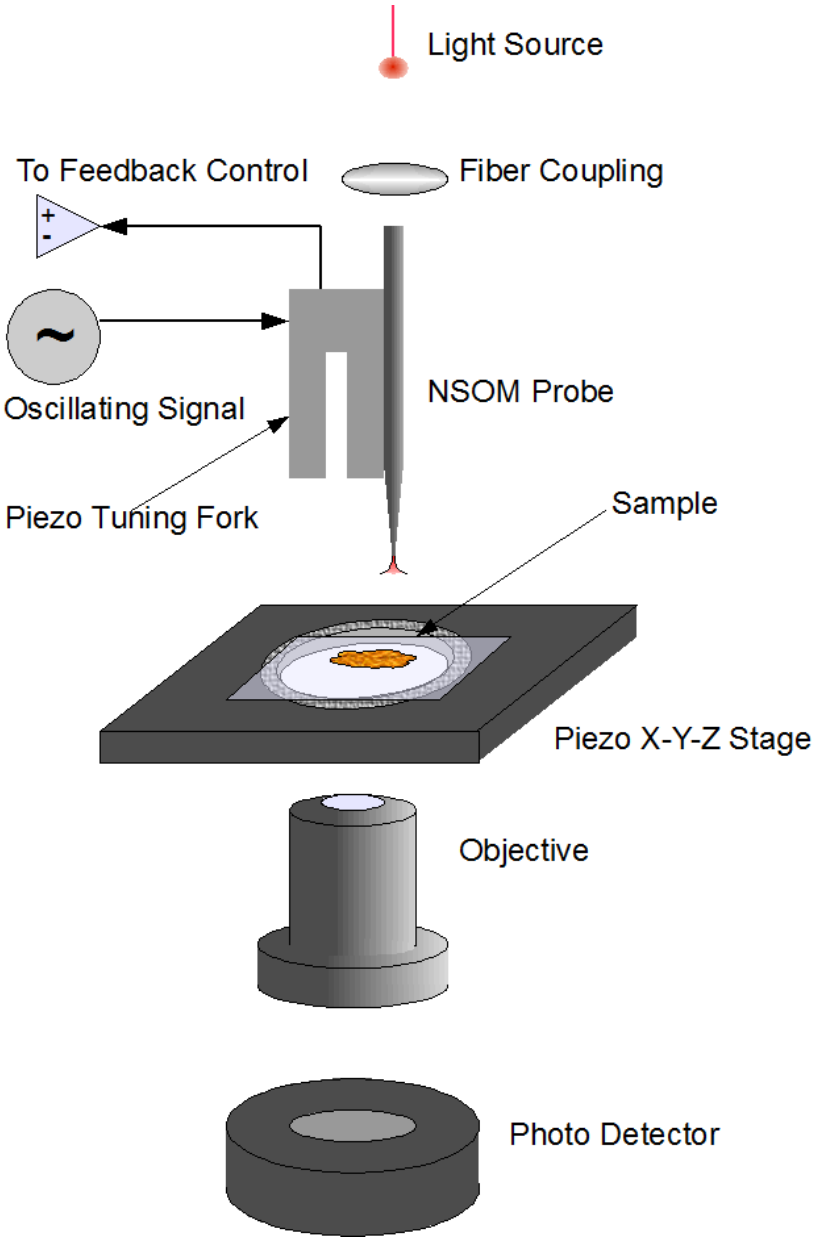

Figure 5.2. Schematic of a NSOM microscope setup.

fiber is tapered, the mode of the fiber is changed and light escapes from the sides. To help eliminate this undesirable effect, aluminium is thermally evaporated to coat the outer area in such a way that the end is left uncovered, seen in figure 5.3. The probe is now an aperture with an optical diameter of $\approx$ 100 nm.

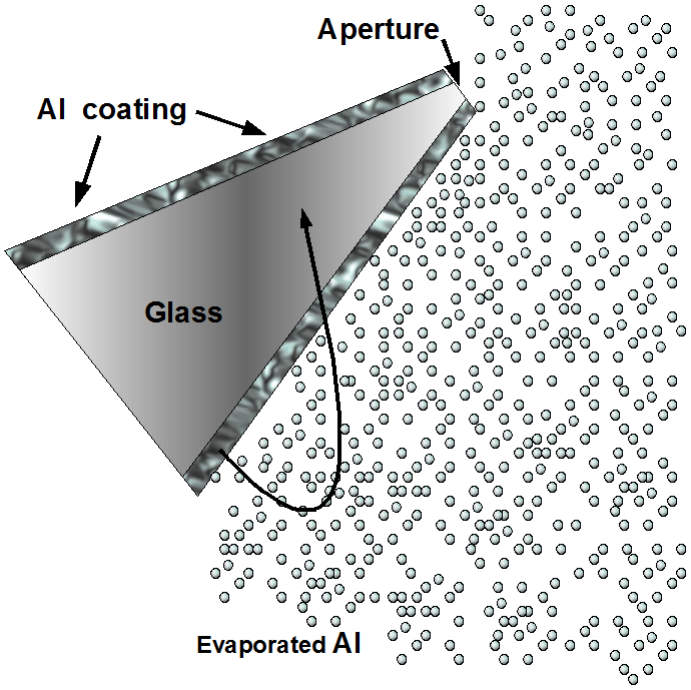

Figure 5.3. Pictorial representation of a NSOM probe being coated with evaporated aluminium. The prove is held at an angle and rotated to evenly coat the sides, leaving the end uncovered and an aperture at the end of the probe.

As light passes through a NSOM probe, the taper width becomes small, where most of the light is reflected back through the fiber or absorbed by the Al coating. The only mode left to propagate through the probe is the HE_{11} [13, 37]. Pass the point where the probe diameter reaches $\sim$ 160 nm [13], the HE_{11} mode is cut off and the electric field exponentially decays beyond the boundary, which can be seen in figure 5.4(b). If the aperture lies within the decay range the dipoles at the end of the tip are stimulated and create an evanescent wave at the end of the probe. This evanescent wave, confined to the diameter of the aperture, is the reason behind the lateral resolution capabilities of NSOM.

The light confinement the probe creates only exists in close proximity to the aperture, shown in figure 5.4(b). The electromagnetic radiation diverges from the end of the probe. To obtain the high lateral optical resolution in NSOM, a tip to sample distance of $\approx$ 10 nm must be maintained. This is accomplished through the use of a shear force mechanism.

5.1.1 Shear-Force

A shear-force mechanism is used to maintain the probe-to-sample distance (further explained in Appendix K.3). To accomplish this, the NSOM probe is attached to a piezo-electric quartz tuning fork with a cyanoacrylate adhesive. Because the quartz is piezo electric, the probe can be oscillated by means of a sinusoidal voltage signal.

The foundation of this method is based on the premise that the tuning fork (TF) serves as a driven RLC circuit with stray capacitance c_p, as seen in figure 5.5. The expected current as a function of frequency, shown in equation 5.1, can be calculated. By plotting the in phase and out of phase portions of the signal expected we are able to visualize the Lorentz line shape of the resonance curve and determine a characteristic

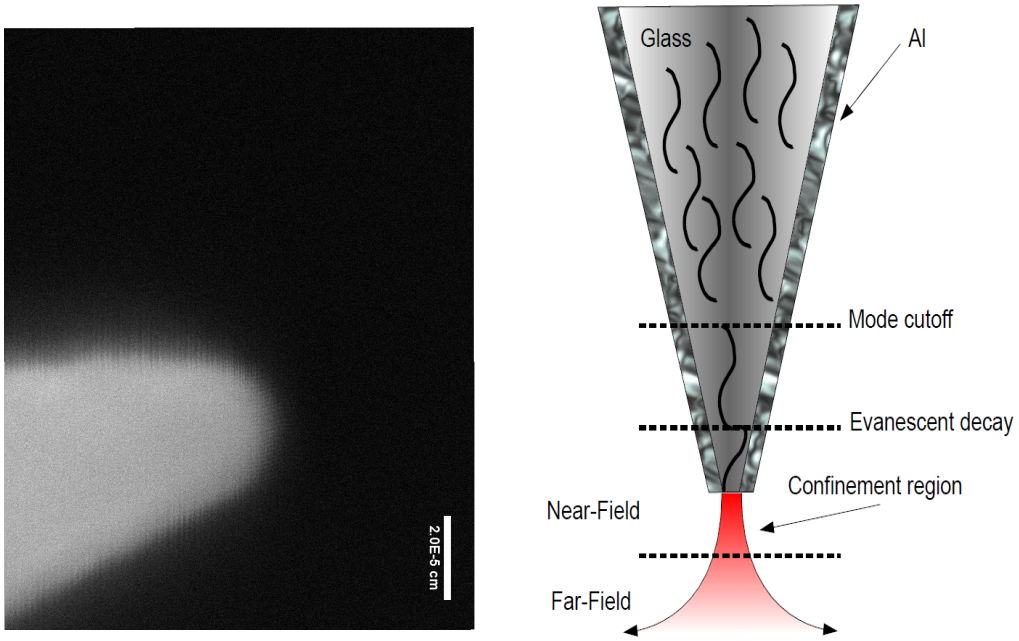

(a) (b)

Figure 5.4. a) Zoomed in SEM image of aluminium coated NSOM probe. b) A pictorial depiction of electromagnetic radiation as it passes through a NSOM probe. Light passes through until the taper no longer supports the optical mode. This is referred to as the mode cut-off region. The light eventually reaches a point where no spacial modes are supported and the electric field exponentially decays. Given that the aperture is within proximity of the decay, light then excites the dipoles at the end of the probe, localizing the light in the near-field region. Beyond the confinement area the electromagnetic radiation diverges quickly, where it propagates normally. This area is referred to as the far-field region.

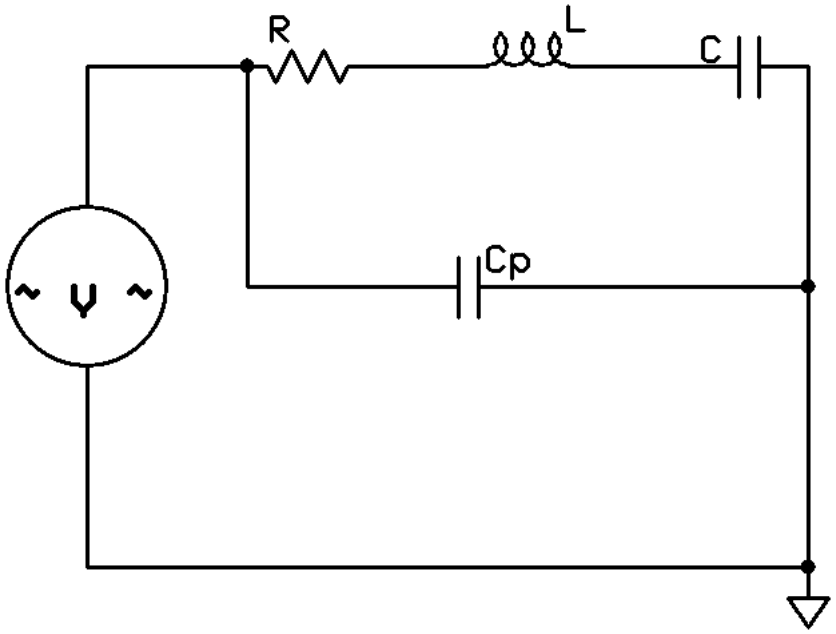

Figure 5.5. Circuit diagram of a RLC circuit with a stray capacitance (c_p) parallel to ground. A simplistic electronic representation of the driven NSOM probe and tuning fork.

resonance frequency Ω, as seen in figure 5.6. Ω is the natural vibration of the physical tuning fork and is where they RLC circuit has a maximum energy transfer.

$$\begin{aligned} I(\omega) &= \frac{V\omega^2 C\Omega}{C^2\omega^2 R^2\Omega + \left(\Omega^2 - \omega^2\right)^2} \\ &\quad + iV\left(\frac{C^2\omega R\left(\Omega^2 - \omega^2\right)}{\left(C^2\omega^2 R^2\Omega^2 + \Omega\left(\Omega^2 - \omega^2\right)^2\right)} + C_p\omega\right), \end{aligned} \tag{5.1}$$

where V is the voltage and ω is the frequency of the excitation provided by the "source".

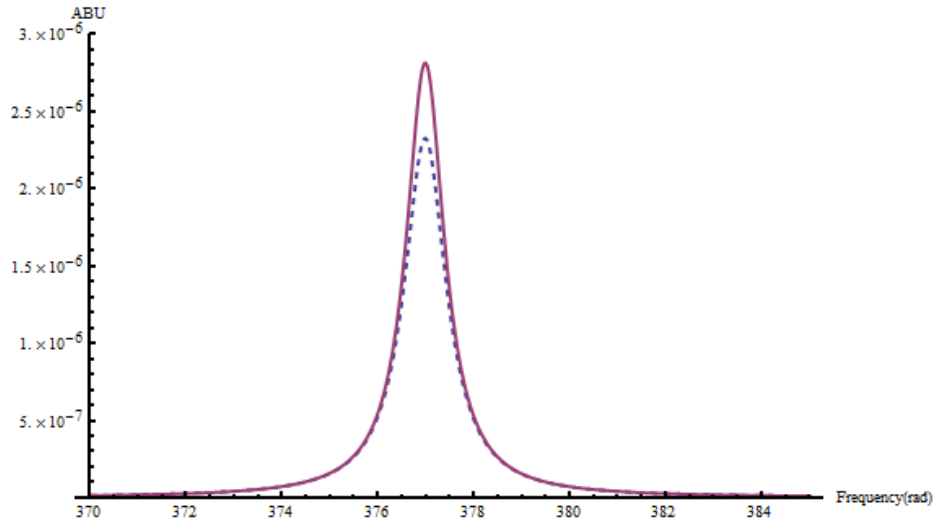

(a)

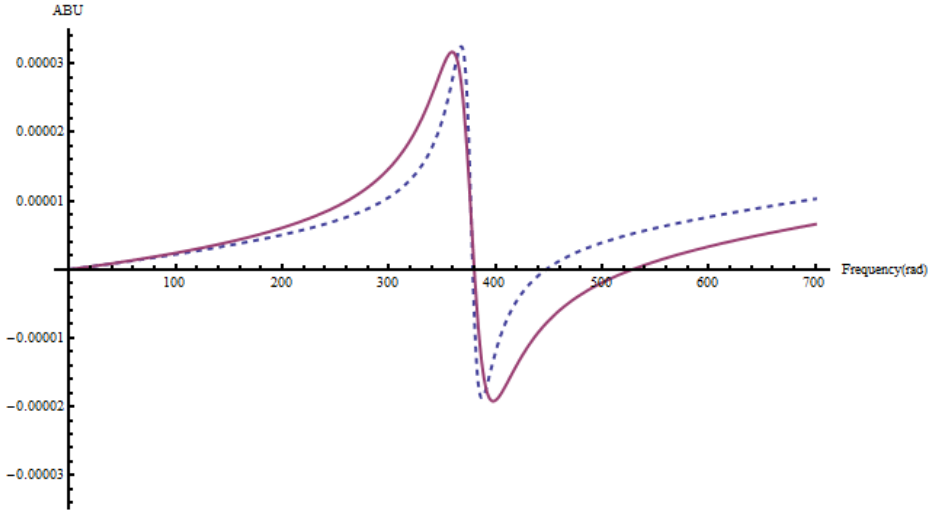

(b)

Figure 5.6. The real and imaginary parts of the current of the RLC circuit in figure 5.5 versus angular frequency. a) The in phase component of the electrical signal, the dotted line showing a decrease in amplitude when the effective resistance increases. b) The out of phase component of the signal in equation 5.1.

The driven damped harmonic oscillator equation, is utilized to model the TF into physical parameters

$$mx''(t) + b\ x'(t) + kx(t) = F\cos(\omega t), \tag{5.2}$$

where F, k, m, and b are the magnitude of the driving force, spring constant associated with the TF, the mass, and damping coefficient respectively. We can determine from equation 5.2 the amplitude of the oscillations frequency dependence [38]

$$A(\omega) = \frac{F/m}{\sqrt{4\omega^2\gamma^2 + \left(\Omega^2 - \omega^2\right)^2}}. \tag{5.3}$$

where Ω is the natural resonance frequency of the TF and γ is proportional to the damping coefficient.

Our resonance frequency Ω is proportional to the effective spring constant and mass of the TF ($\Omega \propto \sqrt{\frac{k}{m}}$). Written in terms the geometrical parameters of the TF and its Young's modulus (Y), $\Omega \propto \frac{t}{L^2}\sqrt{\frac{Y}{\rho}}$ is obtained, with t, L, and ρ being the thickness, length and density of the quartz tuning fork's arm respectively [39].

On resonance a maximum amplitude, with a Lorentz line shape is evident. As γ increases, which can arise from an external interaction, a drop in amplitude occurs, as is displayed in figure 5.7. This physical response can be seen in the electrical signal of the TF similar to what is seen in figure 5.6. We can use this direct relationship to determine the local interactions of the probe, thereby distinguishing when the NSOM aperture is in the region of light confinement as seen in figure 5.4(b).

To measure this signal a lock-in amplifier was incorporated into the setup. This device inputs the incoming signal, amplifying the current while converting it into a voltage and multiplying it to a pure sine function at a given reference frequency [40].

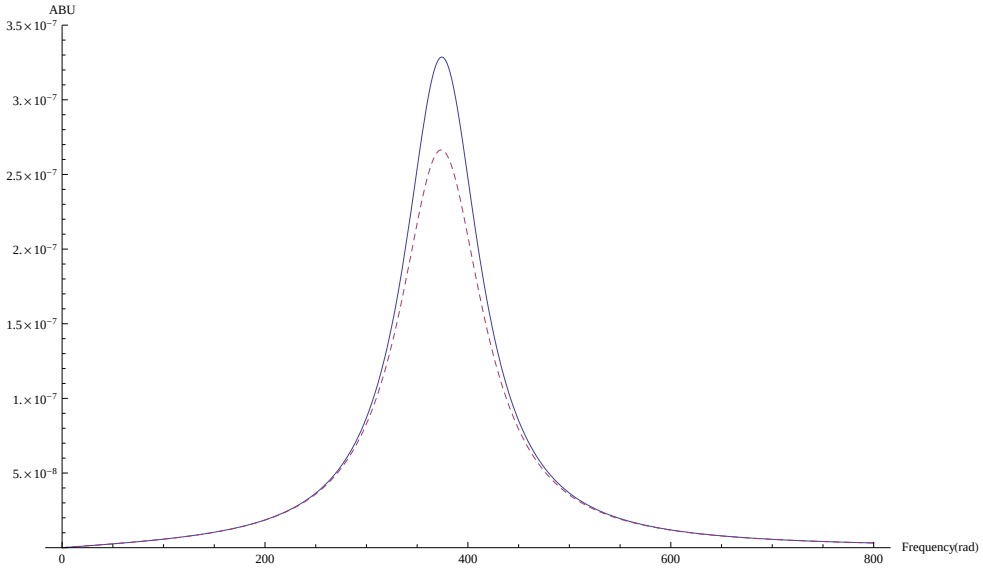

Figure 5.7. The amplitude response as a function of frequency of the shear force equation 5.2. As the damping coefficient (γ) increases, the amplitude decreases as shown by the dotted line.

Following the multiplier stage the signal is averaged, using a low pass filter, which yields zero for all signals off of the reference. The lock-in returns a root mean squared (rms) value of the signal along with the relative phase shift. A projection can be made of the given information on the complex plane determining the in-phase and in quadrature portions of the signal.

Figure 5.8 depicts actual data from the in phase portion of the resonating tuning fork. From the figure it can determined that the resonance frequency is ≈ 32758 Hz. It is expected that because $\Omega \propto \sqrt{\frac{k}{m}}$, attaching the NSOM probe, increasing the mass, resulting in a likely decrease in the position of the resonance maximum. However, from figure 5.9(a) it is clearly apparent that there is an increase in the position of the resonance frequency. The NSOM probe being attached with cyanoacrylate adhesive to the TF does in fact change m, but also the rigidity. This plays a dominant role in increasing Ω by increasing Y.

Having the information about the resonance frequency of the NSOM probe, the probe can be driven so that it oscillates at Ω. When the sample and probe reach a certain distance ($\approx$ 100 nm), an increase in the dissipative forces cause a damping of the oscillation's amplitude [35]. The distance of the interaction between probe and sample is dependent on probe shape, materials and ambient conditions [41]. The amplitude is then lowered to ≈ 90 % of the maximum on resonance to assure that the probe to sample distance is $\sim$ 10-20 nm. The amplitude is monitored with a lock-in amplifier, where a feedback mechanism is used to maintain the probe to sample distance (further explained in Appendix K.3). The relative height information is used to obtain a topographical map of the surface.

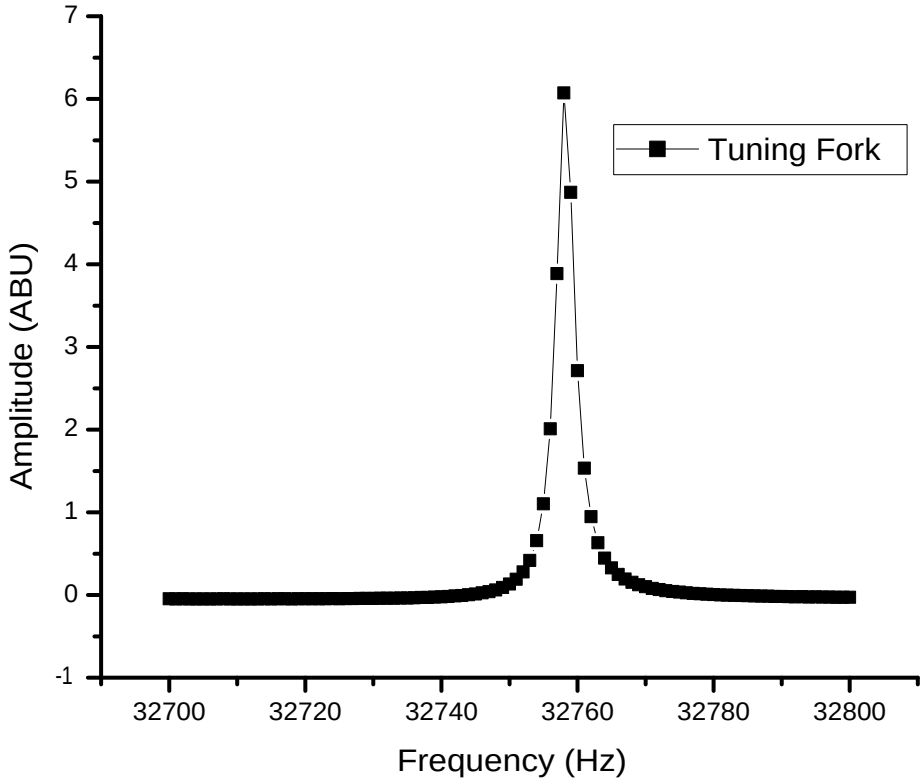

Figure 5.8. Amplitude versus frequency graph from the frequency response of a quartz tuning fork (the amplitude is in arbitrary units (ABU)). The peak indicates the presence of a resonance at $\approx$ 32.76 kHz.

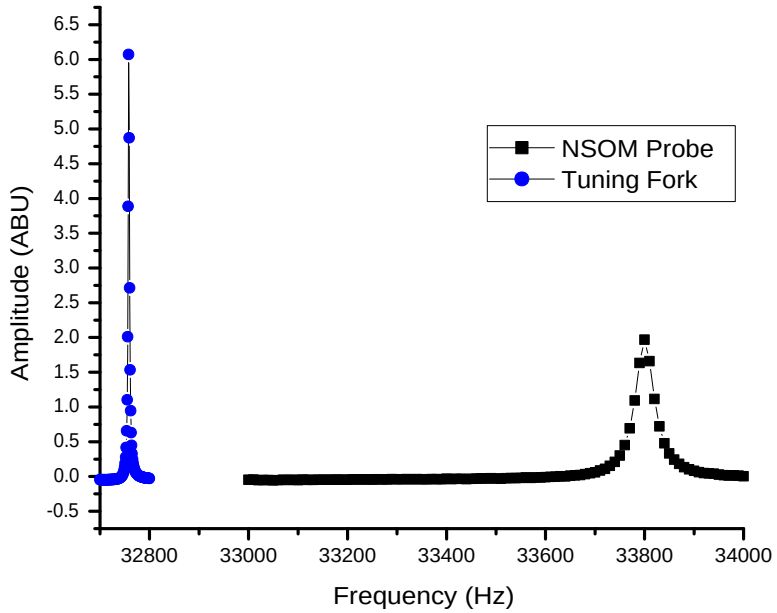

(a)

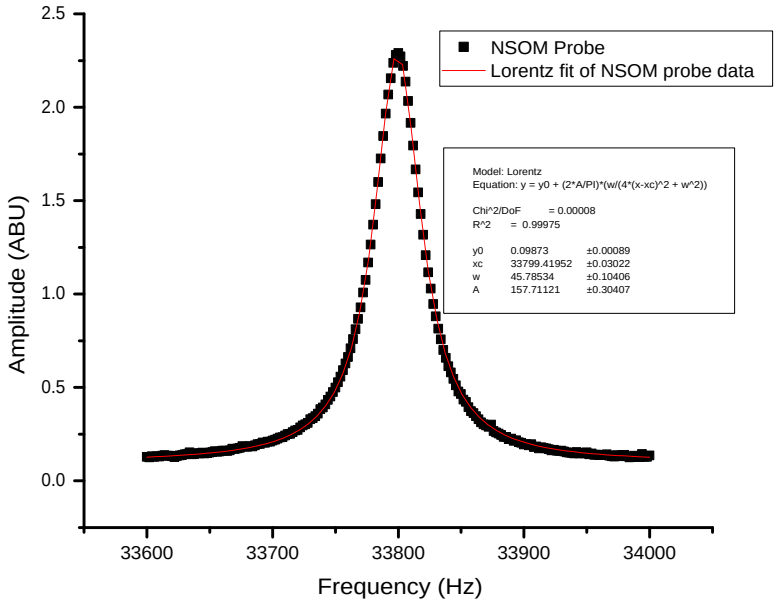

(b)

Figure 5.9. a) Data from the resonance response of a quartz tuning fork and with a NSOM probe attached to it.Ω increases when the probe is attached due to the change in the overall Young's modulus of the oscillator. The amplitude decreases and a broadening occurs. b) The resonance response of the NSOM probe, showing an Ω of $\approx$ 33799 Hz, determined with a Lorentz line fitting.

5.1.2 Light Collection

Light is gathered from the probe, using an objective lens and Si pin diode photo detector. Because the power from the tip is low [42] ($\sim$ 1 nW), it is essential that the maximization of efficiency and amplification of the signal occurs. The information from the intensity is then collected, where a point by point mapping of the optical information complements the topographical data discussed in the previous section.

The electromagnetic wave that propagates through the NSOM probe experiences differences in phase between the two perpendicular components of the electric field vector. When light propagating in the z direction is referred to as linearly polarize, both the $\mathbf{E}_x$ and $\mathbf{E}_y$ are in phase with each other, where the direction of the polarization is $\propto \arctan\left(\frac{\mathbf{E}_y}{\mathbf{E}_x}\right)$, an example is seen in figure 5.10(a). When the phase between the two components shift, the polarization rotates and becomes elliptical, or the electromagnetic wave spirals through space and time, as seen in figure 5.10(b). When the two vector components become out of phase by $\frac{\pi}{2}$ and $\mathbf{E}_x = \mathbf{E}_y$, the polarization is called circular, due to the circular motion the resultant electric field vector exhibits as a function of time, as seen in figure 5.10(d). This phase difference between the two components of the electric field is referred to as its retardance and the state of the electric field vector is described as its polarization. Due to the effects of the NSOM probes taper on the polarization output, the probe shape is chosen to best enhance the polarization control of the NSOM system.

For polarization dependent experiments, a universal polarizer controls the polarization into the tip. To nullify the effects of the probe on the polarization, we adjust the polarization into the probe and fiber, using the fiber paddles. The paddles themselves bend the fiber at a particular radius. The bending stresses the fiber along a preferential axis which changes its index of refraction along that axis. This difference in indices of refraction (or birefringence), yields a net retardance. The resulting re-

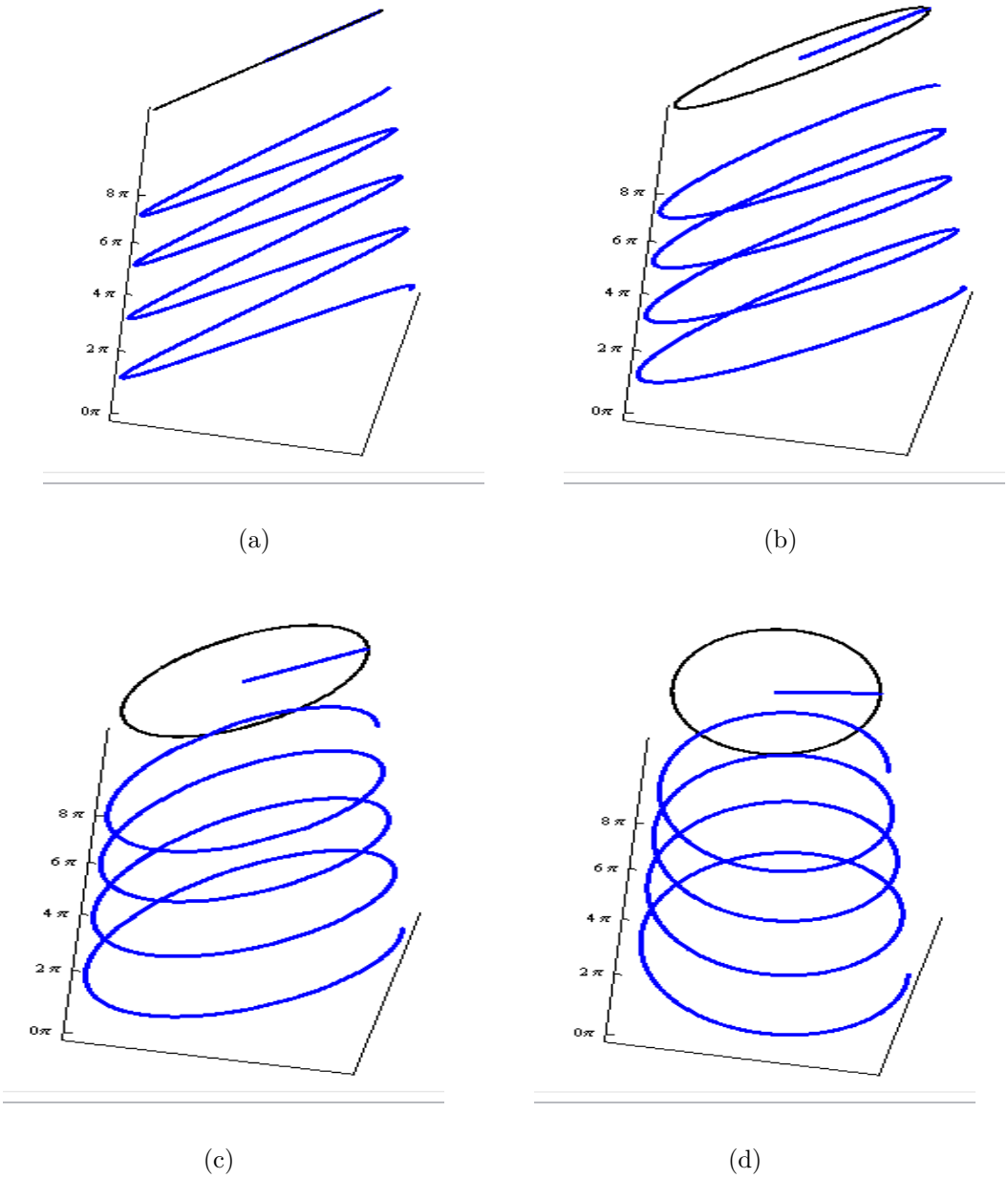

Figure 5.10. Graphic display of an electromagnetic wave travelling through space and time with different phase lags. The resultant electric field vector is displayed at the top portion of each image. a) Representation of linear a polarized wave, where $\mathbf{E}_x$ and $\mathbf{E}_y$ are in phase. The orientation of the resultant electric field vector is equal to $\arctan\left(\frac{\mathbf{E}_y}{\mathbf{E}_x}\right)$ b) Representation of a polarized wave with the resultant electric field vector rotating elliptically, where $\mathbf{E}_x$ and $\mathbf{E}_y$ are out of phase by $\frac{\pi}{10}$. c) Representation of an elliptical polarized wave, where $\mathbf{E}_x$ and $\mathbf{E}_y$ are out of phase by $\frac{3\pi}{10}$. d) Representation of circular polarized wave, where $\mathbf{E}_x$ and $\mathbf{E}_y$ are equal in magnitude and out of phase by $\frac{\pi}{2}$, where the resulting electric field vector rotates in a circle as a function of time.

tardance effect is dependent on the fiber material, wavelength of light, path length and any event that may change the structure of the optical fiber. The number of turns of the fiber on each paddle is chosen in such a way that allows them to shift the phase by $\approx \frac{\pi}{2}$ *or* π. The paddles are then twisted to change the axis of the retarder to obtain the desired polarization into the probe. Some probe geometries do not allow for this to work effectively and are therefore rejected when doing experiments.

NSOM allows for the study of optical properties of samples beyond the diffraction limit. Outside of obtaining optical information, topographical images on the order of the size of the probe can be resolved as well. Unlike the contact and tapping methods of AFM, later to be discussed, NSOM has the advantage of not physically contacting the surface, allowing for a less intrusive way of studying samples.

5.2 Measuring the Retardance and Optical Orientation Simultaneously

To perform PM-NSOM measurements, the system consisted of a linear polarizer, Photo Elastic Modulator (PEM), two quarter wave plates, sample, fiber paddle, and an analyzer, seen in figure 5.11. The NSOM probe and fiber paddles are treated as one entity, which we intend to make aligned with the system with minimal retardance effects. To simultaneously obtain the retardance S and the optical orientation θ from our sample, the components need to be properly aligned. The linear polarizer defines an arbitrary preferential direction, which is defined as 0°. With respect to this direction, the PEM is oriented at 45°, both quarter wave plates have their fast axis at are aligned at 0° and the analyzer positioned at $-45°$ with respect to the system's axis, which is determined by the first polarizer.

Because the initial state of polarization is known, we are able to use Jones' matrices to describe each component within the system. As an example, when polarized light with vector components $\mathbf{E}_x$ and $\mathbf{E}_y$ passes through a waveplate, (with its fast and

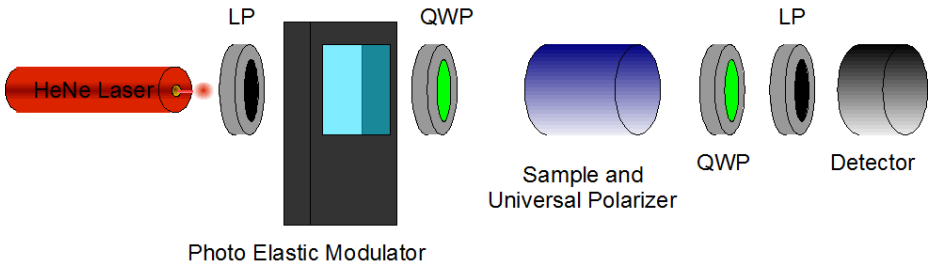

Figure 5.11. System arrangement to measure both S and θ simultaneously. The setup contains a helium neon laser, followed by a linear polarizer at 0°, a PEM at 45°, two quarter wave plates at 0°, an analyzer at ±45° and finally a photo detector.

slow axis aligned with the x and y-axis of the system) there will be a phase shift between the two perpendicular vector components. Mathematically we can represent this vector in terms of $\mathbf{E}_x$ and $\mathbf{E}_y$ and give it an associated phase lag $\Delta\kappa$

$$\mathbf{E}_x = E_o e^{\mathrm{i}\omega t} \qquad \text{and} \qquad \mathbf{E}'_x = E_o e^{i\left(\omega t + \frac{\Delta\kappa}{2}\right)}. \tag{5.4}$$

From equation 5.4 we see the electric field experiences a phase lag, where is goes from $\mathbf{E_x}$ before the polarizing element, to $\mathbf{E'_x}$ after it. Making use of Jones' matrices, the effect of the polarizing element can be represented as

$$\begin{pmatrix} e^{\frac{\mathrm{i}\,\Delta\kappa}{2}} & 0 \\ 0 & e^{\frac{-\mathrm{i}\,\Delta\kappa}{2}} \end{pmatrix} \begin{pmatrix} \mathbf{E}_x \\ \mathbf{E}_y \end{pmatrix} = \begin{pmatrix} \mathbf{E}'_x \\ \mathbf{E}'_y \end{pmatrix}.$$

When this phase lag is on the order of π the net phase difference is on the order of half the wavelength, hence the reason we refer to such an object as a half wave-plate. Also, when the phase lag is $\frac{\pi}{2}$ is is called a quarter wave-plate, because the phase lag is proportional to shifting the two waves in length by $\lambda/4$.

5.2.1 Polarization Modulation

To modulate the polarization the electromagnetic radiation's polarization is changed from linear to quasi-circular at a particular rate. To shift from linear to circularly polarized light, a phase lag between the $\mathbf{E}_x$ and $\mathbf{E_y}$ components of the electric field is created. The resulting effect is displayed in figure 5.10, where it goes from linear to circularly polarized light by adjusting the phase difference of $\frac{\pi}{2}$ between the $\mathbf{E}_x$ and $\mathbf{E}_y$ components of the resulting electric field vector.

In order to modulate the polarization, it is mandatory that the relative speed of the two wave components is adjusted. To accomplish this task a PEM was utilized [43].

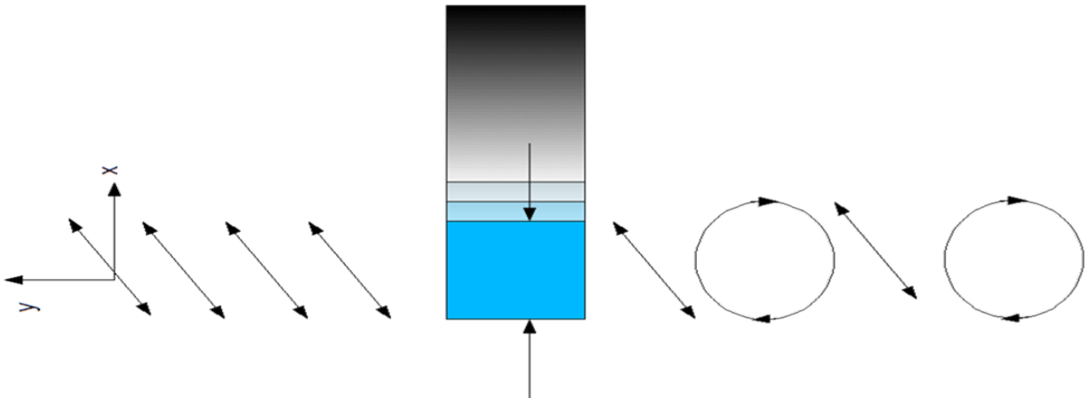

Figure 5.12. Pictorial representation of a photo-elastic modulator that stresses a piece of quartz along one of its axis, shown by the opposing arrows, using piezo-electric device. Polarized light orientated at 45° with respect to the PEM's axis enters the PEM. For a judiciously chosen value of the amplitude of modulation on the PEM (see Eq. 5.5), the outgoing electromagnetic wave's polarization modulates between linear and circular at a frequency determined by the PEM.

A PEM is a device that uses a piezo-electric material to stress a piece of quartz along a preferential axis at a given frequency ($f_\circ$). The stress along the preferential axis changes the index of refraction (n) along that direction. By adjusting the amplitude of the stress we control the strength of Δn. Sending an electromagnetic wave through the PEM we then can induce a dynamic phase shift at $f_\circ$, as illustrated in figure 5.12. The PEM effective modulation can be mathematically modelled

$$\begin{pmatrix} \cos(\beta) & \sin(\beta) \\ -\sin(\beta) & \cos(\beta) \end{pmatrix} \begin{pmatrix} e^{\frac{iB\cos(\omega t)}{2}} & 0 \\ 0 & e^{-\frac{iB\cos(\omega t)}{2}} \end{pmatrix} \begin{pmatrix} \cos(\beta) & -\sin(\beta) \\ \sin(\beta) & \cos(\beta) \end{pmatrix}, \tag{5.5}$$

where $\omega = 2\pi f_\circ$ and B are the the angular frequency and amplitude of the PEM's oscillation and β is the orientation of the device in the system with respect to the x and y axis, defined by the first LP, see figure 5.13.

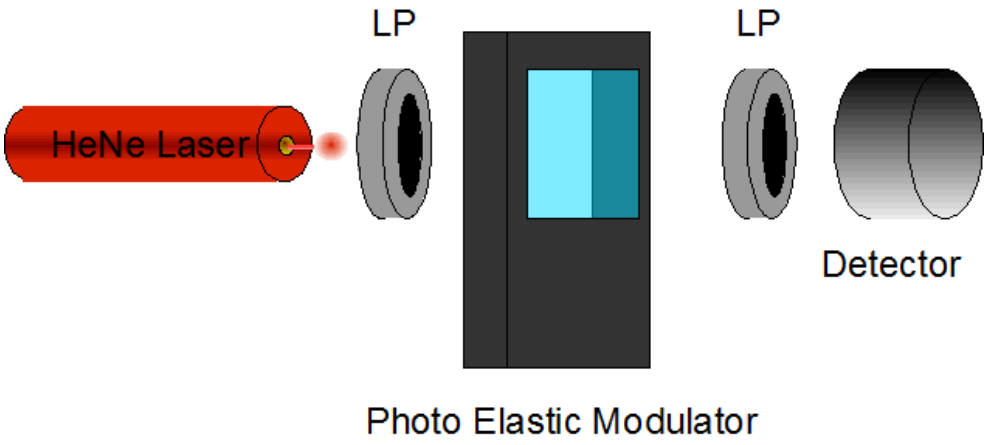

Figure 5.13. System arrangement with a PEM, linear polarizer and analyzer, used to align and calibrate the PEM.

We now have all the tools needed to both physically modulate the polarization and mathematically model its behavior in a given system.

5.3 System Alignment

To define the systems axis we first align the surface normal of the PEM, polarizer and analyzer to be parallel with the direction of the laser beam's propagation, seen in figure 5.13. Using Jones' matrices to model the system, we obtain an expression that is proportional to the intensity ($\mathbf{E} \cdot \mathbf{E}^*$)

$$\mathbf{E} \cdot \mathbf{E}^* \propto \frac{1}{2}\left(\cos^2(\alpha) + \cos^2(\alpha - 2\beta)\right) - \frac{1}{2}J_0(B)\sin(2(\alpha-\beta))\sin(2\beta) + J_2(B)\cos(2\omega t)\sin(2(\alpha-\beta))\sin(2\beta) + ..., \quad (5.6)$$

where β, B and ω are the orientation, amplitude and angular frequency of the PEM, which is aligned with the first polarizer and α is the position of the analyzer. Simplification of the equation occurs when the axis of the polarizer and analyzer coincide

$$\mathbf{E}\cdot\mathbf{E}^{*}\propto\frac{1}{2}\left(1+\cos^{2}(2\beta)\right)+\frac{1}{2}J_{0}(B)\sin^{2}(2\beta)-J_{2}(B)\cos(2\omega\mathrm{t})\sin^{2}(2\beta)+\ldots\ . \quad (5.7)$$

The second harmonic (R_2) is

$$R_{2}\ =\ -J_{2}(B)\cos(2\omega\mathrm{t})\sin^{2}(2\beta), \quad (5.8)$$

resulting in R_2 reducing to zero when the PEM is aligned 45° with respect to the polarizer.

In practice, because of the PEM's shape, it is more convenient to define the axis of the system around the fast axis of the PEM. First, we align the polarizer 45° with respect to the PEM's horizontal axis by eye. We then use an analyzer to measure the expected intensity from the polarizer and PEM, an example of the setup can be seen in figure 5.13. From Appendix E the expression for intensity is

$$\begin{aligned}\mathbf{E}\cdot\mathbf{E}^{*}\ \propto\ & \tfrac{1}{2}-\tfrac{1}{2}\sin(2\alpha)\sin(2\beta)+\tfrac{1}{2}\cos(2\alpha)\cos(2\beta)J_{0}(B)\\ & -J_{2}(B)\cos(2\alpha)\cos(2\beta)\cos(2\omega\mathrm{t})+\ldots.\end{aligned} \quad (5.9)$$

With an assumption that $\beta\approx 45^{\circ}$ R_2, reduces to

$$R_{2}\ =\ -J_{2}(B)\cos(2\alpha). \quad (5.10)$$

R_2 decreases to zero when the analyzer's orientation value is $n90^{o}+45^{o}$, with n as an integer. Placing the analyzer 90^{o} with respect to the polarizer, with the PEM off, results in a minimum signal. With the PEM turned on, making sure that R_2 is

minimized, small adjustments are made to the polarizer until both the signal, when the PEM is on and off, are zero within measuring capabilities.

B is adjusted to obtain a zero value for the $J_o(B)$ Bessel term, seen in equation 5.9. This becomes an integral aspect of the setup to ensure that the DC term is not a function of S or θ. To do this we first place a quarter wave plate (QWP) after the PEM and orient its fast axis with the system's (determined by the direction of the first polarizer). The analyzer is then rotated 90° with the PEM off, to obtain a minimum signal. The QWP should then be rotated until the lowest possible intensity is achieved. Following this, the PEM is turned on, the analyzer is rotated and the signal is monitored. The resulting intensity is,

$$\mathbf{E}\cdot\mathbf{E}^{*} \propto \frac{1}{2}+\frac{1}{2}J_0(B)\cos(2\alpha)+J_1(B)\cos(\omega \mathrm{t})\sin(2\alpha) \\ -J_2(B)\cos(2\omega \mathrm{t})\cos(2\alpha)+... \tag{5.11}$$

We could either monitor the DC term of the intensity found in equation 5.11 or use a lock-in measurement to monitor the $R_2 = -J_2(B)\cos(2\omega \mathrm{t})\cos(2\alpha)$ of the PEM's frequency (Monitoring R_2 also gives us the advantage of measuring from zero when $\alpha = 45°$.). It was not feasible in the experiment to monitor the DC term, due to the lack of a normalizing reference signal to account for laser instabilities. Instead R_2 was monitored and utilized the DC term in normalizing the signal, removing any unwanted fluctuations due to laser drift. Figure 5.14(a) shows that for $B \neq 2.405$, the intensity becomes less symmetric. By measuring how this changes we can easily determine where the $J_o(B)$ term vanishes in

$$I_{2\omega}(\alpha)=\frac{R_2}{DC} = \frac{-J_2(B)\cos(2\alpha)}{\frac{1}{2}+\frac{1}{2}J_0(B)(\cos(2\alpha))}. \tag{5.12}$$

The theoretical data plotted in figure 5.14 can be used to quantify the shift of the curves from the curve with the expected value of $B = 2.405$. The problem implementing this is that the actual peak value is unknown. It is only known that when the $J_o(B)$ term goes to zero $I_{2\omega}(\alpha)$ collapses into a symmetric $\cos(2\alpha)$ function. Figure 5.14(b) shows how by normalizing the data by the maximum amplitude a similar graph can be extracted. By analysing the non-symmetric nature we can obtain the difference between the amplitude of the function and a perfect $\cos(2\alpha)$ function. The line shown in figure 5.15 shows how theoretically the data can be used to determine what value of B will make $J_o(B)$ vanish.

Figure 5.14 shows the normalized data from the measurements made for different values for B. Mathematically $J_o(B)$ goes to zero at 2.405. This value is extremely far from the observed value of B. In figure 5.16(b) a more precise depiction of the amplitude differences around the expected $\cos(2\alpha)$ function is obtained.

A plot of the amplitude difference in figure 5.17 was determined via theoretical data. The value of 2.25 for B was obtained by determining where the difference is minimized, i.e. at what value of B. The linear interpolation in figure 5.17, also verifies that the measurement obtained is the best possible result within the resolution of the PEM controller. This was corroborated through the monitoring of the DC signal as a function of α, but could not be fully resolved due to reasons discussed previously.

After the PEM is calibrated the final two components to be placed into the system are the two quarter wave plates. Both need to be aligned with respect to the PEM's axis. To accomplish this the procedure previously mentioned was implemented. This process minimized our signal using the analyzer. The sensitivity of our measurement is determined on how well the signal produced in the configuration found in figure 5.11, is referenced to zero when measured. To achieve a minimum for the signal just mentioned, the two quarter wave plates must produce exactly a $\lambda/2$ phase shift of

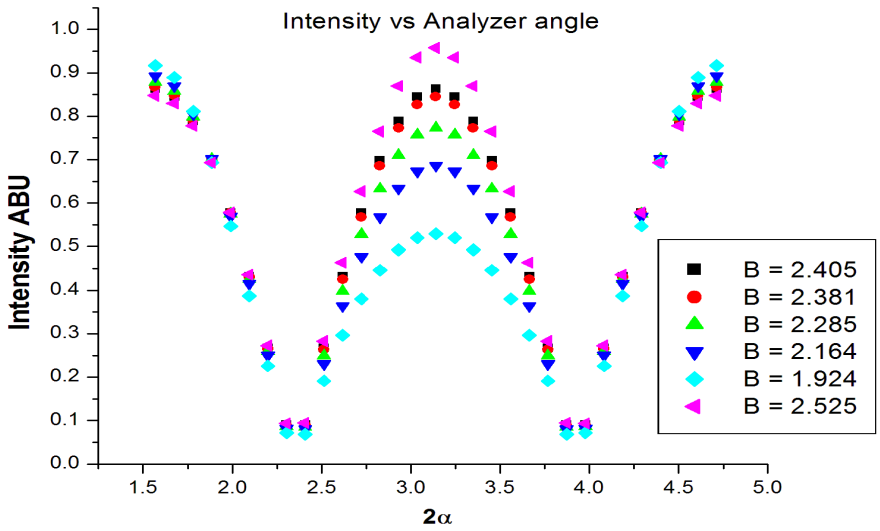

(a)

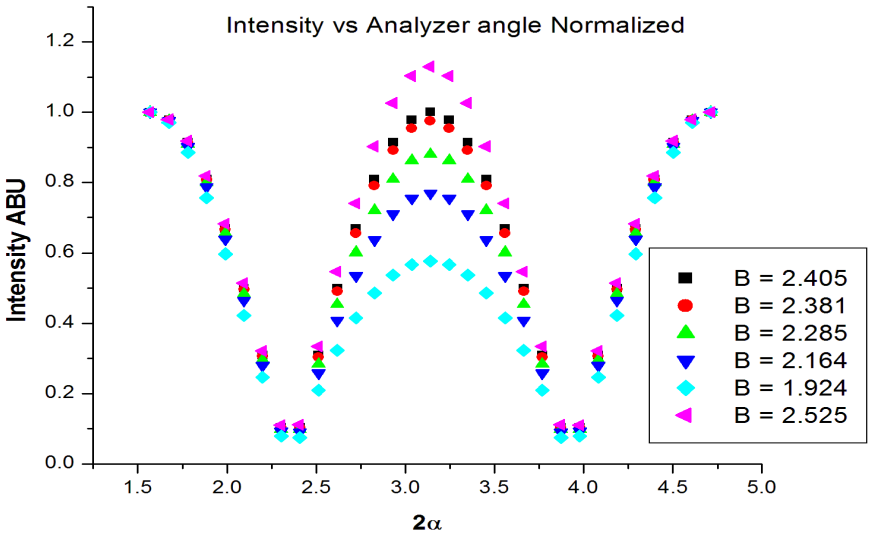

(b)

Figure 5.14. Theoretical plots of the Intensity versus analyzer angle of various values of B. a) Intensity versus analyzer angle for varying values of B. This graph shows how the function's shape becomes less symmetric for values of B further away from $B = 2.405$. b) Graph of the intensity normalized versus the analyzer angle for varying values of B (All data was normalized with the first point of each set of data.

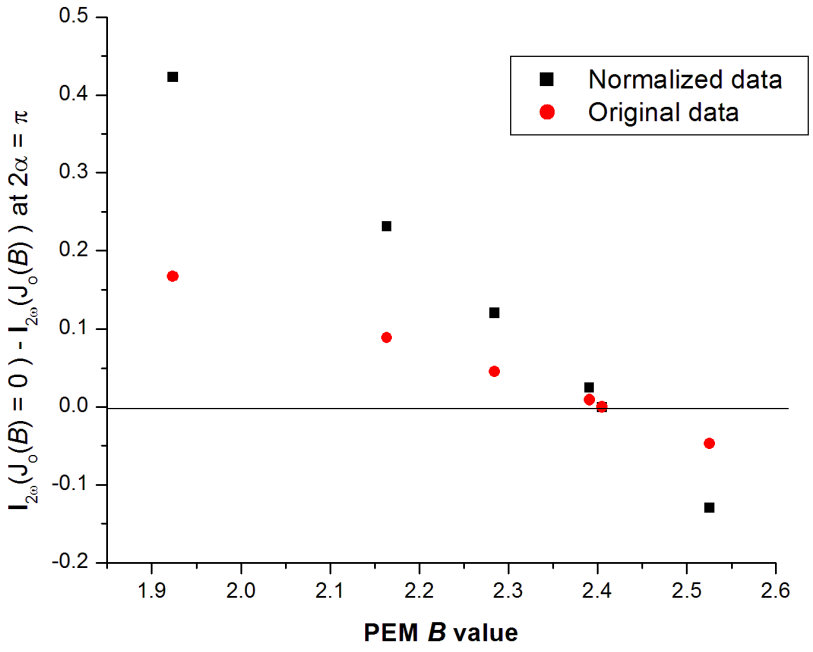

Figure 5.15. Plot of $I_{2\omega}(J_o(B) = 0)$ subtracted from $I_{2\omega}(J_o(B))$ at $2\alpha = \pi$ for the original and normalized data from figures 5.14(a) and 5.14(b). We obtain from the line graph of $I_{2\omega}(J_o(B) = 0) - I_{2\omega}(J_o(B))$ versus B at $2\alpha = \pi$ that $J_o(B) \longrightarrow 0$ when the function crosses zero at $B = 2.405$.

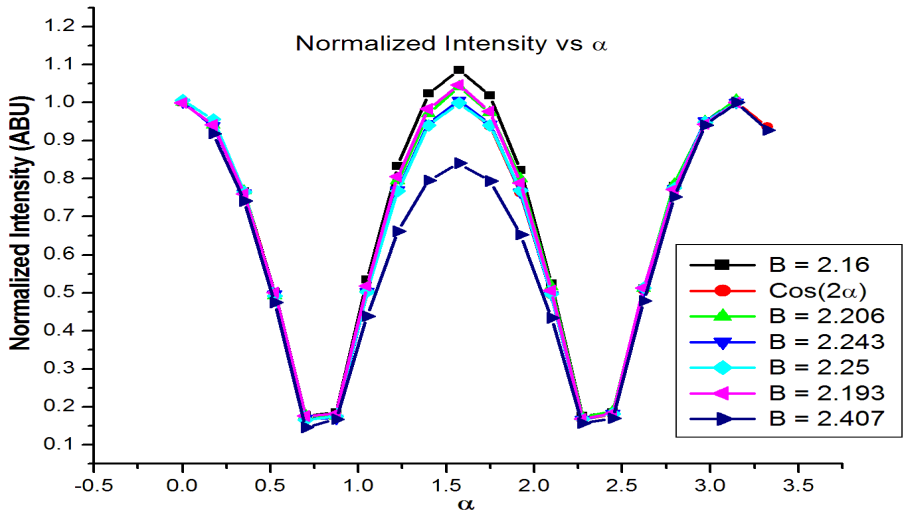

(a)

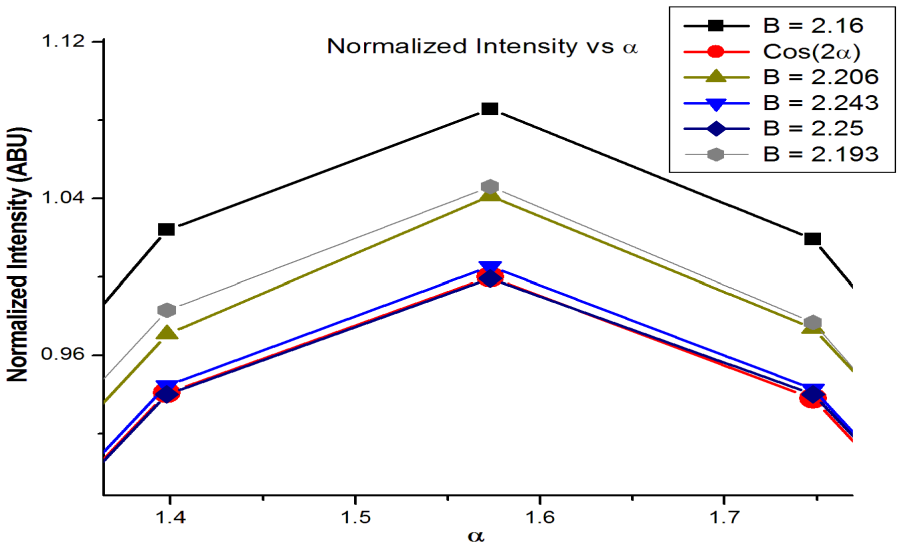

(b)

Figure 5.16. Data from various measurements of the intensity versus analyzer angle at various values of B. a) Normalized plots of intensity values, for varying analyzer angles for different values of B. b) Normalized intensity plot versus analyzer angle, showing the trend as the of $J_o(B)$ term is nullified.

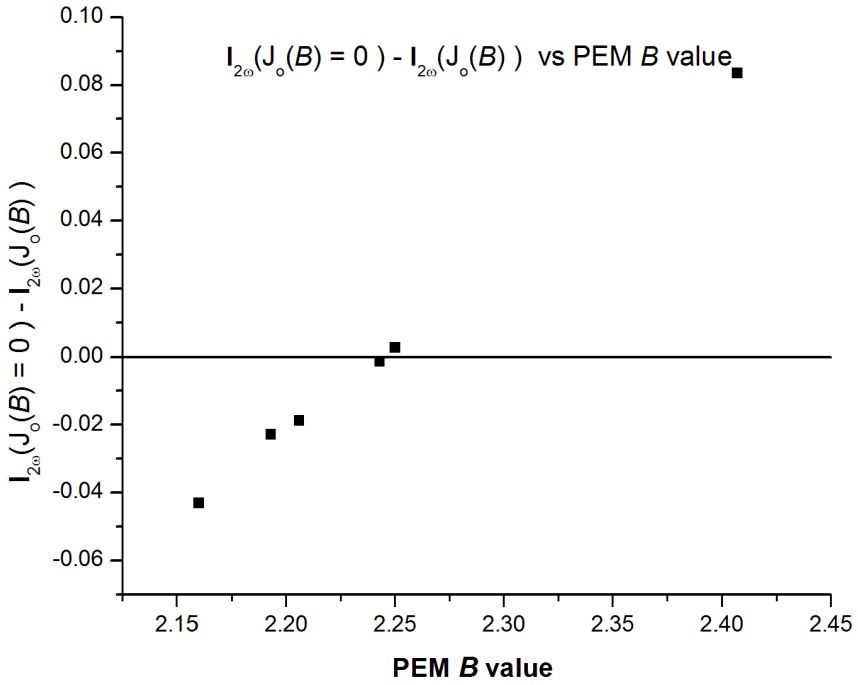

Figure 5.17. Plot of $I_{2\omega}(J_o(B) = 0) - I_{2\omega}(J_o(B))$ versus PEM B values, when α is located at the central peak of the plotted data in figure 5.16(b). From the graph it can be determined that $B = 2.25$ gives a minimum value for the $J_o(B)$ term.

the polarization. To better understand how to control the alignment, small angle approximations in the calculations were performed, where each quarter wave plate's retardance and orientation within the system are slightly shifted from their optimal values. Following the details outlined in Appendix G, we obtained the expression

$$\mathbf{E} \cdot \mathbf{E}^* \propto \frac{1}{2} + J_1(B)(\delta + \Delta)\cos(\omega t) - J_2(B)(\gamma + \theta)\cos(2\omega t), \tag{5.13}$$

where Δ and θ are the small retardance and small orientation for the first quarter wave plate and δ and γ are the respective values for the second, with $J_o(B) = 0$. We see that the signal from the first harmonic is dependent on the retardance values of both wave plates,

$$R_1 = J_1(B)\,(\delta + \Delta) \tag{5.14}$$

Where as, the signal from the second harmonic R_2 only arises if the two wave plates are not aligned with the systems axis,

$$R_2 = -J_2(B)\,(\gamma + \theta)\,. \tag{5.15}$$

From these results a zero R_1 signal can only be obtained if the total phase shift of the polarization from the two quarter wave plates is exactly a multiple of π. Within our alignment capabilities, $\gamma + \theta = 0$ are easily made zero with the PEM off, by aligning the two quarter wave-plates with the PEM's axis, but to achieve zero values for $\delta + \Delta$, it is solely dependent on our ability to align the QWP's surface normal with the beam's direction. Small adjustments of the orientation of the QWP are made to adjust R_1 make the net retardance zero, while observing R_2 verify the orientation of the QWP maintains its alignment with the system. This property of the setup allows

for the determination of the total S as zero. Furthermore this method assists with the initialization of the experiments.

All other optical elements were aligned by minimizing the signal using the analyzer, but to align the analyzer, the second harmonic signal of the intensity is monitored,

$$\mathbf{E} \cdot \mathbf{E}^* \propto \frac{1}{2} - J_1(B)\delta \sin(2\alpha)\cos(\omega t) - J_2(B)\cos(2\alpha)\cos(\omega t) + ..., \tag{5.16}$$

where the small retardance $\delta = \delta + \Delta$ is the combined residual effect of both QWP, and α is the orientation of the analyzer. It can be seen that R_2 is independent of any retardance effects from the quarter wave plates and therefore can be used to find the exact orientation for the analyzer,

$$R_2 = J_2(B)\cos(2\alpha). \tag{5.17}$$

Hence once the analyzer is aligned adjustments to the wave plates' position are made until a zero signal in R_1 (from equation 5.15) is met.

The results from this alignment and calibration procedure yields a zero signal of $\approx 1\times 10^{-4}$ rad and is limited to the noise of the instruments used. Without performing these calibrations and tests it would be impossible to make precise measurements of S and θ.

5.4 Total Experimental Setup

The digram in figure 5.18, displays the total setup for performing PM-NSOM measurements. The light from the laser mechanically chopped. The optical information is extracted using a silicon photo detector, a pre-amplifier and three lock-ins to mea-

sure the R_1, R_2 and DC components of the intensity. All information was collected on a computer with a data acquisition board in conjunction with LabView software, where two dimensional images for $\frac{R_1}{DC} = I(1\omega)$, $\frac{R_2}{DC} = I(2\omega)$, S, θ and topographical information were stored.

5.5 Experimental Modifications for Temperature Controlled Near-Field Microscopy Measurements

To control the temperature of the sample, a chamber was placed over the existing system, where the temperature was controlled using a thermo-electric cooler (TEC) (a schematic can be seen in figure 5.19(a)). The chamber was chosen to have cylindrical symmetry to minimize the effects of lateral thermal gradients across the sample. The sample was placed on an aluminium sample holder with an embedded temperature sensor to accurately monitor the temperature (see figure 5.19(c)). To thermally isolate the sample from the environment, the sample holder was elevated with a separator made from Delrin (Thermal conductivity ≈ 0.360 W/m-K) [44] with an added stainless steel bottom to increase stability (see figure 5.20(c)). To thermally isolate the chamber from the outside environment, a base plate was machined from Delrin, where an aluminium insert was attached (see figure 5.20(b)). The base plate allowed for the separator and stage to move the sample within the chamber, while decoupling it from the outside thermal environment. To maintain 100 percent relative humidity a water trough was machined from Delrin that attached to the aluminium insert and extended the length of the sample separator. The top chamber was fitted precisely within a groove of the aluminium insert to firmly attach it to the apparatus. A slit was machined in the chamber to allow for it to be slid into place around the NSOM probe and piezo elements after pre-engagement procedures. A TEC was placed in a recessed groove of the chamber, where a heat sink with a matching grove was at-

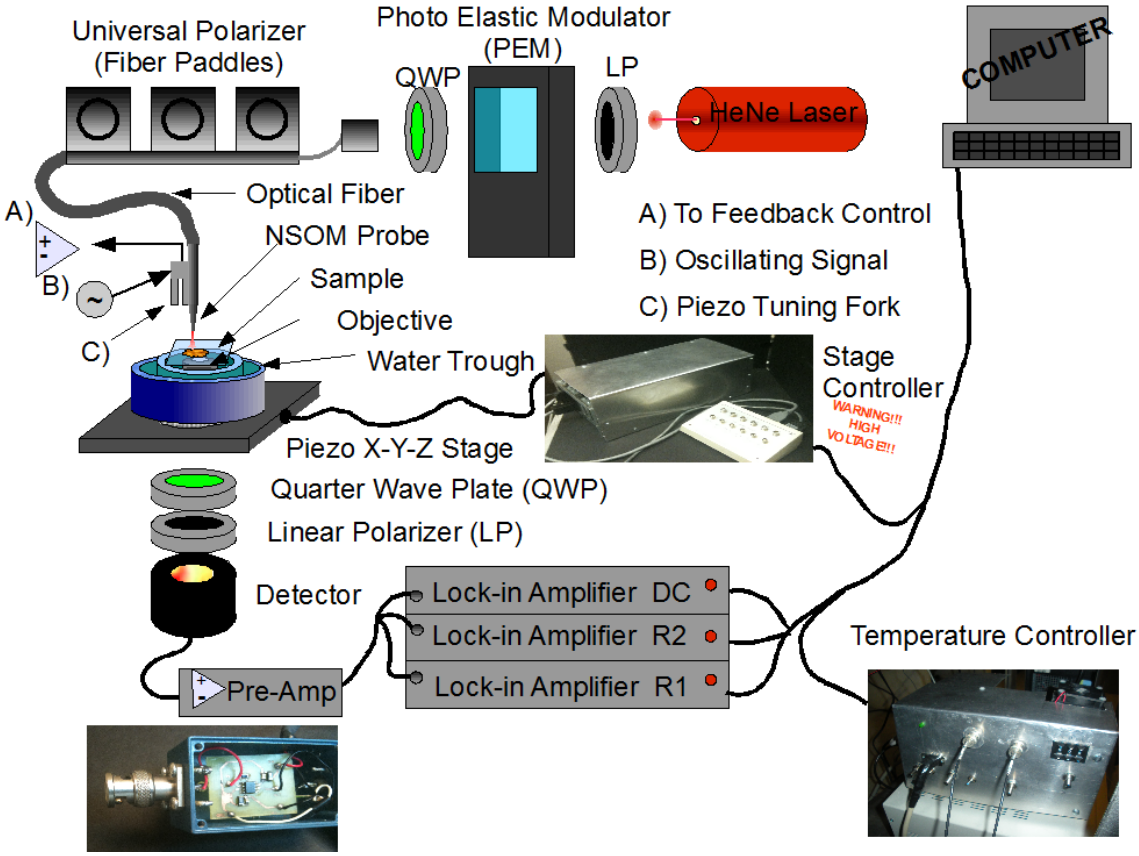

Figure 5.18. Pictorial representation of the total system setup for polarization modulation near-field scanning microscope. The light source is a HeNe laser. The beam travels through a linear polarizer, PEM, and quarter wave plate before being coupled into a optical fiber. The light then travels through a universal polarizer (fiber paddles) and NSOM probe. The fiber paddles are used to control the state of polarization at the NSOM probe. The light then travels through the sample, quarter wave plate and analyzer before being collected with a silicon PIN detector. The signal is amplified by a pre amp, where a lock-in measurement is preformed. The optical and shear force data are collected by a computer.

tached above. Nylon screws were used to firmly connect the components together and thermal paste was applied to enhance the thermal contact of the heating and cooling elements. The temperature of the chamber was monitored with an attached thermistor. The system was thermally isolated further with a Styrofoam insulating outer layer. Various points within the chamber where thermally characterized and calibrated. Significant mechanical instabilities were identified and minimized in order to meet the qualifications for conducting NSOM measurements. Such requirements on height stability were necessary to perform measurements without crashing the probe into the sample.

5.6 Atomic Force Microscopy

Like NSOM, Atomic Force Microscopy (AFM) is a scanning probe microscopy [45]. It uses a cantilever to map the topography of a given surface by collecting data at points across a sample. To accomplish this, a cantilever (see figure 5.21), usually etched from silicon, is attached to a piezo-element. A laser beam is focused on the back of the probe. The light reflected is then collected by a position-sensitive detector. When the cantilever bends, its motion can be determined by the position of the laser spot on the detector (see figure 5.22). Using this information the location of the probe relative to the surface is maintained to create a surface map of the object.

The two basic topographical imaging modes of operation for AFM, are contact and tapping modes [12]. In contact mode the probe is lowered until it touches the sample, where the cantilever bends a particular amount depending on its given force constant (k) and the contact force. An attached piezo element is then utilized to maintain the bend of the cantilever across the sample. Keeping the relative distance constant with a feedback mechanism the topography of the surface can be determined.

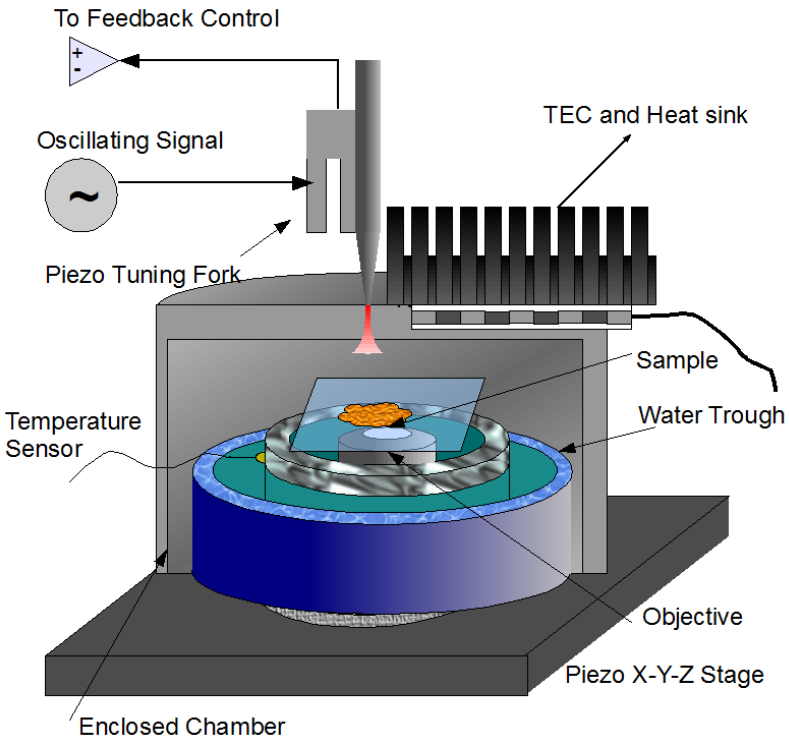

(a)

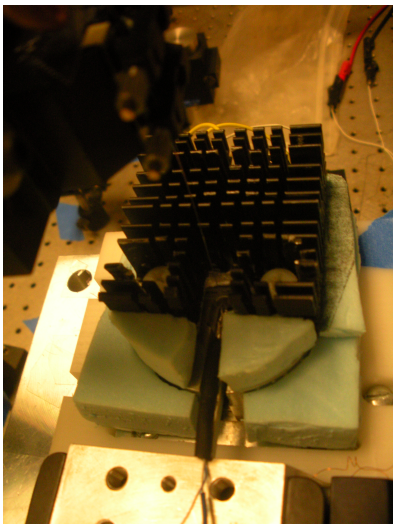

(b)

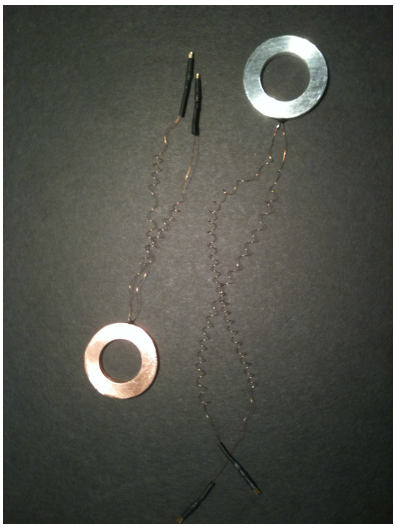

(c)

Figure 5.19. Diagram and picture of temperature controlled NSOM set up. a) Graphic representation of the experimental temperature controlled setup. b) Picture of the temperature controlled chamber mounted on the NSOM system. c) Aluminium and copper sample mounts with embedded temperature sensors.

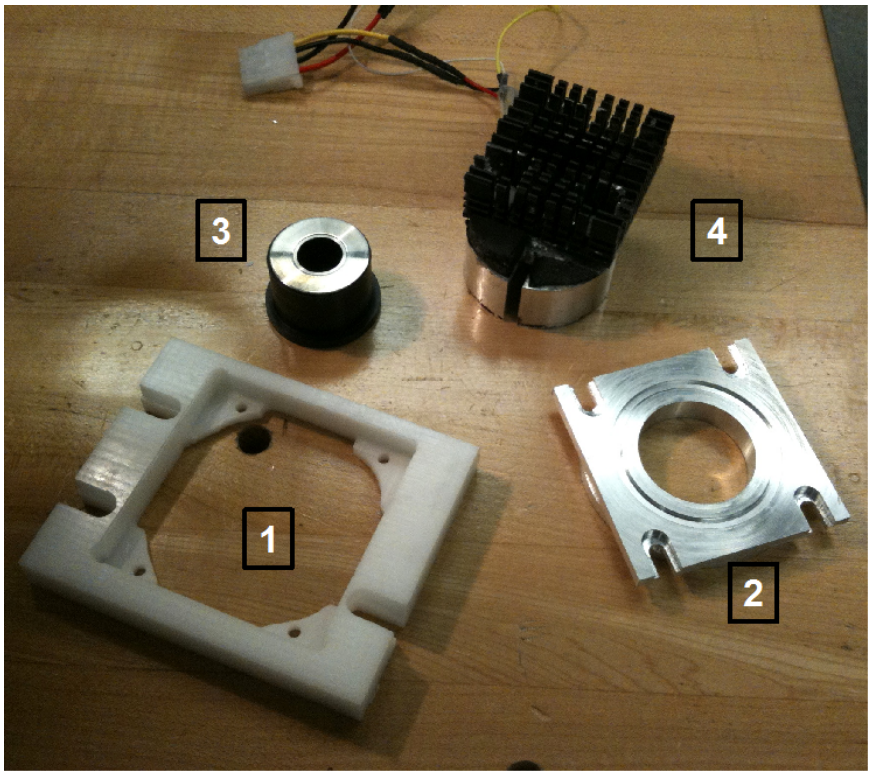

(a)

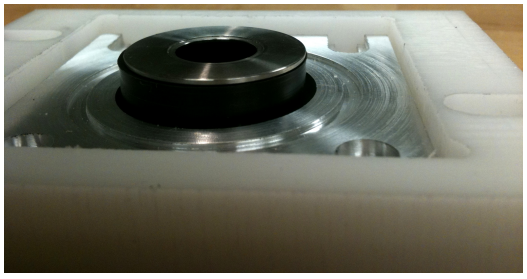

(b)

(c)

Figure 5.20. a) All of the machined components incorporated in the chamber of the temperature controlled experiments. 1) Delrin isolating plate 2) Aluminium insert to hold chamber in place. 3) Delrin separator 4) Temperature controlled chamber. b) Delrin isolation plate with aluminium insert, including the sample elevator protruding from the center. This shows how pieces one, two and three, are to be put together on the system. c) Delrin sample separators with stainless steel bottoms.

Figure 5.21. Two SEM images of a silicon AFM probe and cantilever. [46]

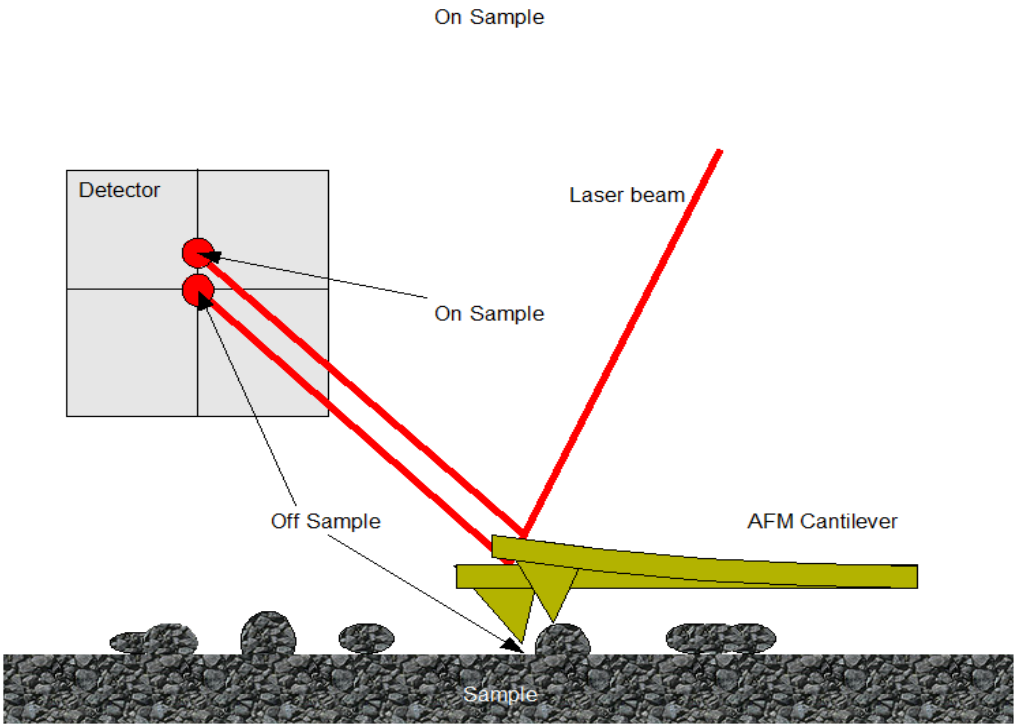

Figure 5.22. Visual representation of contact mode in AFM. As the probe touches the sample, due to strong repulsive forces, it bends. The laser spot on the detector is directed upward and that position is maintained through scanning, utilizing a feed-back mechanism. The information is collected to create a topographical map of the surface structure.

Similar to NSOM, in tapping mode the cantilever is oscillated at its natural resonance frequency. In this mode, the amplitude of the probes oscillations are monitored using the detector, shown in figure 5.23. When contacting the surface the amplitude at a given frequency decreases as the resonance peak shift due to a change in k of the cantilever. The relative distance can be mapped by maintaining the decrease in amplitude constant. The advantage of tapping mode is that the probe is not in constant contact with the surface while scanning, which is important when dealing with softer samples. Also from the tapping mode the phase of the oscillations can be monitored, which can provide additional information about the hardness of the sample. When the cantilever strikes the sample the energy loss in the impact is dependent on the probe and substrate properties. This difference in energy loss due to the deformation of materials across the object can be tracked using the phase shift of the signal. The phase signal can then be used to determine if the area the probe is in contact with is different across regions, even in the case of topologically flat samples.

From the topographical information of the sample a three dimensional representation of the surface can be obtained. The AFM image in figure 5.24, is a three dimensional representation of an array of silica beads supported on a glass substrate. This allows the visualization of sub-micron structures of surfaces to characterize local configurations of materials.

5.6.1 Contact Mode - Measuring Adhesion Forces

In contact mode we cannot only measure the topography of a particular sample, but have the ability to characterize the forces the cantilever has with the sample. This is done by tracking the probes' deflection as a function of distance as it approaches the substrate. To perform the measurement, the cantilever is brought within the

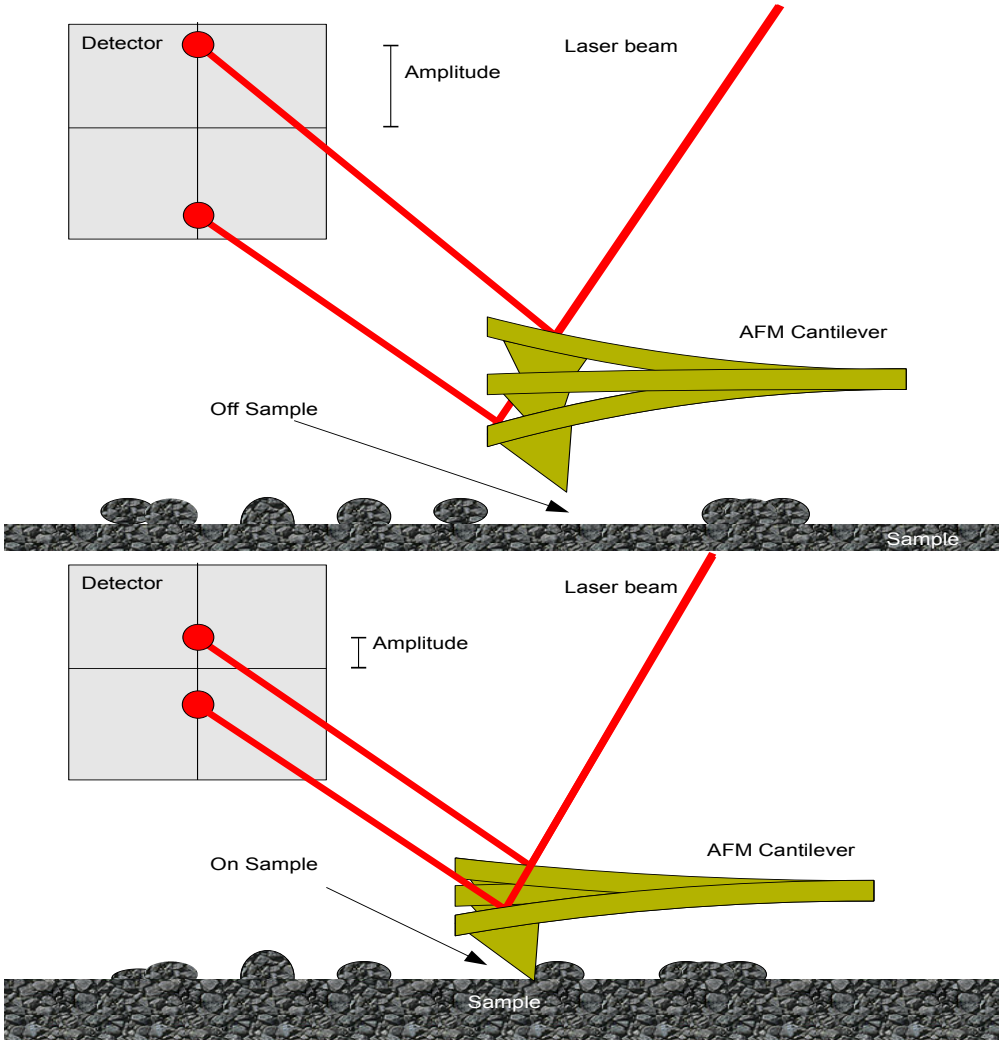

Figure 5.23. Visual representation of tapping mode in AFM. The top picture shows the probe being oscillated, resulting in having a particular amplitude. Just as in contact mode when the probe comes in contact with the sample, due to van der Waals interactions, a force is applied to the probe. The laser spot on the detector is tracked, giving the amplitude and phase of the signal.

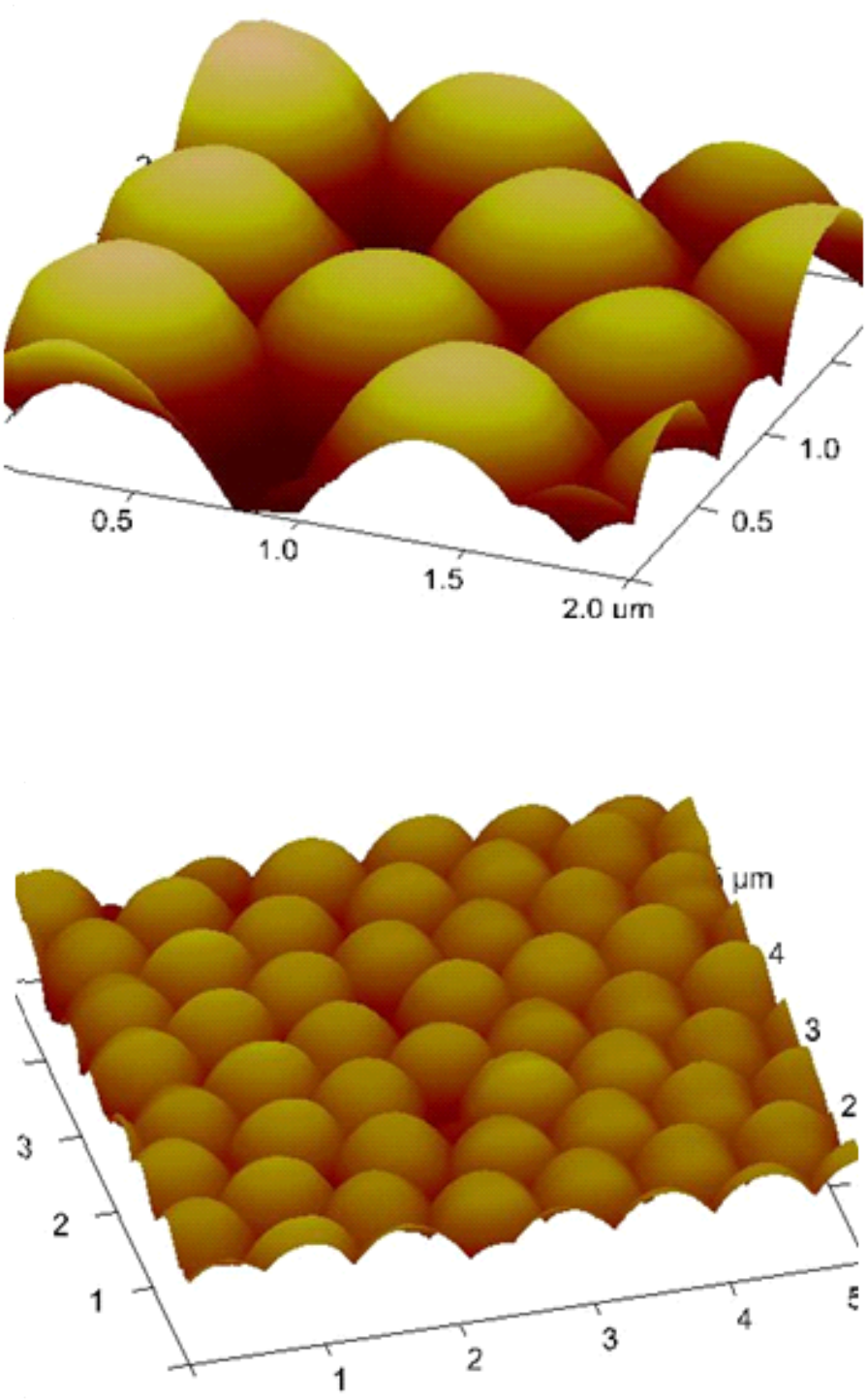

Figure 5.24. Topographical AFM images of 800 nm silica beads, supported on a glass substrate.

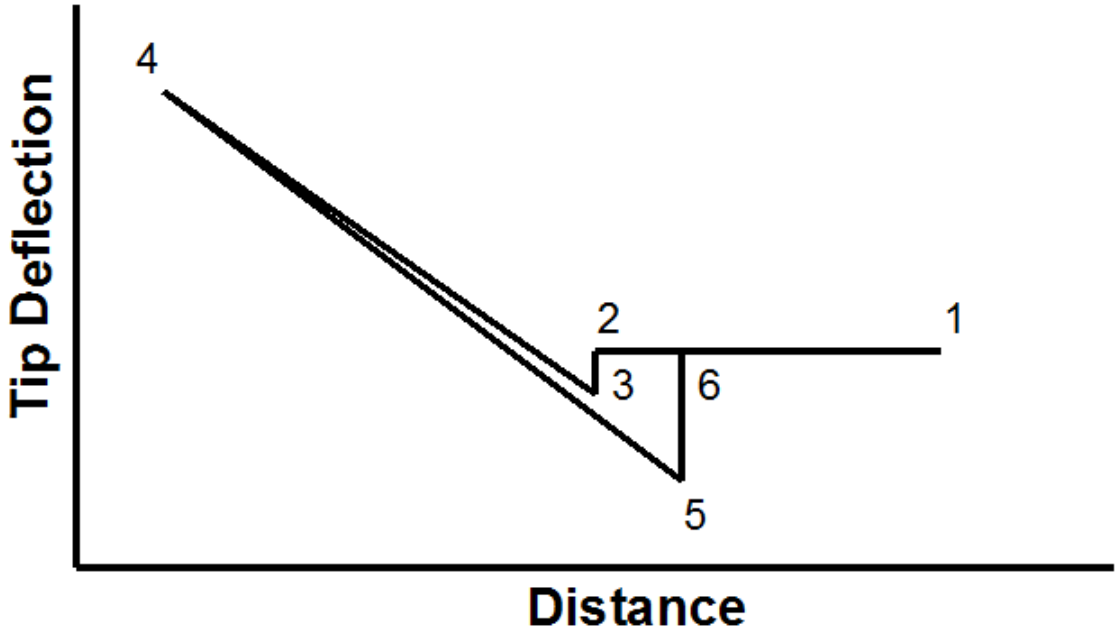

Figure 5.25. Representation of an AFM-Force curve. From point 1 to 2, the probe approaches the substrate. There is an attractive force from 2 to 3. From point 3 to 4 the probe is in direct contact with the surface, which bends according to its' spring constant (k). The AFM probe is then retracted from point 4 to 5. From point 5 to 6 the adhesion forces are overcome. From the tip deflection distance of points 3 and 5 we can determine the approximate adhesion force, using $F_{adhesion} \approx k\Delta z$, where Δz is the distance between points 3 and 5.

range of the piezos' expansion distance. The deflection is measured as a function of distance and from this the attractive forces involved in the extension and retraction of the probe can be determined, under the conditions that k and the actual distance are precisely known.

Providing more detail, figure 5.25 shows a diagram of a contact mode force curve. From point 1 to 2, the probe approaches the substrate until there is an attractive force, shown from 2 to 3. From point 3 to 4 the probe is in direct contact with the surface and bends according to the cantilever's flexing properties, which are characterized by

the spring constant (k). The AFM probe is then retracted from point 4 to 5, until the adhesion forces are overcome and the graph goes from point 5 to 6. From the tip deflection distance of points 3 and 5 we can determine the approximate adhesion force, using $F_{adhesion} \approx k\Delta z$, where Δz is the distance between points 3 and 5. A quantitative comparison of a materials mechanical properties can be accomplished by comparing the transition from 2, 3 and 4. When the tip contacts the surface from 2 and 3, strong repulsive forces cause both the cantilever and material to deform as the probe to brought from 3 to 4. This deformation is a function of tip radius and material composition of all contacting surfaces. Comparing types of graphs in figure 5.26, indicates that the sharper the transition, the harder the substrate, and the smoother (or having a shallower slope), the softer the substrate. These properties of the force curves can be utilized to determine physical characteristics of the sample, beyond surface structure.

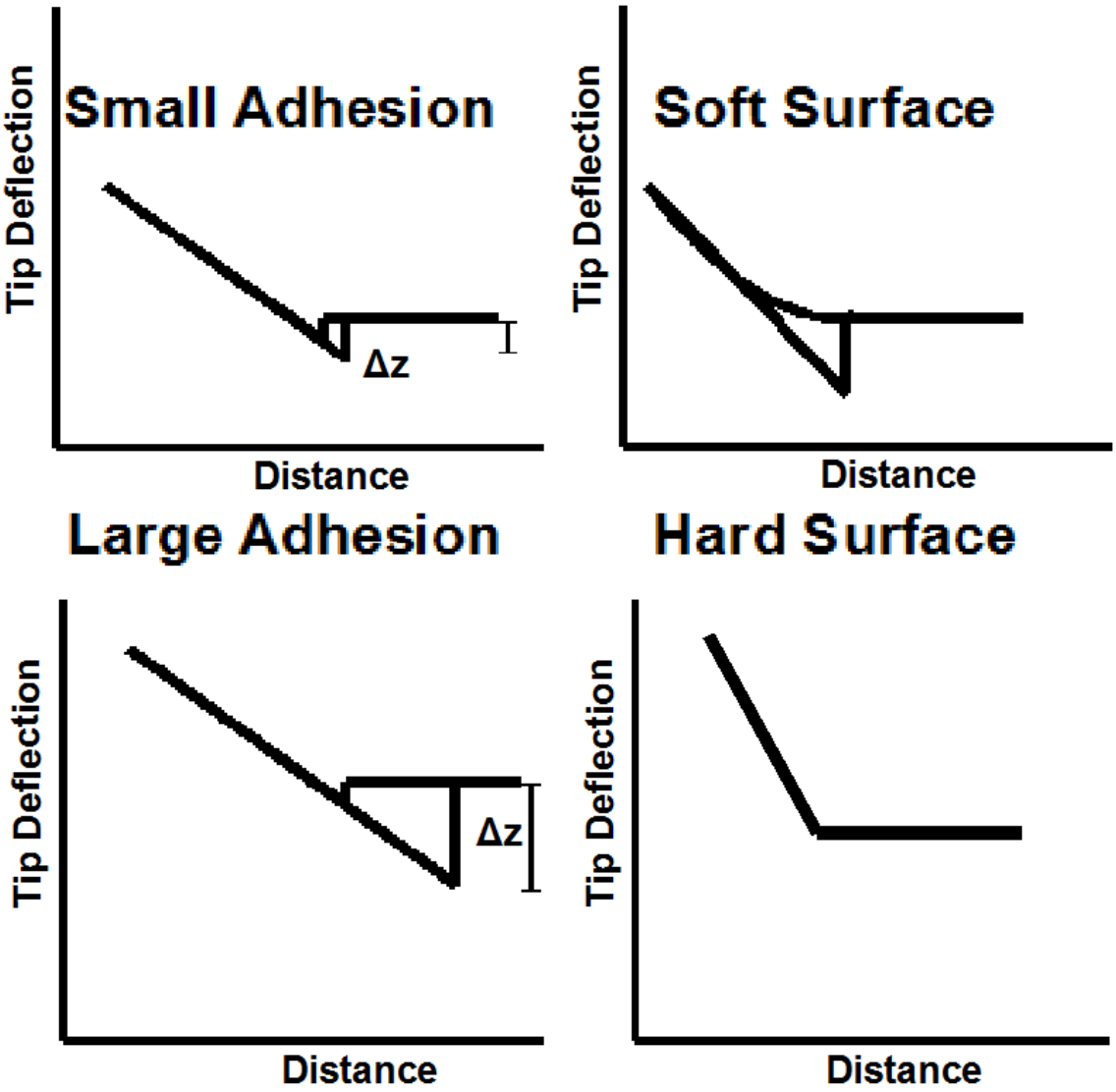

Figure 5.26. Display of different examples of AFM force curves. Each associated with varying surface interactions. There is a small adhesion when Δz is small, and a large adhesion when Δz is large. The substrate is softer if the approach curve has a shallow slope as the cantilever is lowered, and harder when the approach curve has a sharp slope when the cantilever contacts the substrate.

5.7 System Characterization

With the alignment procedures discussed in Section 5.3 a measurement of S with an accuracy $\sim 10^{-4}$ rad was achieved. In figure 5.27 graphs of S and θ are plotted versus time, with S minimized and not minimized. With the system not aligned, S yielded fluctuations of $\approx .3$ mrad, but when S was minimized the fluctuations were $\approx 1{\times}10^{-4}$ mrad. Such fluctuations make properly aligning the system to precisely measure S significantly important.

Before conducting PM-NSOM measurements, the system was aligned with no sample using the fiber paddles. The sample then was slid underneath the NSOM probe on the piezo stage. To engage the sample the probe was brought to the surface by eye. Then a feedback mechanism was utilized in bringing the stage the remaining distance. When the probe was physically moved, a small change in stress occurred, altering the total retardation effect of the fiber. This may also occur due to temperature shifts that induce changes on the effective S of the fiber. The ability to realign the system quickly without compromising the measurement capabilities of S or damaging the NSOM probe was desirable.

To do so, a proposal to align the system with the sample in place was made. It was hoped that as the signals were zeroed over the sample, S and θ found in our original equations remained measurable quantities,

$$I_{1\omega}(S,\theta) = \frac{R_1}{\mathrm{DC}} = J_1(B)\pi\cos(2\theta)\sin(S) \tag{5.18}$$

$$I_{2\omega}(S,\theta) = \frac{R_2}{\mathrm{DC}} = J_2(B)\pi\sin(2\theta)\sin(S) \tag{5.19}$$

To further explore how minimizing the system's signals affects our final result, we employed Jones' matrices. Now the sample and fiber paddles are treated as two separate objects with different effects on the retardance, where δ and θ are the retardance

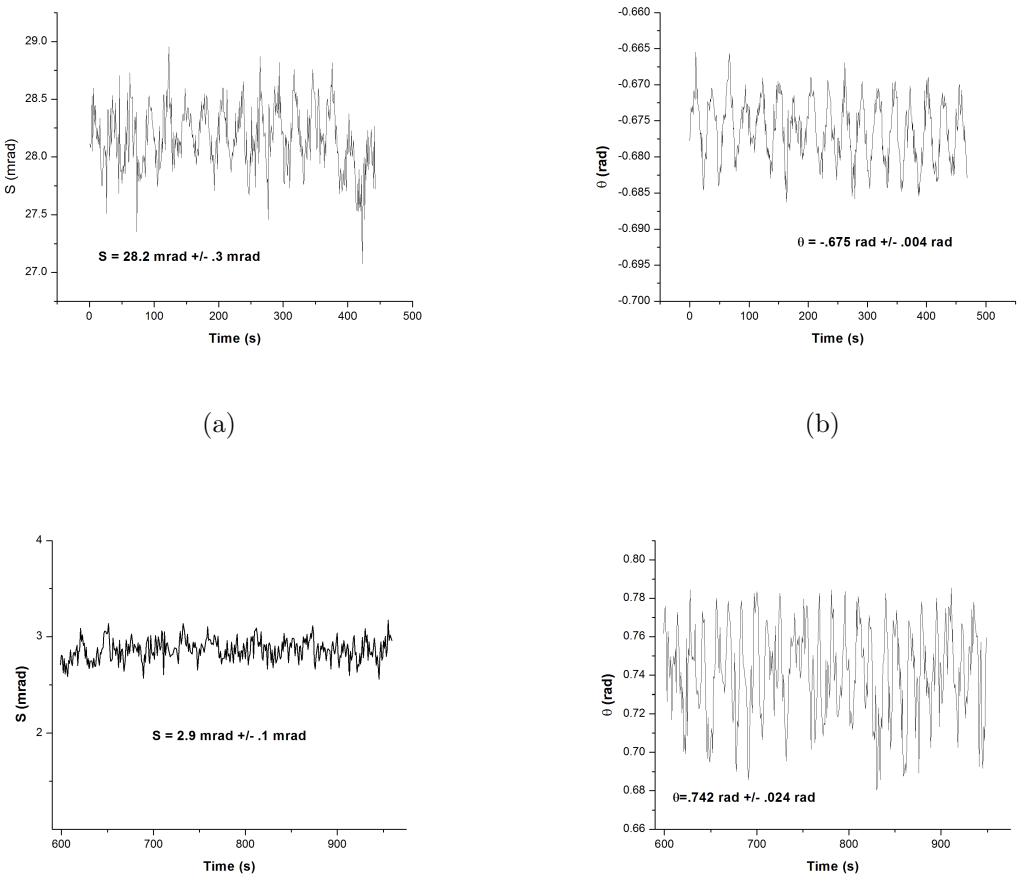

(a) (b)

(c) (d)

Figure 5.27. Graphs of S and θ as a function of time. a) Graph of S showing fluctuations centered around $\approx$ 28 mrad, with S not minimized using a universal polarizer. b) Graph of θ as a function of time, with no minimization of S. c) Graph of S showing fluctuations centered around $\approx$ 2.6 mrad, with S minimized using a universal polarizer. d) Graph of θ as a function of time, after minimizing S.

and optical orientation for the first object and Δ and γ are the respective values for the second. Following the procedures in Appendix H the expression for the signal at the first harmonic was determined,

$$\begin{aligned} R_1 = & -\tfrac{J_1(B)}{2}(\cos(2\gamma)(1+\cos(\delta))\sin(S) - \\ & 2\cos(2\gamma-4\theta)\sin(S)\sin^2\left(\tfrac{\delta}{2}\right) + 2\cos(S)\cos(2\theta)\sin(\delta)) \end{aligned} \tag{5.20}$$

and second harmonic,

$$\begin{aligned} R_2 = & \tfrac{J_2(B)}{2}(1+\cos(\delta))\sin(S)\sin(2\gamma) + 2 \\ & \sin(S)\sin^2\left(\tfrac{\delta}{2}\right)\sin(2\gamma-4\theta) + 2\cos(S)\sin(\delta)\sin(2\theta))) \end{aligned} \tag{5.21}$$

During the alignment θ and γ are made equivalent. This suffices, due to the fact that only the relative orientation can be determined. For S and δ small, equations 5.20 and 5.21 can be reduced to,

$$R_1 = -J_1(B)\cos(2\gamma)\sin(S+\delta) \tag{5.22}$$

and

$$R_2 = J_2(B)\sin(2\gamma)\sin(S+\delta) \tag{5.23}$$

If we minimize δ ($\delta \Rightarrow 0$) the equations above reduce to the original equations 5.18 and 5.19.

Clearly for small S measurements obtaining the change across the sample is theoretically acceptable. To extend this into practice, we used a birefringent crystal to

Table 5.1
Muscovite's optical data

$$Z = b;\ X \wedge c = 0^\circ - 5^\circ;\ Y \wedge a = 1^\circ - 3^\circ$$
$$n_\alpha = 1.552\text{-}1.576,\ n_\beta = 1.582\text{-}1.615,\ n_\gamma = 1.587\text{-}1.618\ [49].$$

check the validity of our proposal. A birefringent material, Muscovite was used in the study and its properties will be discussed in the next subsection.

5.7.1 Muscovite

Muscovite is a monoclinic crystal that perfectly cleaves on the {0,0,1}, which makes it very desirable as a flat clean substrate in various lab applications [47, 48]. In areas where glass was not readably available, it was commonly utilized in making windows. In these regions it was referred to as muscovy glass. What makes it interesting for our applications, is that Muscovite is a negative biaxial crystalsv. In biaxial crystal all components of the indicatrix are inequivalent to each other ($n_\alpha \neq n_\beta \neq n_\gamma$). We follow the steps found in Chapter 4.3 to calculate the effective birefringence (or the difference in indices of refraction along perpendicular axis Δn). The crystallography data in Table 5.1 was utilized to describe how the biaxial indicatrix of Muscovite aligns with its real lattice structure.

From Table 5.1 we determined that the c-axis of the crystal was oriented at an angle ranging from $0^\circ - 5^\circ$ with the n_α axis of the indicatrix, The n_γ axis of the indicatrix is aligned with the b-axis, and the n_β with the a-axis. A visual representation of the real lattice can be seen in figure 5.28(a) and its corresponding indicatrix in figure 5.28(b).

Using the small orientation angle of our indicatrix with the c-axis of the crystal, we approximated Δn to be $\approx$ (n_γ -n_β) (For a full calculation please see Appendix-

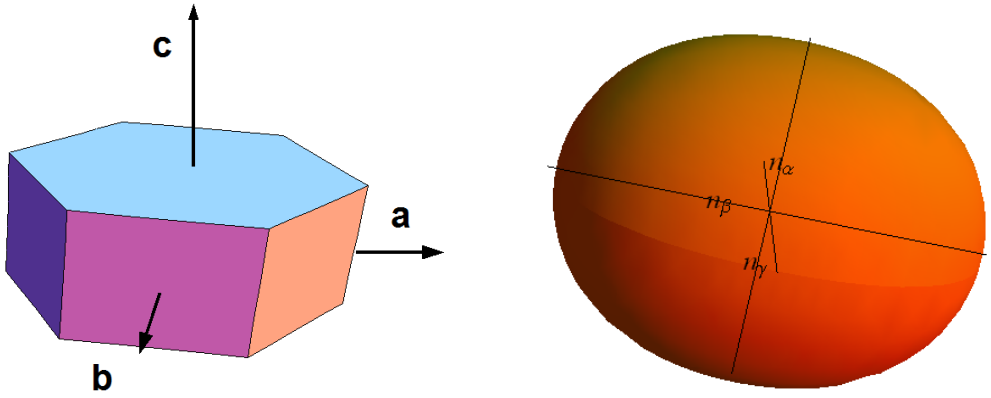

(a) (b)

Figure 5.28. a) Pictorial representation of the hexagonal Bravais lattice of muscovite. b) Indicatrix positioned corresponding to the orientation of the real crystal lattice.

J.). This yields possible values for (Δn) ranging from $0 - 0.036$ depending on the orientation of the indicatrix relative direction of electromagnetic wave propagation. Because Muscovite is a negative biaxial crystal the n_γ and n_β axes tend to be closer together [49]. As a result it is expected (Δn) to be closer to ≈ 0.003, which would yield an optical retardance of $\approx 6 \times 10^{-5}$ rad for a mono-layer of muscovite at the wavelength of 632.8 nm.

5.7.2 Experimental Evidence

To determine if aligning the system with the sample in place yielded consistent measurements of S, far-field measurements were conducted. Cleaved Muscovite or "mica" pieces were used, since they display variations in retardance as a function of thickness. Each sample was fabricated by mechanically removing layers of crystal to create uneven areas across the sample. A step was located employing a stereoscope, using light reflected from an edge. The system was first aligned in air. The

Table 5.2
PM-NSOM Far-Field Measurements of Muscovite

Measurements where the system was aligned in air	0.01225 rad
	0.01350 rad
Measurements where the system was aligned over the sample	0.01223 rad
	0.01106 rad
	0.01311 rad
	0.01252 rad

NSOM probe was positioned over one side of the edge and then across the boundary where data was taken at each point. Following these procedures, the signals were then reduced to minimize S over the sample. Data was collected at one side of the edge, followed by the opposite. Each step was first aligned in air, followed by the realignment over the sample and repeated. The results of the average values of the change in S are found in Table 5.2 for each condition.

An average retardance (S_{avg}) of ≈ 0.0129 rad was measured when the signals were minimized in air, and a S_{avg} of ≈ 0.0122 rad when the signals were minimized over the sample. Within figure 5.29, the measurements values overlap within their experimental uncertainty. Also we are able to observe an uncertainty of $\approx 4 \times 10^{-4}$ rad in the measurements where the signal was minimized over the sample. We are able to safely conclude that far-field PM-NSOM measurements can consistently determine small changes in S, even while incorporating the sample within the alignment.

To expand this work, near-field images of the same sample were taken. The same procedure used in the far-field measurements was implemented for the near-field studies. The system was aligned in air, the sample was then slid into place and measurements were taken. Following this the system was aligned with the NSOM probe over the sample and the same procedure was followed. Figures 5.30 and 5.31

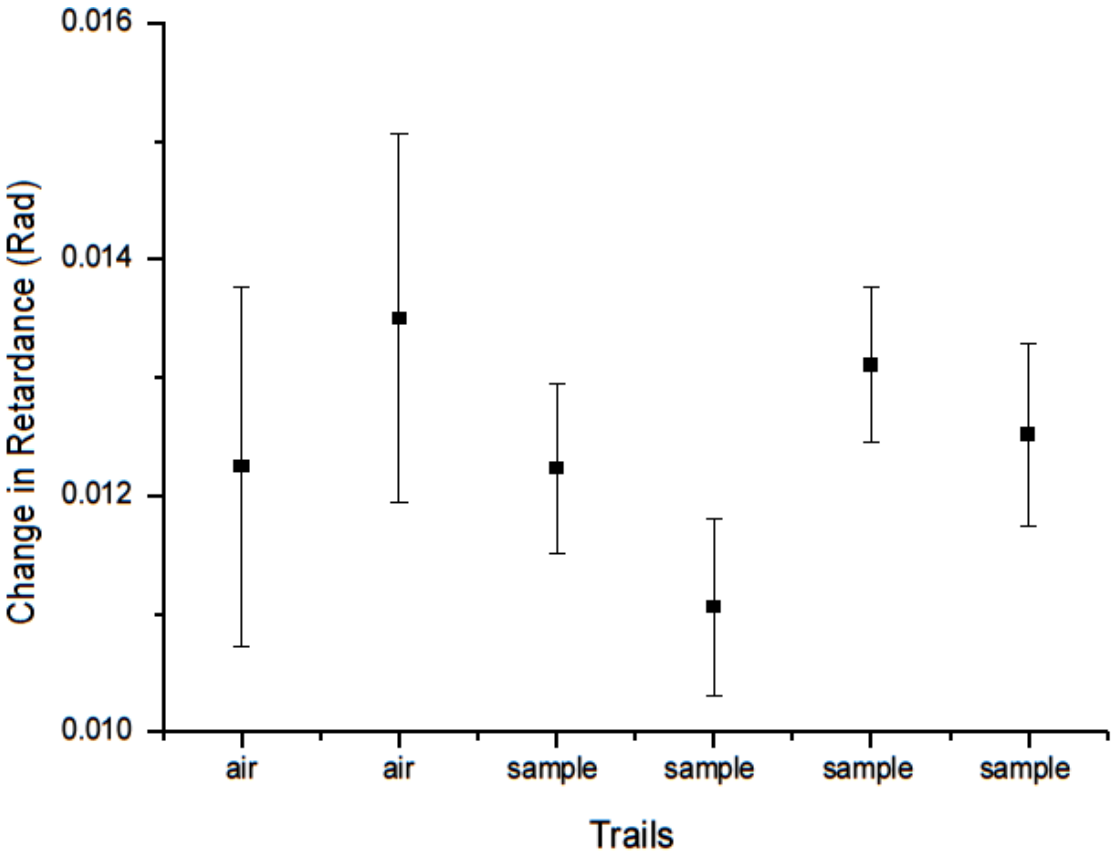

Figure 5.29. Graph of the far-field data from Table 5.2. The measurements where the system was aligned in air are listed as air. Where the system was aligned over the sample before the measurement are labeled sample. S vales are given for each measurement with corresponding error bars attached.

were taken from PM-NSOM scans of the same area of muscovite, where the signal was zeroed in air, followed by zeroing R_1 and R_2 over the sample, repeating the process.

To determine the change in S for each measurement, line cuts for each set of images were taken, seen in figure 5.33(c). The near-field measurements where R_1 and R_2 were not minimized over the sample, a $\Delta S_{avg} = 7.1\,\text{mrad}$. The same sample was measured after the sample was aligned within the system, where R_1 and R_2 were both zeroed, a value of $\Delta S_{avg} = 6.8\,\text{mrad}$ was obtained. The two measurements yielded $\approx 0.3\,\text{mrad}$ difference. A noticeable difference between the two measurements is the resolution increase on θ, which can be seen in figure 5.31(b). Numerous defects within the crystal structure are clearly viewed when measuring from a zero signal versus one with a S background. If the system is not aligned over the sample, we appear to gain a factor of ≈ 2 in the fluctuation on S. The average deviations on S taken from the image in figure 5.31, in the region with the fewest defects, is ≈ 0.2 mrad , and from the same area in figure 5.30 is ≈ 0.4 mrad.

Beyond the line cuts taken from figure 5.31, the distribution of S across the sample was analyzed. Figure 5.34 displays the distribution of S of both images, where blue represents the distribution of figure 5.30(a) and red of figure 5.31(a) (which are slightly offset downward for viewing purposes). The histograms show very good overlap from both sets of data. If we decide to fit a Gaussian peak to each distribution and view the overlap, as seen in figure 5.35, the two distributions are almost identical. This should be the final verification that the theoretical assumptions are correct. With such findings, alignment of the system over the sample can occur with precise values for changes in S obtained.

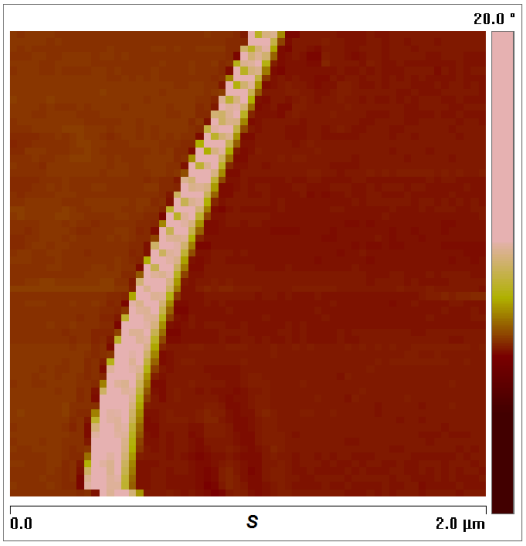

(a)

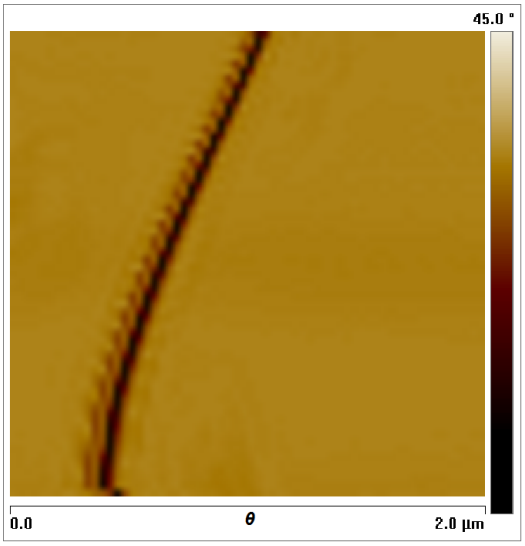

(b)

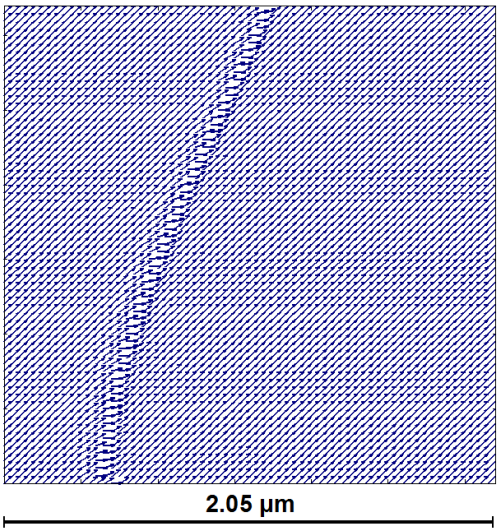

(c)

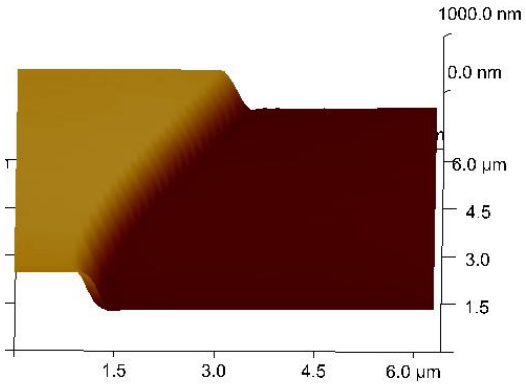

(d)

Figure 5.30. a) Image of S of a section of muscovite where the system was aligned in air. b) Image of θ of the same section of muscovite. c) Vector plot using the values of θ. d) Topography of the mica step showing a change in height of ≈ 673 nm.

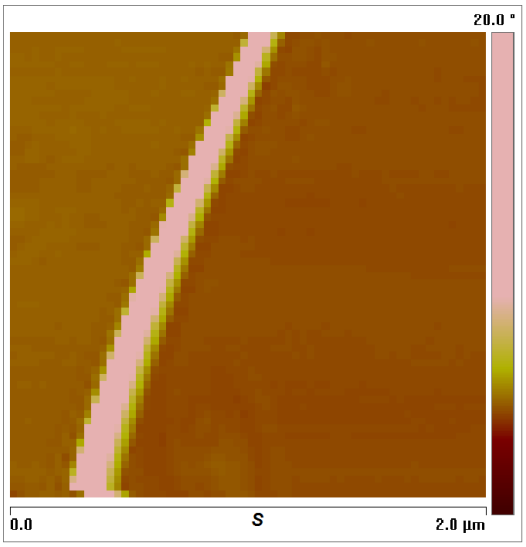

(a)

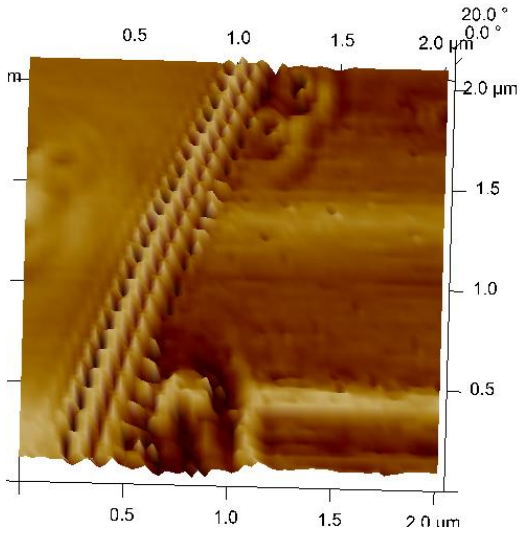

(b)

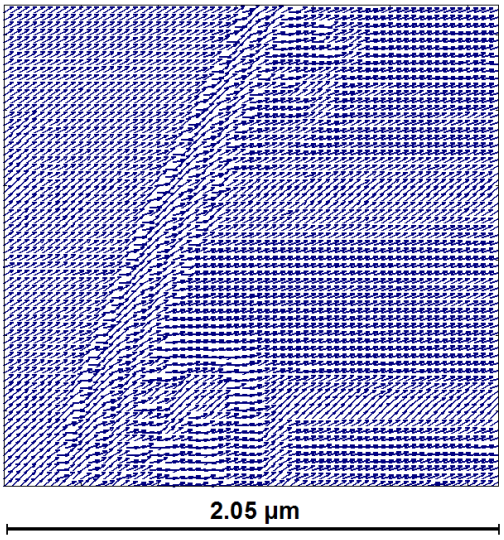

(c)

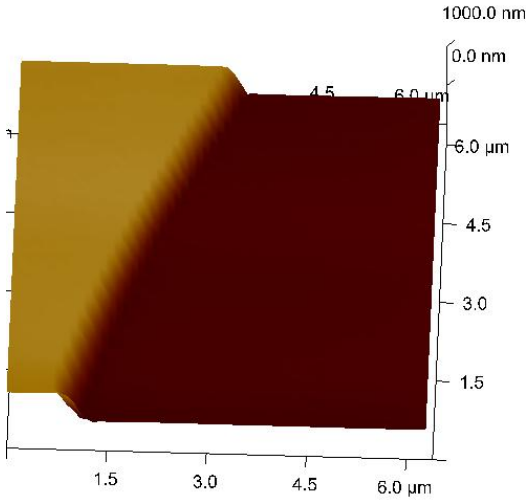

(d)

Figure 5.31. a) Image of S of a section of Muscovite where the system was aligned over the sample. b) Image of θ of the same section of muscovite. c) Vector plot using the values of θ. d) Topography of the mica step showing a change in height of ≈ 673 nm.

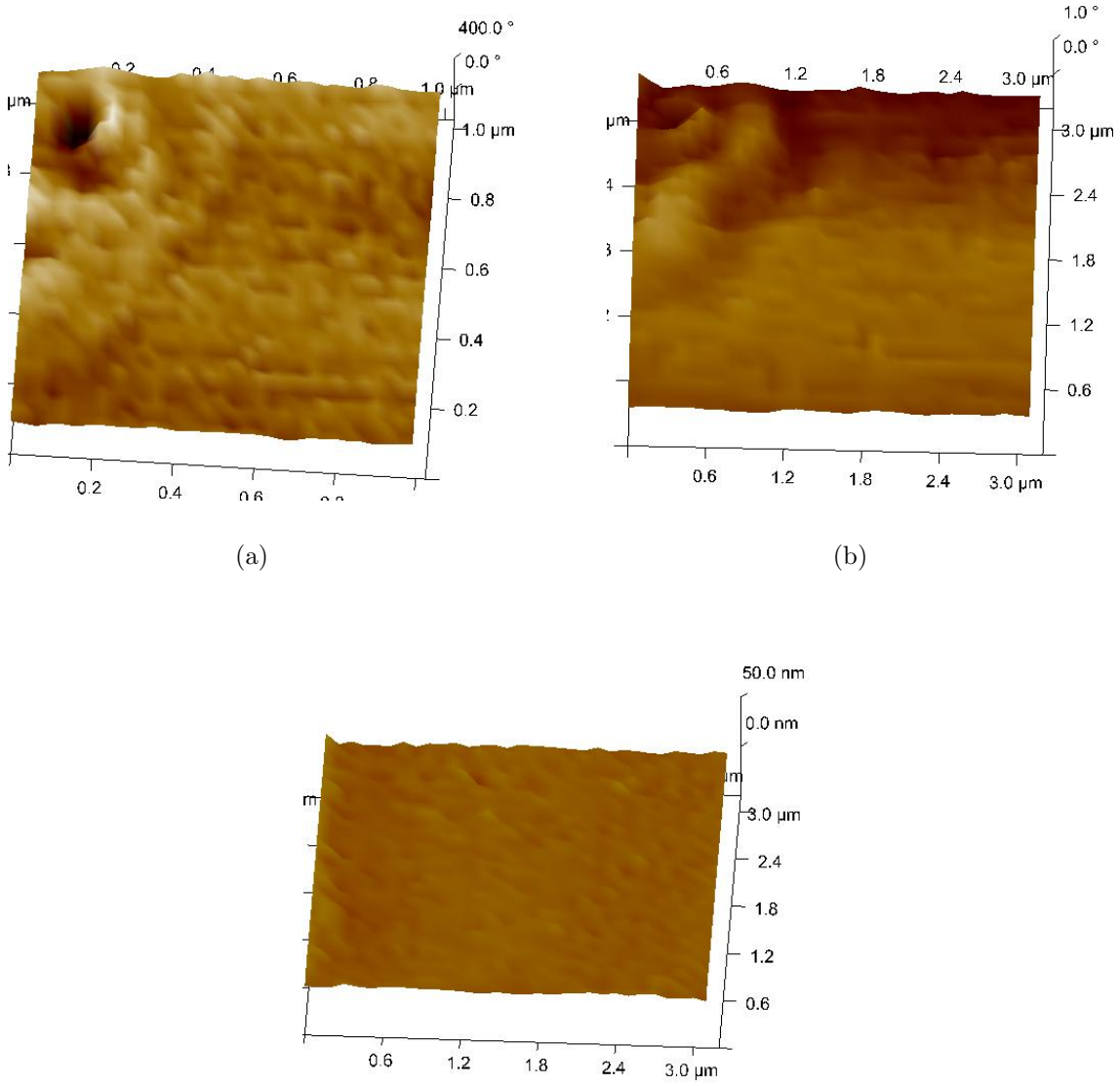

(a) (b)

(c)

Figure 5.32. a) Zoomed image of S of the same piece of Muscovite, showing structural defects in the crystal that were resolved on the order of $\approx$ 100 nm. b) Image of θ. c) Topography of the image showing that it was an actual structural defect of the crystal and not topographical variation.

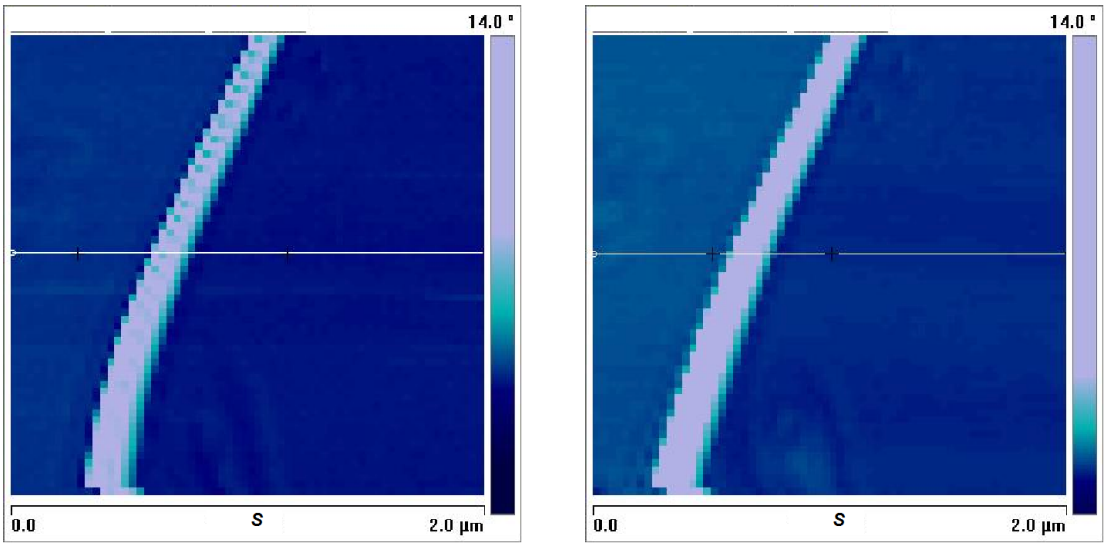

(a) (b)

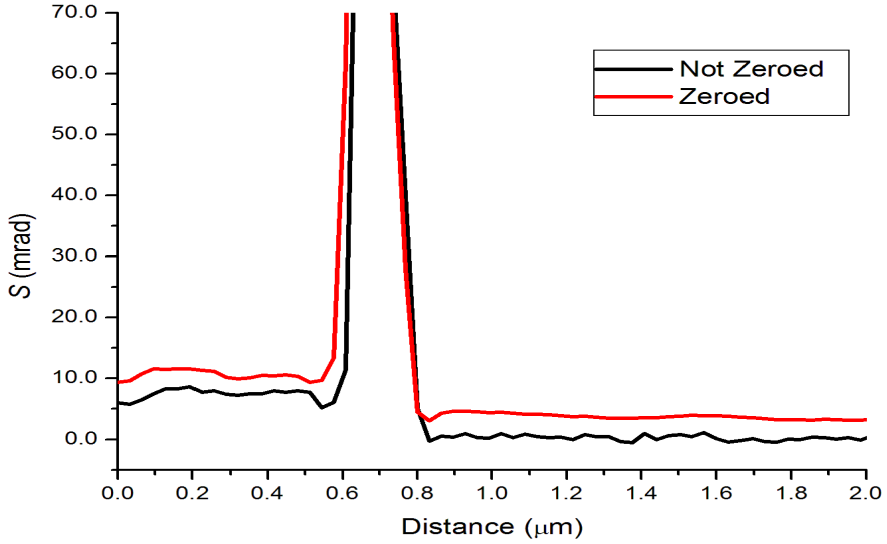

(c)

Figure 5.33. a) Image S from figure 5.30(a) with the line cut section marked with a line. b) Image S from figure 5.31(a) with the line cut section marked with a white line. c) The line cut data from the figures in a) and b) showing nearly identical results. (The data was offset for visualization purposes.)

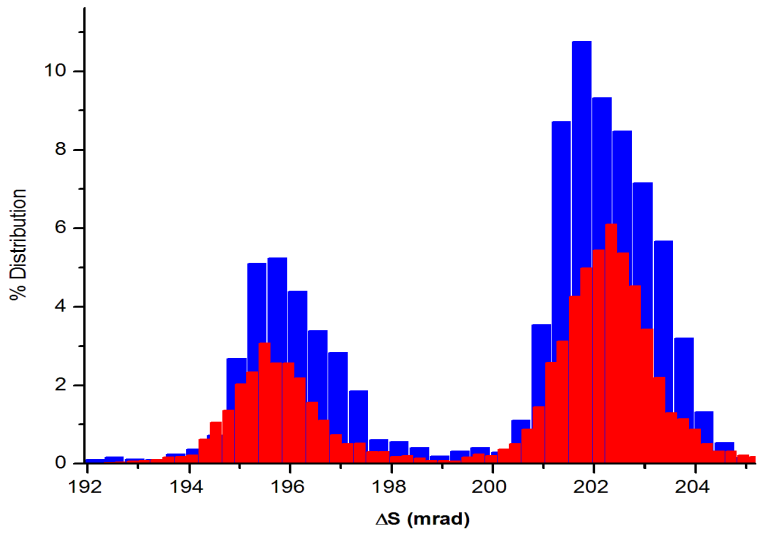

(a)

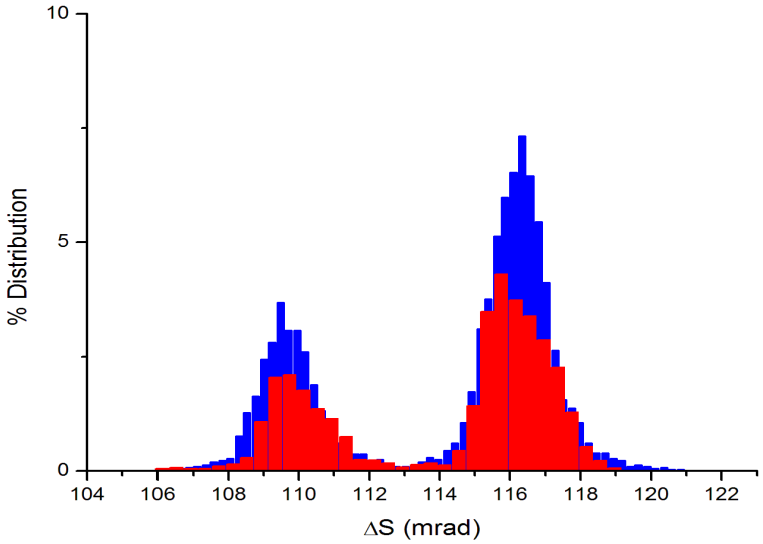

(b)

Figure 5.34. Histograms of the distribution of S in the images found in figures 5.30(a) (Blue) and 5.31(a) (Red). (The data was slightly offset downward to display both plots effectively.) a) The distribution of S over the entire image. b) The distribution of S over an area across the center section of each image.

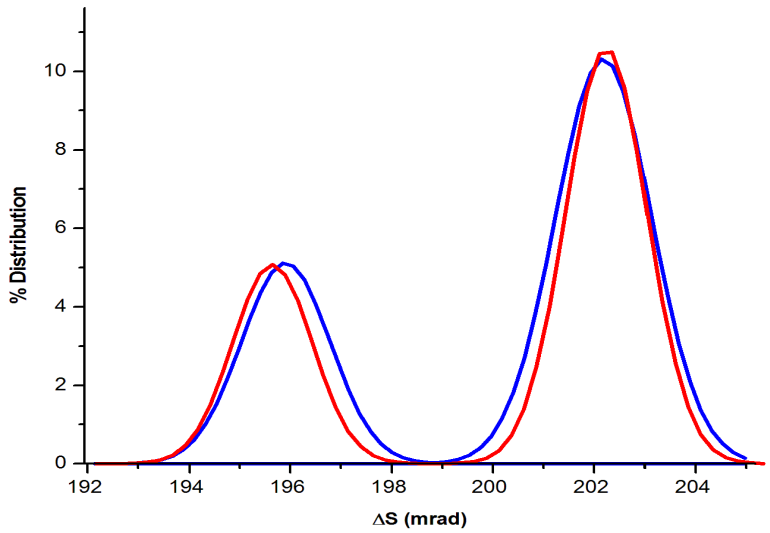

(a)

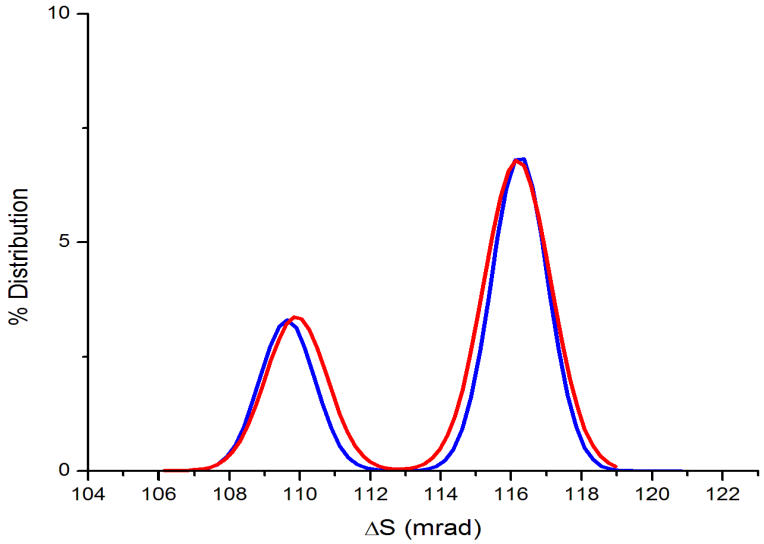

(b)

Figure 5.35. Plots of the Gaussian peak functions fitted to the distribution of S in the images found in figures 5.30(a) (Blue) and 5.31(a) (Red). The data was scaled to display near perfect overlap. a) The Gaussian fits for the distribution peaks of S over the entire image. b) The Gaussian fits for the distribution peaks of S over a area across the center section of each image.

5.8 Information Extraction of Muscovite Samples

Multiple measurements of different areas of the sample were performed, where we were able to extract different values of S at different heights (see figure 5.36). From each measurement a value for the birefringence Δn was extracted, to yield an average value of $\approx 1 \times 10^{-3}$. Through this method the function of S includes any background retardance that come from sample defects or experimental error. To eliminate any background terms that exist on all measurements we plotted $\frac{\Delta S \lambda}{2\pi}$ versus the change in height (Δh) (see figure 5.37). Figure 5.37(a) depicts good agreement to what was obtained before and falls within what was expected, which can range from 0 to *approx* 3×10^{-3} (see Appendix-J).

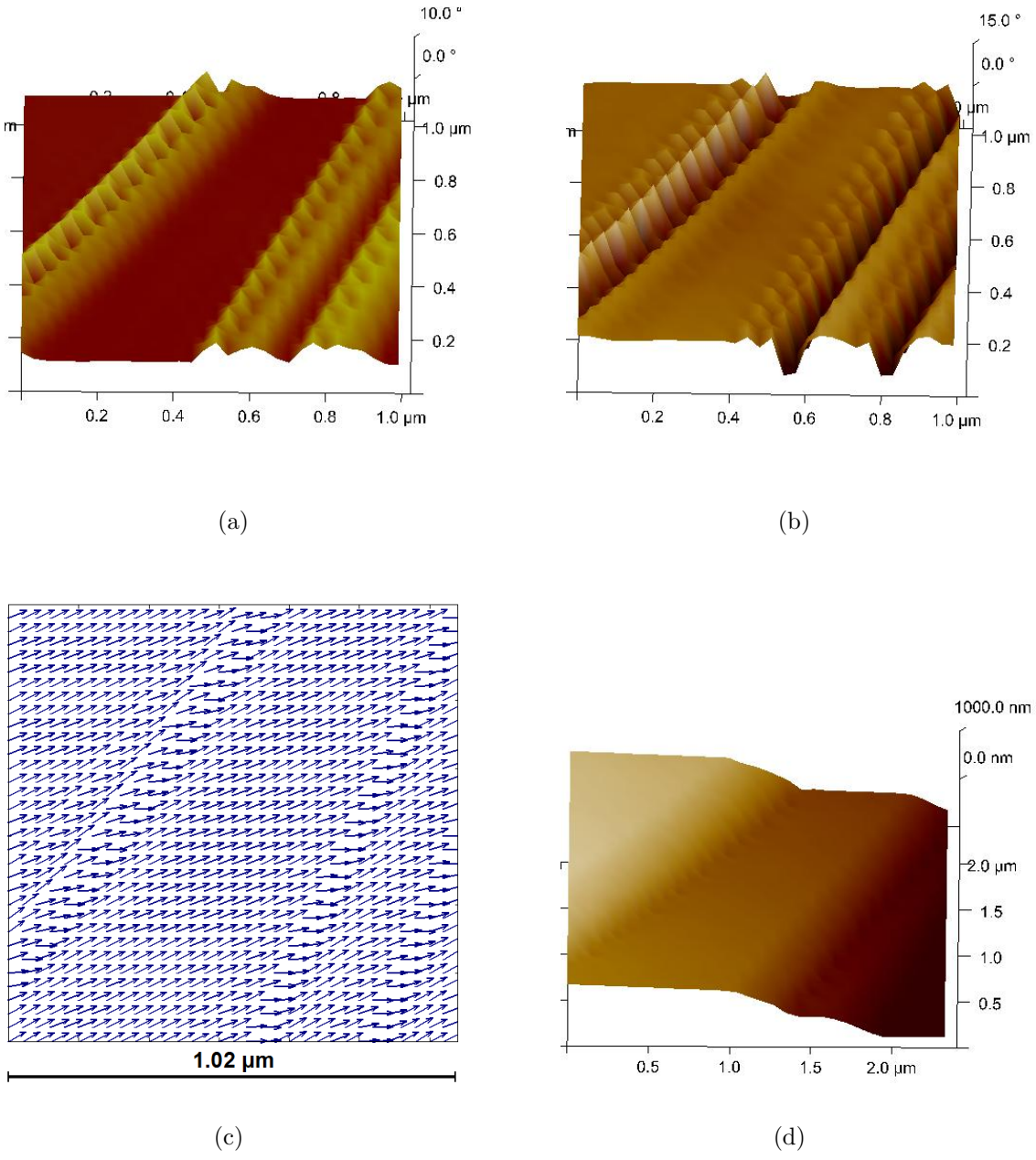

(a) (b)

(c) (d)

Figure 5.36. Measurement on mica with multiple layers exposed. a) Image of S. b) Image of θ of the same area of muscovite. c) Vector plot using the values of θ, showing how the crystal layers are oriented in the same direction. d) Topography showing a multitude of steps.

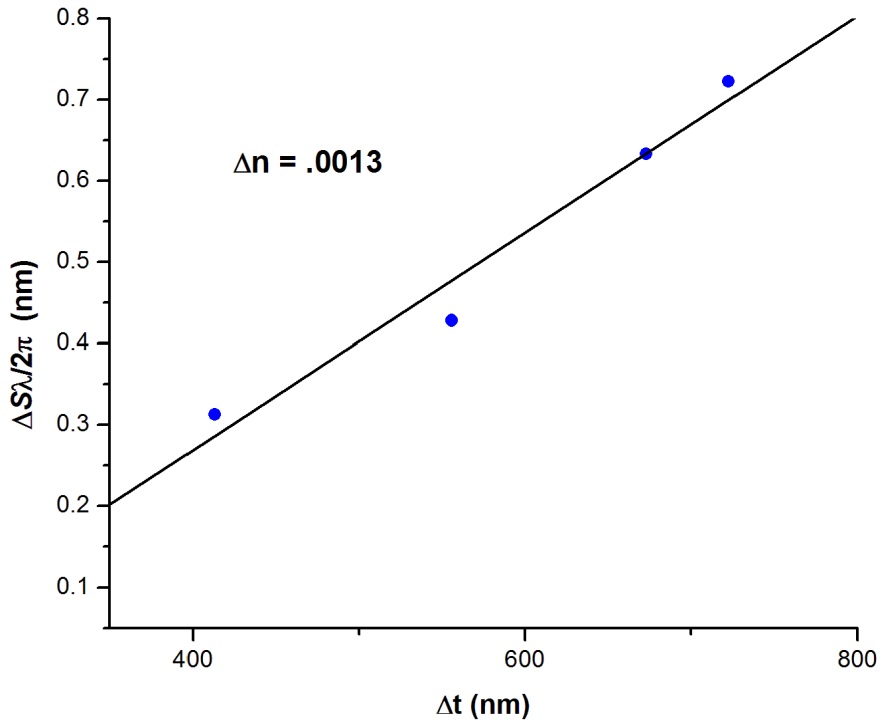

Figure 5.37. Plot of $\frac{\Delta S\lambda}{2\pi}$ versus the Δt, to yield values of Δn that are equivalent to the slope of the fitted line, yielding $\Delta n \approx 0.0013$.

6. LIPID SAMPLE PREPARATION

This chapter will outline the procedures used in creating planar supported lipid bilayers on glass substrates. The method used for creating hydrophilic glass substrates will be presented. Vesicle fusion and Langmuir trough techniques are outlined for creating supported planar bilayers.

6.1 Glass Preparation

Preparing the glass included the removal of any organic material from the surface as well as making the surface as hydrophilic as possible. To do this the glass surface was adjusted to contain silanol groups ($Si - OH$). This could be done by either thermally growing oxides on the surface [50], or by wet-chemical means. [51]

The method, of glass preparation within this study consisted of sonicating the glass cover slips in detergent and deionized (DI) water separately for $\sim 15 - 20$ minutes each. This was followed with a wet-chemical oxidation process using a piranha solution ($H_2SO_4 : H_2O_2 = 3 : 1$) for about 5 mins. The cover slips were then rinsed and sonicated for ~ 30 mins in DI water and finally thermally dried.

6.2 Planar Bilayer Formation-Through Vesicle Fusion

Supported bilayers were formed on hydrophilic glass substrates by vesicle fusion [52, 53]. 1.0 - 0.5 mg/ml of 1,2-dipalmitoyl-sn-glycero-3-phosphocholine (DPPC) in 100mM NaCl : 30mM NaH_2PO_4 was sonicated at $\approx 60°C$ until clear to create small unilamellar vesicles (SUVs). 100 μL of solution was placed on the glass substrates

and left to equilibrate at room temperature for $\approx$ 30 mins. The samples were then baked at 60°C for 45 mins to 1 hr. They were then rinsed, and either rehydrated and characterized with the AFM, or kept at 100% relative humidity in a chamber until imaged using the PM-NSOM system.

Vesicle fusion is a process where unilamellar vesicles are taken and placed over a substrate, where they are left to fall upon the surface. The temperature is then raised so the lipids are well into the L_α state (for DPPC 60°C is utilized because it is $\approx 15^\circ$ over the L_α transition temperature). This increases the diffusion coefficient so that the membrane flows across the surface. After a given time the substrate is fully covered by a planar membrane.

6.2.1 Langmuir Trough

Samples that were prepared with a Langmuir trough used 1 mg/ml of DPPC dissolved in chloroform placed in the trough until $\approx$ 30 mN/m was achieved, creating a lipid monolayer on the surface of the water in the trough. A glass coverslip, previously submerged in the trough, is slowly brought up through the monolayer while maintaining the lateral surface pressure to create an even transfer. This creates a monolayer of DPPC on the cover slip. Next the trough was equilibrated, followed by holding the cover slip over the trough with the monolayer facing the surface. The cover slip was then pressed quickly down onto the surface of the trough, in an attempt to combine the two monolayers together. This creates a continuous membrane very similar to what was obtained with vesicle fusion. The most significant difference between the two methods is that the bilayer is under constant lateral pressure when prepared on the trough.

7. SAMPLE CHARACTERIZATION

To characterize the supported membranes on glass substrates AFM was used to obtain high lateral (∼10 nm) and height (∼0.5 nm) topographical information. The methods primarily used were fluid tapping and contact modes with probes having spring constants (k) ranging from ≈ 0.06 to 0.56 N/m, where the softer probes were primarily incorporated in contact mode and the stiffer ones were used in tapping mode. Before characterizing the final sample, characterization of the substrate was necessary. We desired a very smooth, clean, hydrophilic surface to support our lipid bilayer samples. To remove all surfactants and prepare a hydrophilic surface we placed the glass in a piranha solution, (discussed in Chapter 6.1). Because the piranha solution oxidized the silica surface, layers of material were removed in the process. Hence, a topographical characterization of the glass after the oxidation is paramount.

First AFM measurements were conducted using Fisherbrand plain microscope slides cleaned with detergent and DI water (see figure 7.1). From the topographical data analysis the substrate's characteristic groves and roughness of ≈ 14 nm rms were obtained. Slides were treated with concentrations of piranha solution ranging from 3:1 to 4:1 for times raging from 2 to 6 minutes. Glass slides treated with 3:1 concentration of piranha solution for ≈ 2 mins, displayed the least surface modification of the trials. From the images it was apparent that the roughness decreases substantially, to ≈ 0.8 nm rms. During the process we removed the groves and create a very bumpy substrate, as seen in figure 7.2. Along with the previous features mentioned, holes as deep as ∼50 nm were observed frequently across the sample.

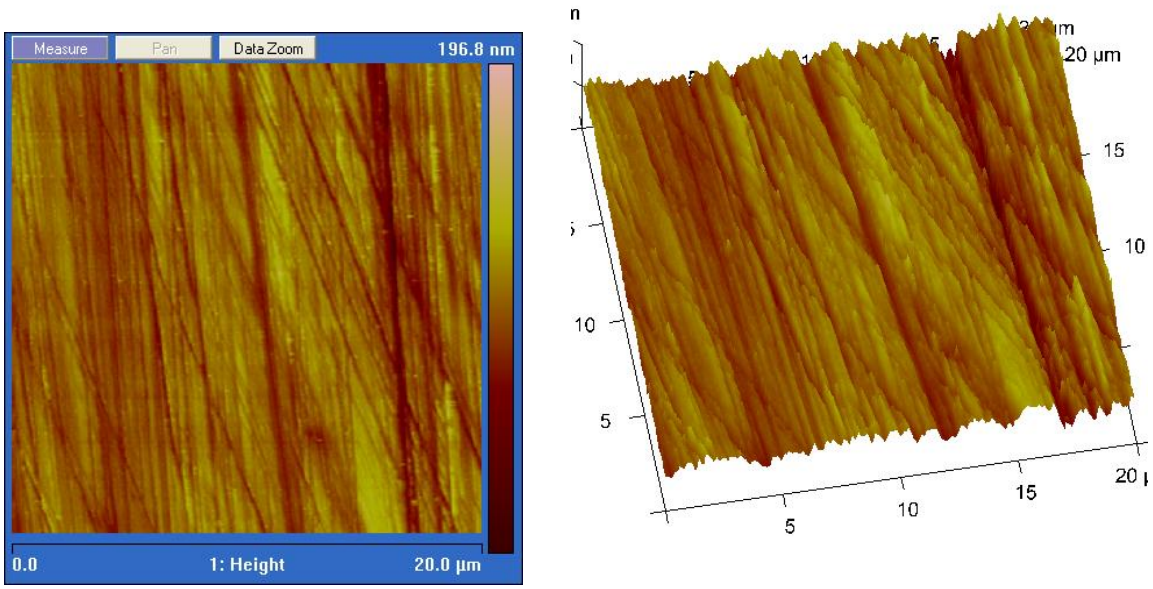

(a) (b)

Figure 7.1. AFM image of Fisherbrand plain microscope slides cleaned with detergent and DI water. a) Topographical contrast image of a Fisherbrand Plain microscope slide. b) Topographical map of the surface of a Fisherbrand Plain microscope slide.

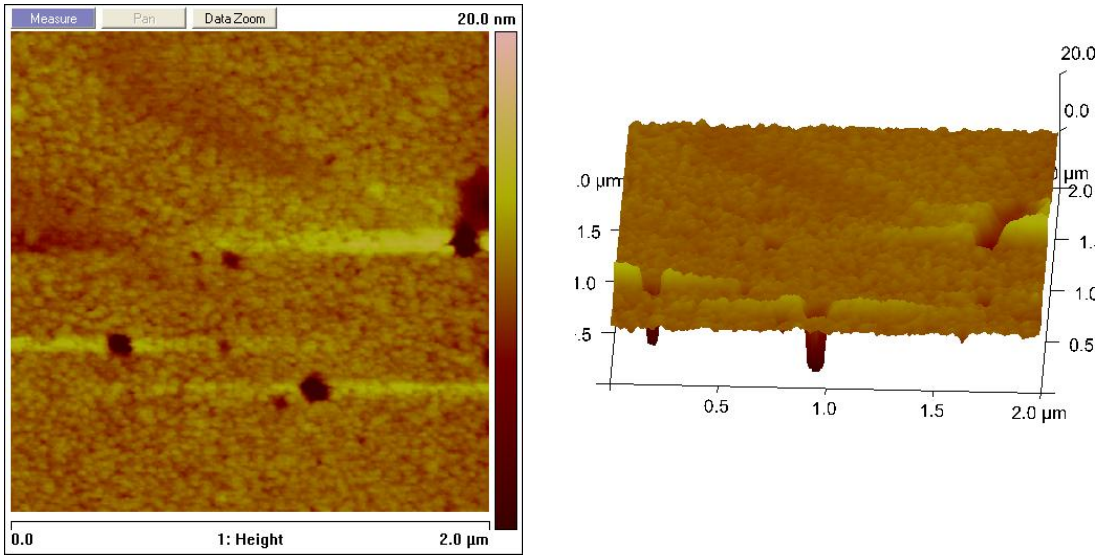

(a) (b)

Figure 7.2. AFM images of glass slides treated 2 minutes with piranha solution 3:1. a) Topographical contrast image of a glass slide treated 2 minutes with piranha solution. b) Topographical map of the surface.

The procedure discussed in Chapter 6 was followed which includes placing DPPC on the glass slides similar to those seen in figure 7.2. The observed surface roughness increased from 0.8 nm without the lipid to about 1.3 nm with the lipid material. It was evident with figure 7.3 that the membrane did not flatten over the substrate, but rather bent slightly to follow the contour of the surface below it. This corresponds with what has been observed with lipid bilayers supported on silica xerogel substrates [54–56]. Here we observed that in order to create a sample where the lipid bilayer was planar and continuous across the surface of the substrate, a better surface was required.

In an attempt to find a smoother substrate, we looked at using a type of glass that may not be as rough prior to the piranha treatment. Fisherbrand precleaned coverslips were then chosen to be tested (see figure 7.4) which have an initial roughness of $\approx$ 0.5 nm rms. They were prepared, as discussed in Chapter 6.1, using concentrations of 3:1 and 4:1. AFM measurements were made, revealing that the observed surface roughness increases $\sim$ .5 nm rms, seen in figure 7.5. This corresponds well with what has been reported in other measurements [**?**]. The (3:1) concentration consistently yielded a smoother surface, as compared to the (4:1) concentration of piranha solution. Also, beyond the 4-5 minutes used for the (3:1) piranha treatment , the cover slips became brittle and were not suitable for use.

Having an suitable hydrophilic substrate, the procedure in Chapter 6 was followed, using the (3:1) piranha treated glass. The result was a single lipid bilayer covered substrate, as seen in figure 7.6. While comparing figures 7.5 and 7.6, it was difficult to determine if the substrate was lipid or glass.

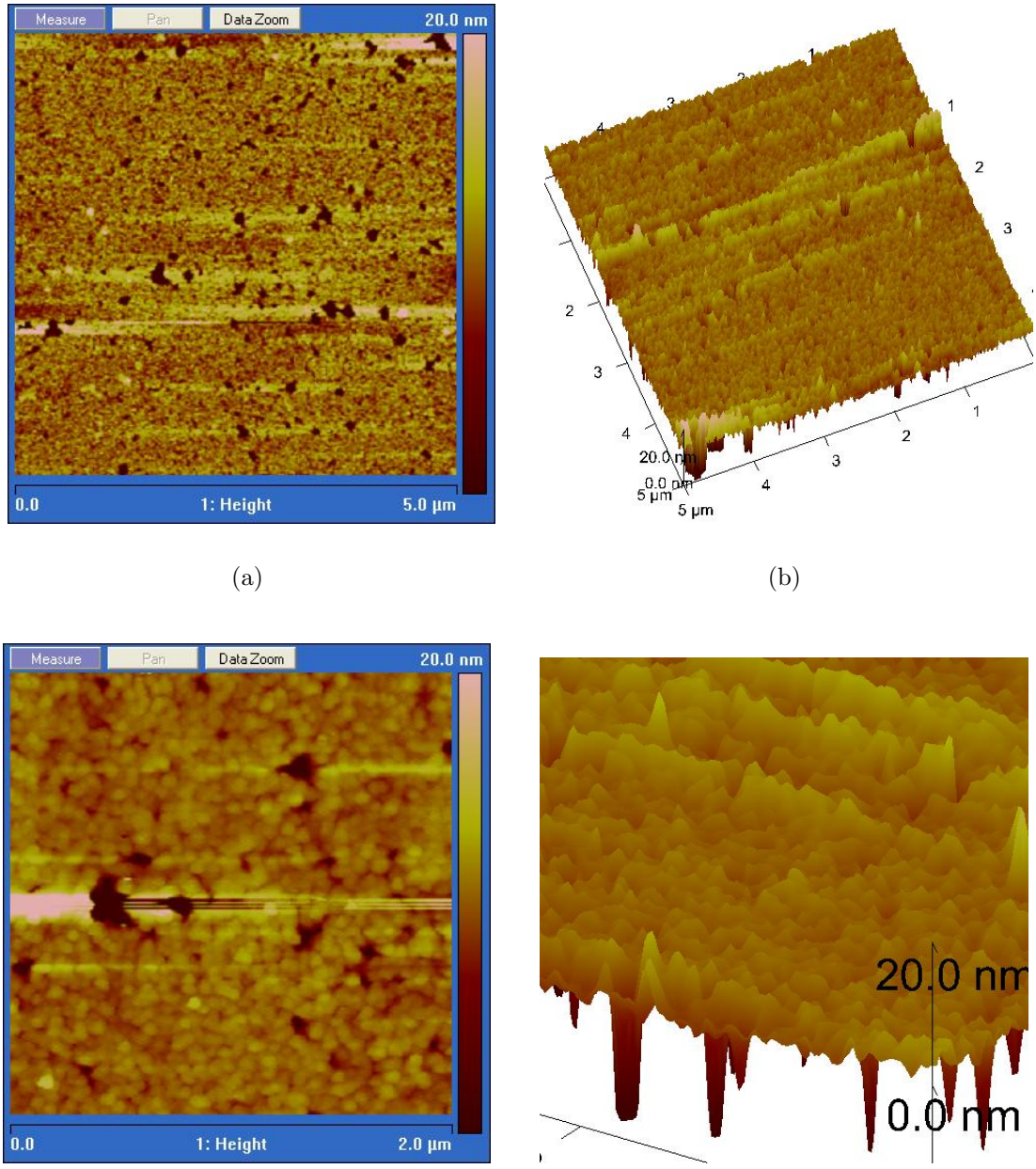

(a) (b)

(c) (d)

Figure 7.3. DPPC bilayer supported on Fisherbrand Plain microscope slides treated with piranha solution (3:1) ∼2 mins. a) 5 μm × 5 μm topographical contrast image of the sample. b) 5 μm × 5 μm topographical surface plot of the sample. c) 2 μm × 2 μm topographical contrast image. d) Zoomed in section of a 2 μm × 2 μm topographical surface plot.

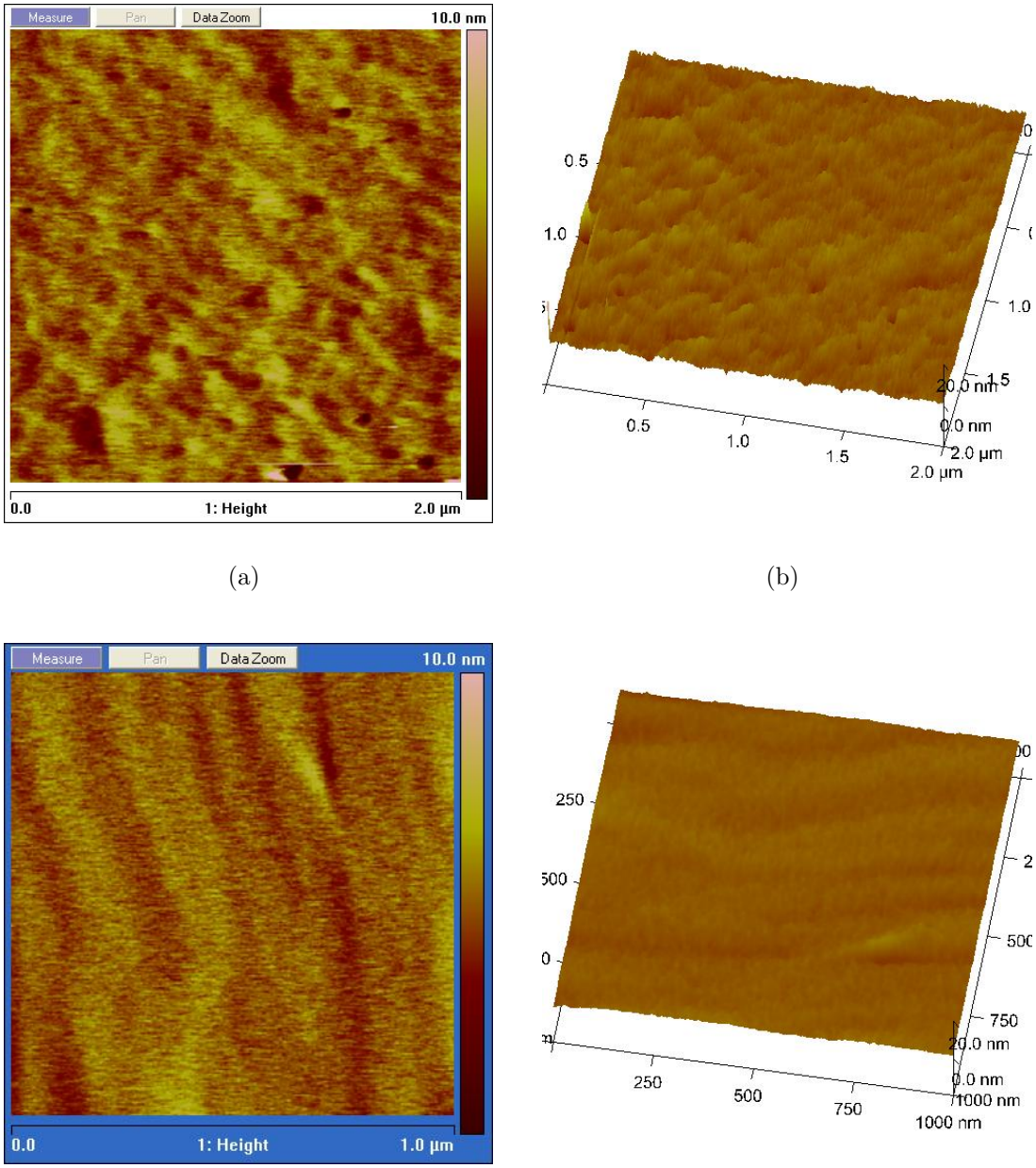

(a) (b)

(c) (d)

Figure 7.4. AFM images of Fisherbrand Precleaned coverslips. a) 2 μm $\times$ 2 μm topographical contrast image. b) 2 μm $\times$ 2 μm topographical surface plot. c) 1 μm $\times$ 1 μm topographical contrast image. d) 1 μm $\times$ 1 μm topographical surface plot.

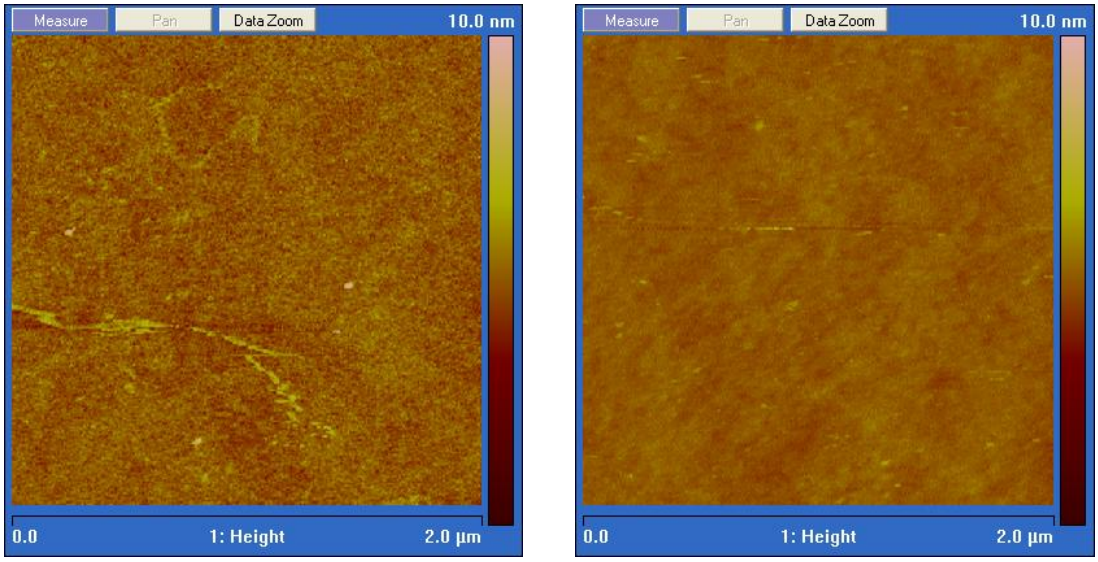

(a) (b)

Figure 7.5. AFM images of cover slips treated with piranha solution with a) concentrations 3:1 b) concentrations 4:1.

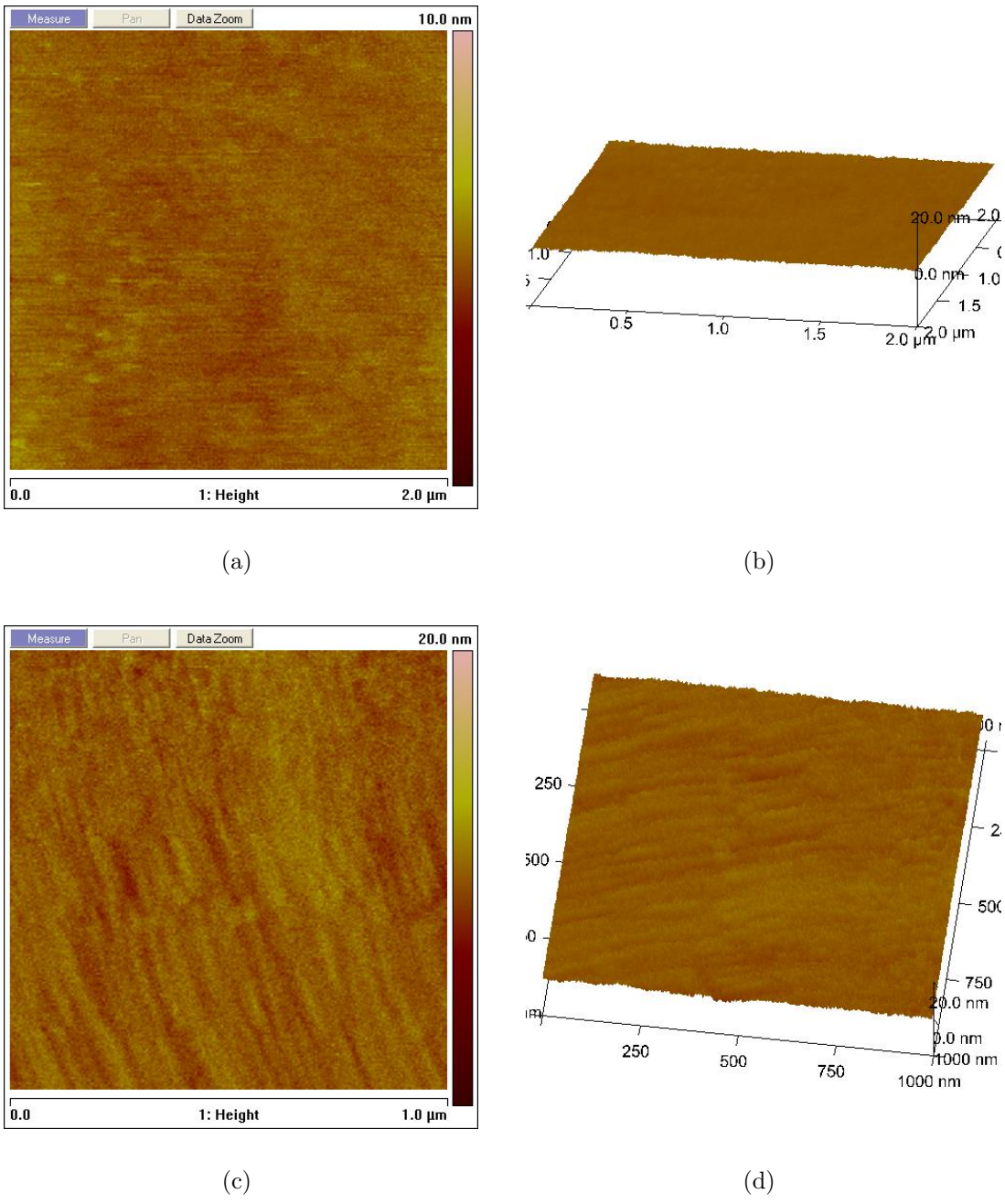

(a) (b)

(c) (d)

Figure 7.6. AFM images of DPPC supported on piranha treated Fisherbrand Precleaned coverslips. With the given parameters a supported planar continuous membrane on glass is obtained. a) 2 μm $\times$ 2 μm topographical contrast image. b) 2 μm $\times$ 2 μm topographical surface plot. c) 1 μm $\times$ 1 μm topographical contrast image. d) 1 μm $\times$ 1 μm topographical surface plot.

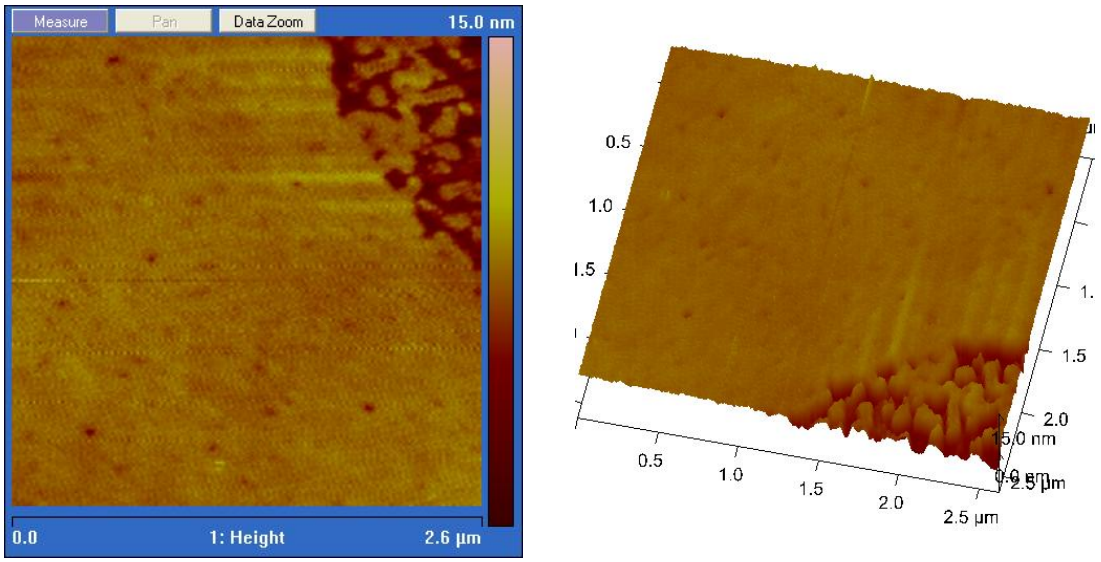

(a) (b)

Figure 7.7. AFM images of a hole in a DPPC bilayer supported on glass a) 2.6 μm $\times$ 2.6 μm topographical contrast image b) 2.6 μm $\times$ 2.6 μm topographical surface plot.

7.1 Lipid or Substrate?

The first and most reliable method of determining if lipids were present on the sample, was to find the edge of the coverage area and find a hole. By looking at a hole in the sample, as seen in figure 7.7, the height of the bilayer can be determined by the AFM. Figure 7.8 displays a line cut of data that spans from the sample to over the hole, where the height was determined to be $\approx$ 5.3 nm. This height agreed with previous reported values of supported bilayers of DPPC [14]. Full membrane coverage across the substrate created difficulty locating holes.

To circumvent this dilemma a quick qualitative measurement was introduced to reveal the substrates properties. As explained in Section 5.6.1, performing a force measurement and plotting the cantilever's interaction with the surface yielded infor-

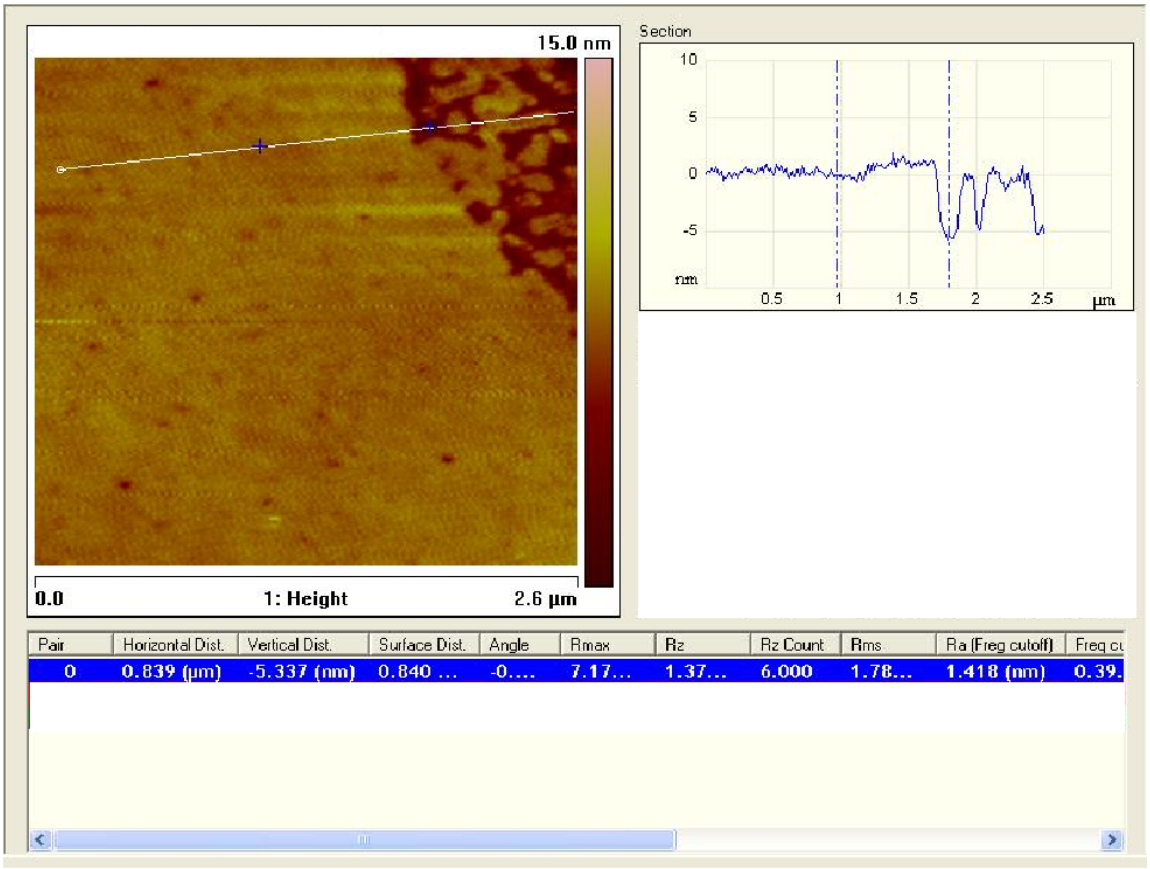

Figure 7.8. Line cut of a 2.6 μm $\times$ 2.6 μm topographical contrast image of a hole in a DPPC bilayer supported on glass showing a height difference of $\approx$ 5.3 nm from the substrate to the top of the bilayer.

mation about the adhesion and "softness" of the surface. Looking at the force curve of glass in figure 7.9(a), we were able to see that as the probe makes contact with the glass it experienced a very small attractive force. When the cantilever was retracted, the adhesion forces were negligible. To inspect a fully covered surface the same measurement was performed to qualitatively determine that the material was more malleable than a hard substrate like glass. Also we saw that the sample interacted with the probe for a longer separation of the measurement, yielding a larger adhesion force as seen in figure 7.9(b). To compare the force curve of a lipid substrate to that of glass, every measurement was not necessary, unless the exact adhesion forces were to be desired. For qualitative purposes, simple observations of the curve shape was sufficient, assuming that the probe type had not changed between measurements. This method proved to be a quick qualitative means of determining if the surface was lipid covered or glass.

The final method proposed was to make a hole in the membrane with the cantilever and determine the height of the lipid in question. To make a hole a small region (≈ 1 μm $\times$ 1 μm) was selected, utilizing contact mode to scan the area quickly with a very low set point (i.e., the probe deflection from the sample was set higher resulting in a larger force against the substrate). The idea was that the AFM probe was pushed into the sample, until the probe met the substrate. The hole was opened by quickly scanning back and forth. The probe was then separated from the substrate and a softer scan of a larger area occurred in an attempt to yield the hole. An example can be seen in figures 7.10 and 7.11. The line cut was then analysed to determine the depth. The method of making the hole within the membrane was time consuming and dependent on how the membrane re-formed based on experimental conditions. In consequence it was not used often.

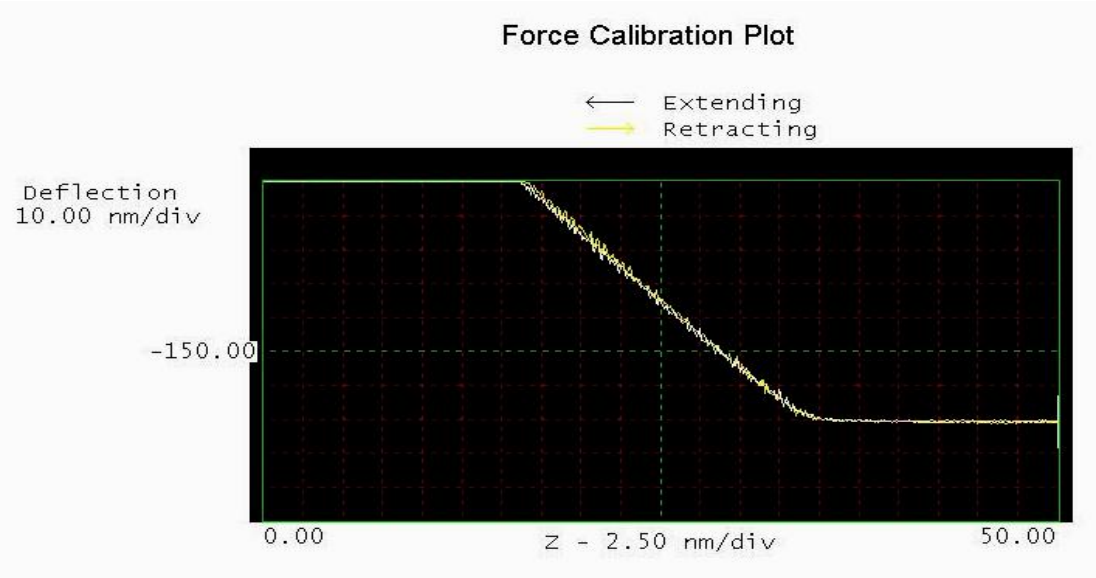

(a)

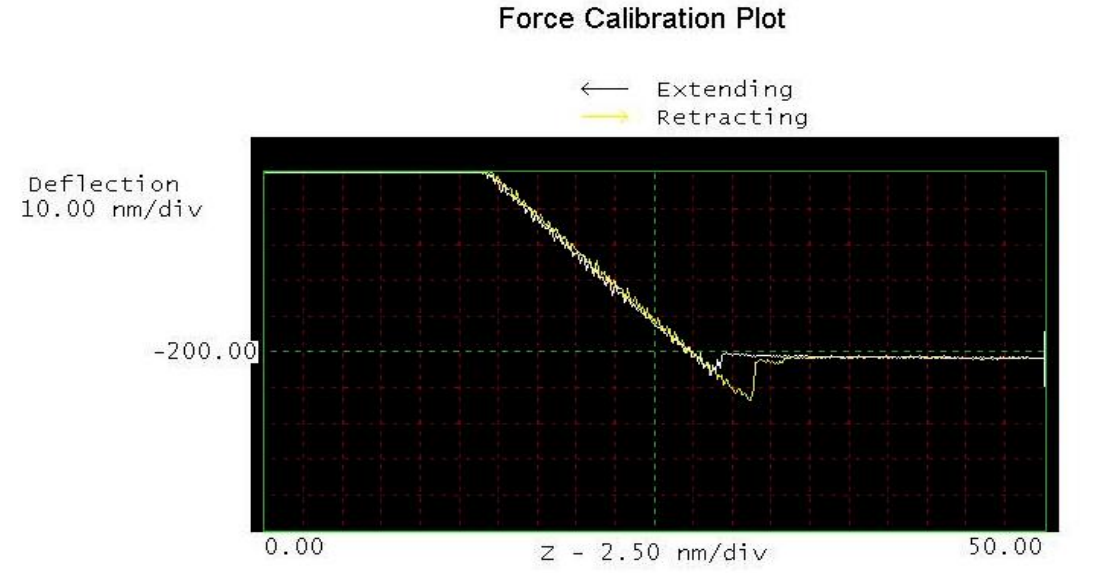

(b)

Figure 7.9. a)Force curve illustrating a cantilever's (k $\approx$ .27 N/m) deflection as it comes into contact with the glass surface. When the probe was retracted, the defection was minimal. b) Force curve of a cantilever's deflection as it made contact with the surface of the supported DPPC bilayer. When the probe was retracted, there was a noticeable adhesion force on the probe.

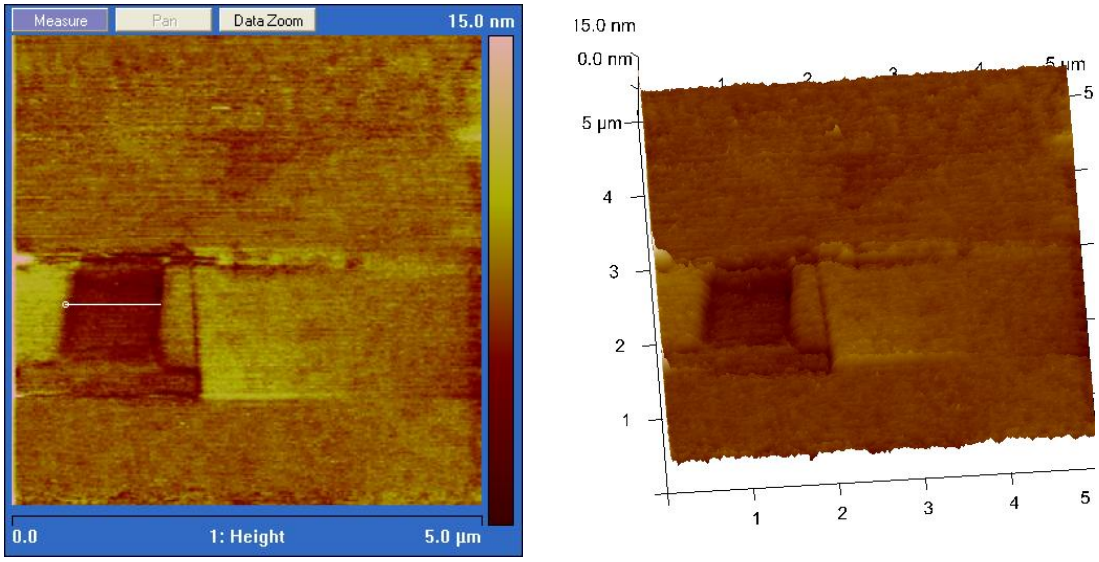

(a) (b)

Figure 7.10. AFM images of a 1 μm $\times$ 1 μm hole in a DLPC bilayer supported on glass a) 5 μm $\times$ 5 μm topographical contrast image b) 5 μm $\times$ 5 μm topographical surface plot.

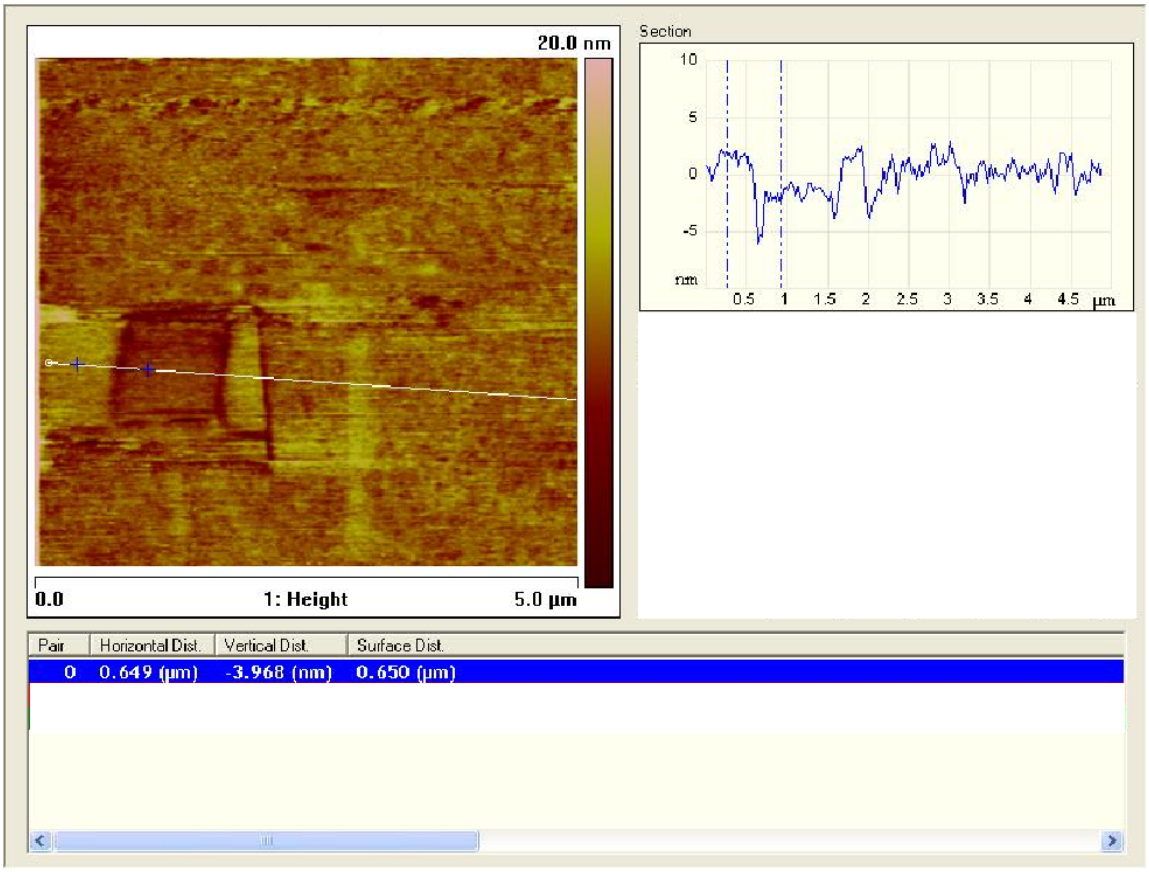

Figure 7.11. Data plot of a section of the AFM image found in figure 7.10. The change in height is ≈ 4 nm, which fall in the range of the accepted value with an error of $\pm$ 0.5 nm [57].

8. NEAR-FIELD POLARIZATION MODULATION STUDIES OF SUPPORTED LIPID BILAYERS

PM-NSOM measurements presented in this section were conducted on supported lipid bilayers, created by vesicle fusion using the method described in Chapter 6. The samples were placed in a humid chamber for at least one day to ensure the water layer on top of the membrane was thinner than 20 nm, suitable to collect NSOM data. All were conducted at 100% relative humidity, to ensure the lipid bilayer remained fully hydrated and presented the characteristic acyl chain tilt of $\approx 32^\circ$ in the $L_{\beta'}$ phase. The system was aligned using the method described in Section 5.3. The measurements were taken at room temperature, with scan times ranging from 100 ms to 300 ms per point, where $I_{1\omega}$, $I_{2\omega}$, ΔS, θ and topography data were collected with a custom written LabView computer program.

S and $\mid \theta \mid$ images from the PM-NSOM measurements of DPPC supported bilayers are shown in figure 8.1. The black arrow in figure 8.1(c) points to a region where there is a 90° discontinuity in θ. This was associated with a hole in the sample. From the image of S, a measured ΔS of $\approx 3.9 \pm 0.4$ mrad was obtained by taking the average S inside the hole and subtracting from a region away from the determined edge. This gave further support for the discontinuity in θ being associated with a hole.

With the value for S of a lipid bilayer, we were able to establish the birefringence $(n_e - n_o) = \frac{\Delta S \lambda}{2\pi t}$, which was $\approx 0.073 \pm 0.008$, using the value of $\lambda = 632.8$ nm and t of ≈ 5.3 nm [58]. From the birefringence, as described in Chapter 4.3, other physical properties, such as the polarizability α_{ij} were determined. Prior to the determination

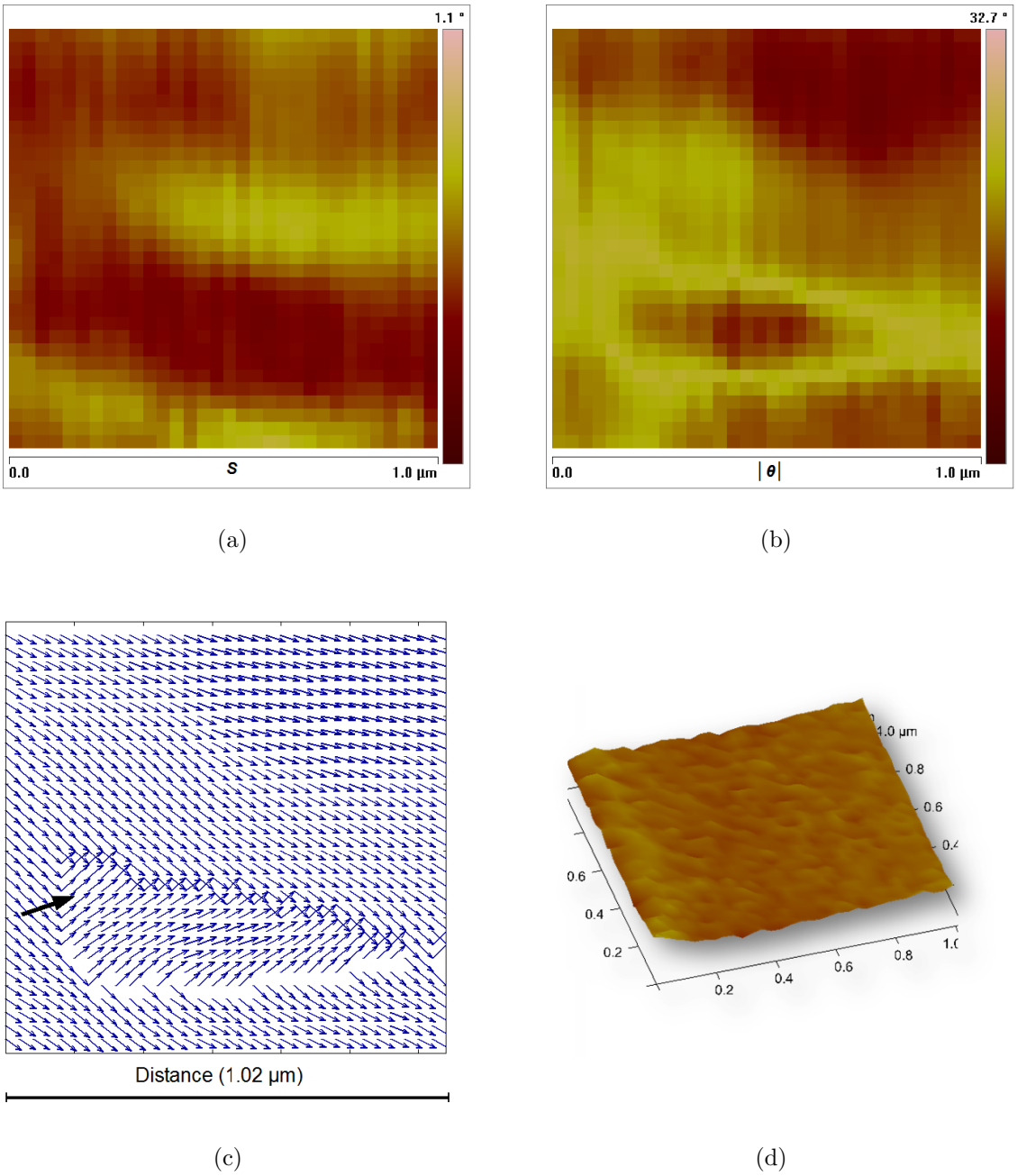

(a) (b)

(c) (d)

Figure 8.1. PM-NSOM picture of DPPC supported on glass, a) Image of S. b) Image of the absolute value of θ, to better outline the boundary of the hole. c) Vector plot created from the image of θ. Where the direction of the arrows are the direction of the projection of the acyl chains in the lipid region. d) Topography of the sample. Because the tip's diameter was larger than the hole's size we were not able to resolve its structure, therefore we have the resulting flat topography image.

of α_{ij}, the indices of refraction along the length and diameter of the acyl chains were needed. From Appendix I we used

$$(n_e - n_o) = \frac{n_{eff}}{\cos(\psi)} - n_\perp, \tag{8.1}$$

where n_{eff} is the effective index of refraction that the extraordinary ray experiences as it passes through the material, ψ is the angle the extraordinary ray has relative to the ordinary ray, and $n_\perp$ is the index of refraction perpendicular to the direction of the acyl chains. From this information we use

$$\frac{n_{\text{eff}}}{\cos(\psi)} - n_\perp = \frac{1}{\sin\left(\arctan\left(\frac{{n_\parallel}^2}{{n_\perp}^2}\cot(\phi)\right) + \phi\right)} \frac{n_\perp n_\parallel}{\sqrt{{n_\perp}^2 \sin^2(\phi) + {n_\parallel}^2 \cos^2(\phi)}} - n_\perp, \tag{8.2}$$

from Chapter 4.1 to determine the index of refraction along the acyl chains ($n_\parallel = 1.654$), assuming that $n_\perp = 1.4$ [15] and ϕ is $= 32°$ [59].

Using equation 8.2 and the relationships found in Appendix B, the transverse (α_t) and longitudinal (α_l) polarizabilites for the two acyl chains were determined to be, $\alpha_t = 44.2\text{Å}^3$ and $\alpha_l = 94.4\text{Å}^3$, assuming the area per lipid (A) and acyl chain length (l) were 47.9 Å^2 and 17.2 Å respectively [17]. The numbers here are fairly close to the theoretically calculated values of a single palmitic acid (C_{16}) $\alpha_t = 25.14$ Å^3 and $\alpha_l = 45.8$ Å^3 [15, 29].

Deepening the analysis of figure 8.1, we measured a ΔS of $\approx$ 0.0075 mrad at the determined edge of the hole. We expected that the lipid molecules orient themselves differently around the edges. Because water was present, the lipid bilayer forms a boundary at an edge where the acyl chains orient at a higher angle to enclose the membrane. We then used the equation 8.2, and solved for an average $\langle\phi\rangle$ of $\approx$ 47.44° of the acyl chains, using $n_\parallel = 1.654$ and assuming the thickness doesn't increase significantly around the edge.

8.1 Measurements on Non-continuous Lipid Bilayers

To complement the previous results, further information was extracted from the images of non-continuous DPPC supported bilayers in figures 8.1 and 8.5. From the images in figure 8.1 we were able to determine that the sample is not uniform across the substrate by looking at the topography, seen in figure 8.2(d). Furthermore we were able to see discontinuities in both θ and S. Because S is a function of ϕ, as $\phi \longrightarrow 0$ the acyl chain projections should posses the same behavior. Where boundaries occur across the sample, higher values of $\langle\phi\rangle$ are expected, therefore the values for the projection length were scaled higher and likewise for the opposite condition. Using this information we were able to combine both quantities to develop an image of the acyl chain projections on the plane of the surface scaled by S, found in figure 8.2(c). The image in figure 8.2(c), better describes how the acyl chains were oriented throughout the membrane. With further analysis we were able to use the information in figure 8.1 to look at the distribution of S, seen in figure 8.4(a), and determined there was a ΔS of ≈ 4 mrad. From this we observed a large distribution of S on the higher peak, which we expected from a sample with many holes because of the increase in ϕ due to the increase of $\langle\phi\rangle$ around the edges.

A line cut of the data was also performed (see figure 8.4(b)) analyzing S along a line across the sample. Doing so we were able to use the graph in figure 8.4(c), and measure the average S at points 1 and 2 on the graph. Points 1 and 2 were chosen to select a region that was in the hole and one that was at a region away from any edges. The result was $\Delta S \approx 3.8 \pm 0.6$ mrad, in close agreement with previous results. From a separate set of images of the same sample, shown in figure 8.5, a ΔS of $\approx 3.9 \pm 0.4$ mrad was extracted from figure 8.5(a). To calculate this value, we used the topography image in figures 8.5(c) and 8.5(d) to locate a hole, circled and labelled "1". A value of S was measured in the hole and then on another position of

the sample away from any detectable imperfections. As previously described it was apparent from figure 8.5(b), that the membrane's $\langle\phi\rangle$ was non-continuous across the substrate.

To further illustrate the length scale of the hole regions of the sample, we measured over a larger area (3.2 μm $\times$ 3.2 μm) and a step size ($\sim$ 100 nm), shown in figure 8.6. Initially it seemed that S was fairly constant across the surface. Nevertheless, in observing the deviations of S we were able to measure changes in ΔS ranging from 1.3 mrad to 1.7 mrad. If we assumed that $\langle\phi\rangle$ is 32° at a corresponding S value of $\approx$ 3.8 mrad,$\langle\phi\rangle$ across the surface ranges from $\approx$ 23° to 40°. Such results adhere to the physical properties of a sample with boundaries that cause the membrane to buckle resulting in large deviations of ϕ. Beyond the qualitative observation, we also further illustrated the high resolution capabilities of NSOM. The results from this study support the rationalization that PM-NSOM is a useful tool in studying localized structural changes in lipid systems.

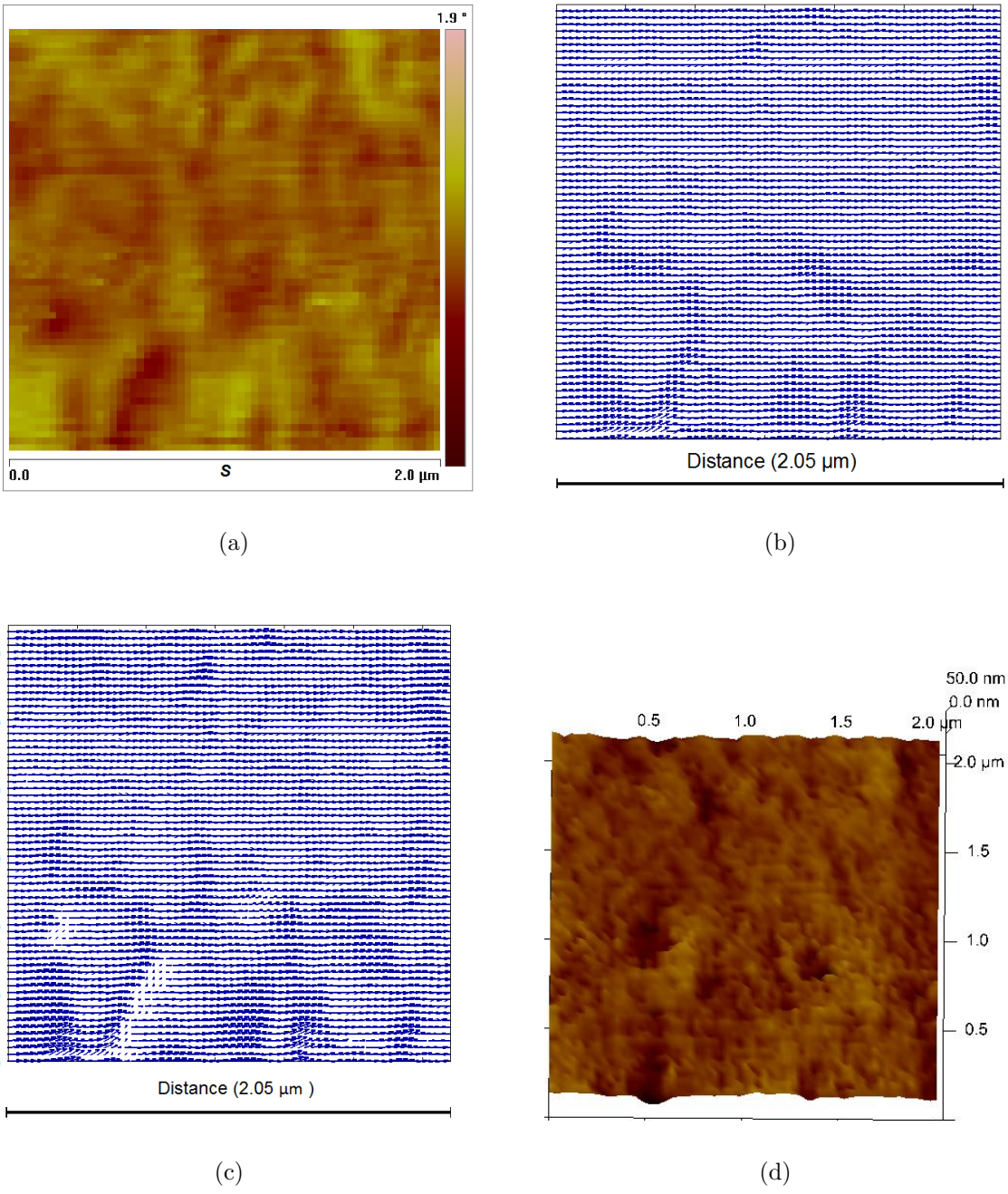

(a) (b)

(c) (d)

Figure 8.2. 2.05 μm $\times$ 2.05 μm image of a DPPC membrane supported on glass, with a 32 nm step size. From the images we determined that the sample had many holes. a) An image of S. b) Vector graph of the projection θ. c) Vector graph of the projection θ scaled by S, showing a decrease in vector length that correspond to the acyl chain tilt ϕ. d) Image showing the map of the surface, extracted from the topography.

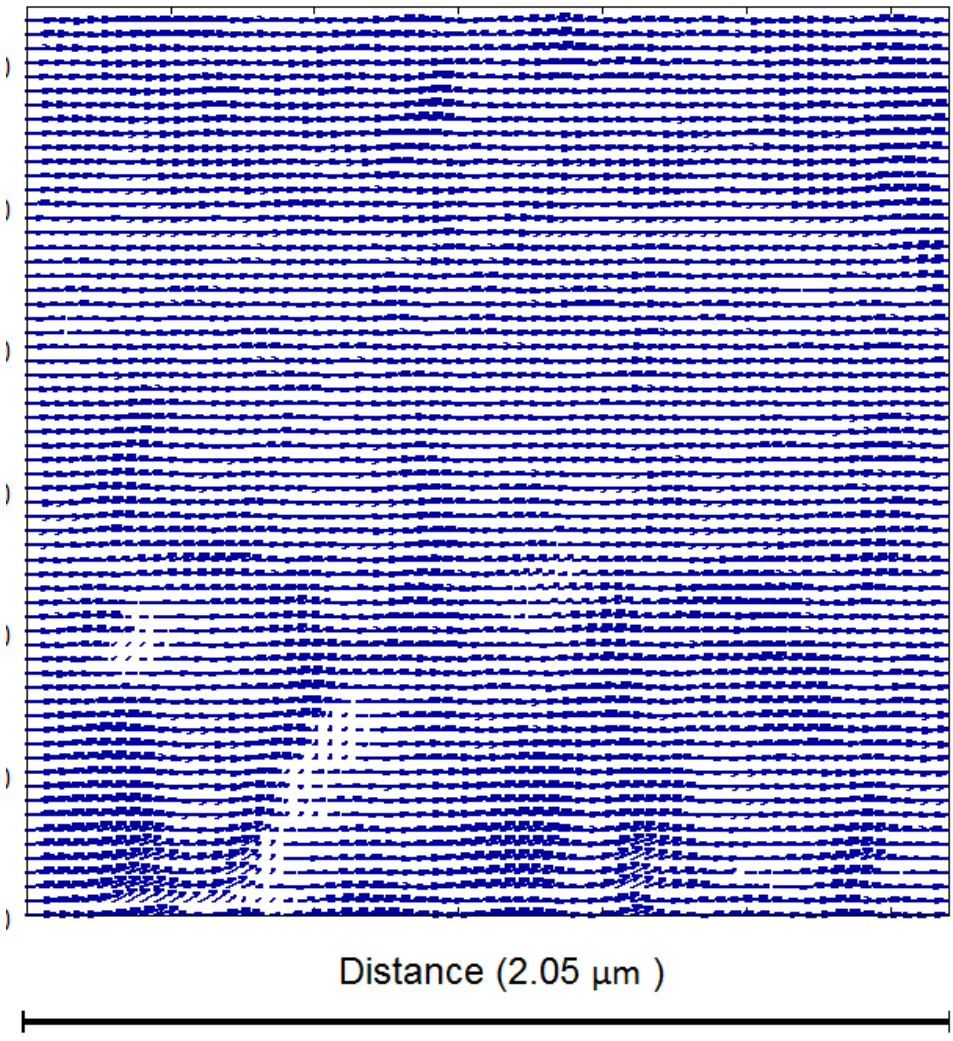

Figure 8.3. Larger representation of a vector graph of the projection θ scaled by S shown in figure 8.1.

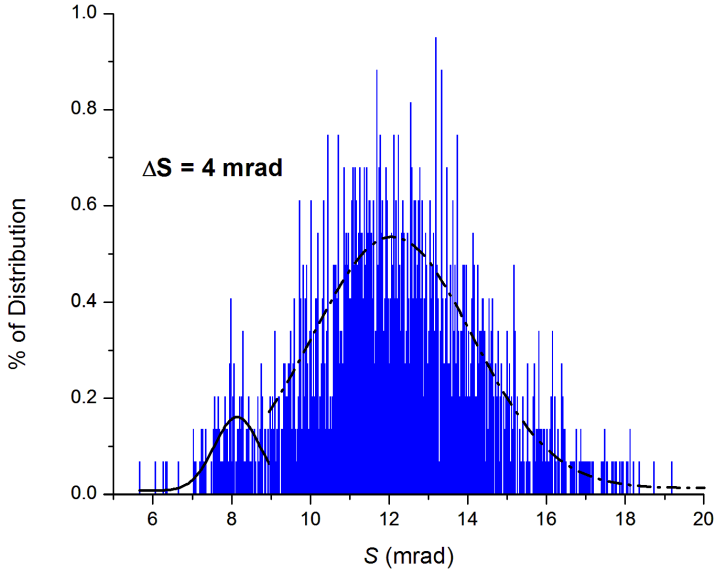

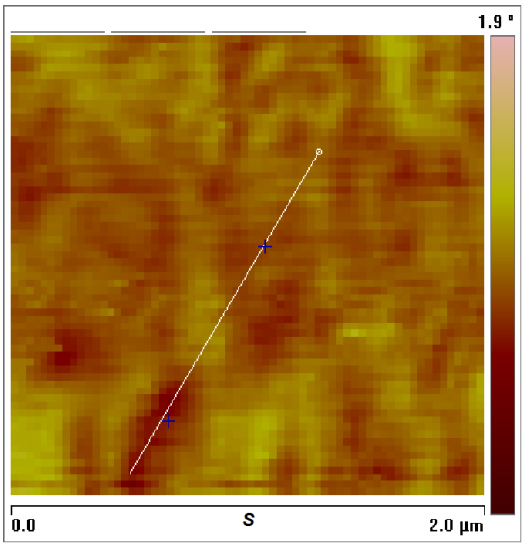

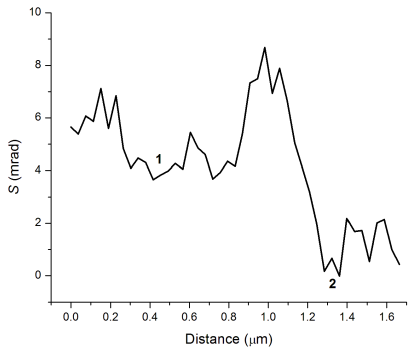

(b) (c)

Figure 8.4. a) Image of the distribution of S in figure 8.1, having a peak at 8.1 mrad and 12.1 mrad yielding a ΔS of ≈ 4 mrad. b) Image of S with a line displaying where the section of data was analysed. c) Line cut data, showing S in mrad as a function of distance across the selection. We measure the value at point 1 and 2 and obtain a ΔS of $\approx 3.8 \pm 0.6$ mrad.

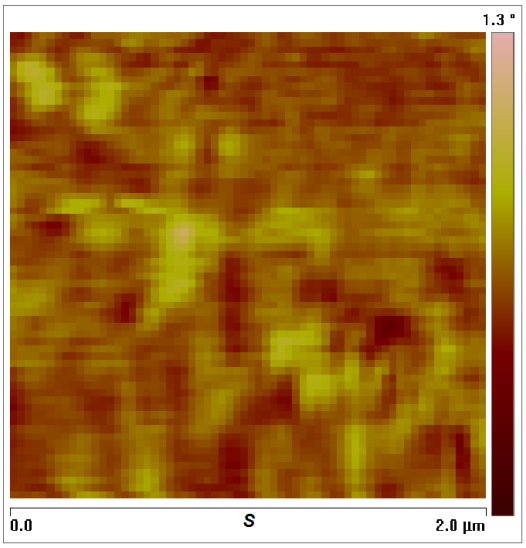

(a)

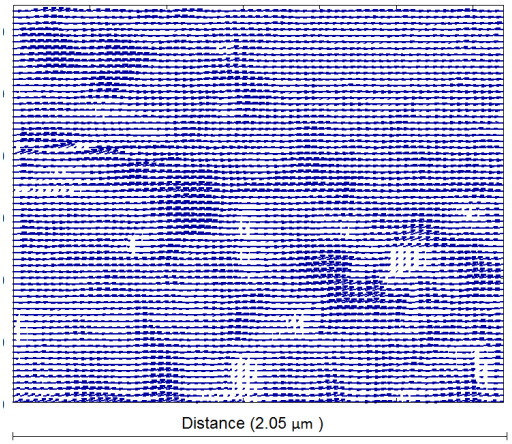

(b)

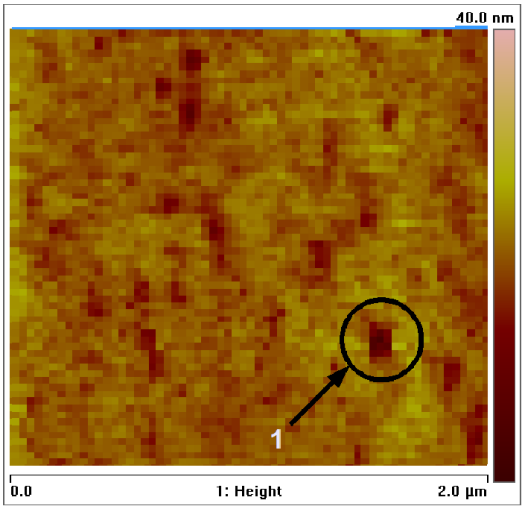

(c)

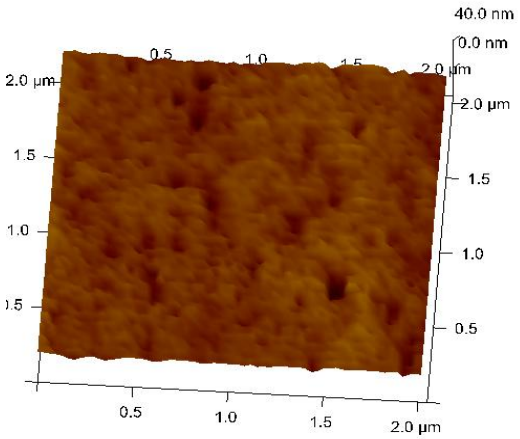

(d)

Figure 8.5. 2.05 μm $\times$ 2.05 μm image of DPPC membrane supported on glass, with a 32 nm step size. From the images we determined that the sample had many holes. a) Image of S. b) Vector graph of the projection θ scaled by S, showing decrease in vector length that correspond to the acyl chain tilt ϕ, c) Contrast image of the topography displaying many holes in the sample. "1" labels the hole where the measurement was taken to calculate ΔS. d) An image showing the topographical map of the surface.

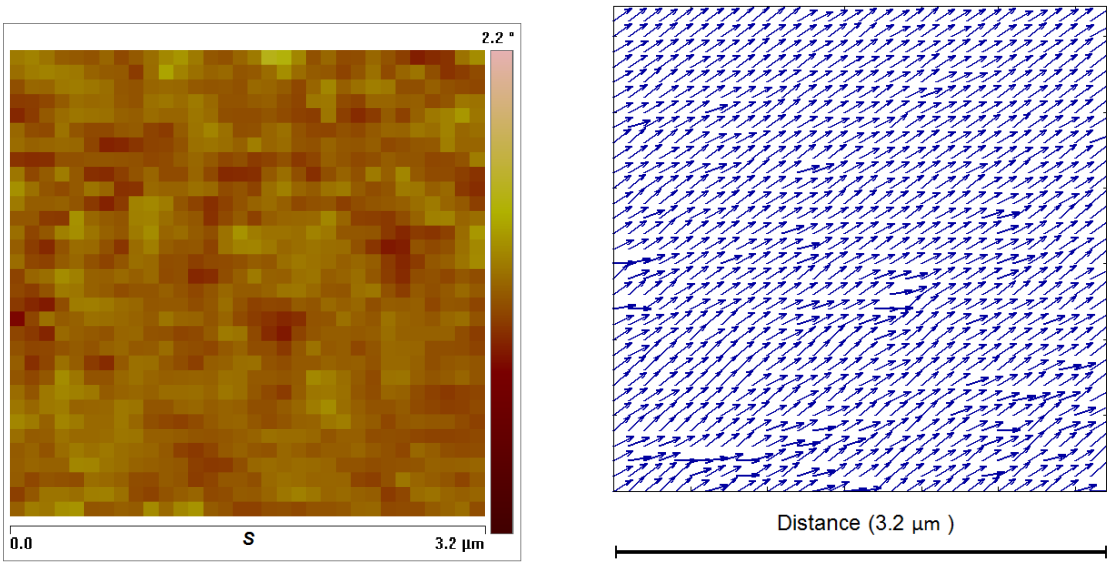

(a) (b)

Figure 8.6. 3.2 μm $\times$ 3.2 μm images of DPPC supported on glass with many holes. 100 nm step size was performed, not resolving the detailed structural changes found in figure 8.5 and 8.1. a) Image of S showing a roughness around 1.7 mrad across the sample. b) Image of θ showing the discontinuity, due to unresolved structural deviations across the sample.

8.2 Structural Defects in Lamellar Bilayers

It was previously shown how physical parameters may be extracted from the PM-NSOM images of supported lipid bilayers in the $L_{\beta'}$ phase. In this section structural changes across a continuous bilayer were determined by measuring S and θ.

In this study samples were prepared on a Langmuir trough, utilizing the method presented in Section 6.2.1. Unlike samples that were prepared using vesicles fusion, where a free standing membrane was created, the lipid bilayer was consistently under lateral pressure due to nature of the preparation, explained in Section 6.2.1. Topographically the samples prepared with the trough carried the same characteristics to the samples that were prepared using vesicles fusion. A set of PM-NSOM images taken from a sample prepared using a trough can be found in figure 8.7. From the topography in figure 8.7(d), a large vesicle was determined to exist on the surface of the bilayer in the top left corner of the image. From the images of S and θ we interpreted that the lipid molecules are reordered, creating a "ripple" around the vesicle. Under the assumption that the region away from the vesicle was in the $L_{\beta'}$ state with a S of ≈ 4 mrad, we determined that the regions with lower values of S correspond to $\langle\phi\rangle$ being parallel to the membranes' normal. Also the regions with larger S values can be interpreted as having a higher $\langle\phi\rangle$, which was an expected result of a membrane that bends or buckles.

The samples used were not imaged immediately after sample preparation. As a result we suspected that vesicles budded from the surface to relax the membrane from constant lateral pressure. The "ripples formed across the surface may have been a result of this relaxation or as a consequence of the vesicle on the surface of the membrane.

The detection of the membrane "buckling" is not unique to this PM-NSOM technique. Methods like AFM are able to resolve topographical undulations with better

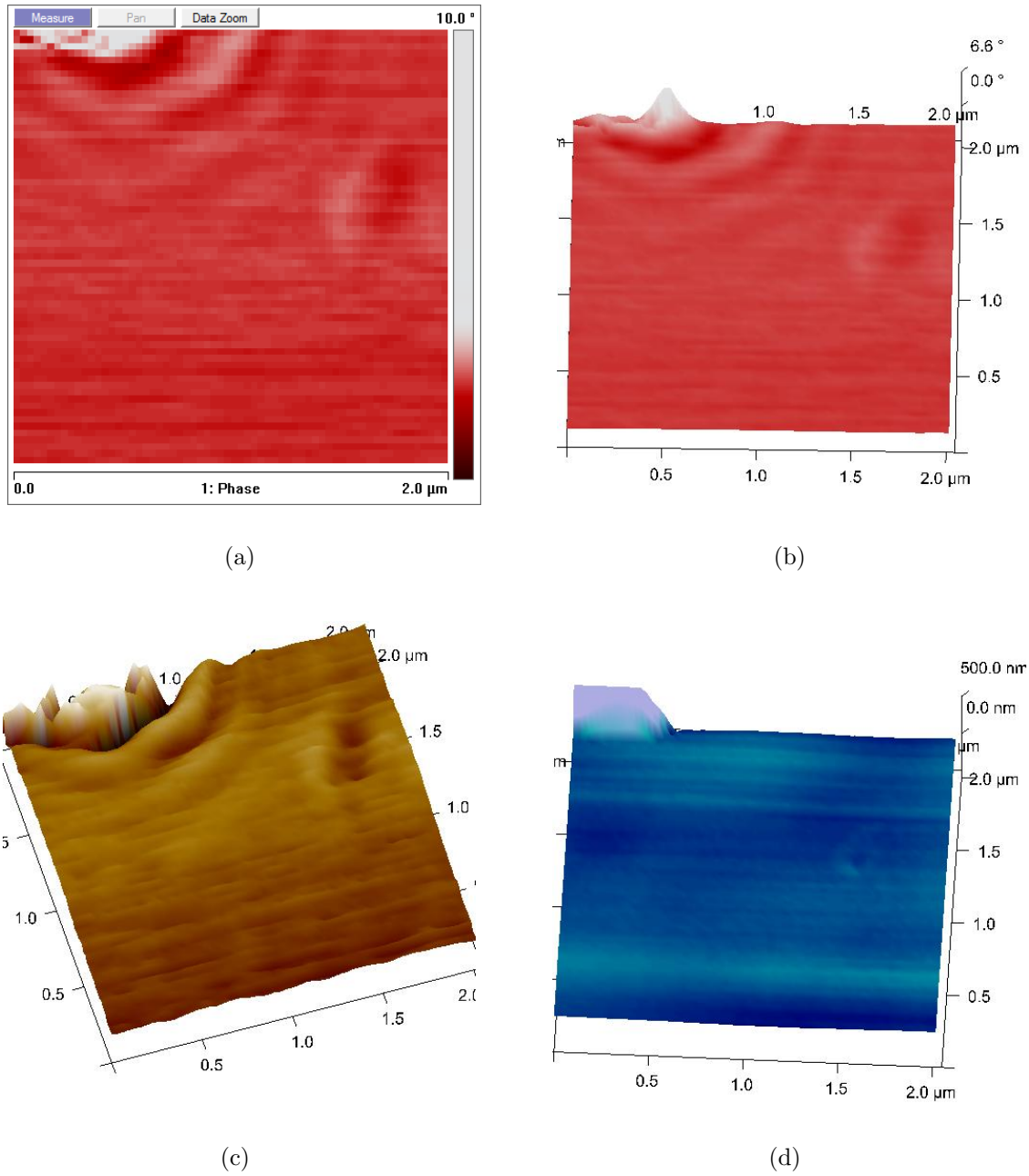

Figure 8.7. PM-NSOM images of a vesicle upon the surface of a supported lipid bilayer. a) Image of S. b) Three dimensional S map with higher regions of S correlated with larger $\langle\phi\rangle$ (i.e. $\langle\phi\rangle > \approx 32°$), with the opposite true for lower S regions. c) Three dimensional θ map showing the variation of the projection of the acyl chains throughout the membrane. d) Topography of the surface showing a large vesicle on the surface.

lateral resolution. Unlike AFM, measurements of θ give us the information about the projection direction of the acyl chains. Localized reorientations of the acyl chains within the membrane are resolvable with PM-NSOM, effects that may show no topological modifications.

8.2.1 Diffusion Measurements

Thus far we have shown how to determine structural changes across a planar membrane in the $L_{\beta'}$ phase with PM-NSOM. The work presented here was extend to include temporal structural changes. PM-NSOM measurements of supported bilayers prepared on a trough were imaged a varying times. Two images of the same area, which contained a "ripple", were analyzed (see figure 8.8). A point on a "ripple" was chosen and the displacement was determined. (Figures 8.9(b) and 8.8(d) use arrows to show the position of interest.) To find the displacement the resultant vector between the vectors in each image was determined. The displacement measured, was verified to be far larger than the stage drift determined from previous measurements and calibrations. Through an approximation, the diffusion rate is proportional to the average of the position squared over time, $\langle r^2 \rangle \propto Dt$. An array of points were analyzed to obtain a value of $\approx 2 \times 10^{-12} \frac{cm^2}{s}$. The vesicle itself was determined to be stationary comparing the relative distance of the S profile around the vesicle, seen from the comparison of images in figure 8.9. Two things were learned from this, one that these "ripples", which were likely due to the relaxation of the membrane, seem to diffuse with the membrane. Two, that localized diffusion rates of the membrane substructure can be extracted using PM-NSOM.

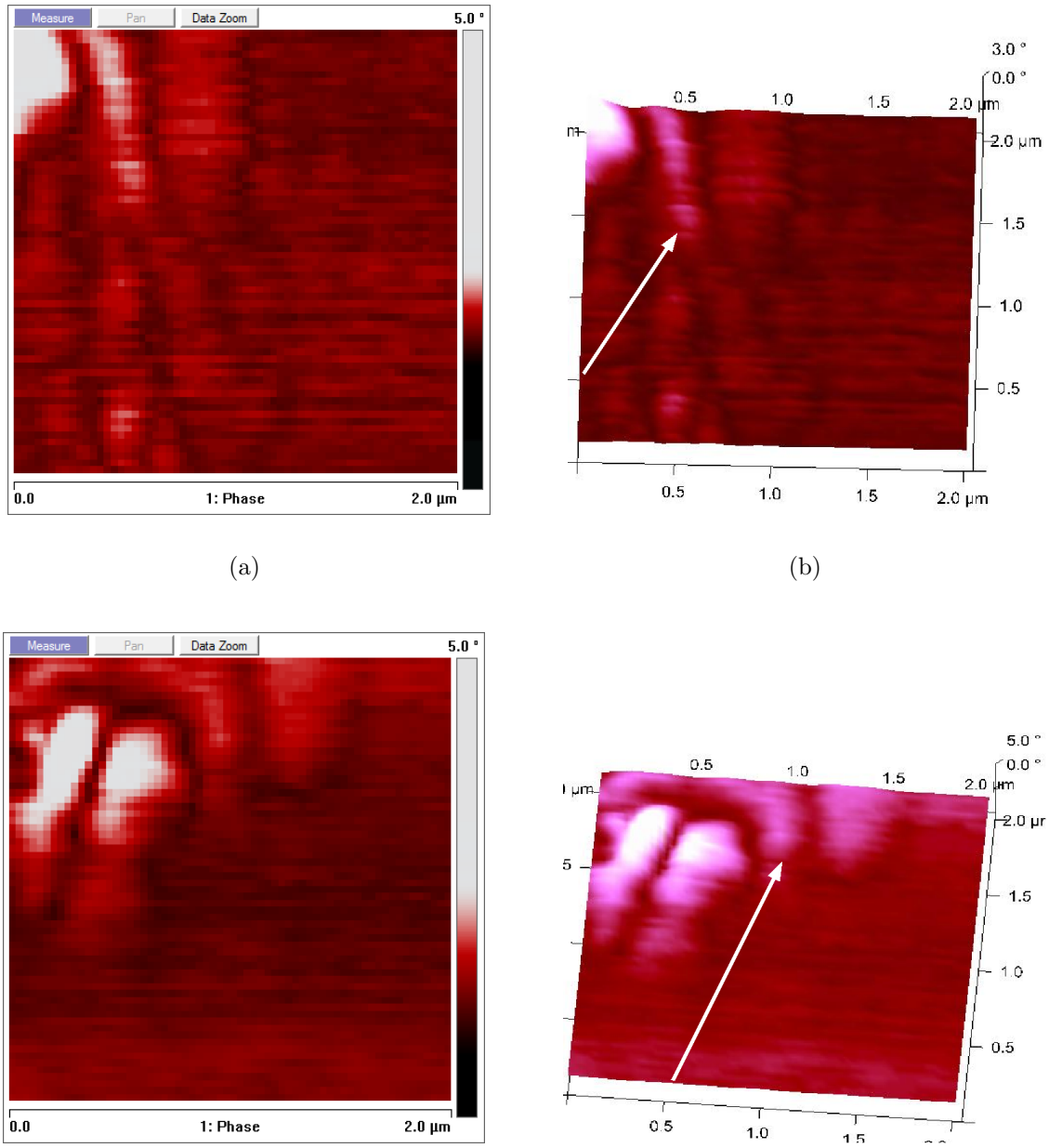

Figure 8.8. S images of "ripples" that were $\approx$ 62.5 min apart. a) Image of S showing ripples around a vesicle. b) Image map of S, with an arrow showing the vector length from a point on the stage to a ripple section on the image. c) Image of S taken 62.5 minutes after the first. d) Map of S, with an arrow displaying the position vector of the ripple relative to the same position on the stage.

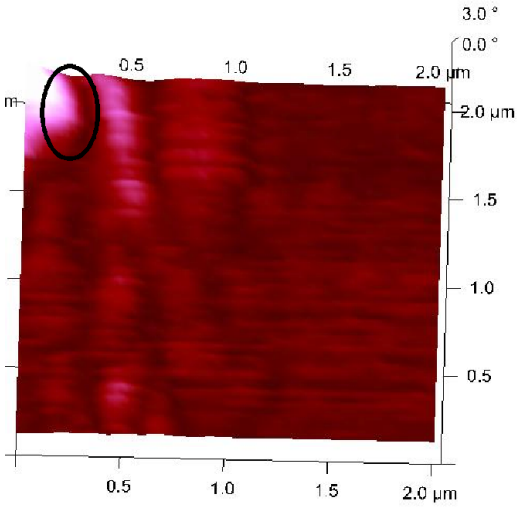

(a)

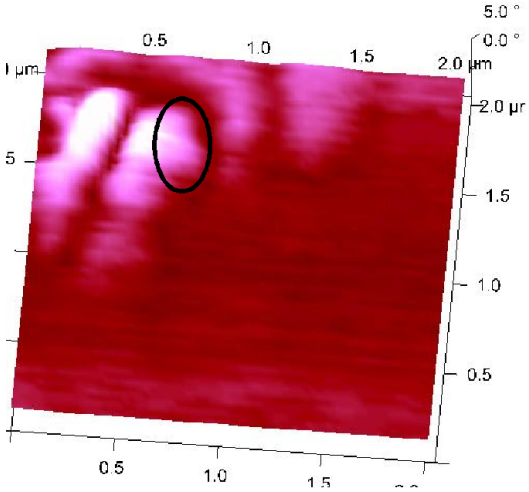

(b)

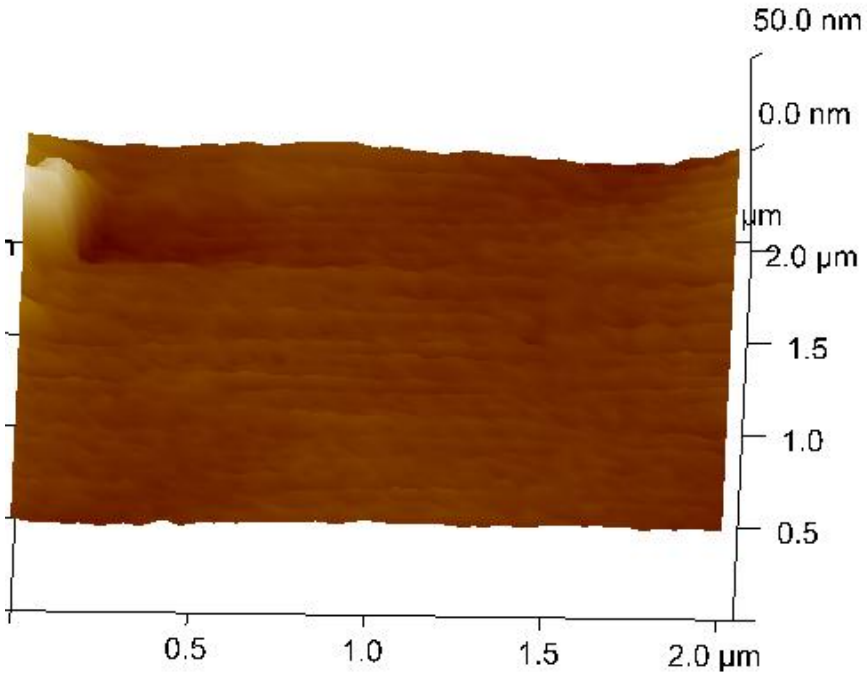

(c)

Figure 8.9. a) Image of S with a circled section of the intensity profile created around a vesicle. b) Image map of S, with a circle section of the same section found in a). c) Topography of the later S image in part b).

9. TEMPERATURE INDUCED STRUCTURAL CHANGES IN SUPPORTED LIPID BILAYERS

Temperature controlled PM-NSOM measurements were conducted on supported lipid bilayers. The temperature was controlled to study the main phase transition of DPPC $T_m \sim 41°C$. Using the experimental procedure described Chapter 5.5, the chamber's temperature was first heated beyond T_m to ensure the lipid membrane was well into the L_α state. The NSOM probe was then engaged with the sample. The chamber was cooled below T_m and heated back to the initial temperature. This was proven to be the most reliable method to counter the probe crashing events that occurred due to the expansion of the Delrin separator.

The first set of experiments consisted of taking consecutive 16 × 16 pixel images over an area of 512 nm^2 at a rate of ≈ 3.5 mins per image. All measurements were preformed at 100% relative humidity, while simultaneously measuring the temperature of the aluminium sample holder. Figure 9.1(a) shows an image of S, which yielded a ΔS of ≈ 3.84 mrad ± 0.2 mrad at ≈ $41°C$, a temperature that can be extracted from the graph in figure 9.1(d). A ΔS of 3.8 mrad was interpreted as the average position of the acyl chains going from their characteristic $\langle\phi\rangle$ of ≈ 32° to zero. This shows that the sample transitions from the $L_{\beta'}$ to the L_α state. Also, from the image of θ, found in figure 9.1(b), a change of ≈ 21° was measured. (As a reminder, the change in θ across the sample with respect to the system's axis was measured.) The change in θ at T_m seen in figure 9.1(b), shows a defined value for θ when the sample was in the $L_{\beta'}$ state, and goes to a different value, characteristic of the remaining retarding elements of the system, while in the L_α state. Since θ is the direction of the

projection of the acyl chains, when $\langle\phi\rangle$ went to zero, θ is no longer well defined on the lipid bilayer. From S, which informed us that $\langle\phi\rangle$ takes a value of zero at $\approx 41^\circ$ C and that θ changes abruptly, we have evidence of a phase change at the characteristic T_m for this supported planar DPPC bilayer.

The information from previous experiments was used to determine the acyl chain motion across the image. Using the values for $n_\perp$ and $n_\parallel$, ϕ was solved for in equation 8.2. This information can now be implemented in the creation of a three dimensional map of acyl chains with thier corresponding $\langle\phi\rangle$. Figure 9.2 displays a three dimensional representation of the acyl chains oriented across the sample (represented as blue rods). As shown, when the membrane is below T_m, $\langle\phi\rangle$ was $\approx 32^\circ$ and below the phase transition temperature it was in the L_α phase, where $\langle\phi\rangle$ is zero.

Beyond the experiments conducted above there were additional temperature controlled experiments performed, where the time per image was decreased to ≈ 50 s. The temperature change per image was $\sim 0.05^\circ$ C, which allowed us to be sure the system reached equilibrium for each measurement. The results for S are seen in figure 9.3, where a ΔS of ≈ 3.5 mrad is observed across T_m. From the graph in figure 9.3(a) S was observed to take on a value of 4.7 mrad $T < T_m$ and ≈ 1 mrad $T > T_m$, which yielded the expected value for ΔS (As was noted in previous sections, only the change in S is relevant and is why the value for S above T_m is not required to be absolutely zero.). This translates to the acyl chains' $\langle\phi\rangle$ transitioning from $\sim 32^\circ$ to zero, calculated using equation 8.2. From θ in figure 9.4(c) it can be observed that when $T < T_m$ the uncertainty in θ was small, but when $T > T_m$ θ was less defined. Because θ is proportional to the projection of the acyl chains, and $\langle\phi\rangle = 0$, it was expected that this uncertainty would exist.

Using this information ϕ was solved for as previously performed. A graph of the acyl chain tilt as we passed through T_m was created (see figure 9.5(b)). From the

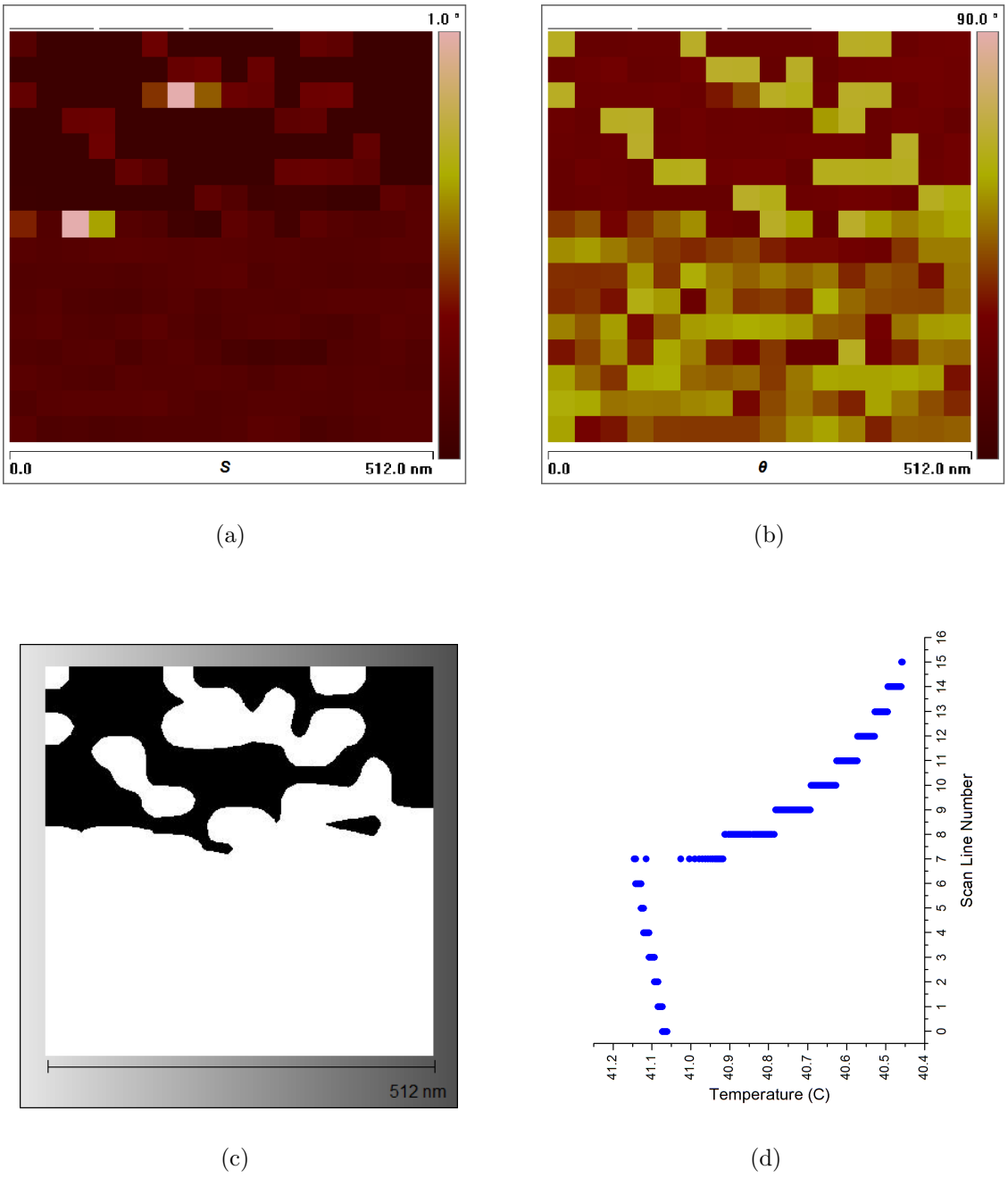

(a) (b)

(c) (d)

Figure 9.1. Temperature controlled PM-NSOM 512 nm × 512 nm images of DPPC supported on glass a) Image of S, showing a Δ S of $\approx$ 3.8 $\pm$ 0.3 mrad, indicating a change of ϕ of the acyl chains. b) Image of θ, showing a change across the phase transition temperature. c) Threshold image of S showing light regions representing regions in the $L_{\beta'}$ phase and dark regions rich in the L_{α} phase. d) Graph of the temperature versus line number, confirming the point at which ΔS occurs is $\approx$ 41°C.

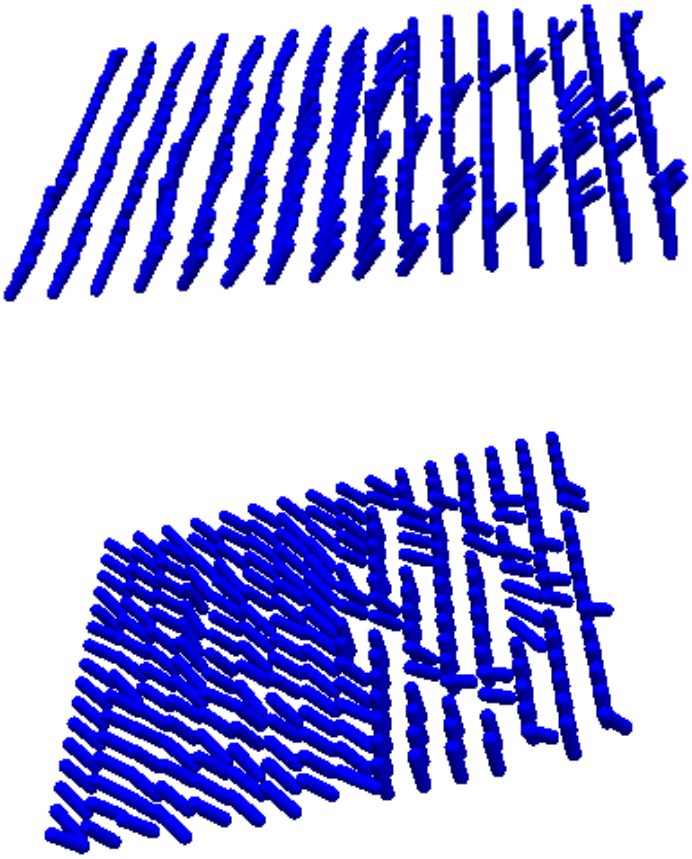

Figure 9.2. Two 3D images of a pictorial representation of the acyl chain orientation throughout the membrane (using the images in figure 9.1(a)). Each tube portrays the average position of many lipid molecules. (The top and bottom images are from the same data and have the chain tilt in different directions for visualization purposes only.)

results, a three dimensional plot of $\langle\phi\rangle$ as a function of T was forged (see figure 9.5(a), where the hydrocarbon tails are represented as blue rods). From the plot it was observed that at T_m the chains orientation changes from $\approx 32^\circ$ to zero. These three dimensional images were intended to better display what physically happens around T_m according to the model used and further showcase the potential behind PM-NSOM.

From figure 9.5(b), it was seen that $\langle\phi\rangle$ fluctuated slightly as T_m was approached. This could be due to the undulations that exist in the $P_{\beta'}$ phase. A characteristic that cannot be confirmed with PM-NSOM, which derives from that fact that the periodicity of of the ripples are less than the diameter of the NSOM aperture [60, 61]. What was not initially evident from the data presented was that as T_m was approached, the fluctuation of S increased, displayed in the graph of the variance (ΔS^2) versus T in figure 9.6. Under a first order phase transition, the gap in energy of the two phases begins to be $\sim k_B T$ as T reaches T_m. Due to thermal energy from the environment, the system fluctuates between the two phases. This behavior is responsible for the existence of physical phenomena such as nucleation [22], where regions of new phases initiate the transition from a point in the structure and grow over time. From the threshold image in figure 9.1(c), as $T_m \approx 41^\circ C$ was reached, the lipid bilayer transitions states as was previously discussed (where the regions in white are rich in $L_{\beta'}$ phase membrane and the dark L_α phase). From the graph in figure 9.1(d) the system's temperature fell below T_m (due to experimental conditions) and the observation of small isles began to form due to this nucleation phenomena.

The temperature where T_m was determine to occur for the heating of the lipid bilayer in figure 9.3(a) is slightly higher than its corresponding temperature in cooling data in figure 9.3(c). This was not expectedly due to experimental error, but related to an additional physical phenomena referred to as super-heating and super-cooling.

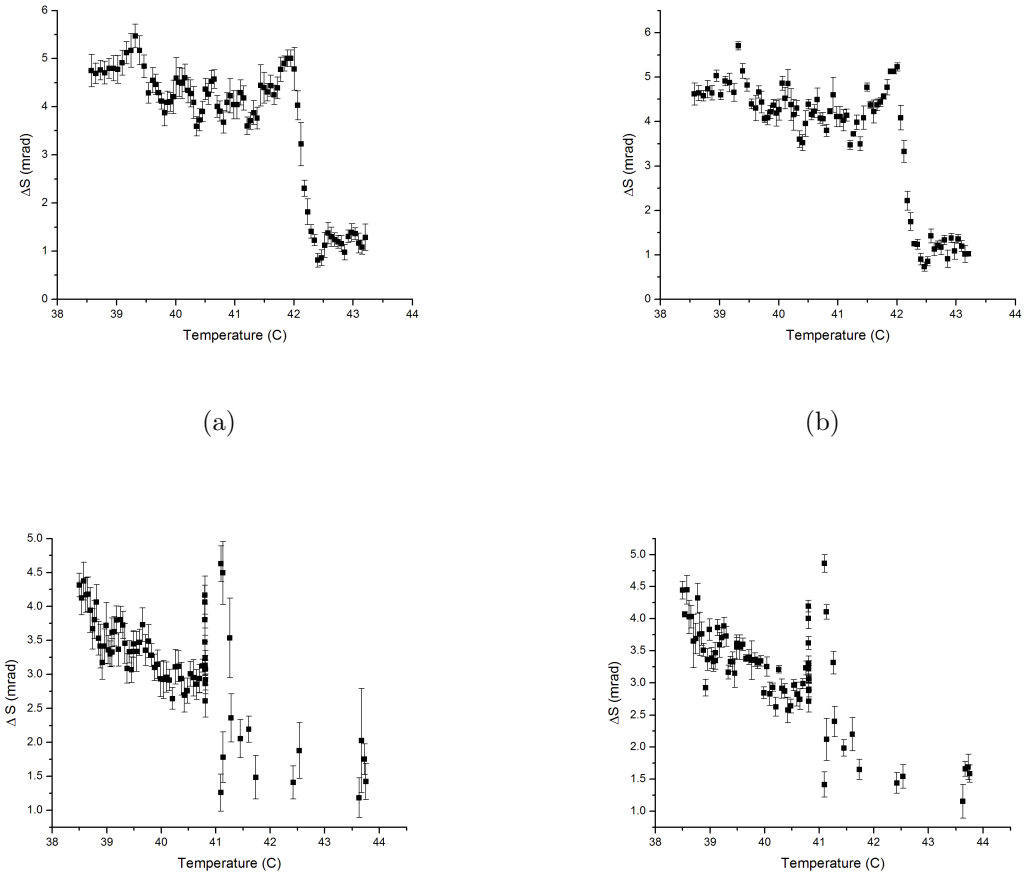

Figure 9.3. ΔS values from a temperature controlled PM-NSOM measurement of DPPC supported on glass. a) Graph of ΔS_{avg} versus temperature as the system was heated, taken from 512 nm^2 images showing a change in S across T_m of $\approx 4 \pm 0.4$ mrad. b) Heating graph of ΔS_{avg} versus temperature, taken from $\sim$100 nm^2 images. c) Graph of ΔS_{avg} versus temperature as the system was cooled, taken from 512 nm^2 images showing a change in S at T_m of ≈ 3.4 mrad $\pm$ 0.5 mrad. d) Cooling graph of ΔS_{avg} versus temperature, taken from $\sim$100 nm^2 images.

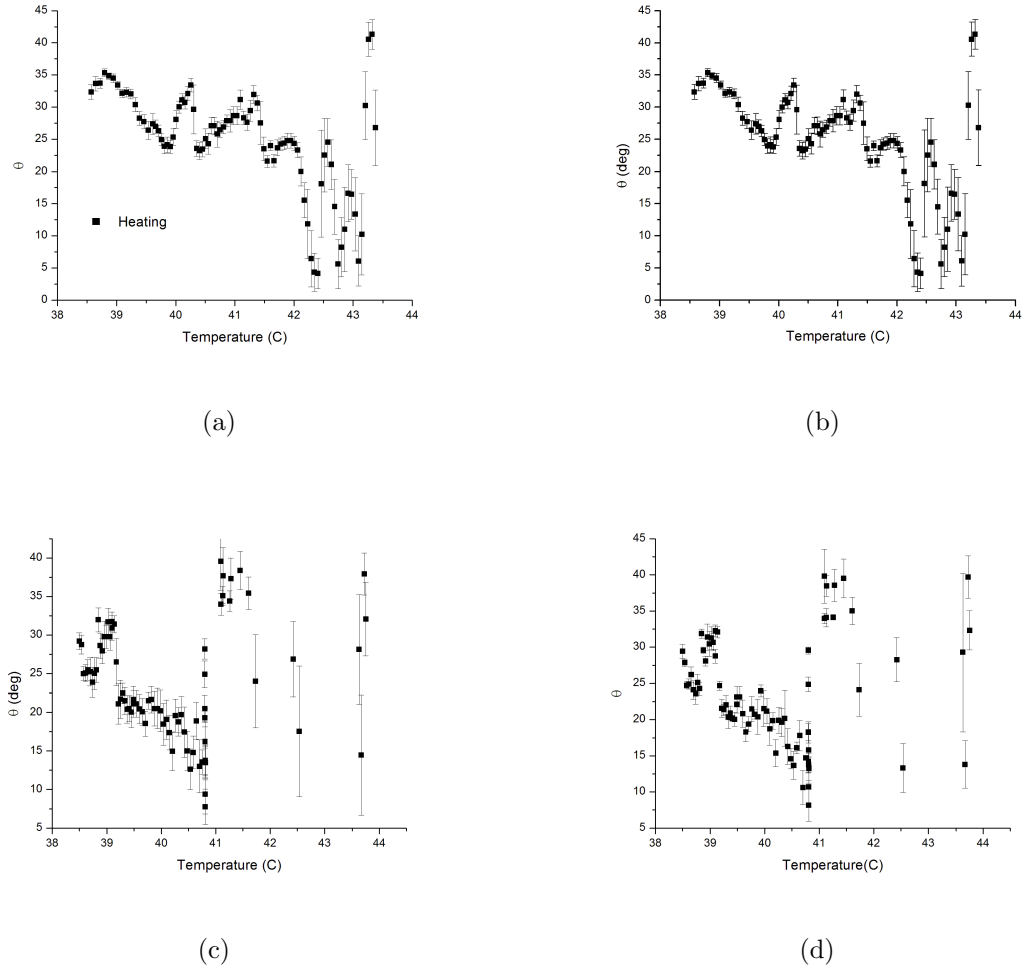

Figure 9.4. Graphs of θ values from a temperature controlled PM-NSOM measurement of DPPC supported on glass. a) Graph of θ_{avg} versus temperature as the system was cooled, taken from 512 nm^2 images showing well define values for $T < T_m$ and less defined above T_m. b) Cooling graph of θ_{avg} versus temperature, taken from ∼100 nm^2 images. c) Graph of θ_{avg} versus temperature as the system was heated, taken from 512 nm^2 images showing well define values for when the system is in the $L_{\beta'}$ phase and less defined in the L_α phase. d) Heating graph of θ_{avg} versus temperature, taken from ∼100 nm^2 images.

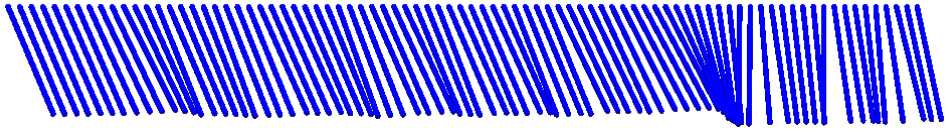

(a)

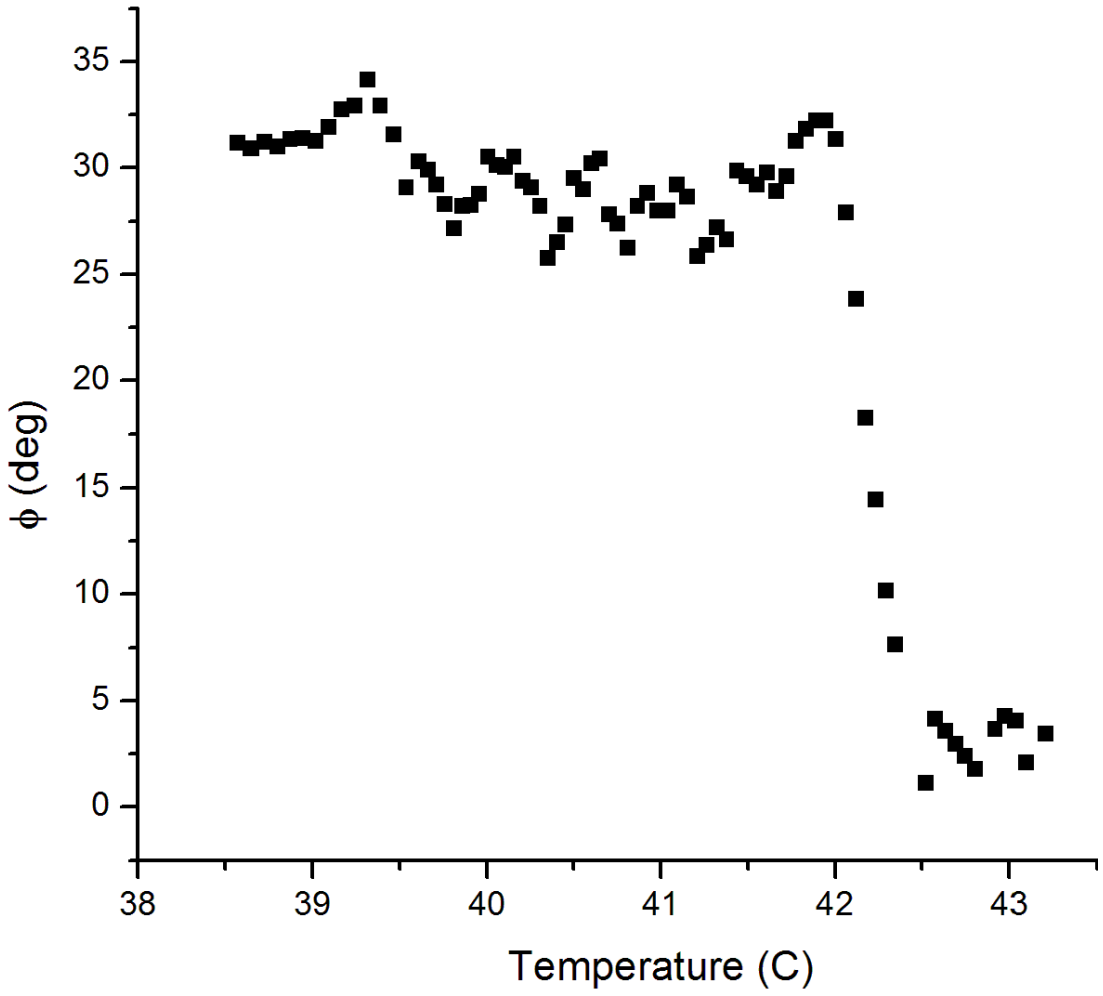

(b)

Figure 9.5. a) Three dimensional representation of the acyl chains orientation, corresponding with the heating graph in figure 9.3. b) Graph of $\langle\phi\rangle$ (degrees) versus T, showing a change from $\approx 32^\circ$ to ≈ 0 at T_m.

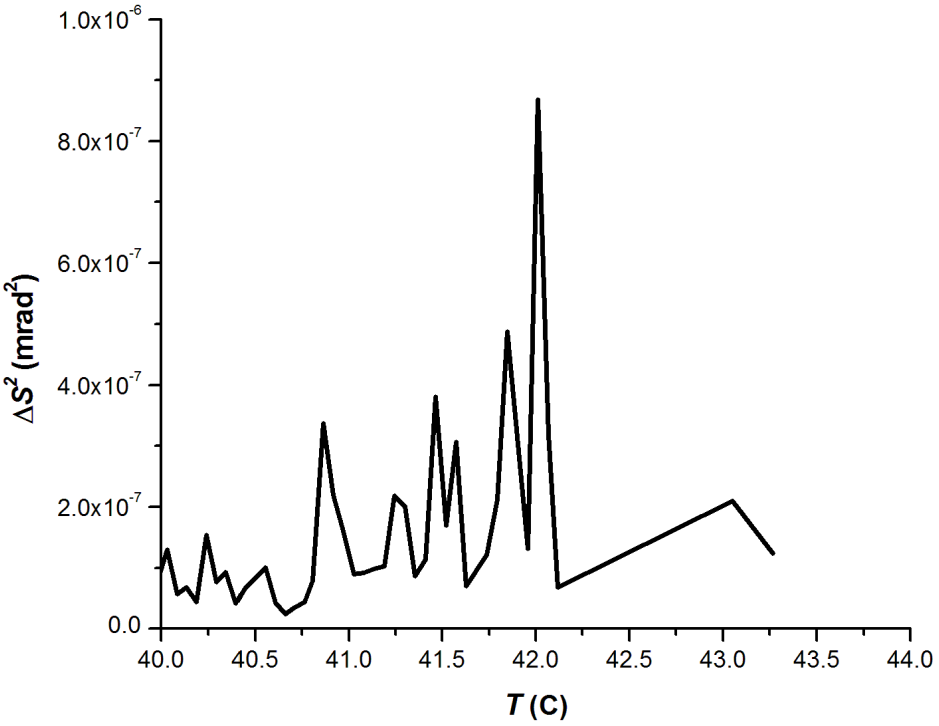

Figure 9.6. Graph of ΔS^2 versus T, extracted from the heating data presented in figure 9.3.

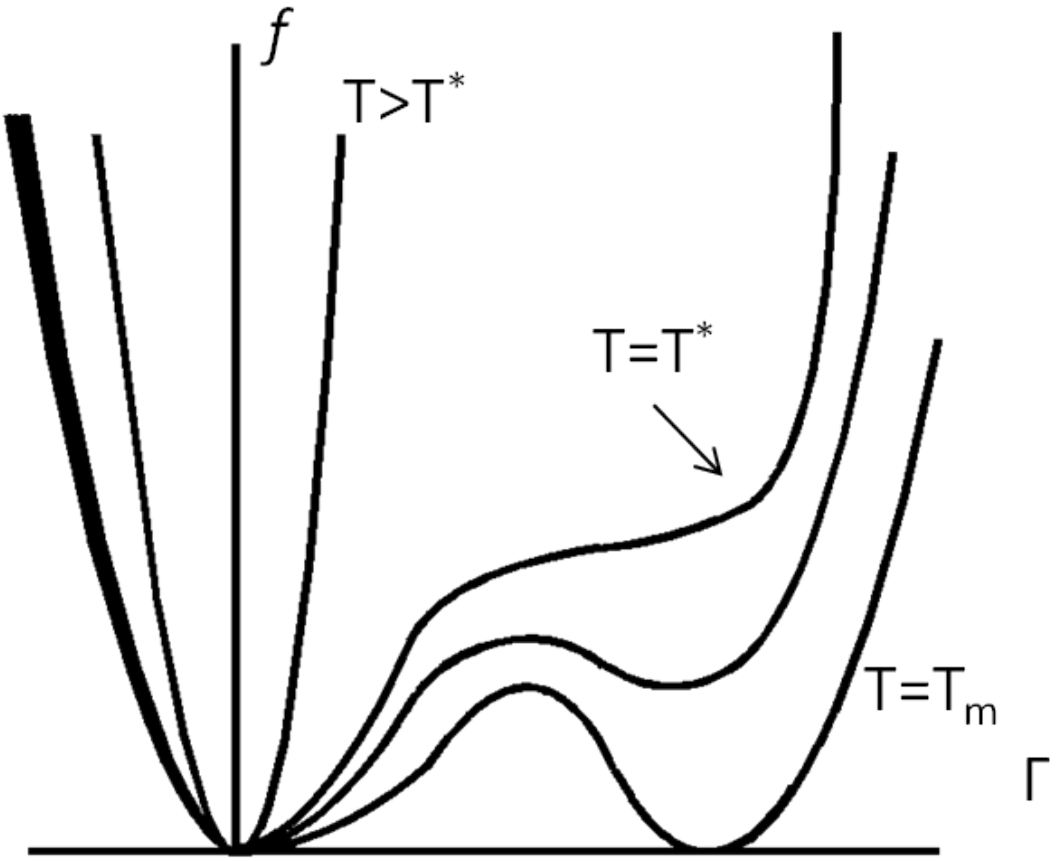

Figure 9.7. Graph of free energy function versus Γ at various temperatures, where T_m is the main phase transition temperature and T^* is the super heated transition temperature.

A characteristic of first order phase transitions is the presence of hysteresis. Upon reaching T_m the phase transition should occur, both when heating and cooling the material. The transition between states can be suppressed, and the system can exist in a metastable state, exhibiting small fluctuations around T_m [23].

We can qualitatively describe this metastable behavior using Landau theory as introduced in Chapter 3. Figure 9.7 is a visual representation of the free energy as a function of order parameter at different temperatures for a super heating event (Recall the function has the form $f(\Gamma) = A\,(T - T_m)\,\Gamma^2 - B\Gamma^3 + \Gamma^4$.). As the temperature of

the system reaches T_m, there are two minimums in the function that represent where the two phases coexist. The transition from phase one to two is suppressed, (there is not enough energy available to go over the large energy barrier between the two minima) and the system exist at the valley away from $\Gamma = 0$ in a metastable state. As $T > T_m$ the width of the valley increases, therefore increasing the variations in Γ from the ambient thermal energy (k_BT). The variations in Γ increase until k_BT is large enough to cause a transition to the stable state at the super heating transition temperature (T^*). This description is how we chose to explain the increase in ΔS^2 observed as T^* was approached, displayed in figure 9.6. With the additional evidence of super heating and super cooling, we highlight the potential of using PM-NSOM on supported lipid bilayers systems.

10. CONCLUSIONS

It was illustrated how lipids membranes thermodynamically change states. In particular it was emphasized how $\langle\phi\rangle$ transitions from a well defined value in the $L_{\beta'}$ state to 0° in the L_α state. Through electrodynamic theory it was unveiled how planar membranes have an effective birefringence that leads to a S that is a function of ϕ. A proposal was introduced to measure S to detect transitions from the $L_{\beta'}$ state to in the L_α state in supported lipid bilayers.

An introduction to AFM and it use in the characterization of substrates and supported planar lipid bilayers was presented. Substrates and supported DPPC lipid bilayers formed using vesicle fusion were showcased. Membrane coated samples were confirmed height measurements yielding ≈ 5.3 nm, along with qualitative force curve comparisons.

A detail overview of NSOM and how it was incorporated with a PEM to conduct PM-NSOM measurements to simultaneously measure S and θ, with a lateral resolution of ~ 100 nm was presented. A method to properly align and calibrate the system was was detailed (A crucial step to perform precise measurements of S and θ.). An analysis of muscovite was provided to verify the reliability and capabilities of the PM-NSOM system.

The use of PM-NSOM for measuring supported DPPC lipid bilayers was shown to produce consistent results (ΔS of ≈ 3.9 mrad), reducing errors in previous work (Lee, *et. al.* (2002)) by a factor of 5. Using the uniaxial model proposed, S yielded a quantity of ≈ 1.654 for $n_\parallel$, using $\phi = 32°$ and $n_\perp = 1.4$. A value for translational and longitudinal polarizabilities were then calculated ($\alpha_t = 44.2$ Å^3 and $\alpha_l = 94.4$

Å^3), which seemed to be consistent with theoretical values for a single palmitic acyl chain of $\alpha_t = 25.1$ Å^3 and $\alpha_l = 45.8$ Å^3.

PM-NSOM measurements were used to determine lateral structural differences across planar membrane systems. Using S and θ, a projection of the acyl chains was created to determine localized ($\sim$ 100 nm) orientation information that is unique to using PM-NSOM. Future work could be extended to multi-component membrane systems to distinguish lateral structural differences in $\langle\phi\rangle$ (given that $\langle\phi\rangle > 0$). Asymmetries in bilayer leaflets could be examined, where domain formation and lateral molecular organization could be studied [62]. Lateral time evolution of these structural variations could be used to better characterize environmental effects on membrane structure.

The final portion of this study demonstrated how by using PM-NSOM, first order phase transitions were detectable in planar lipid bilayers with a lateral resolution of $\sim$ 100 nm. A ΔS of $\sim$ 3.8 mrad was measured at the expected T_m for DPPC. This implied that $\langle\phi\rangle$ transitioned from 32° in the $L_{\beta'}$ state to 0° in the L_α state. Also by assuming that $S(\phi = 32°) = 3.9$ mrad in the $L_{\beta'}$ phase, three dimensional pictorial models were created displaying the average orientation of the acyl chains within the membrane across the sample. Evidence of super heating and cooling was present when analyzing the hysteresis within the temperature dependent data (which is a characteristic of first order phase transistors). Fluctuations of S were shown to increase as the transition temperature was approached. Future work could explore the dynamics in phase transitions of various lipid membrane system utilizing these variances in S. Multi-component systems could be explored to expose how domain size (i.e., line tension) shifts the main phase transition temperature. With further work on substrate modification, membrane surface interactions could be better characterized by measuring changes in θ across the sample to determine lateral molecular organiza-

tion. Expanding the temperature range of the current system could be beneficial in exploring the two-dimensional molecular arrangements that exist in the sub-gel phase of DPPC [63].

Overall it was shown how PM-NSOM measurements characterize average molecular organizations in supported lipid bilayers. With S (a function of ϕ) and θ, high resolution ($\sim$ 100 nm) three dimensional orientation models of lipid molecules can be developed. Future work should be extended to multi-component lipid systems where localized reordering and structural deviations could be examined and better modelled. Taking even further leaps, this work should go beyond model systems where localized membrane alteration could help unfold new answers about cellular membrane organization and function. Using a temperature controlled PM-NSOM system introduces an interesting tool for conducting studies in biophysics. One that should be be added to the everlasting tools for exploring lipid membrane systems.

LIST OF REFERENCES

LIST OF REFERENCES

[1] M. Luckey. *Membrane Structural Biology with Biochemical and Biophysical Foundations*. Cambridge University Press, 2008.

[2] M. M. Banaszak Holl. *Cell Plasma Membranes and Phase Transisitons in Cell Biology*. Springer, 2008.

[3] C. C. Curtain, R. C. Aloia and L. M. Gordan, editors. *Lipid Domains and the Relationship to Membrane Function*. Alan R. Liss, Inc., 1988.

[4] J. F. Nagle. Theory of biomembrane phase transitions. *Journal of Chemical Physics*, 58:252–264, 1973.

[5] P. Tevlin, F. P. Jones and L. E. H. Trainor. Phase transitions of lipid bilayers. ii. mean field theory. *Journal of Chemical Physics*, 91:1918–1924, 1989.

[6] F. Jhnig. Molecular theory of lipid membrane order. *Journal of Chemical Physics*, 70:3279–90, 1979.

[7] E. Jakobsson, A. Grama, S. A. Pandit, G. Khelashvili and H.L. Scott. Lateral organization in lipid-cholesterol mixed bilayers. *Biophysical Journal*, 92:440–447, 2007.

[8] J. H. Davis. Deuterium magnetic resonance study of the gel and liquid crystalline phases of dipalmitoyl phosphatidylcholine. *Biophysical Journal*, 27:339–358, 1979.

[9] C. Hidalgo, editor. *Physical Properties of Biological Membranes and Their Functional Implications*. Plenum Press, 1988.

[10] M. Wiechmann, F. Leisten H. A. Kolb, O. Enders and A. Ngezahayo. Structural calorimetry of main transition of supported dmpc bilayers by temperature-controlled afm. *Biophysical Journal*, 87:2522–2531, 2004.

[11] S. C. Lee, K. Kim, S. Lee, J. H. Yi, S. W. Kim, K. Ha, and C. Cheong. One micrometer resolution nmr microscopy. *Journal of Magnetic Resonance*, 150:207–213, 2001.

[12] C. Y. Feng, K. C. Khulbe and T. Matsuura. *Synthetic Polymeric Membranes Characterized by Atomic Force Microscopy*. Springer, 2008.

[13] U. P. Wild, V. Deckert, R. Z. Olivier, J. F. Martin, B. Hecht, B. Sick and D. W. Pohl. Special topic: Near-field microscopy and spectroscopy - scanning near-field optical microscopy with aperture probes: Fundamentals and applications. *Journal of Chemical Physics*, 112(18):7761–7774, 2000.

[14] S. R. Wassall, C. W. Lee, R. S. Decca and J. J. Breen. Direct imaging of domains in the $L_{\beta'}$ state of 1,2-dipalmitoylphosphatidylcholine bilayers. *Physical Review E*, 67:061914, 2002.

[15] Z. Salamon and G. Tollin. Optical anisotropy in lipid bilayer membranes: Coupled plasmon-waveguide resonance measurements of molecular orientation, polarizability, and shape. *Biophysical Journal*, 80:1557–1567, 2001.

[16] A. Erbe and R. Sigel. Tilt angle of lipid acyl chains in unilamellar vesicles determined by ellipsometric light scattering. *The European Physical Journal E*, 22:303–309, 2007.

[17] J. F. Nagle and S. Tristram-Nagle. Structure of lipid bilayers. *Biochimica et Biophysica Acta.*, 1469:159–195, 2000.

[18] M.I. Gurr and J. L Harwood. *Lipid Biochemistry*. S. Edmundsbury Press, fourth edition edition, 1991.

[19] W. Tsuzuki. cis trans isomerization of carbon double bonds in monounsaturated triacylglycerols via generation of free radicals. *Chemistry and Physics of Lipids*, 163:741–745, 2010.

[20] J. L. Harwood, F. D. Gunstone and F. B Padley. *The Lipid Handbook*. University Press, second edition edition, 1994.

[21] V. Luzzati and A. Tardieu. Lipid phases: Structure and structural transisitons. *Annual Review of Physical Chemistry*, 25:79–94, 1974.

[22] P. H. E. Meijer, P. Papon and J. Lebold. *The Physics of Phase Transitions concepts and applications*. Springer, 1999.

[23] P. M. Chaikin and T. C. Lubensky. *Principles of Condensed Matter Physics*. Cambridge University Press, 2000.

[24] S. Mabrey and J. M. Sturtevant. Investigation of phase transitions of lipids and lipid mixtures by high sensitivity differential scanning calorimetry. *Proc. Natl. Acad. Sci. USA*, 73:3862–3866, 1976.

[25] G. Lehner. *Electromagnetic Field Theory for Engineers and Physicist*. Springer, 2010.

[26] D. J. Griffiths. *Introduction to Electrodynamics*. Prentice Hall Inc., second edition edition, 1989.

[27] M. Zahn. *Electromagnetic Field Theory: a problem solving approach*. Robert E Krieger Publishing Company, Inc, 1979.

[28] J. D. Jackson. *Classical Electrodynamics*. John Wiley and Sons, Inc., second edition, 1975.

[29] D. Den Engelsen. Optical anisotropy in ordered systems of lipids. *Surface Science*, 56:272–280, 1976.

[30] A. Sihvola. Dielectric polarization and particle shape effects. *Journal of Nanomaterials*, 2007:9, 2007.

[31] C. J. F. Böttcher and P. Borewijk. *Theory of Electric Polarizaion-Dielectrics in time-dependent fields*, volume 2. Elsevier Scientific Publishing Company, 2 edition, 1978.

[32] E. E. Burnell and C. A. de Lange. *NMR of Ordered Liquids*. Academic Publishers, 2003.

[33] E. Collett. *Polarized Light Fundamentals and Applications*. Marcel Dekker, Inc., 1993.

[34] E. E. Wahlstrom. *Optical Crystalogrphy*. John Wiley and Sons, Inc., forth edition, 1969.

[35] P. L. Finn, E. Betzig and J. S. Weiner. Combined shear force and near-field scanning optical microscopy. *Applied Physics Letters*, 60:2484–2486, 1992.

[36] G. H. Morrison G. A. Valaskovic and M. Holton. Parameter control, characterization, and optimization in the fabrication of optical fiber near-field probes. *Applied Optics*, 34:1215, 1995.

[37] L. Novotny and C. Hafner. Light propagation in a cylindrical waveguide with a complex, metallic, dielectric function. *Physical Review E*, 50(5):4094–4106, 1994.

[38] G. R. Fowles and G. L. Cassiday. *Analytical Mechanics*. Saunders College Publishing, sixth edition, 1999.

[39] Y. Qin and R. Reifenberger. Calibrating a tuning fork for use as a scanning probe microscope force sensor. *Review of Scientific Instruments*, 78:063704, 2007.

[40] About Lock -In Amplifiers. Technical report, Stanford Research Systems www.thinkSRS.com, 2010.

[41] K. Hsu and L. A. Gheber. Tip-sample interaction in a shear-force near-field scanning optical microscope. *Review of Scientific Instruments*, 70:3609–3613, 1999.

[42] M. A. Lee, C. E. Talley and Robert C. Dunn. Single molecule detection and underwater fluorescence imaging with cantilevered near-field fiber optic probes. *Applied Physics Letters*, 72(23):2954, 1998.

[43] Hinds Instruments. Photoelastic modulators.

[44] *http://plastics.dupont.com/plastics/dsheets/delrin/DELRIN150NC010.pdf*.

[45] H. Fuchs and B. Bhushan, editor. *Applied Scanning Probe Methods VIII: Scanning Probe Microscopy Techniques (NanoScience and Technology)*. Number 8. Springer, 2008.

[46] *http* : *//www.nanosensors.com/pointprobe_plus.pdf*.

[47] A. A. Baski and H. Fuchs. Epitaxial growth of silver on mica as studied by afm and stm. *Surface Science*, 313:275–288, 1994.

[48] J. J. Weimer, D. D. Hawn, L. S. Shlyakhtenko, A. A. Gall and Yuri L. Lyubchenko. Atomic force microscopy imaging of dna covalently immobilized on a functionalized mica substrate. *Biophysical Journal*, 77:568–576, 1999.

[49] K. W. Bladh, J. W. Anthony, R. A. Bideaux and M. C. Nichols. *Handbook of Mineralogy*. Mineral Data Publishing, 2001.

[50] J. P. Chang, Y. J. Chabal, A. B. Gurevich, J. Sapjeta, K. T. Queeney, M. K. Weldon and R. L. Opila. Infrared spectroscopic analysis of the si/sio2 interface structure of thermally oxidized silicon. *Journal of Applied Physics*, 87(3):1322, 200.

[51] H.F. Okorn-Schmidt. Characterization of silicon surface preparation processes for advanced gate dielectrics. *IBM Journal of Research and Development*, 43(3):351–326, 1999.

[52] P. S. Cremer and S. G. Boxer. Formation and spreading of lipid bilayers on planar glass supports. *Journal of Physical Chemistry B*, 103:2554–2559, 1999.

[53] F. Haque, E. A. Proctor, A. E. Ribbe, K. J. Seu, A. P. Pandey and J. S. Hovis. Effect of surface treatment on diffusion and domain formation in supported lipid bilayers. *Biophysical Journal*, 92:2445–2450, 2007.

[54] B. A. Nellis, C. Xing, R. Faller, C. W. Frank, S. H. Risbud, J. H. Satcher Jr., M. L. Longo, E. I. Goksu and M. I. Hoopes. Silica xerogel/aerogel-supported lipid bilayers: Consequences of surface corrugation. *Biochimica et Biophysica Acta (BBA) - Biomembranes*, 1798:719–729, 2010.

[55] E. I. Goksu and M. L. Longo. Ternary lipid bilayers containing cholesterol in a high curvature silica xerogel environment. *Langmuir*, 26:8614–8624, 2010.

[56] D. J. Duval, S. H. Risbud, K. C. Weng, J. J. R. Stålgren and C. W. Frank. Fluid biomembranes supported on nanoporous aerogel/xerogel substrates. *Langmuir*, 20:7232–7239, 2004.

[57] N. Chu, H. I. Petrache, S. Tristram-Nagle, N. Kučerka, Y. Liu and John F. Nagle. Structure of fully hydrated fluid phase dmpc and dlpc lipid bilayers using x-ray scattering from oriented multilamellar arrays and from unilamellar vesicles. *Biophysical Journal*, 88:2626–2637, 2005.

[58] M. A. Knewtson, C. R. Worthington,-S. Tristram-Nagle, W.J. Sun, R. M. Suter and J. F. Nagle. Order and disorder in fully hydrated unoriented bilayers of gel phase dipalmitoyphosphtidylcholine. *Physical Review E*, 49:4665–4676, 1994.

[59] R. M Suter, C. R. Worthington, -W.J. Sun S. Tristram-Nagle, R. Zhang and J. F. Nagle. Measurements of chain tilt angle in fully hydrated bilayers of gel phase lecithins. *Biophysical Journal*, 64:1097–1109, 1993.

[60] J. H. Crowe, O. G. Mouritsen, T. Kaasgaard, C. Leidy and K. Jrgensen. Temperature-controlled structure and kinetics of ripple phases in one- and two-component supported lipid bilayers. *Biophysical Journal*, 85:350–360, 2003.

[61] J. H. Crowe, O. G. Mouritsen, C. Leidy, T. Kaasgaard and K. Jrgensen. Ripples and the formation of anisotropic lipid domains: Imaging two- component supported double bilayers by atomic force microscopy. *Biophysical Journal*, 83:2625–2633, 2002.

[62] T. V. Ratto, W. Lin, C. D. Blanchette and M. L. Longo. Lipid asymmetry in dlpc/dspc-supported lipid bilayers: A combined afm and fluorescence microscopy study. *Biophysical Journal*, 90:228–237, 2006.

[63] E. J. Dufourc, J. Katsaras, V. A. Raghunathan and J. Dufourcq. Evidence for a two-dimensional molecular lattice in subgel phase dppc bilayers. *Biochemistry*, 34:4684–4688, 1995.

[64] M. Born and E. Wolf. *Principles of Optics, electromagnetic theory of propagation, interference and diffraction of light*. University Press, 2006.

[65] R.N. McElhaney, R. Bittman, T.P. McMullen and C. Vilchze. Differential scanning calorimetric study of the effect of sterol side chain length and structure on dipalmitoylphosphatidylcholine thermotropic phase behavior. *Biophysical Journal*, Biophysical Journal 69(1):169–176, 1995.

[66] R. N. A. H. Lewis, D. A. Mannock and R. N. McElhaney. Comparative calorimetric and spectroscopic studies of the effects of lanosterol and cholesterol on the thermotropic phase behavior and organization of dipalmitoylphosphatidylcholine bilayer membranes. *Biophysical Journal*, 91:3327–3340, 2006.

[67] G. A. Voth J. Liam McWhirter and Gary Ayton. Coupling field theory with mesoscopic dynamical simulations of multicomponent lipid bilayers. *Biophysical Journal*, 87:3242–3263, 2004.

[68] *http://www.avantilipids.com*.

[69] T. Gutberlet and J. Katsaras, editor. *Lipid Bilayers structure and interactions*. Springer, 2001.

[70] M. Gitterman and V. Halpern. *Phase Transitions a brief account with modern applications*. World Scientific Publishing Co., 2004.

[71] H. E. Stanley. *Introduction to Phase Transitions and Critical Phenomena*. Oxford University Press, 1971.

[72] P. Oswald and P. Pieranski. *Nematic and Cholesteric Liquid Crystals*. Taylor & Francis Group, 2005.

[73] M. E. Starzak. *The Physical Chemistry of Membranes*. Academic Press, 1984.

[74] F.Reif. *Fundamentals of Statistical and Thermal Physics*. McGraw-Hill Inc, 1965.

[75] K. Binder. Theory of first-order phase transitions. *Reports on Progress in Physics*, 50:783–859, 1987.

[76] P. H. Bligh and R. Haywood. Latent heat - its meaning and measurement. *European Journal of Physics*, 7:245–251, 1986.

[77] M. Caffrey. *Lipidat - A Database of Thermodynamic Data and Associated Information on Lipid Mesomorphic and Polymorphic Transitions*. CRC Press, Inc, 1993.

[78] G. G. Raju. *Dielectrics in Electric Fields*. Marcel Dekker, Inc, 2003.

[79] C. D'Ambriosio and L. Powers. Optical studies of the phase behavior of monodomain samples of dipalmitoylphosphatidylcholine containing calcium chloride. *Biophysical Journal*, 27:15–20, 1979.

[80] J. Popplewell, M. Textor, A. Mashaghi, M. Swann and E. Reimhult. Optical anisotropy of supported lipid structures probed by waveguide spectroscopy and its application to study of supported lipid bilayer formation kinetics. *Analytical Chemistry*, 80:3666–3676, 2008.

[81] K. Satoh, K. Mishima and T. Ogihara. Optical birefringence of phosphatidylcholine liposomes in gel phases. *Biochimica et Biophysica Acta*, 898:231–238, 1987.

[82] M. Ferreira T. Charitat C. Scomparin, S. Lecuyer and B Tinland. Diffusion in supported lipid bilayers: Influence of substrate and preparation technique on the internal dynamics. *The European Physical Journal E*, 28:211–220, 2009.

[83] S. C. McClain E. B. McDaniel and J. W. P.Hsu. Nanometer scale polarimetry studies using a near-field scanning optical microscope. *Applied Optics*, 37:84–92, 1998.

[84] O. L. Mooren, N. E. Dickenson, E. S. Erickson and R. C. Dunn. Characterization of power induced heating and damage in fiber optic probes for near-field scanning optical microscopy. *Review of Scientific Instruments*, 78:053712, 2007.

[85] A. L. Campillo and J. W. P. Hsu. Near-field scanning optical microscope studies of the anisotropic stress variations in patterned sin membranes. *Journal of Applied Physics*, 91:646, 2002.

[86] M. J. Fasolka, F. Renaldo,J. Hwang, L. S. Goldner, S. N. Goldie and J. F. Douglas. Near-field polarimetric characterization of polymer crystallites. *Applied Physics Letters*, 85:1338, 2004.

[87] M. D. Greenberg. *Advanced Engineering Mathematics*. Prentice Hall Inc., 1998.

[88] R. Oldenbourg. Polarized light field microscopy: an analytical method using a microlens array to simultaneously capture both conoscopic and orthoscopic views of birefringent objects. *Journal of Microscopy*, 231:419–432, 2008.

[89] F. J. Giessibl. Advances in atomic force microscopy. *Reviews of Modern Physics*, 75, 2003.

[90] M. E. Gunter Melinda Darby Dyar and Dennis Tasa. *Mineralogy and Optical Mineralogy*. Mineralogical Society of America, 2008.

[91] T.S. Sorensen, editor. *Surface Chemistry and Electrochemistry of Membranes surfactant science series volume 79*. Marcel Dekker, Inc., 1999.

[92] E. Finotb, Z. Leonenkoa and D. Cramb. Afm study of interaction forces in supported planar dppc bilayers in the presence of general anesthetic halothane. *Biochimica et Biophysica Acta (BBA) - Biomembranes*, 1758:487–492, 2006.

APPENDICES

A. PROPERTIES OF AN ELLIPSE

The equation for an ellipse is,

$$\frac{x^2}{a^2} + \frac{y^2}{b^2} = 1 \tag{A.1}$$

where a and b are the semi major and minor axes. We can represent this equation in polar coordinates by equating,

$$x = r\cos(\theta), \qquad \text{and} \qquad y = r\sin(\theta). \tag{A.2}$$

Resulting in,

$$\frac{r^2\cos^2(\theta)}{a^2} + \frac{r^2\sin^2(\theta)}{b^2} = 1 \tag{A.3}$$

Where,

$$r^2 = \frac{a^2b^2}{a^2sin^2(\theta) + b^2cos^2(\theta)} \tag{A.4}$$

At any point $\mathbf{r_1} = (x_1, y_1)$ on the ellipse, the line tangent to the point is of the form,

$$\begin{aligned} y &= mx + k \\ &\quad \text{and at point } (x_1, y_1) \\ y_1 &= mx_1 + k. \end{aligned} \tag{A.5}$$

By subtracting the two equations we can obtain,

$$(y - y_1) = m\,(x - x_1) \tag{A.6}$$

Note that at point (x_1, y_1) the slope of the tangent line is equal to the derivative of the ellipse.

From equation A.1 we can obtain,

$$y = \sqrt{\left(b^2 - \frac{b^2x^2}{a^2}\right)}. \tag{A.7}$$

Hence,

$$\frac{dy}{dx} = -\frac{b^2x}{a^2}\frac{1}{\sqrt{\left(b^2 - \frac{b^2x^2}{a^2}\right)}}. \tag{A.8}$$

We evaluate equation A.8 at (x_1, y_1), where the it reduces to,

$$\frac{dy}{dx} = -\frac{b^2x_1}{a^2y_1} \; = m \tag{A.9}$$

Substituting equation A.9 into equation A.6 we obtain

$$(y - y_1) = -\frac{b^2x_1}{a^2y_1}\,(x - x_1)\,, \tag{A.10}$$

resulting in,

$$\frac{{x_1}^2}{a^2} + \frac{{y_1}^2}{b^2} = \frac{x_1x}{a^2} + \frac{y_1y}{b^2} = 1. \tag{A.11}$$

From equation A.11 we note that at $y = 0$, $x_1x = a^2$ and when $x = 0$, $y_1y = b^2$.

Dividing the two expressions,

$$\frac{y_1 y}{x_1 x} = \frac{b^2}{a^2} \tag{A.12}$$

From Figure A.1 we see that

$$\frac{y_1}{x_1} = \tan(\theta) \tag{A.13}$$

and

$$\frac{y}{x} = \tan(\psi) \tag{A.14}$$

Revealing the following equation,

$$\tan(\psi) = \frac{b^2}{a^2}\cot(\theta) \tag{A.15}$$

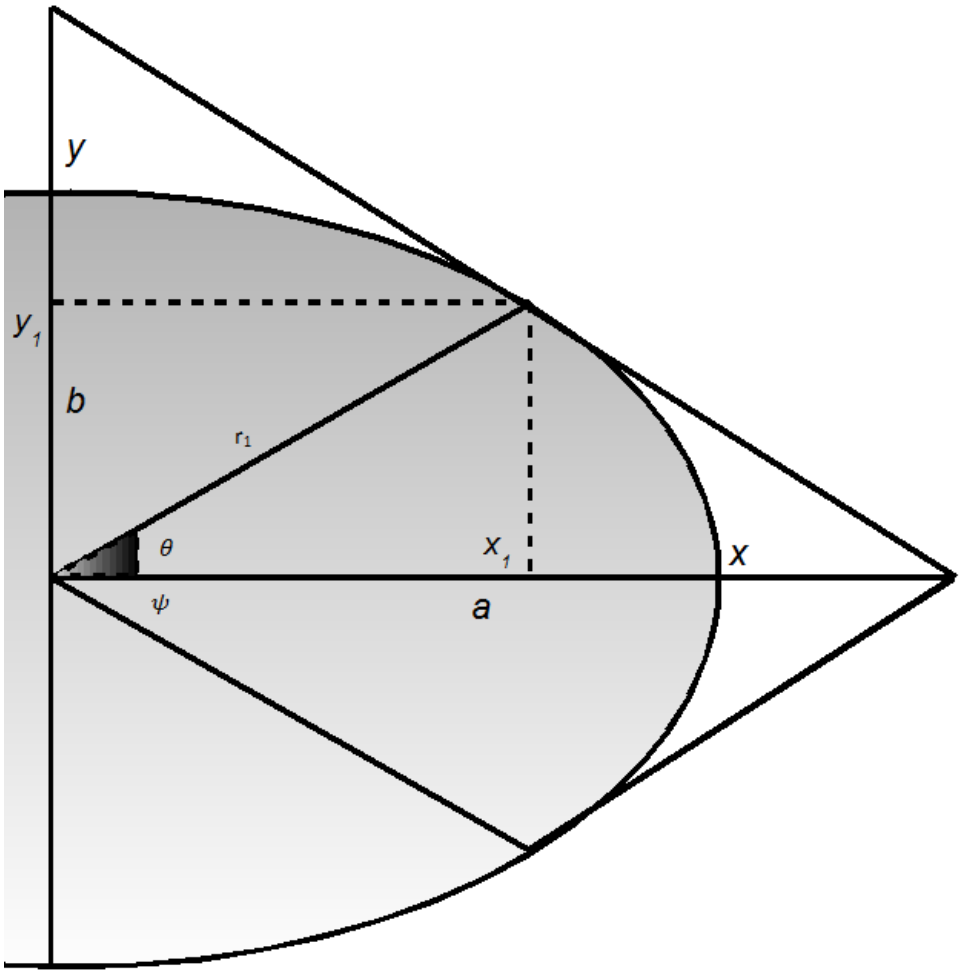

Figure A.1. Diagram of an ellipse used to display the geometry discussed in this section.

B. PERMITTIVITY'S RELATION TO POLARIZABILITY

We begin with the dielectric response of the material,

$$\mathbf{D} = \epsilon_o \mathbf{E} + \mathbf{P}, \qquad \text{where} \qquad \mathbf{D} = \epsilon_i \mathbf{E} \tag{B.1}$$

where $\mathbf{D}$ is the displacement field, $\mathbf{E}$ is the macroscopic electric field, $\mathbf{P}$ is the polarization of the material, ϵ_o is the permittivity of free space and ϵ_i is the permittivity of the material (Note, that all tensors are aligned along the principle axis.). We now use the following

$$\mathbf{P} = (\epsilon_i - \epsilon_o)\,\mathbf{E} \qquad \text{and} \qquad \mathbf{E} = \mathbf{E}^{local} - L_i \mathbf{P}. \tag{B.2}$$

Where $\mathbf{E}^{local}$ is the local electric field and L_i is the shape factor. We can now solve for the permittivity using the previous equations

$$\epsilon_i = \frac{\mathbf{P}}{\mathbf{E}} + \epsilon_o = \frac{\mathbf{P}}{\mathbf{E}^{local} - L_i \mathbf{P}} + \epsilon_o, \tag{B.3}$$

now substituting in $\mathbf{P} = \frac{\alpha_i \mathbf{E}^{local}}{V}$, where α_i and V are the polarizability and volume of the material, we obtain,

$$\epsilon_i = \frac{\alpha_i \mathbf{E}^{local}}{V\left(\mathbf{E}^{local} - \frac{L_i \alpha_i \mathbf{E}^{local}}{V}\right)} + \epsilon_o \tag{B.4}$$

Now the final expression

$$\epsilon_i = {n_i}^2 = \frac{\alpha_i}{(V - \alpha_i L_i)} + \epsilon_o, \tag{B.5}$$

which relates the index of refraction (n_i) to α_i. Utilizing

$$\alpha_z = \alpha_{\text{avg}} + \frac{2}{3}(\alpha_l - \alpha_t)\,\Omega \tag{B.6}$$

and

$$\alpha_x = \alpha_{\text{avg}} - \frac{1}{3}(\alpha_l - \alpha_t)\,\Omega, \tag{B.7}$$

we are able to determine the translational (α_t) and longitudinal (α_l) polarizabilities (α_l), knowing the order parameter ($\Omega = \frac{1}{2}(3\cos^2(\theta) - 1)$), n_i and L_i for the corresponding lipid molecule [15].

C. ENERGY PROPAGATION THROUGH AN ANISOTROPIC MEDIUM

Here we will show how through an anisotropic medium the energy propagation and plane wave propagation may not be in the same direction. We state with Maxwells equation [26–28, 64], and assuming the current density $\mathbf{J}$ is equal to zero,

$$\nabla \times \mathbf{H} = \frac{\partial \mathbf{D}}{\partial t}\,, \text{ and } \nabla \times \mathbf{E} = -\frac{\partial \mathbf{B}}{\partial t}, \tag{C.1}$$

Where,

$$\mathbf{D}\,,\ \mathbf{E},\ \mathbf{H},\ \text{and } \mathbf{B} \propto e^{\mathrm{i}\omega\left(\frac{n}{c}\mathbf{k}\cdot\mathbf{r}-t\right)}. \tag{C.2}$$

We note that $\frac{\partial}{\partial t}$ and $\frac{\partial}{\partial j}$ with functions of this type, is equivalent to multiplying by $-i\,\omega$ and $\frac{\mathrm{i}\omega n k_j}{c}$ respectively [64]. We then obtain

$$\frac{\partial \mathbf{E}}{\partial t} = -\mathrm{i}\omega\mathbf{E}, \tag{C.3}$$

$$\nabla \times \mathbf{E} = \frac{\mathrm{i}\omega\ n}{c}\,(\mathbf{k}\times\mathbf{E})\ =\ \mathrm{i}\,\omega\mu\mathbf{H}\,,\ \nabla\times\mathbf{H}\ =\ -\mathrm{i}\,\omega\mathbf{D}. \tag{C.4}$$

Taking the curl of both sides of the equations, results in,

$$-\frac{n^2}{c^2}\,\mathbf{k}\times(\mathbf{k}\times\mathbf{E})\ \ =\ \mu\mathbf{D}\,, \tag{C.5}$$

$$\begin{aligned}\mathbf{D} &= \frac{-n^2}{\mu c^2}(\mathbf{k}(\mathbf{k}\cdot\mathbf{E}) - \mathbf{E}(\mathbf{k}\cdot\mathbf{k})) \\ &= \frac{n^2}{\mu c^2}\left(\mathbf{E} - \mathbf{E}_{\|_k}\right) \\ &= \frac{n^2}{\mu c^2}\mathbf{E}_{\perp_k} \end{aligned} \tag{C.6}$$

Where in terms of the energy density w,

$$\begin{aligned} w &= w_E + w_m \\ &= \frac{1}{2}(\mathbf{E}\cdot\mathbf{D} + \mathbf{B}\cdot\mathbf{H}) \\ &= \frac{n}{2c}(-(\mathbf{E}\cdot\mathbf{k}\times\mathbf{H}) + (\mathbf{k}\times\mathbf{E})\cdot\mathbf{H}) \\ &= \frac{n}{c}\mathbf{k}\cdot(\mathbf{E}\times\mathbf{H}) \\ &= \frac{n}{c}\mathbf{k}\cdot\mathbf{S} \end{aligned} \tag{C.7}$$

We know that the speed of $\mathbf{S}$ is equal to,

$$v_S = \frac{|\mathbf{S}|}{w} = \frac{c}{n\hat{\mathbf{k}}\cdot\hat{\mathbf{S}}}. \tag{C.8}$$

(The energy equation in differential form is -$\nabla\cdot\mathbf{S} = \frac{\partial w}{\partial t}$ [64]) The speed of the plane wave can be written as

$$v_k = v_S\hat{\mathbf{k}}\cdot\hat{\mathbf{S}} = v_S\cos(\Theta). \tag{C.9}$$

where Θ is the direction the energy propagates relative to the wave normal in an anisotropic medium.

D. EXPECTED INTENSITY FOR THE ENTIRE SYSTEM

A Jones' matrix representation of an optical set up that is able to measure the retardance S and its optical orientation θ simultaneously is presented in this appendix. First linearly polarized light (represented by vector $\binom{1}{0}$, which determines the system's axis) propagates through the Polarization Elastic Modulator (PEM) oriented at 45°, with a retardance of A. It then propagates through a quarter wave plate (QWP) aligned system's axis, followed by a sample with a retardance S and optical orientation θ. Post sample the light travels through a QWP in the same configuration as the first and finally through an analyzer oriented at -45°.

$$\begin{aligned}\begin{pmatrix} \mathbf{E}_x \\ \mathbf{E}_y \end{pmatrix} = \frac{1}{2}&\begin{pmatrix} 1 & -1 \\ -1 & 1 \end{pmatrix} \cdot \begin{pmatrix} e^{i\frac{\pi}{4}} & 0 \\ 0 & e^{-i\frac{\pi}{4}} \end{pmatrix} \cdot \begin{pmatrix} \cos(\theta) & \sin(\theta) \\ -\sin(\theta) & \cos(\theta) \end{pmatrix} \\ &\cdot \begin{pmatrix} e^{i\frac{S}{2}} & 0 \\ 0 & e^{-i\frac{S}{2}} \end{pmatrix} \cdot \begin{pmatrix} \cos(\theta) & -\sin(\theta) \\ \sin(\theta) & \cos(\theta) \end{pmatrix} \\ &\cdot \begin{pmatrix} e^{i\frac{\pi}{4}} & 0 \\ 0 & e^{-i\frac{\pi}{4}} \end{pmatrix} \cdot \begin{pmatrix} \cos\left(\frac{\pi}{4}\right) & \sin\left(\frac{\pi}{4}\right) \\ -\sin\left(\frac{\pi}{4}\right) & \cos\left(\frac{\pi}{4}\right) \end{pmatrix} \\ &\cdot \begin{pmatrix} e^{i\frac{A}{2}} & 0 \\ 0 & e^{-i\frac{A}{2}} \end{pmatrix} \cdot \begin{pmatrix} \cos\left(\frac{\pi}{4}\right) & -\sin\left(\frac{\pi}{4}\right) \\ \sin\left(\frac{\pi}{4}\right) & \cos\left(\frac{\pi}{4}\right) \end{pmatrix} \cdot \begin{pmatrix} 1 \\ 0 \end{pmatrix}\end{aligned} \tag{D.1}$$

The resulting electric field is,

$$\begin{pmatrix} \mathbf{E}_x \\ \mathbf{E}_y \end{pmatrix} = \tfrac{1}{2}\left(i\cos\left(\tfrac{1}{2}(A+S-2\theta)\right)+\sin\left(\tfrac{1}{2}(A-S-2\theta)\right)\right) (\cos(\theta)-i\sin(\theta)) \begin{pmatrix} -1 \\ 1 \end{pmatrix}. \tag{D.2}$$

The intensity $(\mathbf{E}\cdot\mathbf{E}^*)$ is proportional to,

$$\mathbf{E}\cdot\mathbf{E}^* \propto \frac{1}{2} - \frac{1}{2}\sin(A)\sin(S)\cos(2\theta) + \frac{1}{2}\cos(A)\sin(S)\sin(2\theta) \tag{D.3}$$

where $A = B\cos(\omega t)$, (B is the magnitude of the retardance and ω is the frequency set by the PEM.). The signal normalized by the DC term at the first harmonic (I_ω) and the second harmonic ($I_{2\omega}$) are,

$$I_\omega = J_1(B)\sin(S)\cos(2\theta) \tag{D.4}$$

$$I_{2\omega} = J_2(B)\sin(S)\sin(2\theta) \tag{D.5}$$

Hence,

$$\theta = \frac{1}{2}\arctan\left(\frac{-I_{2\omega}\ J_1(B)}{I_\omega J_2(B)}\right) \tag{D.6}$$

and the retaradance S is,

$$S = \arcsin\left(\frac{I_\omega}{J_1(B)\cos(2\theta)}\right) = \arcsin\left(\frac{-I_{2\omega}}{J_2(B)\sin(2\theta)}\right) \tag{D.7}$$

E. PHOTO ELASTIC MODULATOR ALIGNMENT

Linear polarized light oriented at angle β travels through the PEM at 45° (where $A = B\cos(\omega t)$) and travels through an analyser at angle α.

$$\begin{pmatrix} \mathbf{E}_x \\ \mathbf{E}_y \end{pmatrix} = \begin{pmatrix} \cos^2(\alpha) & -\cos(\alpha)\sin(\alpha) \\ -\cos(\alpha)\sin(\alpha) & \sin^2(\alpha) \end{pmatrix} \begin{pmatrix} \cos\left(\frac{\pi}{4}\right) & \sin\left(\frac{\pi}{4}\right) \\ -\sin\left(\frac{\pi}{4}\right) & \cos\left(\frac{\pi}{4}\right) \end{pmatrix} \begin{pmatrix} e^{i\frac{A}{2}} & 0 \\ 0 & e^{-i\frac{A}{2}} \end{pmatrix} \begin{pmatrix} \cos\left(\frac{\pi}{4}\right) & -\sin\left(\frac{\pi}{4}\right) \\ \sin\left(\frac{\pi}{4}\right) & \cos\left(\frac{\pi}{4}\right) \end{pmatrix} \begin{pmatrix} \cos(\beta) & -\sin(\beta) \\ \sin(\beta) & \cos(\beta) \end{pmatrix} . \begin{pmatrix} 1 \\ 0 \end{pmatrix} \tag{E.1}$$

The resulting E-field is,

$$\begin{pmatrix} \mathbf{E}_x \\ \mathbf{E}_y \end{pmatrix} = \left(\cos\left(\frac{A}{2}\right)\cos(\alpha+\beta) + i\sin\left(\frac{A}{2}\right)\sin(\alpha-\beta)\right) \begin{pmatrix} \cos(\alpha) \\ -\sin(\alpha) \end{pmatrix} \tag{E.2}$$

and

$$\begin{aligned} \mathbf{E}\cdot\mathbf{E}^* \propto \; & \tfrac{1}{2} - \tfrac{1}{2}\sin(2\alpha)\sin(2\beta) + \tfrac{1}{2}\cos(2\alpha)\cos(2\beta)J_0(B) \\ & -J_2(B)\cos(2\alpha)\cos(2\beta)\cos(2\omega\mathrm{t})\ldots \end{aligned} \tag{E.3}$$

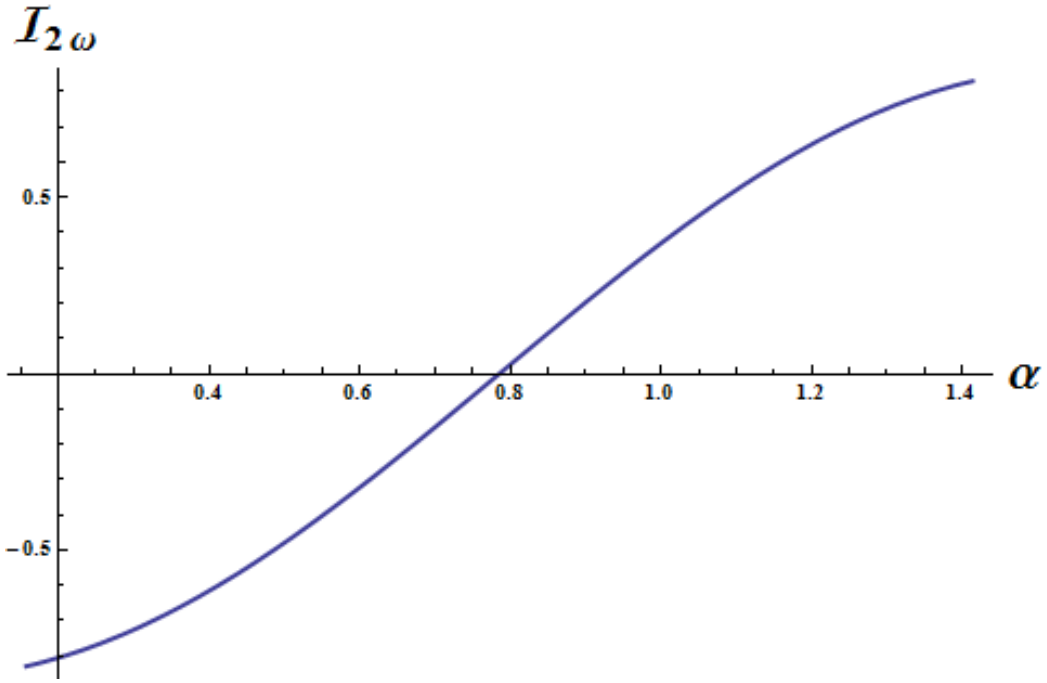

Figure E.1. Graph of $I_{2\omega}$ as a function of analyzer angle α, showing the overall signal approaching zero as it is aligned with the axis of the PEM.

Where we can use the signal at the second harmonic (R_2) and determine the intensity at the second harmonic ($I_{2\omega}$) by normalizing R_2 with the DC signal,

$$I_{2\omega} = \frac{R_2}{\mathrm{DC}} = J_2(2.407)\frac{-\cos(2\alpha)\cos(2\beta)}{\frac{1}{2} - \frac{1}{2}\sin(2\alpha)\sin(2\beta)}. \tag{E.4}$$

Within the experimental limitations β can be made ~ 0, where $I_{2\omega} \approx 0$ for $\alpha = \pi/4$. It can then be seen graphically in figure E.1 that a zero signal can only be obtained when α is aligned with the PEM.

F. PHOTO-ELASTIC MODULATOR-ALIGNMENT WITH LINEAR POLARIZER

Linear polarized light with its resultant electric field vector pointing at 0° passes through a Photo Elastic Modulator (PEM), with a retardance $A = B\cos(\omega t)$ and positioned at an angle β. The light is then analyzed with a linear polarizer positioned at an angle α,

$$\begin{pmatrix} \mathbf{E}_x \\ \mathbf{E}_y \end{pmatrix} = \begin{pmatrix} \cos^2(\alpha) & -\cos(\alpha)\sin(\alpha) \\ -\cos(\alpha)\sin(\alpha) & \sin^2(\alpha) \end{pmatrix} \cdot \begin{pmatrix} \cos(\beta) & \sin(\beta) \\ -\sin(\beta) & \cos(\beta) \end{pmatrix} \cdot \begin{pmatrix} e^{i\frac{A}{2}} & 0 \\ 0 & e^{-i\frac{A}{2}} \end{pmatrix} \cdot \begin{pmatrix} \cos(\beta) & -\sin(\beta) \\ \sin(\beta) & \cos(\beta) \end{pmatrix} \cdot \begin{pmatrix} 1 \\ 0 \end{pmatrix} \tag{F.1}$$

the resulting electric field is,

$$\begin{pmatrix} \mathbf{E}_x \\ \mathbf{E}_y \end{pmatrix} = \left(\cos\left(\frac{A}{2}\right)\cos(\alpha) + i\cos(\alpha - 2\beta)\sin\left(\frac{A}{2}\right)\right) \begin{pmatrix} \cos(\alpha) \\ -\sin(\alpha) \end{pmatrix} \tag{F.2}$$

With $A = B\cos(\omega t)$, the intensity $(\mathbf{E}\cdot\mathbf{E}^*)$ is proportional to

$$\mathbf{E}\cdot\mathbf{E}^* \propto \frac{1}{2}\left(\cos^2(\alpha) + \cos^2(\alpha - 2\beta)\right) - \frac{1}{2}J_0(B)\sin(2(\alpha-\beta))\sin(2\beta) + J_2(B)\cos(2\omega t)\sin(2(\alpha-\beta))\sin(2\beta) + \ldots \tag{F.3}$$

When the first and second polarizers are aligned, $\alpha = 0$,

$$\mathbf{E} \cdot \mathbf{E}^* \propto \frac{1}{2}\left(1 + \cos^2(2\beta)\right) + \frac{1}{2}J_0(B)\sin^2(2\beta) - J_2(B)\cos(2\omega \mathrm{t})\sin^2(2\beta) + ... \quad \text{(F.4)}$$

G. SMALL ANGLE APPROXIMATIONS

G.1 Total System with Small Angle Approximations

Here small angle approximations for the total system are performed, where the positions and retardance values of the two quarter wave plates and analyzer are deviated from their desired values. Below we have the Jones' matrix representation of linear polarized light travelling through a PEM (45°) a QWP (θ) and an additional retardance (Δ). It then passes through an additional QWP (γ) and with an additional retardance δ and finally through the analyzer (α).

$$
\begin{aligned}
\begin{pmatrix} \mathbf{E}_x \\ \mathbf{E}_y \end{pmatrix} \;=\; & \begin{pmatrix} \cos^2(\alpha) & -\cos(\alpha)\sin(\alpha) \\ -\cos(\alpha)\sin(\alpha) & \sin^2(\alpha) \end{pmatrix} \cdot \\
& \begin{pmatrix} 1 & \gamma \\ -\gamma & 1 \end{pmatrix} \cdot \begin{pmatrix} e^{i\left(\frac{\pi}{4}\right)}\left(1+i\frac{\delta}{2}\right) & 0 \\ 0 & e^{-i\left(\frac{\pi}{4}\right)}\left(1-i\frac{\delta}{2}\right) \end{pmatrix} \cdot \begin{pmatrix} 1 & -\gamma \\ \gamma & 1 \end{pmatrix} \cdot \\
& \begin{pmatrix} 1 & \theta \\ -\theta & 1 \end{pmatrix} \cdot \begin{pmatrix} e^{i\left(\frac{\pi}{4}\right)}\left(1+i\frac{\Delta}{2}\right) & 0 \\ 0 & e^{-i\left(\frac{\pi}{4}\right)}\left(1-i\frac{\Delta}{2}\right) \end{pmatrix} \cdot \begin{pmatrix} 1 & -\theta \\ \theta & 1 \end{pmatrix} \cdot \\
& \begin{pmatrix} \cos\left(\frac{\pi}{4}\right) & \sin\left(\frac{\pi}{4}\right) \\ -\sin\left(\frac{\pi}{4}\right) & \cos\left(\frac{\pi}{4}\right) \end{pmatrix} \cdot \begin{pmatrix} e^{i\frac{A}{2}} & 0 \\ 0 & e^{-i\frac{A}{2}} \end{pmatrix} \cdot \\
& \begin{pmatrix} \cos\left(\frac{\pi}{4}\right) & -\sin\left(\frac{\pi}{4}\right) \\ \sin\left(\frac{\pi}{4}\right) & \cos\left(\frac{\pi}{4}\right) \end{pmatrix} \cdot \begin{pmatrix} 1 \\ 0 \end{pmatrix}
\end{aligned}
\tag{G.1}
$$

And we obtain an expression for the intensity,

$$\begin{aligned}\mathbf{E}\cdot\mathbf{E}^{*} \propto \ & \tfrac{1}{2} + \sin(A)\left((\gamma+\theta)\ \cos(2\alpha) - \tfrac{1}{2}(\delta+\Delta)\sin(2\alpha)\right) \\ & + \tfrac{1}{2}\cos(A)(\cos(2\alpha) + 2(\gamma+\theta)\sin(2\alpha))\end{aligned} \tag{G.2}$$

where $A = B\cos(\omega t)$, which yields,

$$\begin{aligned}\mathbf{E}\cdot\mathbf{E}^{*} \propto \frac{1}{2} + 2J_1(B)\cos(\omega t)\left((\gamma+\theta)\ \cos(2\alpha) - \frac{1}{2}(\delta+\Delta)\sin(2\alpha)\right) \\ - J_2(B)\cos(2\omega\mathrm{t})(\cos(2\alpha) + 2(\gamma+\theta)\sin(2\alpha)) + \ldots\end{aligned} \tag{G.3}$$

when $\alpha = 45°$,

$$\mathbf{E}\cdot\mathbf{E}^{*} \propto \ \tfrac{1}{2} - J_1(B)(\delta+\Delta)\cos(\omega t) - 2J_2(B)(\gamma+\theta)\cos(2\omega\mathrm{t}) + \ldots \tag{G.4}$$

Where we obtain a signal at the first and second harmonics,

$$R_1 \ = \ -J_1(B)(\delta+\Delta) \quad \text{and} \quad R_2 \ = \ -2J_2(B)(\gamma+\theta) \tag{G.5}$$

We can see from this that R_1 is sensitive on the small deviations in the retardance and R_2 on the optical orientation of the wave plates.

G.2 Total System with Small Retardance Error

Here a similar small angle approximation is performed where the two quarter wave plates are aligned with the system's axis and a sample with a retardance S and

orientation θ. The wave plates can be aligned by minimizing the intensity of the system with the PEM off, using the polarizers. Below the Jones' matrix representation is used to describe linear polarized light travelling through a PEM (45°) a QWP (0°) and with an additional retardance (Δ). Followed by travelling through a sample of retardance S and oriented at a position (θ). Then passing through a QWP (0°) and finally through an analyzer (-45°).

$$\begin{aligned}\begin{pmatrix} \mathbf{E}_x \\ \mathbf{E}_y \end{pmatrix} \;=\; & \frac{1}{2}\begin{pmatrix} 1 & -1 \\ -1 & 1 \end{pmatrix}\cdot\begin{pmatrix} e^{i\left(\frac{\pi}{4}\right)} & 0 \\ 0 & e^{-i\left(\frac{\pi}{4}\right)} \end{pmatrix}\cdot \\ & \begin{pmatrix} \cos(\theta) & \sin(\theta) \\ -\sin(\theta) & \cos(\theta) \end{pmatrix}\cdot\begin{pmatrix} e^{i\frac{S}{2}} & 0 \\ 0 & e^{-i\frac{S}{2}} \end{pmatrix}\cdot\begin{pmatrix} \cos(\theta) & -\sin(\theta) \\ \sin(\theta) & \cos(\theta) \end{pmatrix}\cdot \\ & \begin{pmatrix} e^{i\left(\frac{\pi}{4}\right)}\left(1+i\frac{\Delta}{2}\right) & 0 \\ 0 & e^{-i\left(\frac{\pi}{4}\right)}\left(1-i\frac{\Delta}{2}\right) \end{pmatrix}\cdot\begin{pmatrix} \cos\left(\frac{\pi}{4}\right) & \sin\left(\frac{\pi}{4}\right) \\ -\sin\left(\frac{\pi}{4}\right) & \cos\left(\frac{\pi}{4}\right) \end{pmatrix}\cdot \\ & \begin{pmatrix} e^{i\frac{A}{2}} & 0 \\ 0 & e^{-i\frac{A}{2}} \end{pmatrix}\cdot\begin{pmatrix} \cos\left(\frac{\pi}{4}\right) & -\sin\left(\frac{\pi}{4}\right) \\ \sin\left(\frac{\pi}{4}\right) & \cos\left(\frac{\pi}{4}\right) \end{pmatrix}\cdot\begin{pmatrix} 1 \\ 0 \end{pmatrix}\end{aligned} \tag{G.6}$$

where $A = B\cos(\omega t)$, B, and ω are the the amplitude and the frequency of the oscillations set by the PEM.

From this we obtain the following expression proportional to the intensity, (only first order terms were included in the expression),

$$\begin{aligned}\mathbf{E}\cdot\mathbf{E}^* \propto\; & \tfrac{1}{2}+\tfrac{1}{2}\sin(A)(\Delta\;\cos(S)+\cos(2\theta)\sin(S)) \\ & +\tfrac{1}{2}\sin(S)\cos(A)\sin(2\theta)\end{aligned} \tag{G.7}$$

where $A = B\cos(\omega t)$, which yields

$$\begin{aligned}\mathbf{E}\cdot\mathbf{E}^* = \; & \tfrac{1}{2} + J_1(B)(\Delta\ \cos(S) + \cos(2\theta)\sin(S))\cos(\omega t) \\ & -J_2(B)\sin(S)\sin(2\theta)\cos(2\omega t) + \ldots\ . \end{aligned} \tag{G.8}$$

With the signals at the first and second harmonic being,

$$\begin{aligned} R_1 &= J_1(B)(\Delta\cos(S) + \cos(2\theta)\sin(S)) \\ R_2 &= -J_2(B)\sin(S)\sin(2\theta) \end{aligned} \tag{G.9}$$

This shows how small retardance errors in the alignment translate to R_1.

H. MINIMIZING SYSTEM OVER SAMPLE

The expressions for a desired measurement of Δ across the sample is presented in this appendix.

$$\begin{pmatrix} \mathbf{E}_x \\ \mathbf{E}_y \end{pmatrix} = \frac{1}{2}\begin{pmatrix} 1 & -1 \\ -1 & 1 \end{pmatrix}\begin{pmatrix} e^{i\frac{\pi}{4}} & 0 \\ 0 & e^{-i\frac{\pi}{4}} \end{pmatrix}\begin{pmatrix} \cos(\gamma) & \sin(\gamma) \\ -\sin(\gamma) & \cos(\gamma) \end{pmatrix} \begin{pmatrix} e^{i\frac{S}{2}} & 0 \\ 0 & e^{-i\frac{S}{2}} \end{pmatrix}\begin{pmatrix} \cos(\gamma) & -\sin(\gamma) \\ \sin(\gamma) & \cos(\gamma) \end{pmatrix}\begin{pmatrix} \cos(\theta) & \sin(\theta) \\ -\sin(\theta) & \cos(\theta) \end{pmatrix} \begin{pmatrix} e^{i\frac{\delta}{2}} & 0 \\ 0 & e^{-i\frac{\delta}{2}} \end{pmatrix}\begin{pmatrix} \cos(\theta) & -\sin(\theta) \\ \sin(\theta) & \cos(\theta) \end{pmatrix}\begin{pmatrix} e^{i\frac{\pi}{4}} & 0 \\ 0 & e^{-i\frac{\pi}{4}} \end{pmatrix} \begin{pmatrix} \cos\left(\frac{\pi}{4}\right) & \sin\left(\frac{\pi}{4}\right) \\ -\sin\left(\frac{\pi}{4}\right) & \cos\left(\frac{\pi}{4}\right) \end{pmatrix}\begin{pmatrix} e^{i\frac{A}{2}} & 0 \\ 0 & e^{-i\frac{A}{2}} \end{pmatrix} \begin{pmatrix} \cos\left(\frac{\pi}{4}\right) & -\sin\left(\frac{\pi}{4}\right) \\ \sin\left(\frac{\pi}{4}\right) & \cos\left(\frac{\pi}{4}\right) \end{pmatrix}\begin{pmatrix} 1 \\ 0 \end{pmatrix} \tag{H.1}$$

where $A = B\ \cos(\omega t)$, δ and θ are the retardance and orientation for the first element, and S and γ are the retardance and orientation for the second element. The resulting electric field is,

$$\begin{pmatrix} \mathbf{E_x} \\ \mathbf{E_y} \end{pmatrix} = (\tfrac{1}{2}(i\cos(\gamma)+\sin(\gamma))(\cos(\tfrac{\delta}{2})(\cos(\tfrac{1}{2}(A+S-2\gamma)) - i\sin(\tfrac{1}{2}(A-S-2\gamma))) + \sin(\tfrac{\delta}{2})(\cos(\tfrac{1}{2}(A-S+2\gamma-4\theta)) + i\sin(\tfrac{1}{2}(A+S+2\gamma-4\theta))))) \begin{pmatrix} 1 \\ -1 \end{pmatrix} \tag{H.2}$$

The intensity is proportional to

$$\begin{aligned} \mathbf{E}\cdot\mathbf{E}^* \propto 2(&\frac{1}{4} - \frac{1}{8}\sin(A)(\cos(2\gamma)(1+\cos(\delta))\sin(S) - \\ &2\cos(2\gamma-4\theta)\sin(S)\sin^2\left(\frac{\delta}{2}\right) + \\ &2\cos(S)\cos(2\theta)\sin(\delta)) + \frac{1}{8}\cos(A)((1+\cos(\delta))\sin(S)\sin(2\gamma) + \\ &2\sin(S)\sin^2\left(\frac{\delta}{2}\right)\sin(2\gamma-4\theta) + 2\cos(S)\sin(\delta)\sin(2\theta))) \end{aligned} \tag{H.3}$$

We then obtain signal at the first harmonic (R_1),

$$\begin{aligned} R_1 = &-\tfrac{J_1(B)}{2}(\cos(2\gamma)(1+\cos(\delta))\sin(S) - \\ &2\cos(2\gamma-4\theta)\sin(S)\sin^2\left(\tfrac{\delta}{2}\right) + 2\cos(S)\cos(2\theta)\sin(\delta)) \end{aligned} \tag{H.4}$$

And signal at the second harmonic (R_2),

$$\begin{aligned} R_2 = &\tfrac{J_2(B)}{2}(1+\cos(\delta))\sin(S)\sin(2\gamma) + 2 \\ &\sin(S)\sin^2\left(\tfrac{\delta}{2}\right)\sin(2\gamma-4\theta) + 2\cos(S)\sin(\delta)\sin(2\theta))) \end{aligned} \tag{H.5}$$

Both θ and γ are made equal through the alignment process. We then obtain,

$$\frac{R_1}{DC} = -J_1(B)\cos(2\gamma)\sin(S+\delta) \tag{H.6}$$

and

$$\frac{R_2}{DC} = J_2(B)\sin(2\gamma)\sin(S+\delta). \tag{H.7}$$

Hence we can determine both ΔS and relative orientation from the expressions above.

I. BIREFRINGENCE

The birefringence ($n_e - n_o$) is shown how to be extracted from the retardance in an anisotropic material. An expression relating the birefringence to the indices of refraction along the different directions of the object will be derived. The phase shift in the electromagnetic radiation, also known as the retradance (S),

$$\Delta S = \frac{2\pi \Delta n t}{\lambda} \tag{I.1}$$

where Δn is the difference in the indices of refraction, t is the thickness of the material and λ is the wavelength of light. Depending on the orientation ϕ of an anisotropic material's indicatrix, the light passing through will emerge in two beams, the extraordinary and ordinary rays, shown in figure I.1. For such a system the Δn becomes ($n_e - n_o$). Yielding,

$$\Delta S = \frac{2\pi (n_e - n_o) t}{\lambda} \tag{I.2}$$

The light propagating in the ordinary direction a distance t maintains the index of refraction of the perpendicular component of the indicatrix ($n_\perp$). The extraordinary ray experiences and effective index of refraction (n_{eff}) along the path distance equivalent to $\frac{t}{\cos(\phi)}$. This yields the expression for the birefringence

$$(n_e - n_o) = \frac{n_{\text{eff}}}{\cos(\psi)} - n_\perp. \tag{I.3}$$

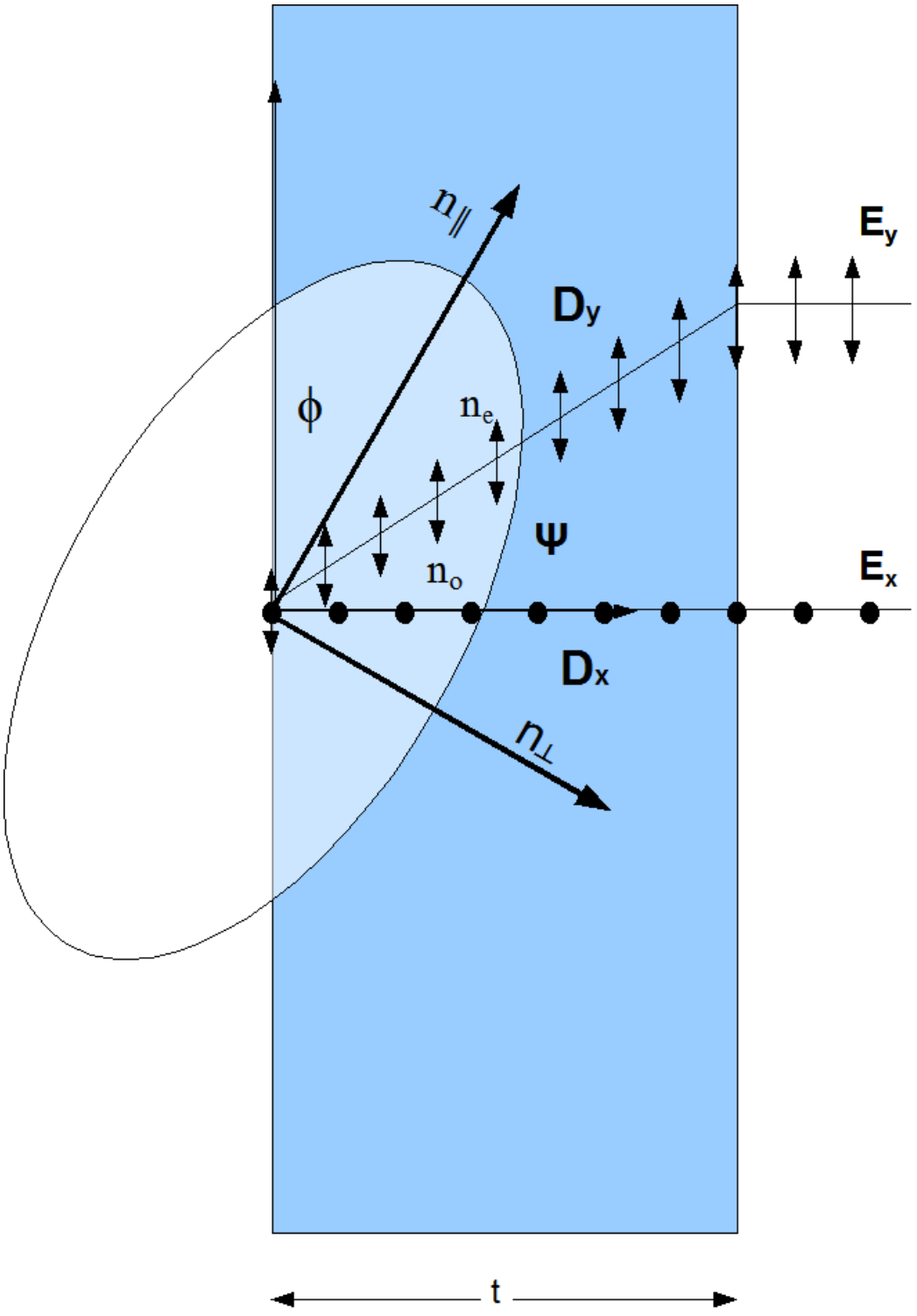

Figure I.1. Representation of the extraordinary and ordinary rays, passing through an anisotropic material, with its indicatrix oriented at an angle ϕ.

By using the properties of an ellipse where $\tan(\xi) = \frac{{n_\parallel}^2}{{n_\perp}^2}\cot(\phi)$ (ξ is the angle the extraordinary ray makes with direction along $n_\parallel$) and $\psi = \frac{\pi}{2} - \phi - \xi$. We then obtain

$$\frac{1}{\cos(\psi)} = \frac{1}{\sin(\arctan(\frac{{n_\parallel}^2}{{n_\perp}^2}\cot(\phi)) + \phi)}. \tag{I.4}$$

We then can solve for n_{eff}, yielding

$$n_{\text{eff}} = \frac{n_\perp n_\parallel}{\sqrt{{n_\perp}^2\sin^2(\phi) + {n_\parallel}^2\cos^2(\phi)}}. \tag{I.5}$$

The final result becomes,

$$\frac{n_{\text{eff}}}{\cos(\psi)} - n_\perp = \frac{1}{\sin(\arctan(\frac{{n_\parallel}^2}{{n_\perp}^2}\cot(\phi)) + \phi)}\frac{n_\perp n_\parallel}{\sqrt{{n_\perp}^2\sin^2(\phi) + {n_\parallel}^2\cos^2(\phi)}} - n_\perp. \tag{I.6}$$

J. MUSCOVITE BIREFRINGENCE CALCULATION

An in depth calculation to determine the birefringence of Muscovite using its indicatrix is performed in this appendix. First the optical data for a Muscovite crystal, Z = b; X $\wedge$ c = $0° - 5°$; Y $\wedge$ a = $1° - 3°$ n_α = 1.552-1.576, n_β = 1.582-1.615, n_γ = 1.587-1.618 [1].

Where n_γ is along the *b*-axis, n_β along the *a*-axis and n_α along the *c*-axis of the bravis lattice of the crystal.

We can solve for the birefringence $(n_e - n_o)$ and determine the following expression from the parameters given

$$n_e - n_o = \frac{n_\alpha n_\gamma}{\sqrt{{n_\gamma}^2 \sin^2(\delta) + {n_\alpha}^2 \cos^2(\delta)}} - n_\beta, \tag{J.1}$$

where δ is the angle the *c*-axis makes with the *a*-axis, and all indices of refraction correspond to those of the indicatrix. The expression found in equation J.1 can be used to determine $n_e - n_o$ to be ≈ 0.0025 for: $\delta = 5°$, $n_\alpha = 1.552$, $n_\beta = 1.615$, $n_\gamma = 1.618$. We can use figure J.1 to illustrate the possible values for $n_e - n_o$ as the angle of the *c*-axis is changed. The area under the curve consist of possible value for the birefringence of the crystal.

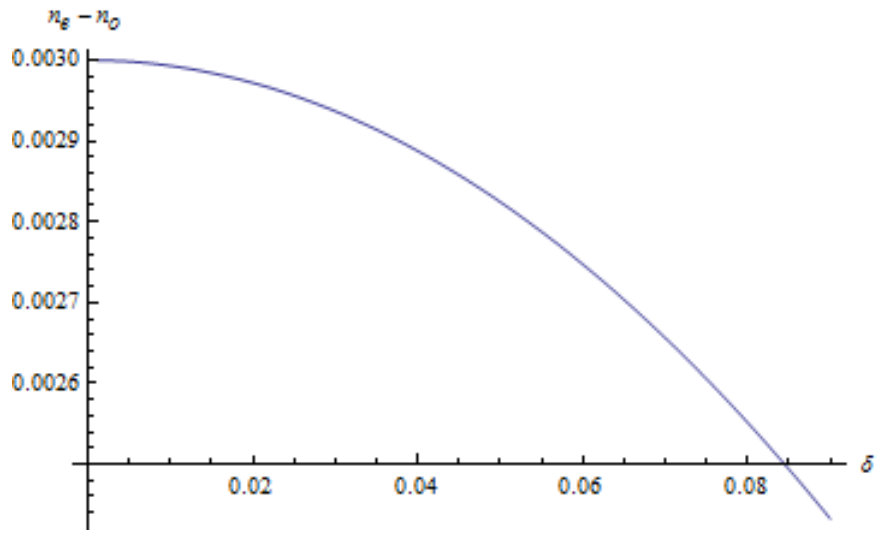

Figure J.1. Graph of $n_e - n_o$ as a function of δ, illustrating how the resulting values change as the angle the c-axis makes with the a-axis increases.

K. APPLICATION NOTES

This appendix contains a few applications notes to assist with a few experimental details presented in this thesis.

K.1 Lock-in Amplifier Signal

When analyzing the signal from the lock-in amplifiers it is be useful to understand the function it uses to measure the signal. A lock-in amplifier first amplifies the input signal and multiplies that signal by a pure sine function at the frequency determined by an input reference signal. The resulting signal is of the form,

$$A_{s,r} \sin(\omega_s t + \theta_s) \sin(\omega_r t + \theta_r) \tag{K.1}$$

where $A_{s,r}$ is the amplitude of the product of the reference and signal voltage amplitudes. Also, ω_s, ω_r, θ_s, and θ_r are the frequency of the signal and reference as well as their corresponding phases.

From this we can use the identity,

$$sin(A+B)sin(C+D) = \frac{1}{2}(cos((A-C)+(B-D)) - cos(A+B+C+D)) \tag{K.2}$$

Hence equation K.1 can be written as,

$$\frac{A_{s,r}}{2}(\cos((\omega_s t - \omega_r t) + (\theta_s - \theta_r)) - \cos(\omega_s t + \omega_r t + \theta_s + \theta_r)) \tag{K.3}$$

The condition, $\omega_s = \omega_r$ is sought after. Using a low-pass filter, the frequencies above the DC term of this signal can be filtered out. This leaves a phase sensitive equation,

$$A_{out} = \frac{A_{s,r}}{2}\left(\cos\left(\varphi\right)\right) \tag{K.4}$$

where information about the amplitude (A) and the effective phase $\varphi = \omega_s t - \omega_r t$ can be extracted. The data expressed is either in terms of A and φ or $x = Acos(\varphi)$ and $y = Asin(\varphi)$.

This gives the lock-in amplifier the advantage of measuring filtered small oscillating signals, with phase sensitive capabilities. In the experiments presented in this work, the lock-in is used to measure signals at various frequencies. The signal created by the PEM is a sine wave referenced at $\approx$ 41kHz. The rms of the measured signal is returned (for a sine wave is $\frac{A}{\sqrt{2}}$). For the DC component of our signal from the photo detector, the signal is mechanically choppped at a particular frequency that ranges from 300 - 1000 Hz. The resulting signal is a square wave function, which can be expressed in terms of a Fourier series,

$$\frac{2A}{\pi}\left(\sin(\omega \mathrm{t}) + \frac{\sin(3\omega \mathrm{t})}{3} + \frac{\sin(5\omega \mathrm{t})}{5} + ...\right) \tag{K.5}$$

where with the lock-in only the rms of the first component is measured, $\frac{A}{2}\left(\sin(\omega \mathrm{t})\right)$. This results in a final signal of $\frac{R_1}{DC}$ or $\frac{R_2}{DC}$ to have a form of,

$$I_\omega = \frac{R_1}{DC} \longrightarrow \frac{R_1\pi}{2DC} \qquad \text{and} \qquad I_{2\omega} = \frac{R_2}{DC} \longrightarrow \frac{R_2\pi}{2DC} \tag{K.6}$$

Understanding the principles of lock-in measurements, correlates with extracting the correct information from the signals. With phase sensitive detection background noise from any additional system instabilities that may exist are diminished using this instrument in the measurements.

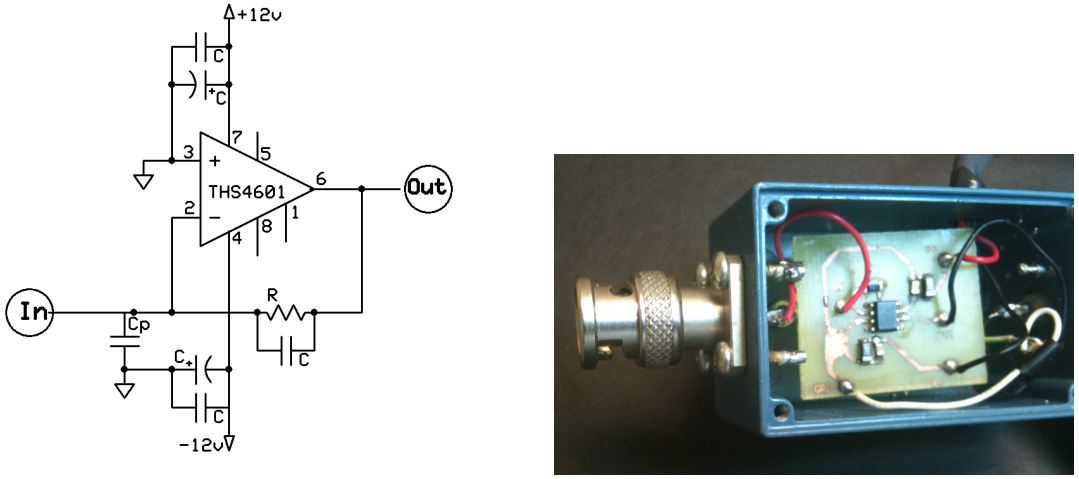

(a) (b)

Figure K.1. Schematic and picture of the tranimpedance amplifier. a) Schematic of the current amplifier. With R being a resistance of ≈ 1 MΩ, the capacitors to ground on the power supply inputs were .1 μF and 6.8 μF (electrolytic). b) Picture of the transimpedance amplifier used in the experiments.

K.2 Signal Detection

To eliminate the impedance matching problems that occur when trying to measure currents on different instruments, it was desirable to amplify and convert the signal to a voltage before being analyzed. To do so an operational amplifier was utilized in the transimpedance configuration. A THS4601 was used to obtain a low noise high gain over the set of frequencies needed in our experiment. Figure K.2 displays images of the circuit design and picture of the apparatus.

K.3 Feedback Control

How the feedback control for the piezo stage was implemented will now be discussed. As was describe in the chapter outlining NSOM, the piezo tuning fork and NSOM probe were oscillated using a driving frequency on resonance from a voltage generator. A lock-in measurement was performed to monitor the amplitude of the oscillations. That signal was then sent to a feedback loop, seen in figure K.2. A set point was then selected for the desired amplitude drop. The feedback loop subtracted the amplitude and set point signals. The voltage then swings either positive or negative depending on the difference between the set point and signal. The resulting signal then was sent to a piezo controller, seen in figure K.3, where it was then used to control the position of the stage. With all of the components in the feedback system the tip to sample distance is maintained.

K.4 Temperature Controlled Measurements

K.4.1 Probe Resonance Behaviour

When performing temperature controlled NSOM measurements it was found important to note the behaviour of the resonance response of the quartz tuning fork and probe. The NSOM probe heated a consequence of the increase in the temperature in the chamber. Because of this the materials were expected to expand and the properties to slightly change. It was also important to determine if the cyanoacrylate adhesive would hold under the temperature increase, due to its maximum operating temperature of $\approx 55°C$. Figure K.4.1 displays a set of graphs that represent the resonance response of a tuning fork and probe at different temperatures. In those graphs the quality factor (Q) decreases along with a frequency shift upward as the temperature rises. Over the experimental temperature range (from 22°C to 45°C),

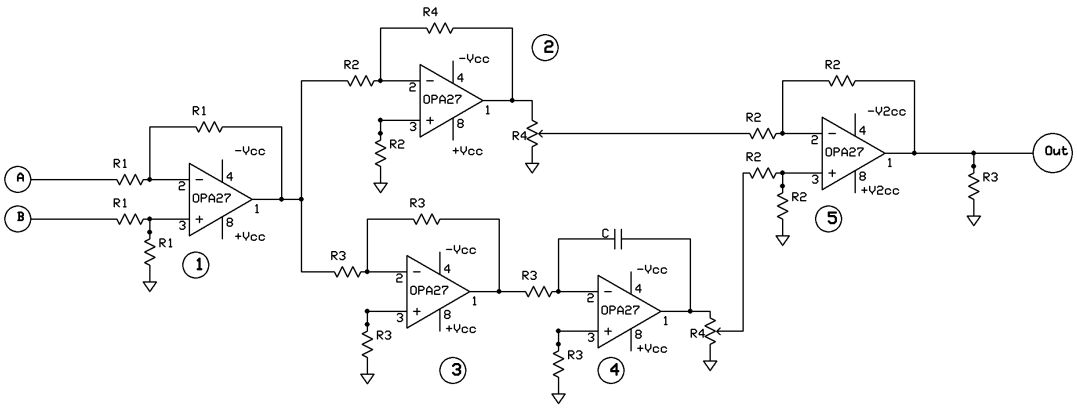

Figure K.2. Schematic of the feedback loop used to subtract the two signals and control the position of the stage. Part 1 is used to subtract signals at point A (the set point) and B (the monitored resonance signal). That signal is then inverted at part 2 and factored down by ≈ 8 at part 3. Part 4 integrates the signal at a rate proportional to the capacitance across the operational amplifier. The signals from part 4 and 5 are then subtracted at part 5 where it is then trimmed to adjust the maximum and minimum output voltages.

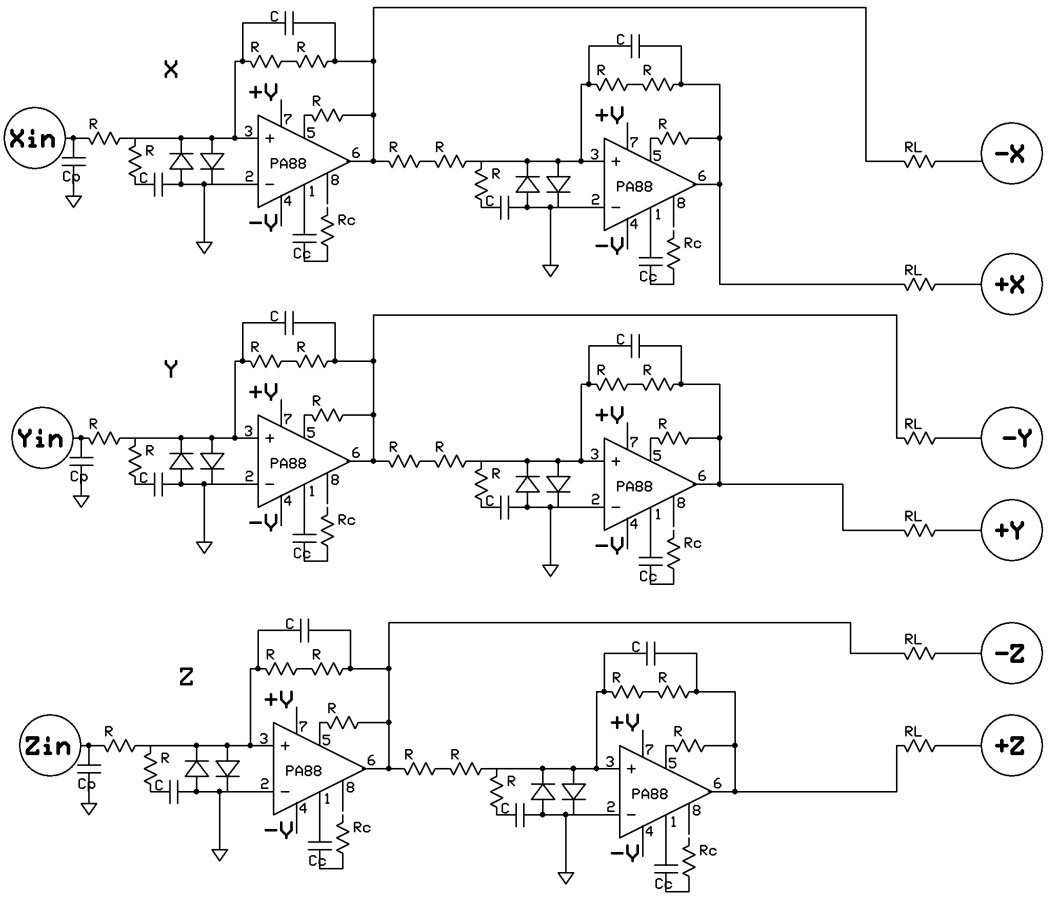

Figure K.3. Schematic of the circuit used to amplify the signal from the feedback loop and supply the voltages to the piezo stage. R is 100 kΩ, the supply voltage (± V) is ≈ 130 V, R_L is ≈ 5 kΩ, $R_c = 100$ Ω, $C_c = 68$ pF, $R_1 = 20$ Ω, $R_2 = 5$ kΩ, and the power amplifiers used are PA88.

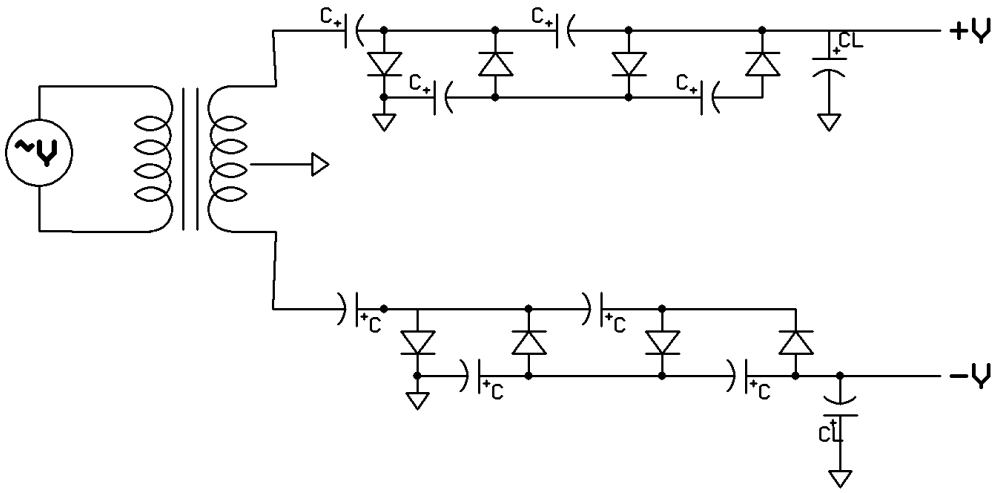

Figure K.4. Schematic of the bipolar power supply for the amplifier. The original voltage was quadrupled from a transformer to achieve a maximum voltage of $\approx \pm$ 130 V. Large capacitors ($C_L \approx 1000$ μF) on the output were used to trim the voltage fluctuations remaining after the last stage of the circuit.

a frequency shift of $\approx$ 80 Hz could be observed, which translates to $\approx 3.2\ \frac{Hz}{C^{\circ}}$. Also the Q decreases by a fourth, which at first may sound like a bad thing, but allows for more stability in the measurement under the condition its signal is over the noise floor.

Retuning the system before engagements of the sample is crucial. Though there are frequency shifts, it was not substantial enough to cause system crashes and disengagements. In fact, through practice it has been found that, once the system has stabilized the shift was not as significant and remains fairly manageable.

K.4.2 Temperature Control Circuit

The schematic of the temperature control circuit is presented (see figure K.4.2). The device compares the signal of the sensor to the desired value, where the two are subtracted. The device swung a voltage up or down to control the voltages on the gates of the two transistors, which determined the direction of the current flow through the thermal electric cooler (TEC). The power supply that fed the TEC power is displayed in figure K.4.2. The power resistors were used to regulate the maximum current through the TEC. Initially current values were $\sim$1.5 A, where that value would typically drop as the TEC's resistance increased with temperature.

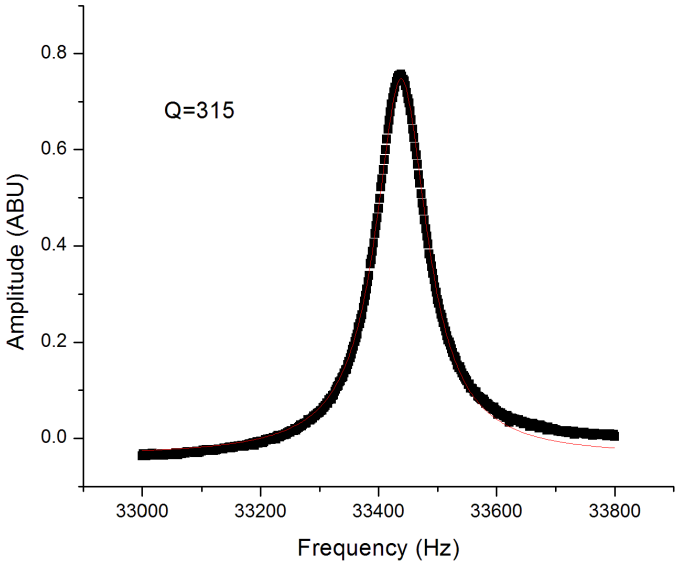

(a)

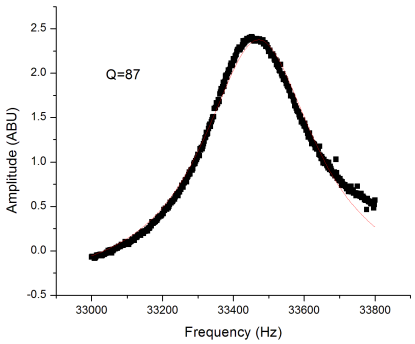

(b)

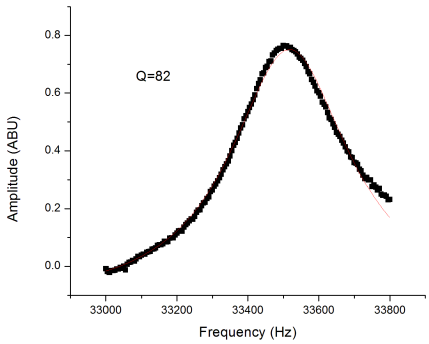

(c)

Figure K.5. Graphs of the resonance response of a NSOM probe at different temperatures. a) Resonance curve at room temperature, having a central peak at 33438 Hz and a Q of ≈ 315. b) Resonance curve at 32° C , having a central peak at 33471 Hz and a Q of ≈ 87. c) Resonance curve at 45° C, having a central peak at 33517 Hz and a Q of ≈ 82.

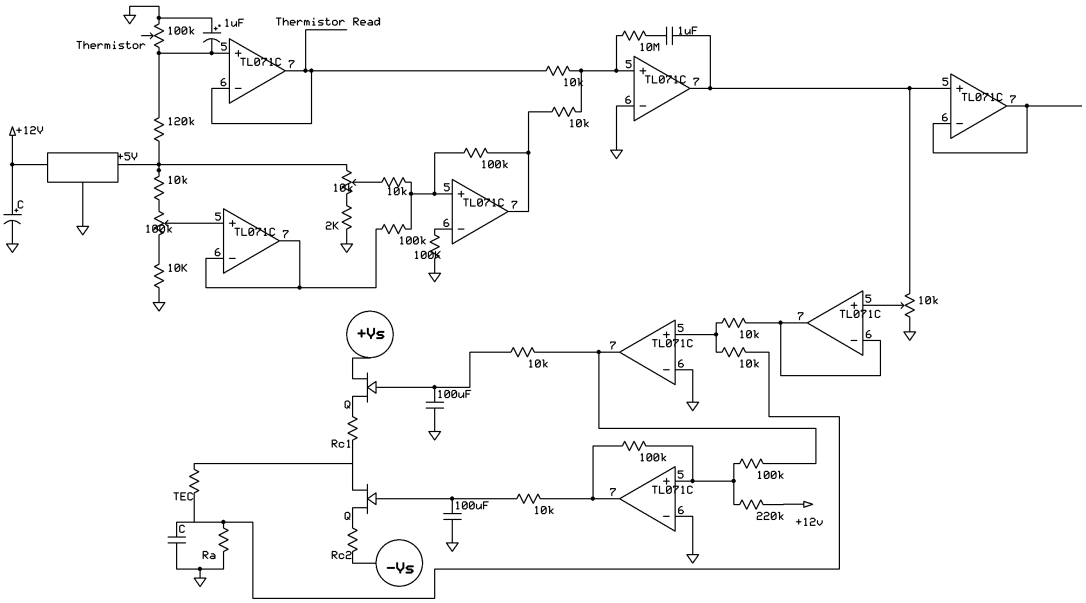

Figure K.6. Schematic of the temperature control circuit used in the experiment. A resistance was used as the set value desired for the thermistor. The two were subtracted and integrated to swing the voltage positive or negative. When this happens the voltage on the gates of the transistors were open or closed to allow current to flow different directions through the TEC. This either heated or cooled the sample, depending on the current direction.

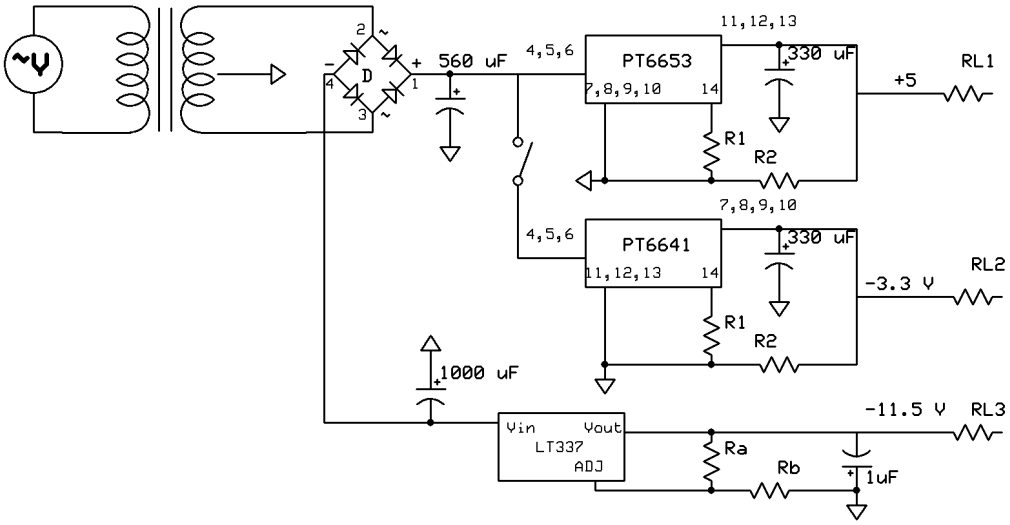

Figure K.7. Schematic of the power supply circuit used to power the TEC (see figure K.4.2). The resistors R_1 and R_2 were used to adjust the output voltage of the regulators PT6653 and PT6641. The resistors R_a and R_b were used to adjust the output voltage of the LM 337 regulator. The final setup only used the LM 337, due to the PT6641 failing over extensive use.

VITA

VITA

Merrell A. Johnson

Education

AUGUST 2011 **Ph.D.** — Major: Physics
Indiana University-Purdue University, *Indianapolis, IN*
Thesis: "Near-Field Investigations of the Anisotropic Properties of Supported Lipid Bilayers"
— Advisor: Prof. RICARDO DECCA

MAY 2005 **M.S.** — Major: Physics
Indiana University-Purdue University, *Indianapolis, IN*
Thesis: "Polarization Extinction Ratio's Contributions in Near-Field Birefringence Studies on Optically Transparent Materials" — Advisor: Prof. RICARDO DECCA

MAY 2002 **A.B.** — Major: Physics / Mathematics — Minor: Music
Wabash College, *Crawfordsville, IN*

Publications

Compartmentalizing a lipid bilayer by tuning lateral stress in a physisorbed polymer-tethered membrane

Soft Matter, 2010, Volume 6, 2723-2732 Amanda P. Siegel, Michael J. Murcia, Merrell A. Johnson, Rainer Jordan, Jrgen Rhe and Christoph A. Naumann

Characterization of iron nanoparticles synthesized by high pressure sputtering

Materials Letters, Volume 63, Issue 8, 31 March 2009, Pages 715-717 Jeff Carvell, Elijah Ayieta, Merrill Johnson and Ruihua Cheng

Dynamics of topological defects in the $L_{\beta'}$ phase of 1,2 dipalmitoylphosphatidycholine bilayers

Optics Communications, Volume 281, Issue 7, 1 April 2008, Pages 1870-1875 M.A. Johnson and R.S. Decca

Teaching Experience

Graduate Lecture and Recitation Instructor, Indiana University Purdue University Indianapolis, Department of Physics Indianapolis, IN *Summer 2010*

Duties included: Co-lecturing for an intense 8 week second semester non-calculus base physics course for technology majors. Personal lectures included topics on Magnetism, AC circuits, and Optics. Lecture duties also involved writing and grading exams and meeting with students during office hours. Recitation duties included presenting solutions to homework problems, personally assigning additional problems and assisting the students with conceptual questions.

Graduate Teaching Assistant, Indiana University Purdue University Indianapolis, Department of Physics Indianapolis, IN *2002-05, 2007-present*

Duties include: Facilitating undergraduate physics labs, assisting and supervising students with introductory physics experiments. Department tutoring, instructing and resolving experimental inquiries provided by students enrolled in numerous beginning undergraduate physics courses. Recitation instructor, delivering creative explanations to students assignment inquiries, utilizing numerous strategies to accommodate students diverse learning needs.

Experimental Competence

Microscopy skill sets include Atomic Force, Magnetic Force, Near Field Optical, Scanning Electron, and Confocal Imaging techniques.
Non-imaging techniques include Small Angle X-ray Scattering and Differential Scanning Calorimetry experiments. Thin film deposition of various metals (Aluminium, Chromium, and Copper), and proficiency utilizing a lathe and milling machinery.
Programming capabilities include Java, C, C++, and LabView. Program knowledge includes AutoCAD, Mathematica, Maple, Origin, and various imaging software.
Competency with various circuit designs and printed board constructions.
List of projects include: rebuilt piezo stage and high voltage amplifier for near-field scanning system, designed and fabricated all electrical components for a temperature controller and chamber for temperature controlled experiments. Wrote all LabView software for data acquisition and controlling near-field microscope.

Current Research and Scientific Interest

My research studies 1^{st} order phase transitions in lipid membrane systems. Because fatty acids are anisotropic in nature, we are able to use a polarization modulation technique to detect the orientation changes that occur when they transition from the gel to liquid disorder state. We use a near-field optical microscope to further enhance our lateral resolution to investigate events on the order of 100nm. A few other interests include non-linear optical properties in materials. (e.g. multiple-photon microscopy or second harmonic generation), quantum optics, and various other areas of condense matter.

Awards

GAANN Fellowship *2008-present*

Outstanding Graduate Student Award- *2011*

IUPUI Physics Department

American Association of Physics teachers (AAPT) 2009 *2009*

Outstanding teaching assistant of the year

Indiana University Purdue University Indianapolis *2005-2008*

School of Science Deans Fellowship

Presentations

Biophysical Society Meeting Near-Field studies on molecular orientation of 1,2-dipalmitoylphosphatidylcholine (DPPC) bilayers in the gel state February 18th -22th 2006 Salt Lake City, UT

Frontiers in Biological Membranes Near-Field studies on molecular orientation of 1,2-dipalmitoylphosphatidylcholine (DPPC) bilayers in the gel state October 16-18 2008 West Lafayette, IN

National Society of Black and Hispanic Physicist Near-Field structural studies of lipid bilayers February 11th 15th 2009 Nashville, TN

American Physical Society Meeting Near-Field structural studies of lipid bilayers March 15th-20th 2009 Pittsburg, PA

Biophysical Society Meeting Near-Field structural studies of lipid bilayers February 20-24, 2010 San Francisco, CA

Meeting of the Prairie Section of the APS Near-Field Studies of Temperature Induced Structural changes in Supported Lipid Bilayer Systems Novemeber 18-20, 2010 Chicago, IL

IUPUI Physics Department Colloquium Near-Field Studies of Temperature Induced Structural Changes in Supported Lipid Bilayer Systems January 27th 2011 Indianapolis, IN

Indiana Academy of Science Annual Meeting Near-Field Studies of Temperature Induced Structural Changes in Supported Lipid Bilayer Systems March 4-5 2011 Indianapolis, IN